



저작자표시-비영리-변경금지 2.0 대한민국

이용자는 아래의 조건을 따르는 경우에 한하여 자유롭게

- 이 저작물을 복제, 배포, 전송, 전시, 공연 및 방송할 수 있습니다.

다음과 같은 조건을 따라야 합니다:



저작자표시. 귀하는 원저작자를 표시하여야 합니다.



비영리. 귀하는 이 저작물을 영리 목적으로 이용할 수 없습니다.



변경금지. 귀하는 이 저작물을 개작, 변형 또는 가공할 수 없습니다.

- 귀하는, 이 저작물의 재이용이나 배포의 경우, 이 저작물에 적용된 이용허락조건을 명확하게 나타내어야 합니다.
- 저작권자로부터 별도의 허가를 받으면 이러한 조건들은 적용되지 않습니다.

저작권법에 따른 이용자의 권리는 위의 내용에 의하여 영향을 받지 않습니다.

이것은 [이용허락규약\(Legal Code\)](#)을 이해하기 쉽게 요약한 것입니다.

[Disclaimer](#)

Doctor of Philosophy

**ENGINEERING THERMOELECTRIC PROPERTIES OF TIN
SELENIDE SINGLE CRYSTAL, POLYCRYSTAL, AND EPITAXIAL
THIN FILM**

**THE GRADUATE SCHOOL
OF THE UNIVERSITY OF ULSAN**

**Department of Physics
Nguyen, Van Quang**

**ENGINEERING THERMOELECTRIC PROPERTIES OF TIN
SELENIDE SINGLE CRYSTAL, POLYCRYSTAL, AND EPITAXIAL
THIN FILM**

Supervisor Sunglae Cho

A Dissertation

**Submitted to
the Graduate School of the University of Ulsan
In partial Fulfillment of the Requirements
for the Degree of**

Doctor of Philosophy in Physics

by

Nguyen, Van Quang

**Department of Physics
Ulsan, Korea
May 2018**

**ENGINEERING THERMOELECTRIC PROPERTIES OF TIN
SELENIDE SINGLE CRYSTAL, POLYCRYSTAL, AND
EPITAXIAL THIN FILM**

This certifies that the dissertation
of Van Quang Nguyen is approved.

Professor Soon-Cheol Hong, Soon Cheol Hong

Committee Chairman.

Professor Park Hyo-yeol, Hyo yeol park

Committee Member.

Professor Yong-Soo Kim, Kim Yong Soo

Committee Member.

Professor Jungdae Kim, Kim

Committee Member.

Professor Sunglae Cho, Sunglae cho

Committee Member.

Department of Physics

University of Ulsan, Ulsan, Korea

May 2018

ACKNOWLEDGMENT

First of all, I would like to present my grateful to my advisor Professor Sunglae Cho for his support and generous guidance me over the years.

I would like to thank all Professors in department of Physics, University of Ulsan who have lectured me and helped me during my Ph.D period.

I would like to thank Mr. Cheng Chang, Professor Li-dong Zhao, Dr. Ji Eun Lee, and Dr. Su-dong Park for their time and effort to help me on thermoelectric measurements. I also appreciated Ms. Thi Ly Trinh and Professor Jungdae Kim for their efforts and discussions on STM experiments. I would like to thank Dr. Christian Meny for his efforts and discussions on magnetic experiments.

I would like to thank all lab-members for their help on growing sample and sharing knowledges as well as experiences. I would like to thank all my friends who usually beside and encourage me.

I would like to thank my wife, Dang Thi Le Tuyen, for her understanding, encouragements, patients and her time to take care our daughter Thuy Anh Nguyen (호아니) as well as her husband.

Finally, last but not least, we would like to thank our grandparents, our parents, ours brothers and sisters who always encourage us and help us to take care our daughter.

This work was supported by the National Research Foundation of Korea [NRF-2009-093818 and NRF-2014R1A4A1071686], by 2011 Research Fund of University of Ulsan, by the National Research Foundation of Korea [NRF-2009-093818 and NRF-2014R1A4A1071686], by the Korea Evaluation Institute of Industrial Technology (KEIT) funded by the Ministry of Trade, Industry and Energy (MOTIE) (Project No. 10050296, Large scale (Over 8^{cm}) synthesis and evaluation technology of 2-dimensional chalcogenides for next generation electronic devices).

ABSTRACT

Nowadays, the global climate is drastically changed due to the use of fossil fuels for transport and energy generation. This situation leads to the increasing research on alternative sources of energy field. Thermoelectric (TE) modules which convert heat energy directly into electrical energy without any moving parts are good candidate for this purpose. Historically, the efficiency of these devices is still very low due to the limit of material's thermoelectric figure of merit ZT . Along a hundred years historical of thermoelectricity research, many efforts have been made to improve the thermoelectric device's efficiency by improving the material's thermoelectric figure of merit ZT . However, this is not an easy job due to the interrelation between Seebeck coefficient S , electrical conductivity σ , and thermal conductivity κ . To optimize these parameters for maximize ZT , band engineering, complex crystal, nano-structures, nano-wire, nano-tube, superlattices etc., approaches have been made aiming on the "electron - crystal" and "phonon - glass" concepts. Bismuth telluride (Bi_2Te_3) and lead telluride (PbTe) have been found to be the best TE material for TE device applications at room temperature and above with $ZT \sim 1$, respectively and still being used in commercial TE devices. These materials are both binary but contain expensive and toxic elements (Bi and Pb). Researchers have focused on finding out alternative materials, which are economically and environmentally friendly, leading to the robust development of thermoelectric materials. In 2014, SnSe has been reported as the lowest thermal conductivity of any bulk materials assigned to its anharmonic bonding, leading to the high ZT value ($ZT = 2.6$ in un-doped p-type and $ZT = 2.2$ in Bi-doped n-type SnSe). It is a layered material with a weak Van de Waals bonding between layers along a-axis. This very weak bonding is one of the main reasons for the low lattice thermal conductivity along a-axis. Our group working on 2D layered chalcogenide materials such as: SnSe, GaSe, SnSe₂, SnS, GeS, GeSe, GeTe, SnTe, GaTe etc., focusing on

their thermoelectric properties. There are two unsolved questions concerning the SnSe system relate to its ultralow thermal conductivity and its low mass density (5.43 g/cm^3) compare to that obtained from neutron diffraction (6.18 g/cm^3). Many other groups have reported different thermal conductivity and higher mass density for SnSe. There is a debate that the reported thermoelectric properties are intrinsic SnSe or not. Therefore, deeper understandings about this system are required such as effects of defects, stoichiometry, etc. This dissertation focuses on the engineering defects in SnSe single crystal from bulk to thin film form and polycrystalline SnSe and investigate the influence of the intrinsic defects on the thermoelectric properties of SnSe. Apart of this dissertation, I focus on the fabrication of mixed phase SnSe and SnSe₂ and its thermoelectric properties.

Approved: _____

Professor Sunghae Cho

TABLE OF CONTENTS

ACKNOWLEDGMENT	i
ABSTRACT.....	ii
TABLE OF CONTENTS	iv
LIST OF TABLES	ix
LIST OF FIGURES	x
CHAPTER 1: INTRODUCTION.....	1
1.1 Description of the research -----	1
1.2 List of publications -----	2
1.2.1 List of patents -----	2
1.2.2 List of journal papers -----	3
1.2.3 References-----	6
CHAPTER 2: BACKGROUND	8
2.1 Physical phenomena of thermoelectricity -----	8
2.1.1 The Seebeck effect -----	8
2.1.2 The Peltier effect -----	10
2.1.3 The Thomson effect-----	12
2.1.4 Kelvin relationship-----	12
2.1.5 Thermoelectric figure of merit -----	14
2.2 Thermoelectric devices -----	16
2.3 Thermoelectric material research-----	20
2.3.1 Brief history of thermoelectricity -----	20
2.3.2 Defects in semiconductor -----	21
2.3.3 Overview about SnSe-----	24

2.4 References	53
CHAPTER 3: EXPERIMENTS	57
3.1 Temperature controlling	57
3.1.1 PID temperature controller.....	57
3.1.2 Impedance matching	59
3.1.3 Heat transfer mechanism	61
3.2 Molecular epitaxy beam MBE for thin film growth	63
3.2.1 Ultra-high vacuum	64
3.2.2 Vacuum pumps	68
3.2.3 MBE setup	73
3.2.4 Calibrations: substrate temperature, growth rate	74
3.3 Bulk growth	75
3.3.1 Single crystal growth techniques.....	76
3.3.2 Polycrystalline growth techniques	80
3.4 Transport properties measurement systems in our lab	86
3.4.1 The Two and Four probe method for resistance measurement	86
3.4.2 The convention Hall effect.....	89
3.4.3 Low temperature measurement system	93
3.4.4 The high temperature measurement system	95
3.5 Characterizations	98
3.5.1 X-ray diffraction XRD	98
3.5.2 Reflection high energy electron diffraction (RHEED)	99
3.5.3 Thermal diffusivity and thermal conductivity: LFA, ZEM 3	100
3.6 Measurement's errors	101

3.6.1 Electrical conductivity measurement error -----	102
3.6.2 Seebeck coefficient measurement's error -----	103
3.6.3 Thermal conductivity measurement error -----	104
3.6.4 Power factor's error -----	104
3.6.5 Figure of merit's error -----	104
3.6.6 Errors of ZEM 3 -----	105
3.7 References -----	106
CHAPTER 4: ENGINEERING DEFECTS IN SnSe SINGLE CRYSTAL	108
4.1 Introduction -----	108
4.2 Experiment -----	111
4.3 Results -----	113
4.3.1 Structural analyses -----	113
4.3.2 Evidences of defects engineering -----	115
4.3.3 Thermoelectric transport properties -----	118
4.3.4 Thermal conductivity and thermoelectric figure of merit ZT -----	123
4.3.5 Anisotropic thermoelectric transport properties -----	125
4.4 Conclusion -----	127
4.5 Supplementary figures -----	129
4.6 References -----	134
CHAPTER 5: LAYERS' ROTATION AND THERMOELECTRIC TRANSPORT	
PROPERTIES OF SnSe EPITAXIAL THIN FILMS	138
5.1 Introduction -----	138
5.2 Experiment -----	140
5.3 Results -----	142

5.4 Conclusion-----	152
5.5 Supplementary figures -----	153
5.6 References -----	157
CHAPTER 6: THERMOELECTRIC PROPERTIES OF HOT PRESS Bi-DOPED N- TYPE POLYCRYSTALLINE SnSe	159
6.1 Introduction-----	159
6.2 Experiment -----	161
6.3 Results-----	163
6.4 Conclusion-----	171
6.5 References -----	172
CHAPTER 7: SYNTHESIS AND CHARACTERIZATION MICROSTRUCTURE AND THERMOELECTRIC PROPERTIES OF SnSe-SnSe₂ COMPOSITES	174
7.1 Introduction-----	174
7.2 Experiment -----	177
7.3 Results-----	178
7.4 Conclusion-----	183
7.5 References -----	184
CHAPTER 8: CONCLUSIONS	186
APPENDIX 1: ANTIFERROMAGNETIC INTERFACES IN CoFe₂O₄/Fe₃O₄ SUPERLATTICES	187
APPENDIX 2: TUNING TRANSPORT AND MAGNETIC PROPERTIES OF Co_xFe_{3-x} O₄ THIN FILMS BY Co CONTENT	203
APPENDIX 3: SEEBECK COEFFICIENT AND ELECTRICAL RESISTANCE MEASUREMENT SYSTEM (제벡계수 및 전기저항 측정장치)	217

APPENDIX 4: COMPACT HOT PRESS APPARATUS (미니 핫 프레스 장치).....232

APPENDIX 5: PATENT CERTIFICATE.....244

LIST OF TABLES

Table 2. 1. Crystallographic and thermoelectric transport parameters of SnSe at 300 K [6].	34
Table 2. 2. The formation energy of defects in different charge states under the Sn-rich condition ($E_{F,Sn}$) and Se-rich condition ($E_{F,Se}$) [14].	35
Table 3. 1. A list of vacuum levels and the corresponding pressure in Torr, Pa, and Atmosphere.	64
Table 3. 2. Root mean square speed of some gases molecule at 300 K.	65
Table 3. 3. Room temperature (300 K) mean free path of air at different pressure.	66
Table 3. 4. Time to form a monolayer at different pressure.	67
Table 5. 1. The detail of deposition rates of Sn and Se elements, growth rates and times of SnSe samples.	141

LIST OF FIGURES

Fig. 2. 1. Cumulation of charge carriers at the ends of n-type (up) and p-type (down) conductors.	10
Fig. 2. 2. Peltier effect, heat is generated at junction B and removed at junction A between conductor X and Y when an electric current I is applied from Y to X.	11
Fig. 2. 3. Thermoelectric refrigerator where a junction is heated up or cooled down, depends on the direction of applied electric current.	12
Fig. 2. 4. Conflicting relation of thermoelectric transport parameters via carrier concentration.	16
Fig. 2. 5. Thermoelectric module which can be used as a thermoelectric generator or a thermoelectric refrigerator.	17
Fig. 2. 6. Thermocouple configuration.	18
Fig. 2. 7. Differential thermocouple configuration.	19
Fig. 2. 8. Thermoelectric figure of merit ZT of state of the art commercial materials for a) n-type, b) p-type, and c) effect of dopant on the peak of ZT	21
Fig. 2. 9. Points defects in semiconductors.	22
Fig. 2. 10. Point defects in ionic crystal semiconductors [Wikipedia].	23
Fig. 2. 11. Edge dislocation (left) and screw dislocation (right) in semiconductors.	24
Fig. 2. 12. (a) A perspective view of one SnSe layer, (b) The cross-sectional view of SnSe layer shows the buckling structure, (c) Top view of SnSe layer, the identical blue and red rectangles represent the unit cell of Se and Sn atoms, respectively. Black lines represent the zigzag bonds of Se and Sn atoms, (d) Side-view of SnSe, where black rectangle represents the bulk unit cell. The layers are stacked by Van der Waals force along a-axis. The length's unit is angstroms.	

Note that, to be consistent with thermoelectric discussions, I have changed the terms *a*-axis to *b*-axis, *b*-axis to *c*-axis, and *c*-axis to *a*-axis. [11]25

Fig. 2. 13. (a - c) High-resolution topographic images for empty states, where the black rectangular represents unit cell of Sn atoms. The images are $4\text{ nm} \times 4\text{ nm}$ in size with $I_{\text{tunneling}} = 50\text{ pA}$. The numbers represent the applied sample bias. (d) Calculated STM image at sample bias of 2.0 eV . The same note as given in figure 2.12 is applied here. [11].....27

Fig. 2. 14. (a) High-resolution TEM image of single-crystal SnSe. The bottom inset is diffraction pattern along [011] zone axis; the top inset is line profile along the dotted line AB showing the d spacing of (100), (b) Simulated crystal structures of Pnma and Cmc₂m phases, viewed along [211] and [121] directions, and (c) SAED patterns at different temperatures, where B is zone axis. [6].....28

Fig. 2. 15. (a) Quasiparticle band structures of Pnma phase (left) and Cmc₂m phase (right) of SnSe with indirect band gap of 0.829 eV and direct band gap of 0.464 eV , respectively. (b) Density of states of Pnma phase (left) and Cmc₂m phase (right) of SnSe around the band gap. [13].....30

Fig. 2. 16. Grüneisen dispersion of SnSe. The inset is average Grüneisen parameters along *a*, *b* and *c* axes. [6]31

Fig. 2. 17. Calculated formation energies as a function of Fermi level (E_F) of the six intrinsic defects in SnSe under the Sn-rich (a) and Se-rich conditions (b). [14]36

Fig. 2. 18. STM image of SnSe (*b-c*) surface showing three intrinsic defects (A, A', and B). Imaging conditions sample bias $V_b = -2.0\text{ V}$ and tunneling current $I_t = 50\text{ pA}$. [20]37

Fig. 2. 19. High-resolution STM topographic images ($2.2\text{ nm} \times 2.1\text{ nm}$, $I_t = 30\text{ pA}$ and $V_b = -1.5\text{ V}$) (top), top view of relaxed structure models, where the blue, red balls and open

circles represent Se, Sn atoms, and vacancies (middle), and DFT simulated images (bottom) of (a) Sn vacancy, (b) Se vacancy, and (c) Se–Sn–Se vacancy. [20].....	38
Fig. 2. 20. Calculate (a) Band structure of bulk SnSe. Unfolded band structure of (b) a $3 \times 3 \times 1$ SnSe supercell containing 35 Sn atoms and 36 Se atoms (one Sn vacancy). (c) a $3 \times 3 \times 1$ SnSe supercell containing 36 Sn atoms and 35 Se atoms (one Se vacancy). (d) a $5 \times 6 \times 1$ SnSe slab (with a 16 \AA vacuum) consisting of 119 Sn atoms and 118 Se atoms (one Sn vacancy and two Se vacancies). The Fermi level is set to zero energy [20].	39
Fig. 2. 21. The dI/dV curves of Sn vacancy. The inset is STM image of Sn vacancy. The pink and green notes indicate the positions where the pink and green lines are obtained. The black curve is obtained from defect free position [20]......	40
Fig. 2. 22. Temperature dependent thermoelectric transport parameters (a – d) and ZT values (f) along a , b , and c – axes of SnSe. [6].....	42
Fig. 2. 23. Temperature dependent thermoelectric transport parameters (a – d) and ZT values (e) of hole doped SnSe along a , b , and c -axes in compare with SnSe un-doped. [7]	43
Fig. 2. 24. Temperature dependent electrical conductivity (a) and ZT values (b) of SnSe based composites with carbon black nano-inclusions. [33].....	44
Fig. 2. 25. Temperature dependent thermoelectric transport parameters (a - e) and ZT values (f) of rock-salt-type nanoprecipitates un-doped polycrystalline SnSe. [27].....	45
Fig. 2. 26. (a – d) Thermoelectric transport parameters as a function of temperature of Bi-doped n-type SnSe with carrier concentration of $-2.1 \times 10^{19} \text{ cm}^{-3}$ at 773 K along a , b , and c -axes. [8]	47
Fig. 2. 27. Temperature dependence of (a) Carrier density of various doping levels of Bi-doped n-type SnSe single crystal along c -axis and (b) ZT values of the highest doping level sample along a , b , and c – axes. [8]	48

Fig. 2. 28. (a) STM topographic image of Bi-doped SnSe, where the Bi dopant is indicated by dotted ellipse, (b) High resolution STM image taken from the circled areas in (a), (c) Simulated STM image of SnSe supercell with Bi dopant at Sn site. ρ in the color bar represents charge density ($e/\text{\AA}^{-3}$). Both experiment and calculation indicate the substitution of Bi atoms in to Sn site. All STM images were taken with $V_b = -1.8$ V and $I_t = 30$ pA. [8].....49

Fig. 2. 29. (a) STM topographic image on the $b-c$ plane of un-doped p-type SnSe with carrier concentration of $5.2 \times 10^{18} \text{ cm}^{-3}$ at 773 K, where Sn vacancies are indicated by dotted ellipse, (b) High resolution STM image taken from black box in (a). (c) STM topographic image on the $b-c$ plane of Bi-doped n-type SnSe with carrier concentration of $-8.7 \times 10^{18} \text{ cm}^{-3}$ at 773 K. The STM scanning conditions: (a), (b) sample bias $V_b = -1.5$ V, tunneling current $I_t = 30$ pA, (c) $V_b = -2.0$ V, $I_t = 18$ pA. [8]49

Fig. 2. 30. Thermoelectric transport parameters (a – f) and ZT values (f) as a function of temperature along the pressing direction for $\text{SnSe}_{1-x}\text{Br}_x$ ($x = 0, 0.01, 0.02, 0.03,$ and 0.04) in compare with those of I-doped SnSe and single SnSe crystals. [39].....50

Fig. 2. 31. Thermoelectric transport parameters (a – e) and ZT values (f) as a function of temperature along the pressing direction for $\text{Sn}_{1-x}\text{Pb}_x\text{Se}_{0.97}\text{Br}_{0.03}$ ($x = 0-0.3$). [39]51

Fig. 3. 1. A control loop (up) and a schematic (down) of PID controller.....58

Fig. 3. 2. Step response of P, PI, and PID controller.59

Fig. 3. 3. Electrical circuit consists of source and load in case of reactive circuit (left) and pure resistive circuit (right).....60

Fig. 3. 4. Schematic illustration working principle (left) and a photo of rotary vane pump (right).69

Fig. 3. 5. Schematic illustration working principle (left) and a side view photo of turbo molecular pump (right).70

Fig. 3. 6. Schematic illustration (left) and a picture of internal structure of ion pump (right).	72
Fig. 3. 7. Diagram of our home-built MBE system and RHEED pattern of SnSe thin film grown on MgO (100) substrate.	74
Fig. 3. 8. Calibration of substrate temperature (left) and growth rate of Se cell (right).	75
Fig. 3. 9. Diagram of (a) Bridgmann vertical furnace and (b) Stockbarg furnace. [4]	78
Fig. 3. 10. Diagram of (a) our temperature gradient vertical furnace, (b) vertical furnace's heater, and (c) single crystal ingot of SnSe grown by temperature gradient technique.	80
Fig. 3. 11. (a) the structure configuration of SPS system [8] and (b) the basic mechanism of neck formation by SPS. [7].....	82
Fig. 3. 12. SEM images of the fracture surfaces of the ultrafine SPS copper sample sintered at 600 °C: (a) partially melted microstructure between two copper particles, (b) the magnification of the melted and sputtered microstructure of copper, (c) the formation of sintering necks on the surface of the copper particles, and (d) the magnification of sintering necks. [8].....	83
Fig. 3. 13. Entire structure of our mini hot pressing system. [10]	85
Fig. 3. 14. The two-point probe configuration to measure resistance.....	86
Fig. 3. 15. Square (up) and colinear (down) four-point probe configuration.	87
Fig. 3. 16. Schematic representation of Hall Effect in a conductor.	90
Fig. 3. 17. Our home-build low temperature transport properties measurement system (TPMS).	94
Fig. 3. 18. Schematic illustration of our low temperature measurement system.	95
Fig. 3. 19. A photo (a) internal components of our home-build high temperature transport measurement system.	96
Fig. 3. 20. Photograph of 30 -1000 K of our home-build transport measurement system with a special design of heater.	97

Fig. 3. 21. a) ΔV vs. ΔT at 300 K of polycrystalline Bi and b) measurement' error. 103

Fig. 4. 1. (a) A picture of SnSe ingot, (b) FE-SEM image of SnSe confirms the layered structure, (c) XRD pattern of SnSe single crystal with cooling rate of 5.0 °C/h. The samples with other cooling rate show the same XRD pattern (supplementary figure S4.4), and (d) PXRD patterns of all samples show the existence of SnSe₂ phase, where SnSe and SnSe₂ peaks are denoted in red and black colors, respectively. The average lattice constants of SnSe calculated from XRD are $a = 11.52$, $b = 4.46$, and $c = 4.18$ Å. 114

Fig. 4. 2. Cross-sectional transmission electron microscopy (TEM) image of sample SnSe 0.5 °C/h. The SnSe₂ phase exists somewhere which is difficult to be recognized. The average lattice constants obtained from TEM image are $a = 11.87$ and $b = 4.59$ Å. 115

Fig. 4. 3. (a) The plots of V_H/I vs. H of all samples at 300 K with positive slopes indicate the p-type characteristic of our samples, and (b) Carrier density as a function of cooling rate at some critical temperatures. 116

Fig. 4. 4. STM topographic images of samples (a) 0.5 °C/h, (b) 1 °C/h, (d) 2 °C/h, (e) 5 °C/h. (c), (f) High resolution STM images taken from single Sn vacancy (solid circles) and one of multi-vacancies (dotted circles) in (a, b) and (d, f), respectively. Here $b = 4.44$ Å and $c = 4.15$ Å. The given numbers at the bottom are sample's bias and tunneling current. The detail number of Sn missing atom in each vacancy is shown in supplementary figure S4.2. 118

Fig. 4. 5. The temperature dependent (a) electrical conductivities, (b) Seebeck coefficients, and (c) thermoelectric PFs of SnSe single crystal along b-axis of samples with cooling rate of 0.5, 1.0, 2.0, 3.0, 4.0, and 5.0 °C/h. All samples exhibited p-type characteristic in consistent with Hall data. 120

Fig. 4. 6. Cooling rate dependent (a) electrical conductivities, (b) Seebeck coefficients, and (c) thermoelectric power factors (<i>PFs</i>) of SnSe single crystal along <i>b</i> -axis of samples at some typical temperatures.	122
Fig. 4. 7. (a) Thermal conductivity and (b) thermoelectric figure of merit (<i>ZT</i>) as a function of temperature along <i>b</i> -axis for all samples. Thermal conductivities are independent on cooling rate, while thermoelectric figure of merit increased with decreased cooling rate.	125
Fig. 4. 8. Anisotropic thermoelectric transport properties of sample 0.5 °C/h. Temperature dependent (a) electrical conductivities, (b) Seebeck coefficients, (c) thermoelectric power factors (<i>PFs</i>), and (d) total thermal conductivities along <i>a</i> , <i>b</i> , and <i>c</i> -axes.	126
Fig. 4. 9. Anisotropic thermoelectric figure of merit of sample 0.5 °C/h. Maximum <i>ZT</i> values are 0.55, 1.2, and 0.71 at 873 K along <i>a</i> , <i>b</i> , and <i>c</i> -axes, respectively.	127
Supplementary Fig. 4. 1. Composition determinations by EDX and EPMA.	129
Supplementary Fig. 4. 2. STM images showed detail of (a) single Sn vacancy and (b-d) multi-vacancies. Note that only the missing of Sn atoms is visibly to be counted.	129
Supplementary Fig. 4. 3. XRD patterns of some samples with different cooling rate, where the extra peaks come from the bending or fragment of layers induced by cleaving process.	130
Supplementary Fig. 4. 4. Reproducibility data of sample at cooling rate of 1 °C/h. Temperature dependent (a) electrical conductivities, (b) Seebeck coefficients, and (c) <i>PFs</i> obtained from five pieces cut from five different ingots along <i>b</i> -axis.	131
Supplementary Fig. 4. 5. (a) Thermal diffusivity of all samples along <i>b</i> -axis and (b) thermal diffusivity of sample at cooling rate of 0.5 °C/h along <i>a</i> , <i>b</i> , and <i>c</i> -axes.	132
Supplementary Fig. 4. 6. The independence of total thermal conductivity on cooling rate at some critical temperatures.	133

Fig. 5. 1. RHEED patterns along [001] azimuth of SnSe thin film with various flux ratio Se/Sn of (a) 0.8; (b) 0.9; (c) 1; (d) 3; (e) 5; and (f) 7. The inset of (a) is that of MgO (100) substrate after preheating. Streaky RHEED patterns were obtained indicating the epitaxial growths with very smooth surfaces, except the sample with flux ratio of 7..... 143

Fig. 5. 2. (a) X-ray diffraction patterns of SnSe/MgO (100) thin films and SnSe single crystal. The calculated average a-axis lattice constants are the same 11.52 Å for all thin film, and 11.50 Å for bulk. (b) Se/Sn flux ratio dependent FWHM fitted from XRD omega scan curves for symmetrical (400) reflection of all samples. The inset is the corresponding rocking curves. (c) Φ -scan using (111) plane of all films in linear scale. The insets are magnified of the splitting peaks in linear scale (left) and of the small peaks in log scale (right). 144

Fig. 5. 3. (a) Φ -scan using (111) plane of orthorhombic SnSe measurement processes. (b) simulation and experimental Φ -scan peaks of SnSe single crystal using (111) plane. (c) Simulation Φ -scan peaks of SnSe single crystal in case of 0° and 90° rotated layers. 147

Fig. 5. 4. Cross-sectional TEM images of samples at $Se/Sn = 3$ in large scale (left) and magnified (right). The average lattice constants were $a = 11.8 \text{ \AA}$ and $b = 4.4 \text{ \AA}$ 148

Fig. 5. 5. (a) Temperature dependent resistivity, (b) the plot of $\ln\rho$ vs $10^3/T$, (c) and (d) temperature dependent Seebeck coefficient and power factor of all samples. 150

Supplementary Fig. 5. 1. Room temperature raman spectra of SnSe/MgO (100) thin films with flux ratio of 1. There are 3 raman peaks at 108 cm^{-1} corresponds to B_{3g} mode, 130, and 153 cm^{-1} correspond to A_g modes. No secondary phases were observed..... 153

Supplementary Fig. 5. 2. Reproducibility. Temperature dependent a) Seebeck coefficient, b) electrical conductivity, and c) PF of sample at flux ratio of 0.8..... 154

Supplementary Fig. 5. 3. Reproducibility. Temperature dependent a) electrical resistivity and b) Seebeck coefficient for sample at flux ratio of 1..... 155

Supplementary Fig. 5. 4. Re-plot of absorption spectra obtained from UV-vis measurement for sample with flux ratio of 1. The determined indirect optical band gap is 0.933 eV in agreement with other report..... 156

Fig. 6. 1. Room temperature XRD patterns for SnSe:Bi 4% along perpendicular (red color) and parallel (blue color) to the pressing direction as illustrated in the inset. The figure showed the orthorhombic structure and the presence of rhombohedral Bi phase. 164

Fig. 6. 2. FE-SEM images of the fractured surfaces along the \perp direction of sample SnSe:Bi 4% (a and b) and SnSe:Bi 6% (c and d). FE-SEM images showed the layered structure and the dominant layers on the plane perpendicular to the pressing direction..... 165

Fig. 6. 3. Temperature dependence of electrical conductivity (a, d), Seebeck coefficient (b, e), and power factor (c, f) of samples with various Bi contents along \perp and \parallel directions as defined in the inset of (a) and (d), where the black arrows indicated the press direction P. The n-type maximum power factor as a function of Bi content is shown in the inset of (c) and (f). 166

Fig. 6. 4. Temperature dependence of heat capacity (C_p) taken from [1] (a), thermal diffusivity (D) (b), and thermal conductivity (κ) of SnSe:Bi 6% and SnSe:Bi 8% samples along both \perp and \parallel directions in compare with Bi doped n-type SnSe single crystal [7] (c, d). 169

Fig. 6. 5. Temperature dependence of dimensionless thermoelectric figure of merit of polycrystalline SnSe:Bi 6% and SnSe:Bi 8% samples along both \perp (a) and \parallel (b) directions. 170

Fig. 7. 1. (a) XRD patterns taken from cleave plane and (b) powder XRD patterns of all samples, $x = 1, 1.2, 1.5, 1.75, \text{ and } 2$. The red numbers indicate the Miller indices of SnSe and the black numbers indicate those of SnSe₂..... 179

Fig. 7. 2. TEM cross-sectional images of sample $x = 1.75$ 180

Fig. 7. 3. Cross-sectional optical microscopy images of all samples after rough polishing with maximum SiC paper grit size of 1200 with, with 0.3 μm Al_2O_3 powder suspension..... 181

Fig. 7. 4. Temperature dependent (a) Seebeck coefficient, (b) electrical conductivity, (c) power factor, and (d) thermal diffusivity of all samples..... 183

CHAPTER 1: INTRODUCTION

1.1 Description of the research

Since 2014, the high ZT in p-type SnSe single crystal has stimulated interests in SnSe based thermoelectric materials. The obtained $ZT = 2.6$ by Li-dong Zhao [1] is achieved at quite high temperature 923 K which is not suitable for applications. The high ZT value of SnSe is assigned to the anharmonic bonding of atoms leading to its ultralow thermal conductivity. Efforts have been made to shift this peak of ZT to medium temperature by doping experiments such as: p-type Na-doped p-type SnSe single crystal with $ZT = 2.0$ at 773 K [2] and Bi-doped n-type SnSe single crystal with $ZT = 2.2$ at 733 K [3]. For applications, polycrystalline SnSe have been focused. Un-doped SnSe polycrystalline, n- and p-type doped SnSe polycrystalline have been prepared mostly by spark plasma sintering SPS and hot-pressing techniques. However, ZT values are quite small ($ZT = 0.5-1.3$ [4-15]) compare to SnSe single crystal. All of these experiments have been done without understanding microscope of SnSe such as the source of p-type characteristic of SnSe. Recently, single Sn vacancy has been theoretically and experimentally reported as the source of p-type characteristic of SnSe [16, 17]. However, there are many intrinsic defects in the crystal which may also contribute to transport properties of SnSe. The experimentally investigate the influence of intrinsic defect to the thermoelectric transport properties of SnSe is needed. On the other hand, there is a lack of reproducibility between groups to produce the high ZT SnSe, indicating the important role of growth technique on fabricating this material. Also, the mass density of SnSe (un-doped SnSe single crystal mass density = 5.45 g/cm^3) is still on debate. Many group reported SnSe single crystal and polycrystalline with double, even triple thermal conductivity compare to the values reported by Zhao *et al.* This thesis aims on the engineering defects in SnSe single crystal from bulk to thin film and Bi-doped SnSe polycrystalline. Defects have been controlled by changing growth

condition where nearly defect free state is achieved in SnSe thin film by MBE, resulting in the change in physical properties of SnSe. The structural properties of samples have been investigated by XRD (theta-2theta, omega, and phi scans), RHEED, SEM, Raman, and TEM. The thermoelectric transport properties were studied using Seebeck effect, Hall effect, and electrical conductivity, thermal diffusivity, etc. We have determined the thermoelectric power factor ($S^2\sigma$), thermal conductivity (κ), and dimensionless thermoelectric figure of merit ZT ($S^2\sigma T/\kappa$).

1.2 List of publications

1.2.1 List of patents

1. Sunglae Cho, Jeong Young Choi, Yooleemi Shin, Duong Anh Tuan, and **Van Quang Nguyen**, “Semiconductor Material Containing the Fe₂SiO₄, And Preparation Method (Fe₂SiO₄ 계 화합물을 포함하는 반도체 소재 및 이의 제조방법)”

The Korean Intellectual Property Office

Patent number: 10-1676186

Registration date: 2016-11-08

2. Sunglae Cho, 권해웅, **Van Quang Nguyen**, 박은지, 박은정, and 김말식, “Compact hot press apparatus (미니 핫 프레스 장치)”

The Korean Intellectual Property Office

Patent number: 10-1753980

Registration date: 2017-06-28

3. Sunglae Cho, Van Quang Nguyen, and Duong Anh Tuan, “Seebeck coefficient and electrical resistance measurement system (제벡계수 및 전기저항 측정장치)”

The Korean Intellectual Property Office

Patent number: 10-1690427

Registration date: 2016-12-21

4. Sunglae Cho, Yooleemi Shin, Van Quang Nguyen, and Duong Anh Tuan, “Thermoelectric material containing higher manganese silicides, and preparation method (고망간실리사이드계 화합물을 포함하는 열전소재 및 이의 제조방법)”

The Korean Intellectual Property Office

Patent number: 10-1726498

Registration date: 2017-04-06

1.2.2 List of journal papers

1. Van Quang Nguyen, Jungdae Kim, and Sunglae Cho, “A Review of SnSe: Growth and Thermoelectric Properties”, J. Korean Phys. Soc, **72**, 841 (2018).

2. Van Quang Nguyen, Thi Huong Nguyen, Van Thiet Duong, Ji Eun Lee, Su-Dong Park, Jae Yong Song, Hyun-Min Park, Anh Tuan Duong, and Sunglae Cho, “Thermoelectric properties of hot-pressed Bi-doped n-type polycrystalline SnSe” Nanoscale Res. Lett., **xx**, xx, (2018).

ACCEPTED.

3. **Van Quang Nguyen**, Cheng Chang, Thi Huong Nguyen, Thi Ly Trinh, Van Thiet Duong, Anh Tuan Pham, Anh Tuan Duong, Li-Dong Zhao, Jungdae Kim, and Sunglae Cho, “Engineering defects in SnSe single crystal”, **TO BE SUBMITTED** (2018).
4. **Van Quang Nguyen**, Van Thiet Duong, Thi Huong Nguyen, Rakwon Kang, Anh Tuan Pham, Cao Khang Nguyen, Anh Tuan Duong, and Sunglae Cho, “Layers’ rotation and thermoelectric transport properties of SnSe epitaxial thin films”, **TO BE SUBMITTED** (2018).
5. **Van Quang Nguyen**, S. H. Rhim, Yooleemi Shin, Anh Tuan Duong, Sunglae Cho* and Christian Meny, “Antiferromagnetic interfaces in CoFe₂O₄/Fe₃O₄ superlattices”, **TO BE SUBMITTED** (2018).
6. **Van Quang Nguyen**, Yooleemi Shin, Anh Tuan Duong, Sunglae Cho*, and Christian Meny, “Tuning transport and magnetic properties of Co_xFe_{3-x}O₄ thin films by Co content”, J. Alloys Compd. **SUBMITTED** (2018).
7. Van Thiet Duong, **Van Quang Nguyen**, Thi Minh Hai Nguyen, Thi Huong Nguyen, Anh Tuan Duong, Duc Dung Dang, Tam Tran Van, and Sunglae Cho “Optimizing the Carrier Density and Thermoelectric Properties of Sb₂Te₃ Films by Using the Growth Temperature” J. Korean. Phys. Soc. **72**, 915, (2018).
8. Jeongyong Choi, **Van Quang Nguyen**, Van Thiet Duong, Yooleemi Shin, Anh Tuan Duong, Sunglae Cho, “Formation of Fe₂SiO₄ thin films on Si substrates and influence of substrate to its thermoelectric transport properties”, Physica B **532**, 80 (2018).
9. Anh Tuan Duong, **Van Quang Nguyen**, Ganbat Duvjir, Van Thiet Duong, Suyong Kwon, Jae Yong Song, Jae Ki Lee, Ji Eun Lee, Su-Dong Park, Taewon Min, Jaekwang Lee, Jungdae

Kim & Sunghae Cho, “Achieving $ZT = 2.2$ in Bi doped n-type SnSe single crystal”, Nat Commun. **7**, 13713 (2016).

10. Wuwei Feng, Anh Tuan Duong, Dorj Odkhuu, Namsrai Tsogbadrakh, Zhidi Bao, Xiaoxue Zhao, **Van Quang Nguyen**, and Sunghae Cho, “Synthetic hybrid $\text{Co}_2\text{FeGe}/\text{Ge}(\text{Mn})$ superlattice for spintronics applications”, Appl. Phys. Lett. **109**, 172401 (2016).

11. Anh Tuan Duong, S. H. Rhim, Yooleemi Shin, **Van Quang Nguyen**, and Sunghae Cho, “Magneto-transport and thermoelectric properties of epitaxial FeSb_2 thin film on MgO ”, Appl. Phys. Lett. **106**, 032106 (2015).

12. Yooleemi Shin, Sung Hyon Rhim, Anh Tuan Duong, **Van Quang Nguyen**, Soon Cheol Hong, Sunghae Cho, and Hyun-Min Park, “New synthesis of MnSi_2 thin film and its thermoelectric properties”, J. Vac. Sci. Technol. A **33**, 061516 (2015).

13. Wuwei Feng, Xiao Fu, Caihua Wan, Zhonghui Yuan, Xiufeng Han, **Van Quang Nguyen**, and Sunghae Cho, “Spin gapless semiconductor like Ti_2MnAl film as a new candidate for spintronics application”, Phys. Status Solidi RRL **9**, No. 11, 641 (2015).

14. Wuwei Feng, Weihua Wang, Chenglong Zhao, **Van Quang Nguyen**, Sunghae Cho, and Dang Duc Dung, “Molecular beam epitaxy growth and magnetic properties of Cr-Co-Ga Heusler alloy films”, AIP Advances **5**, 117223 (2015).

1.2.3 References

- [1] L.D. Zhao, S.H. Lo, Y.S. Zhang, H. Sun, G. Tan, C. Uher, C. Wolverton, V.P. Dravid, M.G. Kanatzidis, *Nature* **508**, 373 (2014).
- [2] L. D. Zhao, G. Tan, S. Hao, J. He, Y. Pei, H. Chi, H. Wang, S. Gong, H. Xu, V. P. Dravid, C. Uher, G. J. Snyder, C. Wolverton, M. G. Kanatzidis, *Science* **351**, 141 (2016).
- [3] A.T. Duong, V.Q. Nguyen, G. Duvjir, V.T. Duong, S. Kwon, J.Y. Song, J.K. Lee, J.E. Lee, S.D. Park, T. Min, J.W. Lee, J. Kim, S. Cho, *Nat. Commun.* **7**, 13713 (2016).
- [4] S. Sassi, C. Candolfi, J. B. Vaney, V. Ohorodniichuk, P. Masschelein, A. Dauscher, and B. Lenoir, *Appl. Phys. Lett.* **104**, 212105 (2014).
- [5] C. L. Chen, H. Wang, Y. Y. Chen, T. Day, and G. J. Snyder, *J. Mater. Chem. A* **2**, 11171 (2014).
- [6] Q. Zhang, E. K. Chere, J. Sun, F. Cao, K. Dahal, S. Chen, G. Chen, and Z. Ren, *Adv. Energy Mater.* **5**, 1500360 (2015).
- [7] G. Tang, Q. Wen, T. Yang, Y. Cao, W. Wei, Z. Wang, Z. Zhang and Y. Li, *RSC Adv.* **7**, 8258 (2017).
- [8] X. Wang, J. Xu, G. Liu, Y. Fu, Z. Liu, X. Tan, H. Shao, H. Jiang, T. Tan, and J. Jiang, *Appl. Phys. Lett.* **108**, 083902 (2016).
- [9] Y. M. Han, J. Zhao, M. Zhou, X. X. Jiang, H. Q. Leng, and, L. F. Li, *J. Mater. Chem. A* **3**, 4555 (2015).
- [10] T. R. Wei, C. F. Wu, X. Zhang, Q. Tan, L. Sun, Y. Pan, and J. F. Li, *Phys. Chem. Chem. Phys.* **17**, 30102, (2015).

- [11] Y. Li, X. Shi, D. Ren, J. Chen, and L. Chen, *Energies* **8**, 6275 (2015).
- [12] S. Chen, K. Cai, and W. Zhao, *Physica B* **407**, 4154 (2012).
- [13] J. H. Kim, S. Oh, Y. M. Kim, H. S. So, H. Lee, J. S. Rhyee, S. D. Park, S. J. Kim, *J. Alloys Compd.* **682**, 785 (2016).
- [14] J. C. Li, D. Li, X. Y. Qin, J. Zhang, *Scripta Materialia* **126**, 6 (2017).
- [15] C. Chang, Q. Tan, Y. Pei, Y. Xiao, X. Zhang, Y. X. Chen, L. Zheng, S. Gong, J. F. Li, J. Hec and L. D. Zhao, *RSC Adv.* **6**, 98216 (2016).
- [16] Y. Huang, C. Wang, X. Chen, D. Zhou, J. Du, S. Wang and L. Ning, *RSC Adv.* **7**, 27612 (2017).
- [17] G. Duvjir, T. Min, T. T. Ly, T. Kim, A. T. Duong, S. Cho, S. H. Rhim, J. Lee, and J. D Kim, *Appl. Phys. Lett.* **110**, 262106 (2017).

CHAPTER 2: BACKGROUND

2.1 Physical phenomena of thermoelectricity

Thermoelectric effect is a direct conversion of temperature difference to electric voltage and vice versa. When a temperature difference is applied to the 2 ends of a substance, a voltage difference is created between these ends, called thermal voltage. Conversely, when a voltage is applied to its ends, a temperature difference is created. The thermoelectric effect involves two physical phenomena: (i) diffusion of charge carrier, and (ii) phonon drag. An applied temperature gradient causes the charge carriers diffusion from hot end to cold end. The phonon drag refers to the electron-phonon scattering at low temperature and phonon-phonon scattering at high temperature. The thermoelectric effect consists of three separated effects called: Seebeck effect invented by Thomas Seebeck - a Baltic German, Peltier effect by a French physicist named Jean Charles Peltier, and Thomson effect by Irish-born William Thomson (Lord Kelvin).

The thermoelectric effect can be used to generate electricity (thermoelectric generator) which directly convert heat to electricity, measure temperature (e.g. thermocouple, differential thermocouple), and change the temperature of an object (e.g. thermoelectric refrigerator).

2.1.1 The Seebeck effect

The Seebeck effect was discovered by Thomas Johann Seebeck in 1821 [1]. He found that a compass needle would be deflected by a closed loop formed by two different metals joined in two places, with a temperature difference between the joints. This phenomenon is due to electron in each metal shifted differently, leading to a potential difference is created at two joints. A current created between joints caused a magnetic field around the wire and act on the needle of the compass. At that time, Seebeck did not recognize the existence of electric current,

he called the phenomenon as “thermo-magnetic effect”. Later, a Danish physicist Hans Christian Orsted recognized that and proposed the term “thermoelectricity”.

The Seebeck effect appears even when we consider only a single conductor of finite rod with a temperature difference between two ends. The temperature gradient causes a diffuse of charge carriers from hot end towards cold end and vice versa until the equilibrium state is established. The charge carriers moved from the hot to cold end rather than from the cold to hot end, leading to a cumulation of charge carriers at cooler end, a potential difference is created between two ends of conductor. The larger temperature gradient, the more charge carriers moved to the cooler side, the higher potential difference is created. This potential difference is limited by the melting point of material. The diffusion of charge carriers leading to the entropy is transported with them. The Seebeck coefficient is entropy transport per charge carrier. Another definition of Seebeck coefficient is the ratio of potential difference and temperature gradient between two ends.

$$S = \frac{\Delta V}{\Delta T} \quad (2. 1)$$

where, S is Seebeck coefficient (or thermopower), ΔV is thermal voltage, ΔT is temperature difference between cold and hot ends. For almost metals and n-type semiconductors, electron is majority charge carrier. The cumulation of electron at the cold end leading to negative voltage between the cold and hot ends, the value of Seebeck coefficient is negative. For p-type semiconductors, hole is majority charge carrier, leading to positive voltage and positive value of Seebeck coefficient (Fig. 2.1).

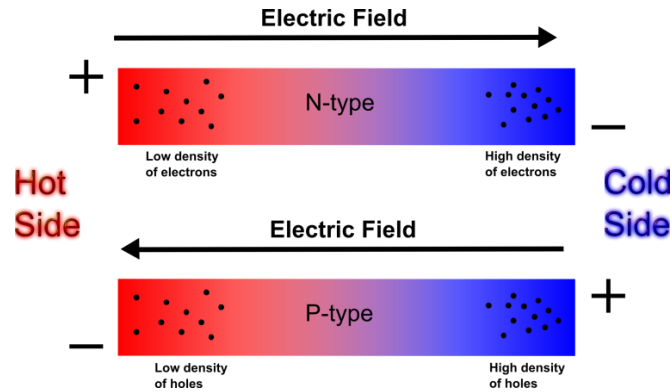


Fig. 2. 1. Cumulation of charge carriers at the ends of n-type (up) and p-type (down) conductors.

The Seebeck coefficient is dependent on temperature and chemical composition of the conductor. The Seebeck coefficient of metals is very small due to the high mobility of free electrons. For semiconductor, The Seebeck coefficient ranges from -100 to $1000 \mu\text{V/K}$ at room temperature. In the thermocouples, the two different conductors are connected at one end, the other ends are placed at a well-known reference temperature (e.g. ice water). By performing voltage measurement between two conductors an absolute temperature can be determined (see section 2.2.3 for detail). The main application of Seebeck effect is thermoelectric generator (TG), thermocouple, and to classify an unknown composition metal (if it is kept at a constant temperature and held in contact with a well-known metal and heated to probe temperature).

2.1.2 The Peltier effect

The Peltier effect is a reversion of the Seebeck effect. When a current is applied to flow through the two joints (A and B) between two dissimilar conductors (X and Y), heat can be generated or removed at these joints. If Peltier heat generated at the junction B per unit time is q , there must be an equal cooling rate at the junction A, $q = \dot{Q}_c = \dot{Q}_h$ (Fig. 2.2). The differential Peltier coefficient between the two conductors is determined by ratio between the rate of heating or

cooling and current.

$$\pi_{XY} = \pi_X - \pi_Y = \frac{q}{I} \quad (2.2)$$

where, π_X and π_Y are the Peltier coefficient of conductor X and Y, and I is the electric current (from Y to X). Note that the total heat consists of not only Peltier heating but also Joule heating and thermal gradient effects. The equation shows that the Peltier coefficients represent how much heat is carried per unit charge.

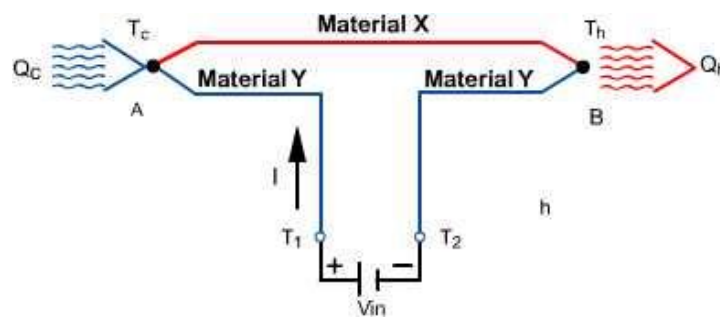


Fig. 2. 2. Peltier effect, heat is generated at junction B and removed at junction A between conductor X and Y when an electric current I is applied from Y to X.

Figure 2.3 shows a thermoelectric device using the Peltier effect (thermoelectric refrigerator). The device consists of a pair of n- and p-type semiconductors which are electrically connected in series and thermally parallel connected. When an electric current I is applied from n- to p-type semiconductors, electrons in the n-type and holes in the p-type semiconductors move down, heat is dissipated at the bottom surface. As a result, the top surface is cooled. The heating and cooling surfaces are changed if we change the current direction. This is a part of thermoelectric module, where many pairs are connected electrically in series and thermally parallel. It is also the principle of thermoelectric refrigerator.

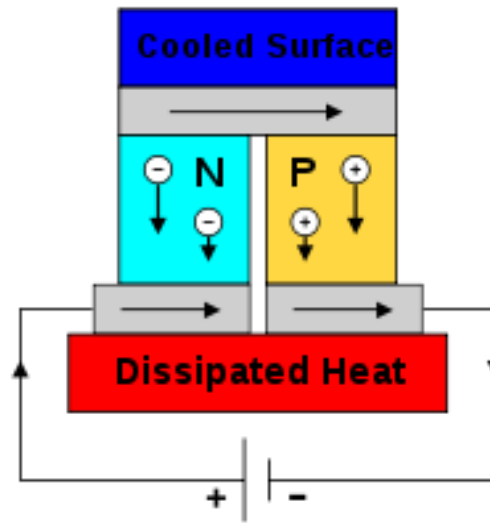


Fig. 2. 3. Thermoelectric refrigerator where a junction is heated up or cooled down, depends on the direction of applied electric current.

2.1.3 The Thomson effect

The Thomson effect was discovered by William Thomson (Lord Kelvin) in 1851 [2, 3]. The effect is occurred when we consider a single homogeneous conductor. It is supposed that, in addition of current I flow, there is a small temperature gradient dT/dx which leads to the rate of heating or cooling per unit length dq/dx . We have

$$t = \frac{dq/dx}{I dT/dx} \quad (2. 3)$$

This equation however neglects Joule heating and ordinary thermal conductivity.

2.1.4 Kelvin relationship

In 1854, Lord Kelvin found the relationships between the three coefficients (Seebeck, Peltier, and Thomson coefficients) by applying the first and second laws of thermodynamics to a simple thermoelectric circuit, assuming it to be a reversible system [2]. His work implied that the Thomson, Peltier, and Seebeck effects are different manifestations of one effect. The

obtained two equations are known as the Kelvin relations. Note that, the thermoelectric phenomena are always accompanied by the irreversible effects of Joule heating and thermal conduction. However, the further reasonable application of theory of irreversible thermodynamic to this problem also leads to the same relations.

The first Kelvin relation is:

$$t_{xy} = \frac{d\pi_{xy}}{dT} - S_{xy} \quad (2.4)$$

where, T is absolute temperature. t , S , π are the Thomson, Seebeck and Peltier coefficients, respectively.

The second Kelvin relation is:

$$\pi_{xy} = TS_{xy} \quad (2.5)$$

Using the second relation the first one can be written as

$$t_{xy} = T \frac{dS_{xy}}{dT} \quad (2.6)$$

Note that, these equations can be applied for single or couple of conductors. That means, we can use the absolute coefficients S , t , and π for each material, instead of differential coefficients described above. The used of these absolute coefficients implies the existence of some metals having zero absolute coefficients (at least in theory), which may be used as standard for reference purposes. If we applied the third law of thermodynamic that the differential Seebeck coefficient of any two conductors must be zero at 0 K, we may suppose that the absolute Seebeck coefficient of all materials at 0 K is zero. The two relationship equations become

$$t = T \frac{dS}{dT} \quad \text{and} \quad \pi = TS \quad (2.7)$$

However, it is difficult to find the values of absolute Seebeck and Peltier coefficients for an individual conductor.

2.1.5 Thermoelectric figure of merit

The conversion efficiency of thermoelectric devices is referred to the coefficient of performance (*COP*) which is given by

$$COP = \eta_c \times M \quad (2.8)$$

where, $\eta_c = \Delta T/T_h$ is Carnot efficiency which is the maximum efficiency of any thermal process, ΔT is gradient temperature between the two sides, T_h is temperature at hot side, and M is merit factor which is positive and finite value. For the power generator, M is given by

$$M = \frac{\sqrt{1+ZT} - 1}{\sqrt{1+ZT} + T_c/T_h} \quad (2.9)$$

where, ZT is dimensionless thermoelectric figure of merit, T_h , T_c , and ΔT are temperature at hot side, cold side, and gradient temperature between the two sides, respectively. The figure of merit Z can be calculated by

$$Z = \frac{S^2 \sigma}{\kappa} \quad (2.10)$$

where, σ and S are electrical conductivity and Seebeck coefficient, and κ is thermal conductivity.

The dimensionless figure of merit is given by

$$ZT = \frac{S^2 \sigma}{\kappa} T \quad (2.11)$$

The thermoelectric figure of merit ZT at a given temperature T is dependent on material properties, σ , S , and κ . Equation (2. 8) and (2. 9) show that the efficiency is proportion to the ZT value. The larger ZT value, the higher is efficiency. To make a TE device with the same efficiency with home refrigerator ($\sim 30\%$) we need ZT value of 4. In principle, ZT value of materials can be increased without any limitation by increasing the numerator or decreasing the denominator. However, obtaining high ZT value is still big challenge for scientists due to the interrelation between transport parameters. The high ZT material need to have: high S , high electrical conductivity, and low thermal conductivity. According to [4] these parameters can be calculated by

$$\begin{aligned}
 S &= \frac{8\pi^2 k_B^2}{3eh^2} m^* T \left(\frac{\pi}{3n} \right)^{2/3} \\
 \sigma &= \mu ne \\
 \kappa &= \kappa_e + \kappa_L = L\sigma T + \kappa_L
 \end{aligned} \tag{2. 12}$$

where, n is carrier concentration, m^* is effective mass, h is Planck constant, k_B is Boltzmann constant, μ is mobility, κ_e and κ_L are electrical and lattice thermal conductivity, and L is Lorentz number. The large S needs to have low carrier concentration and high effective mass or low mobility. In contrast, the high electrical conductivity needs to have high mobility and high carrier concentration. The low thermal conductivity needs to have low carrier concentration and low mobility. This conflicting relation is demonstrated in Fig. 2.4 for Bi_2Te_3 . The optimized carrier concentration is 10^{19} to 10^{20} cm^{-3} which is in between common metals and semiconductors or in heavily doped semiconductors.

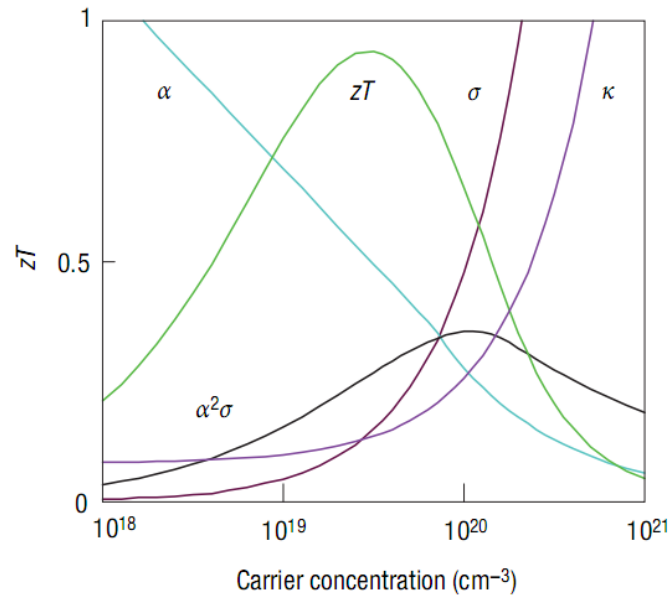


Fig. 2. 4. Conflicting relation of thermoelectric transport parameters via carrier concentration.

2.2 Thermoelectric devices

- Thermoelectric (TE) devices contain many couples of n- and p-type thermoelectric elements connected electrically in series and thermally parallel [4] as shown in Fig. 2.5. The TE devices can be classified in to two categories: TE generators (TEG) and TE refrigerators. These TE devices have many advantages such as environmentally friendly (no pollution), no moving part involve, long life time, etc. However, they are expensive and low efficiency. TEG is a solid state device that converts temperature difference directly into electrical energy through the Seebeck effect. This device can be used to convert waste heat into electricity and therefore increase the fuel efficiency in automobiles. For example, in combustion engine the efficiency is about 30%. TEG can be used here to convert waste heat in to electricity, recharge the battery and increase the engine's efficiency up to 40%.

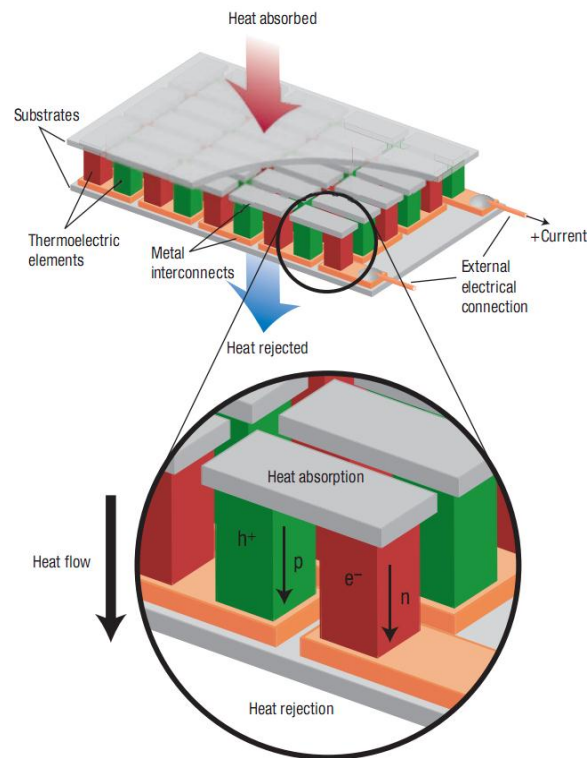


Fig. 2. 5. Thermoelectric module which can be used as a thermoelectric generator or a thermoelectric refrigerator.

In principle, when a temperature difference is applied to hot and cold side of the device, electron in n-type and hole in p-type elements diffuse towards the cold side and create a voltage between two elements. A direct current will flow in the load circuit. In contrast, if we apply a current in to circuit one side of the device becomes cold and the other side becomes hot, that is the working principle of a TE refrigerator. The commercial TE material used for this device is Bi_2Te_3 which is good for application near room temperature. Another kind of TE generator is Radioisotope TE generator (RTG) which can be used in space probes. The mechanism of RTG is same with TEG. But RTG uses heat released by the decay of an appropriate radioactive material to generate the require heat difference. This RTG have been used as power sources in satellites, spaces probes. The most popular TE material used for RTG is SiGe. The most

common radioactive materials used for RTG are Plutonium-238 metal and Strontium-90.

- Thermocouple: Thermocouple is a TE device used to measure temperature which consists of two dissimilar conductors forming electrical junctions at different temperature. The thermocouple produces a thermal voltage between two junctions. This voltage can be used to determining temperature of one junction when the other junction is place at a known reference temperature. Figure 2.6 shows the working principle of a thermocouple which consists of two dissimilar materials A and B. When the junction is placed in a temperature T , the other ends are placed at same temperature T_0 , potential differences are built between two ends of A and B (V_A, V_A', V_B, V_B'). We have

$$\begin{aligned}
 V_A' - V_A &= S(T - T_0) \\
 V_B' - V_B &= S(T - T_0) \\
 \Rightarrow V_B - V_A &= (S_A - S_B)(T - T_0)
 \end{aligned}
 \tag{2.13}$$

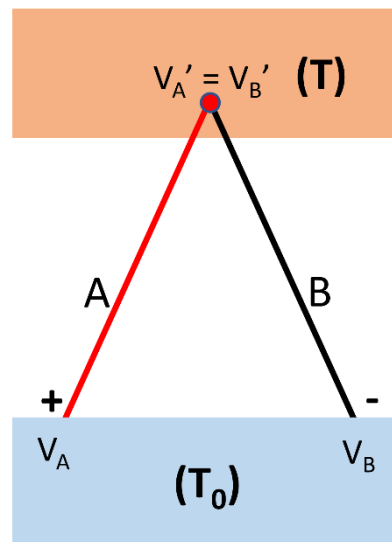


Fig. 2. 6. Thermocouple configuration.

Provide that we know the value of Seebeck coefficients S_A and S_B and T_0 , by measuring $V_A - V_B$, we can determine the temperature T .

- Differential thermocouple: Another application of thermocouple is differential thermocouple which is used to determine temperature difference between two regions I and II as shown in Fig. 2.7. The differential thermocouple consists of two thermocouples connected oppositely.

When two junctions are placed at T_1 and T_2 and the other ends are placed at same temperature T_0 we have

$$\begin{aligned} A: V'_{1A} - V_{1A} &= S_A (T_1 - T_0) & A: V'_{2A} - V_{2A} &= S_A (T_2 - T_0) \\ B: V'_{1B} - V_{1B} &= S_B (T_1 - T_3) & \text{and} & & B: V'_{2B} - V_{2B} &= S_B (T_2 - T_3) \end{aligned}$$

Note that $V_{2A} - V_{1A} = S_A (T_1 - T_2) - S_B (T_1 - T_2) = (S_A - S_B)(T_1 - T_2)$

Here $V'_{2A} = V'_{2B}$ $V_{1B} = V_{2B}$ $V'_{1A} = V'_{1B}$

$$\Rightarrow \Delta V = (S_A - S_B) \cdot \Delta T \quad (2.14)$$

By measuring ΔV we can calculate ΔT .

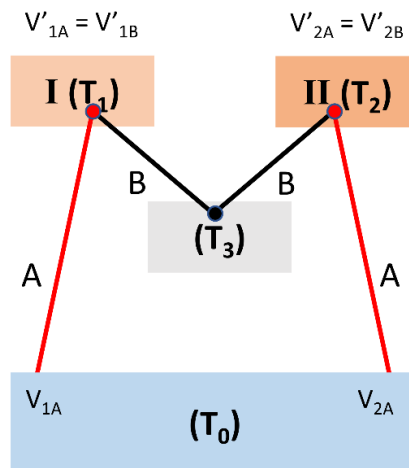


Fig. 2. 7. Differential thermocouple configuration.

2.3 Thermoelectric material research

2.3.1 Brief history of thermoelectricity

Thermoelectric research has been started since the Seebeck and Peltier effects were discovered in 1820s and 1834. Thomas Johann Seebeck discovered that a closed circuit made of two dissimilar metal connected at two junctions can deflect the compass needle when two junctions are placed at two different temperatures. Initially, Seebeck believed that the effect is magnetism induced by the temperature difference then he called this is “thermo-magnetic effect”. Later Hans Christian Orsted realized that is thermoelectricity which we use nowadays and known as Seebeck effect. In this effect, the electrical potential difference between two junctions proportion to temperature difference. The proportionality constant is call Seebeck coefficient ($\mu\text{V/K}$). In 1834, Jean Charles Athanase Peltier discovered the inverse effect. In 1838 Lenz showed that depending on the direction applied current, heat can be removed or generated. This amount of heat is proportional to the applied current. The proportionality constant is called Peltier coefficient. In 1851 Lord Kelvin (William Thomson) discovered the effect which describes the heating or cooling of a current carrying conductor with a temperature difference. He provided the Kelvin relations between the Seebeck, Peltier, and Thomson coefficients as shown in section 2.1.4. In 1929 Abram Fedorovich Ioffe introduced a concept of the “figure of merit” ZT for thermoelectric materials. He also brings semiconductors to thermoelectricity field which have much higher thermoelectric figure of merit than metals with ability to make n doped and p doped. His activities lead to some first develop of commercial thermoelectric power generation and cooling devices. The dimensionless thermoelectric figure of merit of a material is given by

$$ZT = \frac{S^2 \sigma}{\kappa} T \quad (2.15)$$

In 1947, the first thermoelectric power generator with efficiency of 5% was constructed by Maria Telkes. In 1954, radioisotope thermoelectric generator RTG was invented by Ken Jordan and John Birden. During the 1970s and 1980s, TE research was declined due to the lack of new semiconducting materials and the lack of new strategies to increase ZT [5]. In 1990s, quantum well superlattices, “phonon-glass, electron-crystal” concept, and a strategy to improve ZT by nanostructure and band engineering were proposed. Over the last two decades, TE materials with ZT values were much improved. Typically, in 2014, SnSe has been reported with excellence TE performance $ZT = 2.6$ in un-doped p-type, $ZT = 2.0$ in Na-doped p-type, and $ZT = 2.2$ in Bi-doped n-type SnSe [6-8]. Figure 2.8. shows the state of the art high ZT materials [4].

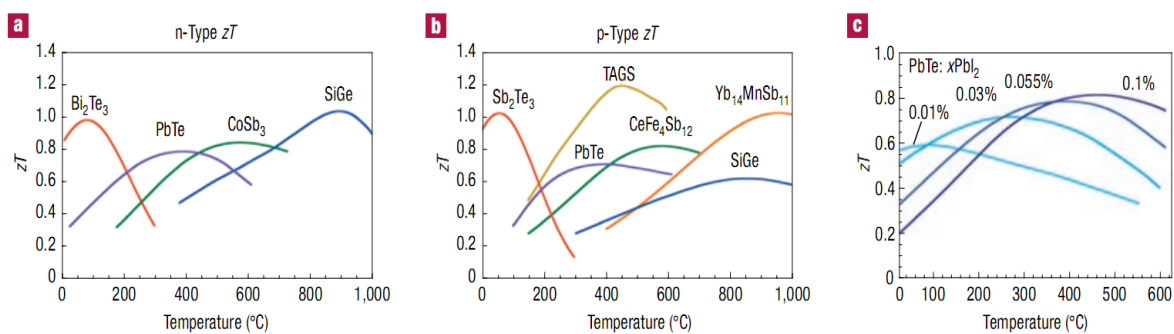


Fig. 2. 8. Thermoelectric figure of merit ZT of state of the art commercial materials for a) n-type, b) p-type, and c) effect of dopant on the peak of ZT .

2.3.2 Defects in semiconductor

Science of semiconductor is defects engineering. There are two categories of defect: chemical imperfection and atomic arrangement imperfection [9]. The chemical imperfection consists of designable defects (dopants, alloying elements) and unwanted defects (impurities). Based on the dimensionality, there are four kinds of defect: 0-dimensional defects (point defects), 1-dimensional defects (line defects), 2-dimensional defects (interfacial defects), and 3-

dimensional defects (bulk defects). This section briefly introduces some basic backgrounds about point defects and line defects.

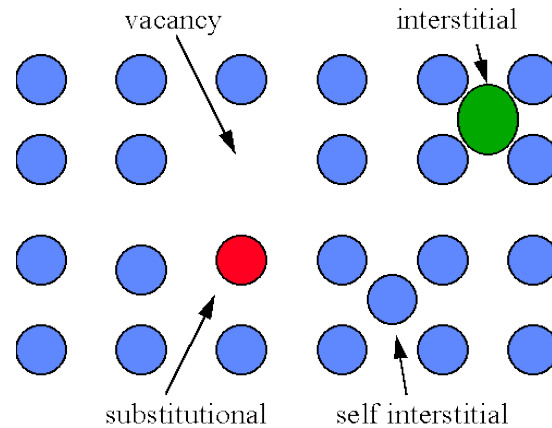


Fig. 2. 9. Points defects in semiconductors.

- 0-dimensional defects (Point defects) is the position with a missing of an atom or in an irregular arrangement of lattice. As shown in Fig. 2.9. There are three kinds of point defect:

+ Substitutional impurities: A substitutional impurity is a replacement of a different atom to one of the bulk atoms' site. Substitutional impurities may dopants (e.g. P in Si, Zn in brass), alloying (e.g. (Ni in Au), or contamination (e.g. Li in NaCl). Usually substitutional atoms have comparable site to the host atoms.

+ Interstitial impurities: The impurity atoms must have much smaller size then the host atoms. Interstitial atoms locate in between host atoms. Interstitial consists of alloying element (e.g. C in Fe to make stainless steel), and contamination (e.g. H in Fe).

+ Vacancies are empty (unoccupied) lattice sites where atoms are missing. Vacancies usually formed at the time of crystallization (strongly depends on growth condition in the growth from the melt techniques) or under extreme conditions.

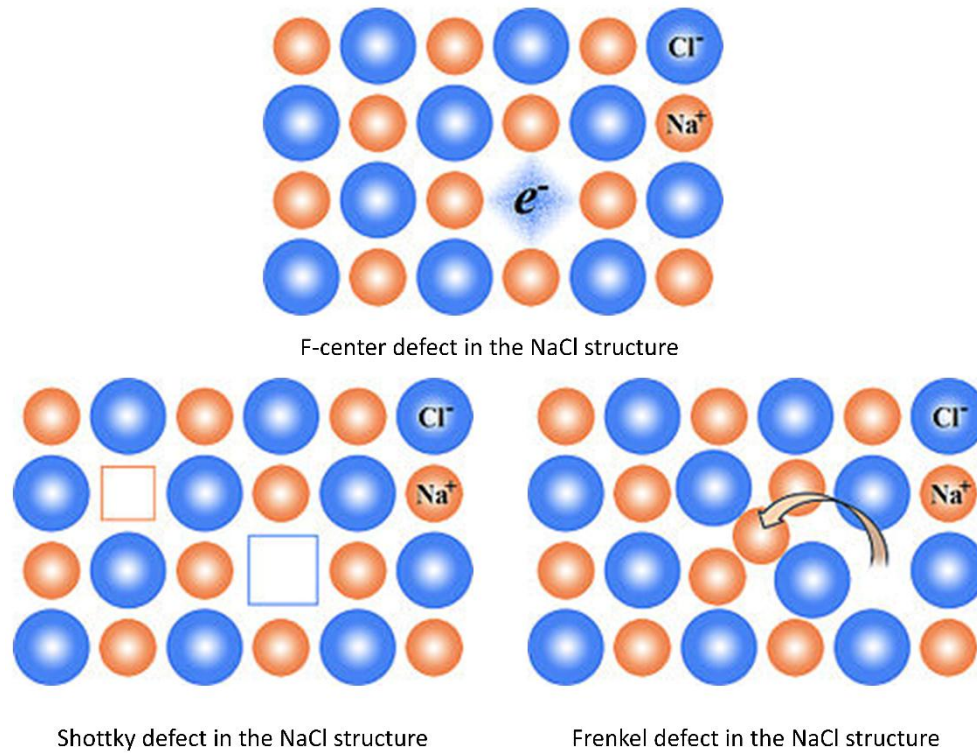


Fig. 2. 10. Point defects in ionic crystal semiconductors [Wikipedia].

In ionic crystals there are three kinds of point defect as shown in Fig. 2.10: Schottky imperfections (one unit of stoichiometry is missing to ensure the charge naturally), Frenkel imperfections (the formation of ion vacancy and an ion interstitial or the displacement of one atom to interstitial position), and F-center defects (the anionic vacancy is occupied by one or more unpaired electrons).

- 2 dimensional defects (line defects or dislocations or linear defects)

Line defects are the lines where the whole row of atoms is irregularly arranged. There are two kinds of line defect: edge dislocation and screw dislocation. Line defects are generated and can be moved by a stress.

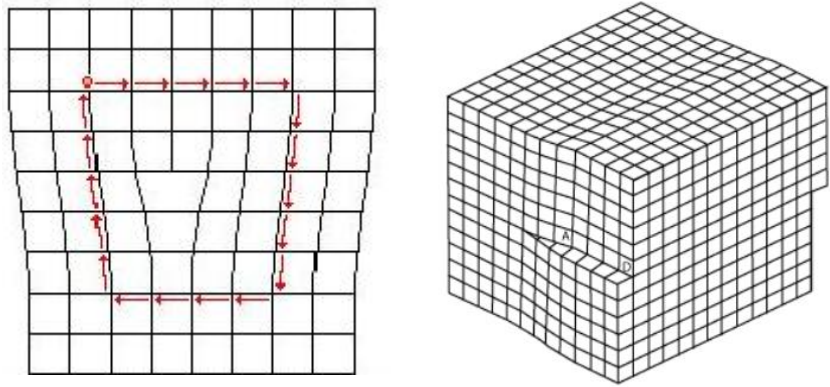


Fig. 2. 11. Edge dislocation (left) and screw dislocation (right) in semiconductors.

2.3.3 Overview about SnSe

Since SnSe is the chosen material of this thesis, in this section, I briefly describe some background about SnSe, including crystal structure, electronic structure, and some physical properties of SnSe [10]. The crystal structure of SnSe with strong anharmonicity leads to its ultralow thermal conductivity. A brief review about the strength of anharmonicity bonding is provided. The origin of p-type characteristic of SnSe, thermoelectric properties and remaining issue of SnSe system are also discussed.

2.3.3.1 Crystal structure

A perspective view of the SnSe structure was provided by Kim *et. al* [11] as shown in Fig. 2.12. SnSe adopts a layered orthorhombic structure at room temperature with $a = 11.49 \text{ \AA}$, $b = 4.44 \text{ \AA}$, and $c = 4.15 \text{ \AA}$, space group $Pnma$ (62) which can be understood as distorted NaCl structure. Note that, to be consistent with the reported thermoelectric properties of SnSe, the authors changed the terms a -axis to b -axis, b -axis to c -axis, and c -axis to a -axis in this reference. Each layer of SnSe consists of two-atomic structure (slabs along b - c plane) with a strong Se-Sn covalence bonding which are stacked with others by weak van de Waals forces along a direction. The crystal structure of SnSe can be also understood as that of black phosphorus,

where phosphorus atoms are replaced by Sn and Se atoms. However, the Sn atoms are slightly buckled upward in a direction [12]. As the consequence, the bonding between Sn and Se atoms creates a zigzag fashion along b - c plane as shown in Fig. 2.12(c). The unit cells of Sn and Se are identical, which are marked by red and blue rectangular, respectively. Figure 2.12(d) represents the side view of SnSe along a - c plane, where the box represents the orthorhombic unit cell and each slab represents one layer of SnSe, connected with others by weak van de Waals forces. One can be easily to be understood that the easy cleavage is along (100) planes.

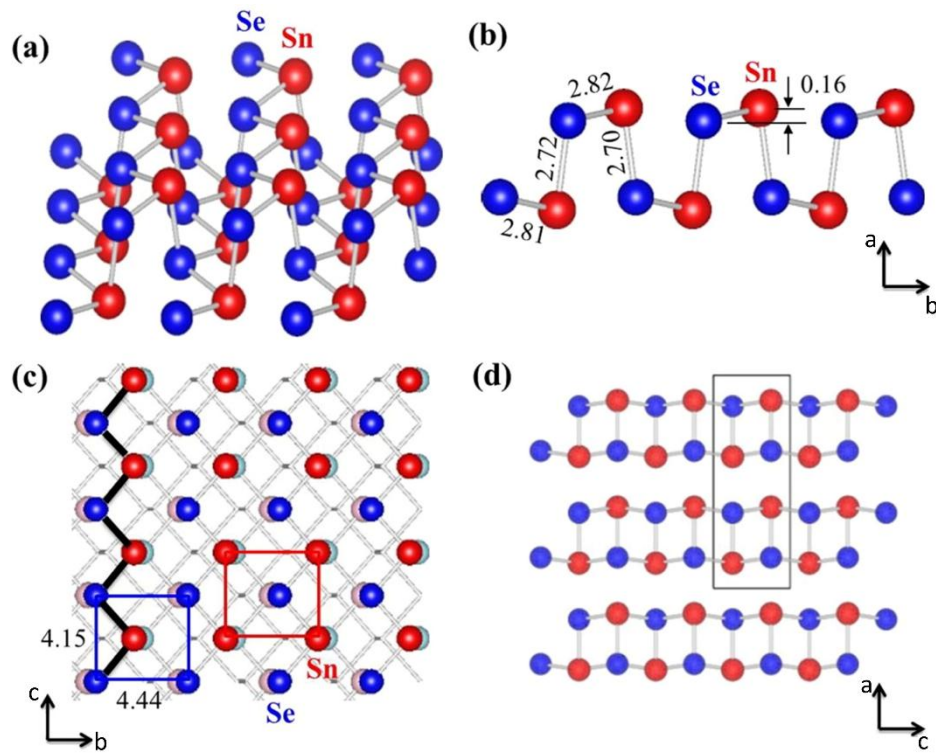


Fig. 2. 12. (a) A perspective view of one SnSe layer, (b) The cross-sectional view of SnSe layer shows the buckling structure, (c) Top view of SnSe layer, the identical blue and red rectangular represent the unit cell of Se and Sn atoms, respectively. Black lines represent the zigzag bonds of Se and Sn atoms, (d) Side-view of SnSe, where black rectangular represents the bulk unit cell. The layers are stacked by Van der Waals force along a -axis. The length's unit is angstroms. Note that, to be consistent with thermoelectric discussions, I have changed the terms a -axis to b -axis, b -axis to c -axis, and c -axis to a -axis. [11]

2.3.3.2 Microscopic structure

The low-temperature orthorhombic (*Pnma*) phase of SnSe has been studied using scanning tunneling microscopy (STM). A high resolution topographic STM images for empty states with various sample bias is shown in Fig. 2.13 [11] In this figure, instead of zigzags pattern they found the rectangular unit cell which may correspond to either Sn or Se unit cell as marked by red and blue rectangular in Fig. 2.12(c). The measured unit cell sizes (4.44 Å and 4.28 Å) agree well with calculated values, as shown above. DFT simulation showed that the pronounced bright spots observed in the STM images are Sn atoms. This observation is exactly same with that of the filled state STM images. When increasing temperature above 750 K, SnSe occurs a transition from *Pnma* phase to higher symmetry *Cmcm* phase. By temperature dependent transmission electron microscope (TEM), Zhao *et. al* [6] has experimentally showed that this phase transition is reversible, as shown in Fig. 2.14. Using TEM image on cleaved plane and selected area diffraction (SAD) pattern, they showed that the sample is defect-free single crystal with orthorhombic structure at low temperature, as shown Fig 2.14(a) and inset. A simulation of crystal structure of the phase at room temperature and at high temperature along [211] and [121] directions is provided in Fig 2.14(b), which can be used to distinguish the low and high temperature phase through the angle between planes (1-1-1) and (-101). According to the simulation, the angles between two planes (1-1-1) and (-101) at low and high temperatures are 86.18° and 89.89°, respectively. To visualize these angles SAD measurement was used because it is sensitive to the change in crystal symmetry, especially angular rotations [6]. Figure 2.14(c) shows the SAD patterns of SnSe single crystal at various points of temperature cycle from room temperature to 800 K, 820 K, and back to room temperature again. The sample was held at each temperature for a time before the patterns were collected to assure that it was stable under the measured temperature. As shown in the figure, the angle changes from 86.5° to 89.11°,

89.04°, and 86.92° at room temperature, 800 K, 820 K, and room temperature again, respectively. These measured angles are matched well with theoretical simulation, indicating that this phase transition is reversible. This observation also confirmed that SnSe is stable at high temperature.

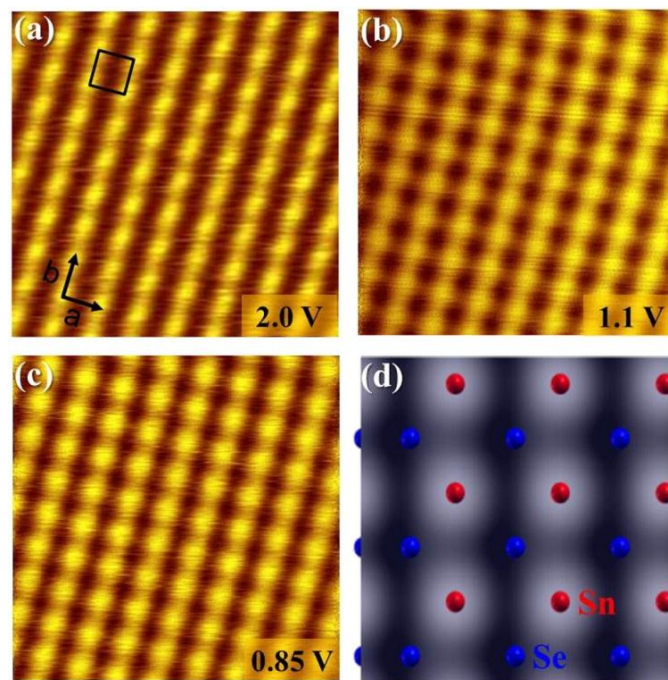


Fig. 2. 13. (a - c) High-resolution topographic images for empty states, where the black rectangular represents unit cell of Sn atoms. The images are $4\text{ nm} \times 4\text{ nm}$ in size with $I_{\text{tunneling}} = 50\text{ pA}$. The numbers represent the applied sample bias. (d) Calculated STM image at sample bias of 2.0 eV. The same note as given in figure 2.12 is applied here. [11]

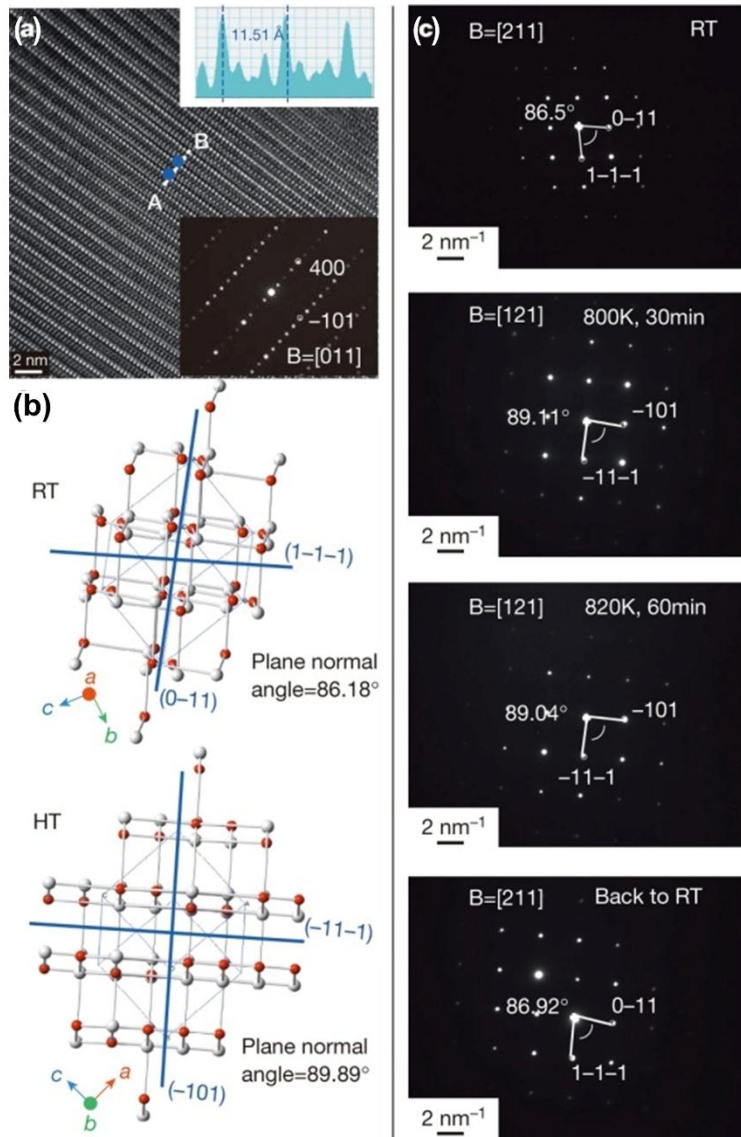


Fig. 2. 14. (a) High-resolution TEM image of single-crystal SnSe. The bottom inset is diffraction pattern along [011] zone axis; the top inset is line profile along the dotted line AB showing the d spacing of (100), (b) Simulated crystal structures of *Pnma* and *Cmcm* phases, viewed along [211] and [121] directions, and (c) SAED patterns at different temperatures, where B is zone axis. [6]

2.3.3.3 Electronic band structure

Figure 2.15 shows the electronic band structure and the density of state (DOS) around the band gap of pristine SnSe for low and high temperature (LT, and HT) phases, which includes the quasiparticle and spin-orbit coupling corrections [13]. In general, the conduction band is taken over by Sn p orbitals, while the valence band is taken over by Se p orbitals [11, 14]. The results show that low temperature *Pnma* SnSe exhibits indirect band gap of 0.829 eV. This value of energy gap is slightly lower than that obtained from optical-absorption measurements (0.860 eV [6] and 0.898 eV [15]) because the excitonic effects was neglected in the calculation. The calculated energy gap for *Cmcm* phase was direct with the value of 0.464 eV. These results indicate a reduction of energy gap after phase transition, which is mainly due to the Sn and Se atomic positions [16]. The same reductions of energy gap have been reported by Zhao *et. al* (0.61 – 0.39 eV) [6] and Kutorasinski *et.al* (0.474 – 0.350 eV) [16]. As shown in the figure for the *Pnma* phase, the valence band maximum (VBM) is located along Γ –Y direction of the first Brillouin zone with a 1 meV lower local VBM. While the conduction band minimum (CBM) is located along Γ –X direction. The CBM and VBM of *Cmcm* phase are located at the same position along the X–A direction of first Brillouin zone, resulting in a direct band gap. There are local VBM and CBM located at 0.031 eV below VBM and 0.07 eV above CBM along Γ –H and X–H1 directions, respectively. The calculated effective masses were different between two phases. For *Pnma* phase the effective masses are 0.74, 0.31, 0.16 at VBM and 2.40, 0.11, 0.15 at CBM along *a*, *b*, and *c*-axes, respectively. For *Cmcm* phase these are 0.34, 0.04, 0.09 at VBM and 3.07, 0.04, 0.10 at CBM along *a*, *b*, and *c*-axes, respectively. One can see that the effective masses are highly anisotropic for both phases, where the higher values are found in *a*-axis due to the nature of layered materials [13]. Therefore, the electrical properties of SnSe will certainly be strong anisotropic. DOS plot showed a smaller DOS effective mass of

electrons than that of hole as shown in Fig 2.15(c) and (d). This result is opposite to the result above for both cases that the effective mass along a -axis at CBM is higher than that at VBM.

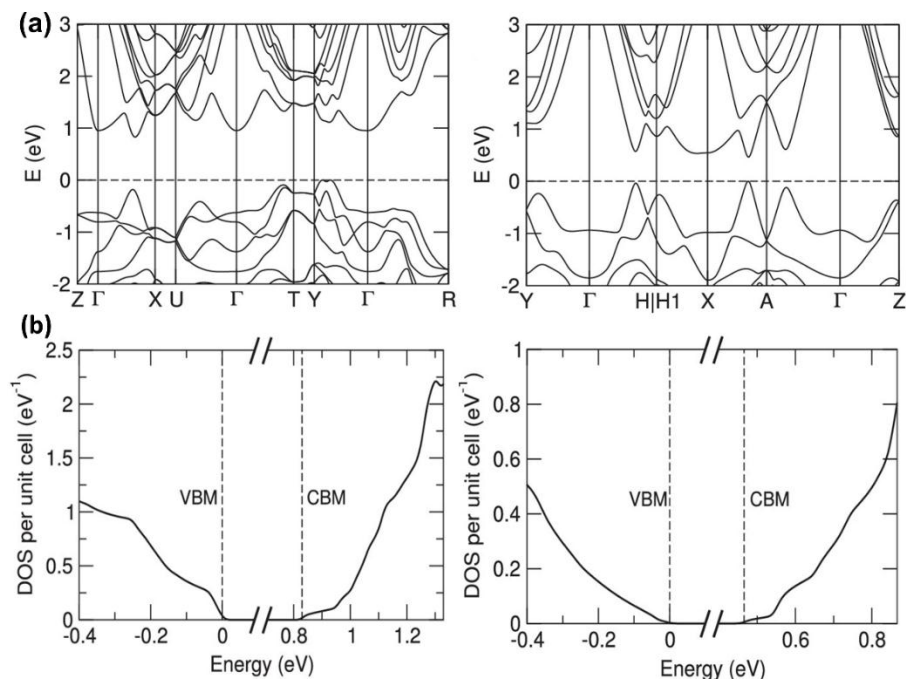


Fig. 2. 15. (a) Quasiparticle band structures of $Pnma$ phase (left) and $Cmcm$ phase (right) of SnSe with indirect band gap of 0.829 eV and direct band gap of 0.464 eV, respectively. (b) Density of states of $Pnma$ phase (left) and $Cmcm$ phase (right) of SnSe around the band gap.

[13]

2.3.3.4 Gruneisen parameter

SnSe have been reported to have strong anharmonicity bonding, leading to its ultralow thermal conductivity [6, 17]. Gruneisen parameter of SnSe has been calculated by Zhao *et. al* [6], which is used to estimate the strength of lattice anharmonicity, as shown in Fig. 2.16. The Gruneisen parameters of SnSe are very large and anisotropic, where the average parameters along a -axis (4.1) are larger than those along b -axis (2.1) and c -axis (2.3), implying the anisotropic thermal conductivity of SnSe [6]. The average Gruneisen parameters of SnSe along a , b , c axes are

larger than those of the state of art thermoelectric materials such as AgSbTe₂ (2.05) [18] and AgSbSe₂ (3.5) [19]. These large Gruneisen parameters lead to strong anharmonicity assigned to the electrostatic repulsion between Sn 5s lone-pair electrons and crystal structures of SnSe [17].

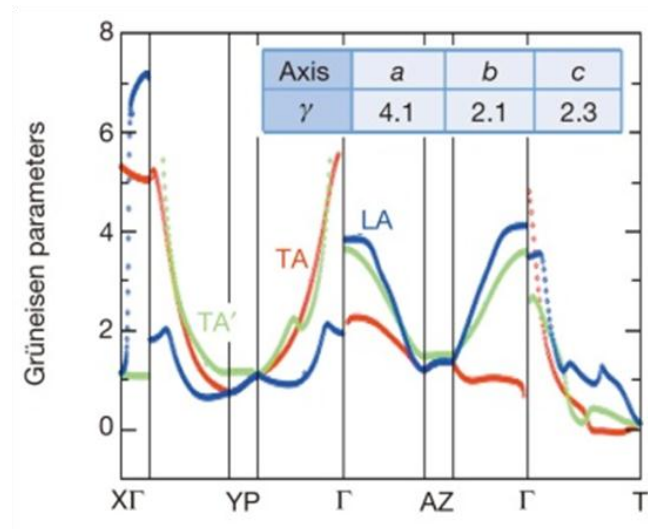


Fig. 2. 16. Gruneisen dispersion of SnSe. The inset is average Gruneisen parameters along a , b and c axes. [6]

2.3.3.5 The origin of p-type characteristic of SnSe

Up to now, there are some theoretical and experimental studies about the origin of p-type characteristic of SnSe [14, 20]. Huang *et. al* [14] has theoretically studied about the source of p-type conduction in SnSe by introducing six kinds of defects including two vacancies (V_{Sn} and V_{Se}), two interstitials (Sn_i and Se_i), and two anti-sites (Sn_{Se} and Se_{Sn}). The contribution of each intrinsic defect to the p- or n-type conduction of materials is mainly dependent on its transition energy level and its formation energy. The defect with shallow transition energy level and relative low formation energy will act as effective source of p- or n-type conduction of material. The intrinsic defects have been studied under Se rich (Sn poor) and Sn rich (Se poor)

condition. This growth condition takes a strong effect to the formation of defects as well as the secondary phases; the most favorable phase is SnSe₂ phase under Se rich condition. The formation energy $\Delta H_{D,q}$ of a defect D in a charge state q can be calculated as following equation [21]

$$\Delta H_{D,q} = E_{D,q} - E_H - \sum n_\alpha \mu_\alpha + q(E_F + E_V + \Delta V) \quad (2.16)$$

where, $E_{D,q}$ is the total energy of a super cell with a defect in charge state q and E_H is the total energy of a perfect super cell of the same size. n_i ($i = \text{Sn}$ and Se) is the number of atoms removed ($n_\alpha < 0$) or added ($n_\alpha > 0$) from the supercell to form a defect, μ_α is the atomic chemical potential and q is number of electron transferred from (to) electron reservoirs. The defects with formation energies below 1.5 eV are considered as relative low and have possibility to affect SnSe electrical properties. As shown in table 2.1, three defects in their neutral charge state (Sn_{Se}, V_{Sn} and V_{Se}) are in the case. Defect introduces level in the band gap and reflects its transition level by position of Fermi level, which decides whether it can act as donor or acceptor. The transition level $\varepsilon(q/q')$ is defined as ratio of different formation energies of a defect in charge state q and q' and the different charges in each state [21]

$$\varepsilon(q/q') = \frac{E_F(q) - E_F(q')}{q - q'} \quad (2.17)$$

Small $\varepsilon(q/q')$ means shallow transition level, which require small energy to elevate an electron or hole from the trap. Figure 2.17 shows the formation energy of each intrinsic defect as a function of Fermi energy under Sn rich and Se rich conditions. The formation energy of V_{Sn} with $q = -2$ is the lowest one under both conditions. The transition energy level of defects reference to VBM for intrinsic defects in SnSe is shown in table 2.2. Among that V_{Sn} shows ultra-shallow transition energy level $\varepsilon(0, 2-)$, which located at very close to VBM, indicating

that V_{Sn} can act as a shallow acceptor and contributes prominently to the p-type conduction of SnSe. According to Fig. 2.17, V_{Sn} and V_{Se} have relative low formation energies. Under Sn-rich condition V_{Se} is energetically more favorable, while under Se-rich condition V_{Sn} is more favorable. The transition level $\varepsilon(I+/0)$ of V_{Se} is very close to the VBM, leading to it is stable in a neutral charge state with high E_F (above 0.38) and acts as a deep donor. Similarly, due to the high formation energies anti-site defects Sn_{Se} can act as deep donor and Se_{Sn} can act as a deep acceptor. For interstitial defects, Sn_i has high transition energy level $\varepsilon(I+/0)$ with respect to the CBM and high formation energy; therefore, it can act a deep donor. Se_i can act as an ultra-deep acceptor due to its ultra-deep transition energy level. These deep acceptor and donor levels are predicted to have an insignificant contribution to the p- and n-type conduction of SnSe.

Table 2. 1. Crystallographic and thermoelectric transport parameters of SnSe at 300 K [6].

Defects	q	E_F (Sn rich)	E_F (Se rich)
V_{Sn}	2-	1.47	0.73
	1	1.42	0.69
	0	1.47	0.73
V_{Se}	2-	1.95	2.68
	1-	1.02	1.75
	0	0.16	0.89
	1+	-0.23	0.51
Sn_i	0	2.48	3.22
	1+	1.73	2.47
	2+	1.17	1.91
Se_i	2-	5.22	4.49
	1-	4.28	3.55
	0	3.41	2.67
	1+	3.24	2.50
Sn_{Se}	2-	1.75	3.22
	1-	1.11	2.58
	0	0.62	2.09
	1+	0.39	1.86
	2+	0.17	1.65
Se_{Sn}	2-	4.11	2.64
	0	3.41	1.94
	1+	3.21	1.74
	2+	3.15	1.68

Table 2. 2. The formation energy of defects in different charge states under the Sn-rich condition (E_F, Sn) and Se-rich condition (E_F, Se) [14].

Defects	q/q'	$\epsilon(q/q')$ (eV)
V_{Sn}	2-/0	0.004
V_{Se}	0/1-	0.86
	1+/0	0.38
Sn_i	1+/0	0.75
	2+/1+	0.56
Se_i	0/1-	0.87
	1+/0	0.17
Sn_{Se}	1-/2-	0.64
	0/1-	0.48
	1+/0	0.24
	2+/1+	0.21
Se_{Sn}	0/2-	0.35
	1+/0	0.20
	2+/1+	0.06

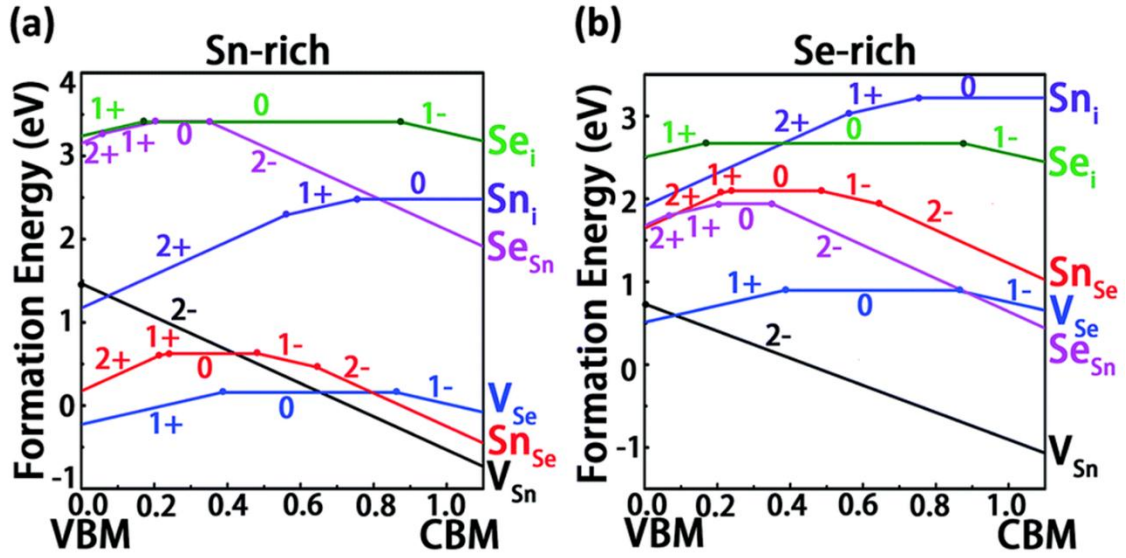


Fig. 2. 17. Calculated formation energies as a function of Fermi level (EF) of the six intrinsic defects in SnSe under the Sn-rich (a) and Se-rich conditions (b). [14]

The above predictions are match well with experimental observations reported by Ganbat *et. al* [20] using STM. STM studies showed that there are three main kinds of defect in SnSe surface, including single Sn vacancy (V_{Sn}), Se vacancy (V_{Se}), and Se-Sn-Se vacancy ($V_{Se-Sn-Se}$). Among them V_{Sn} is the most dominant defect with 81%, followed by 17% V_{Se} , and 2% ($V_{Se-Sn-Se}$). Figure 2.18 shows the large area STM image of SnSe surface. Three kinds of defects on the SnSe surface are labeled as A, B, and A' corresponding to the V_{Sn} , V_{Se} , and $V_{Se-Sn-Se}$. The formations of these vacancies are confirmed by DFT calculation as shown in Fig. 2.19. The effects of these vacancies also have been studied by first principle DFT calculation as shown in Fig. 2.20. Pristine SnSe exhibits a wider indirect band gap and non-parabolic multiple valence band (Fig. 2.20(a)), while with the presence of V_{Sn} the Fermi energy is significantly moved inside the dispersive valence band, indicating that V_{Sn} provides extra hole to the crystal. In contrast, V_{Se} creates nondispersive donor states near valence band (Fig. 2.20(c)) and provide immobile electron localized within few angstroms around the vacancy site. In the case of V_{Se} .

s_{n-Se} , it creates two very nondispersive flat bands near the mid gap (green dash-dotted line in Fig. 2.20(d)) and takes the similar effects as V_{Se} to the electronic properties of SnSe. The differential conductance (dI/dV) measurement taken around V_{Sn} showed broad peaks in the filled state as shown in Fig. 2.21. This means that the V_{Sn} site and around are relatively negative and donate extra holes to the crystal. Therefore, V_{Sn} is theoretically and experimentally confirmed as the main source of p-type characteristic of SnSe single crystal.

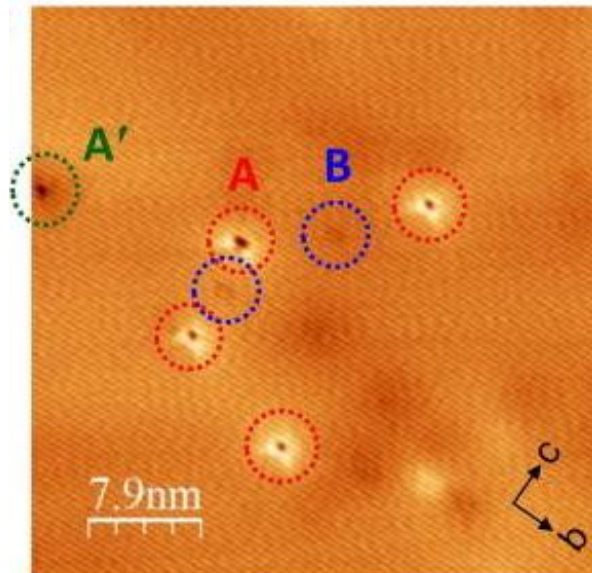


Fig. 2. 18. STM image of SnSe (b - c) surface showing three intrinsic defects (A, A', and B).

Imaging conditions sample bias $V_b = -2.0$ V and tunneling current $I_t = 50$ pA. [20]

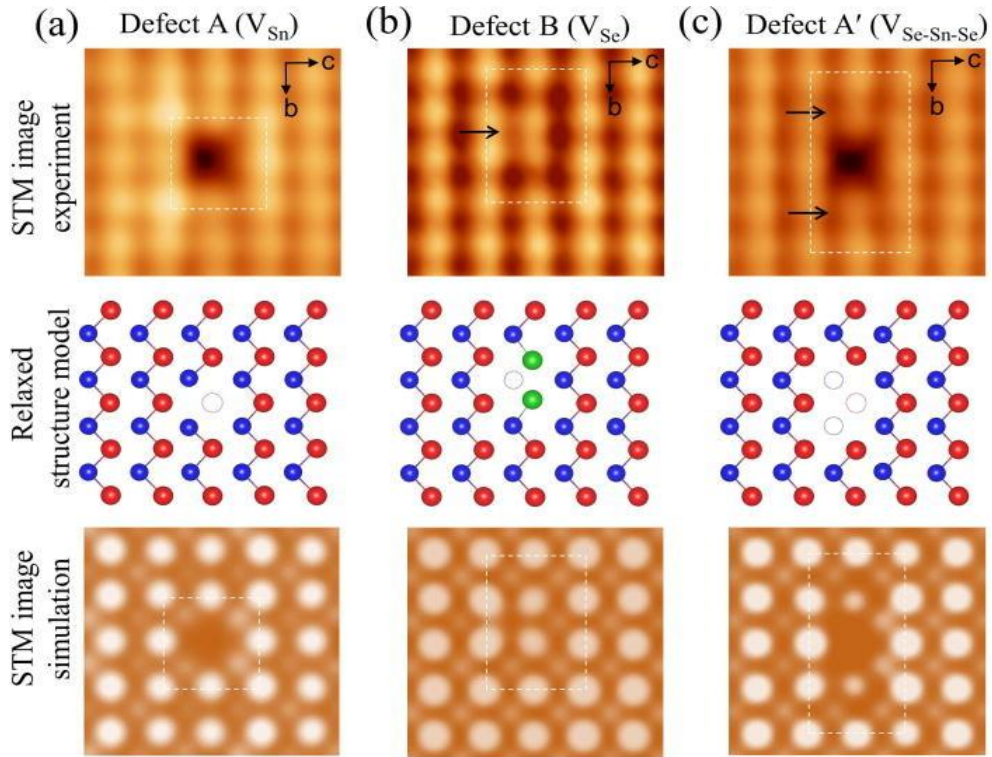


Fig. 2. 19. High-resolution STM topographic images ($2.2 \text{ nm} \times 2.1 \text{ nm}$, $I_t = 30 \text{ pA}$ and $V_b = -1.5 \text{ V}$) (top), top view of relaxed structure models, where the blue, red balls and open circles represent Se, Sn atoms, and vacancies (middle), and DFT simulated images (bottom) of (a) Sn vacancy, (b) Se vacancy, and (c) Se–Sn–Se vacancy. [20]

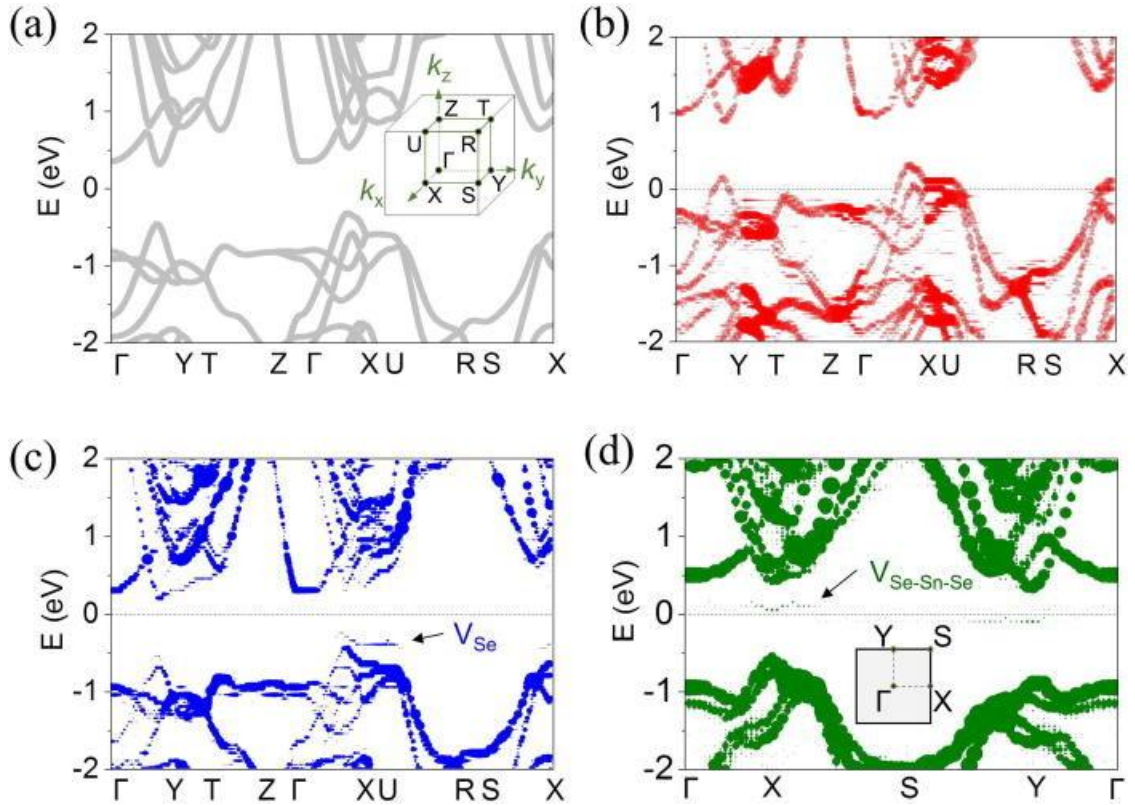


Fig. 2. 20. Calculate (a) Band structure of bulk SnSe. Unfolded band structure of (b) a $3 \times 3 \times 1$ SnSe supercell containing 35 Sn atoms and 36 Se atoms (one Sn vacancy). (c) a $3 \times 3 \times 1$ SnSe supercell containing 36 Sn atoms and 35 Se atoms (one Se vacancy). (d) a $5 \times 6 \times 1$ SnSe slab (with a 16 \AA vacuum) consisting of 119 Sn atoms and 118 Se atoms (one Sn vacancy and two Se vacancies). The Fermi level is set to zero energy [20].

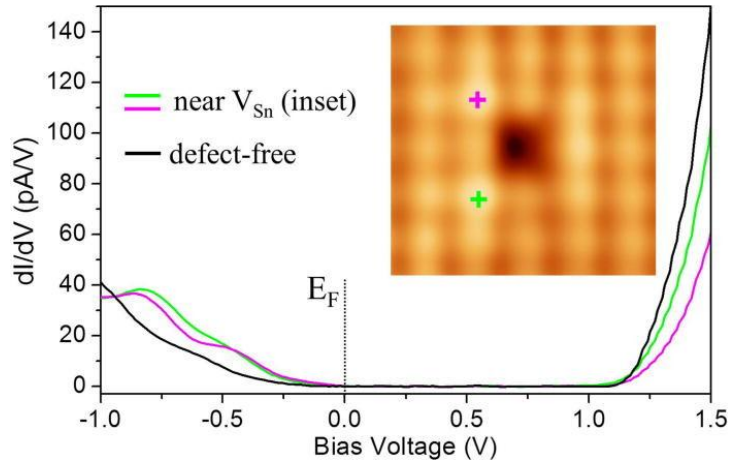


Fig. 2. 21. The dI/dV curves of Sn vacancy. The inset is STM image of Sn vacancy. The pink and green notes indicate the positions where the pink and green lines are obtained. The black curve is obtained from defect free position [20].

2.3.3.6 Thermoelectric properties

a. p-types SnSe

Since 2014, a number of studies about SnSe based thermoelectric materials have been reported. Thermoelectric properties of un-doped, Na, and Ag doped p-type SnSe single crystals grown by Bridgman technique have been reported with remarkable high ZT values of 2.6, 2.0, and 0.95, respectively [6, 7, 22, 23]. Thermoelectric properties of p-type SnSe polycrystalline also have been reported with much smaller ZT values from 0.5 to 1.3 [24-37]. The high ZT value in un-doped single crystal mainly came from its moderate power factor and ultra-low thermal conductivity. Figure 2.22 shows the transport parameters and ZT values as a function of temperature of un-doped p-type SnSe along a , b , and c -axes [6]. Anisotropic thermoelectric transport properties were observed. The maximum power factor was achieved along b -axis (about $10.1 \mu\text{W}/\text{cmK}^2$) around 850 K. The maximum power factor at 850 K along a and c -axes are $2.1 \mu\text{W}/\text{cmK}^2$ and $7.7 \mu\text{W}/\text{cmK}^2$, respectively. These power factor values are moderate

compared to other thermoelectric materials. The thermal conductivity decreased with temperature and reached ultralow values (the lowest among any bulk materials $0.23-0.34$ W/m-K) at 973 K. As a result, ZT value increased with temperature and reach maximum values 0.8, 2.62, and 2.3 at 923 K along a , b , and c -axes, respectively. This high ZT value is obtained at quite high temperature (923 K), which is high temperature for realization in applications. Efforts have been done to bring ZT peak down to moderate temperature range by optimizing carrier concentration through Na or Ag doped SnSe single crystal [7, 22, 23]. The peak $ZT = 2.0$ at 773 K was achieved in Na-doped SnSe [7]. Figure 2.23 shows temperature dependent transport parameters and ZT value of Na-doped SnSe single crystal in comparison with those of undoped SnSe single crystal. Na seems to very active dopant for SnSe crystal, raising electrical conductivity to very high value at 300 K up to $1300-1500$ Scm^{-1} and decreased with temperature, indicating a very high carrier concentration at 300 K. Lower Seebeck coefficient of 160 $\mu\text{V/K}$ was achieved as a result of high carrier concentration. The combination of high electrical conductivity and Seebeck coefficient results in a high $PF \sim 40$ $\mu\text{W/cmK}^2$ at 300 K. Thermal conductivity of hole doped SnSe is still as low as that of un-doped and reached ultralow values at high temperature. As a result, a vast increase in ZT from 0.1 to 0.7 at 300 K and a maximum ZT value of 2.0 at 773 were achieved along b -axis.

Due to the high cost of fabrication and long growth duration and its weak mechanical property of single crystal, polycrystalline SnSe have widely been studied as listed in table 2.3 [25, 27-37]. Among these the electrical conductivity as high as that of single crystal was achieved in polycrystalline SnSe based composites with carbon black of nano-inclusions [32] and with mixed rock-salt cubic phase [26], resulting in high ZT values of 1.2 at 903 K and 1.3 at 850 K, respectively, as shown in Fig. 2.24 and Fig. 2.25.

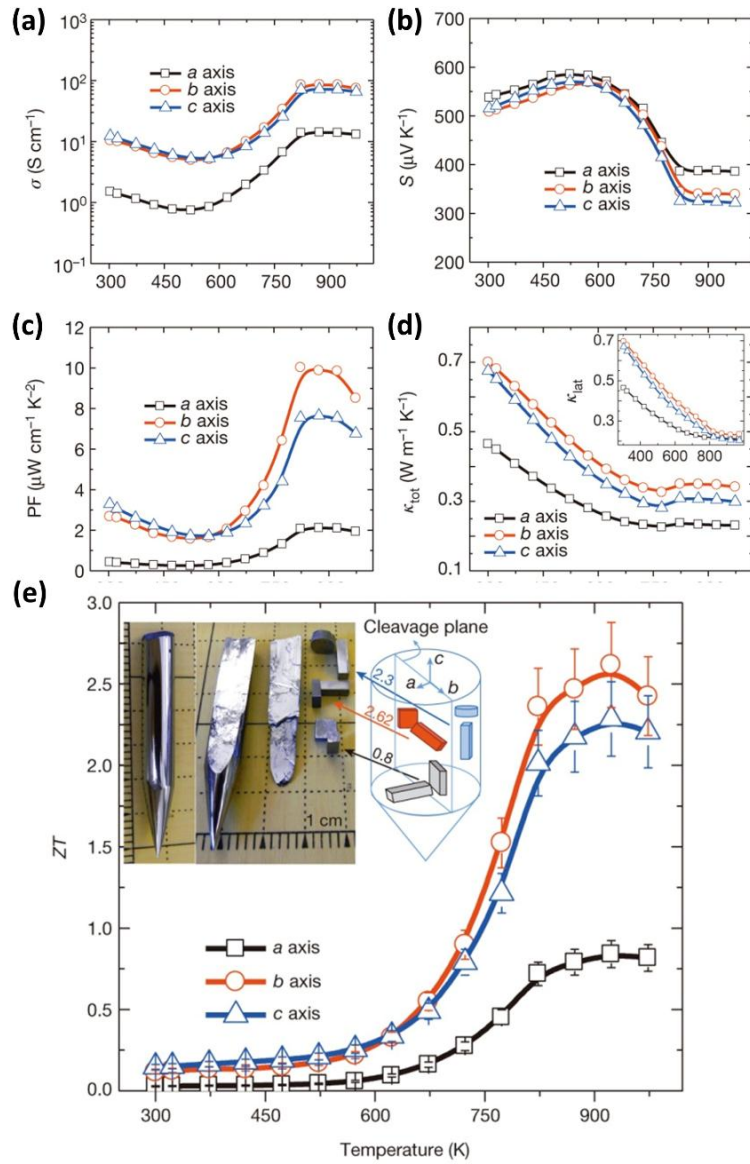


Fig. 2. 22. Temperature dependent thermoelectric transport parameters (a – d) and ZT values (e) along a , b , and c – axes of SnSe. [6]

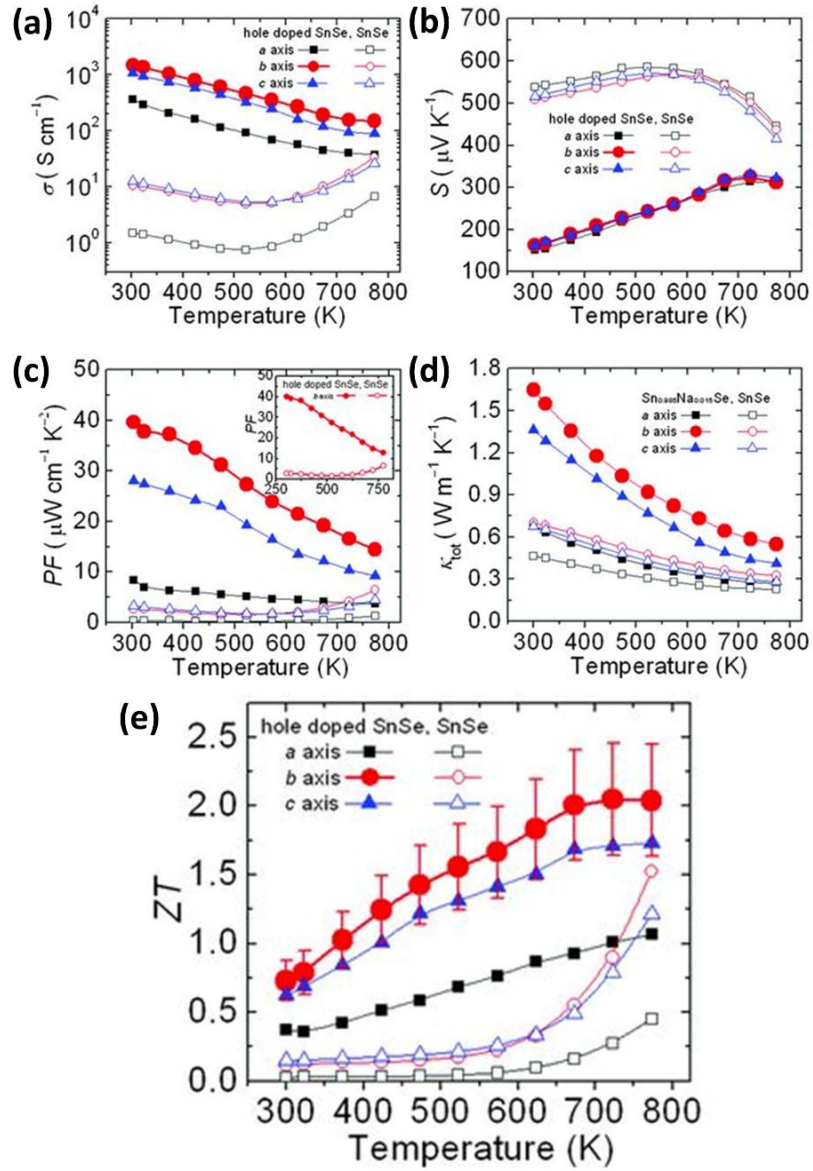


Fig. 2. 23. Temperature dependent thermoelectric transport parameters (a – d) and ZT values

(e) of hole doped SnSe along *a*, *b*, and *c*-axes in compare with SnSe un-doped. [7]

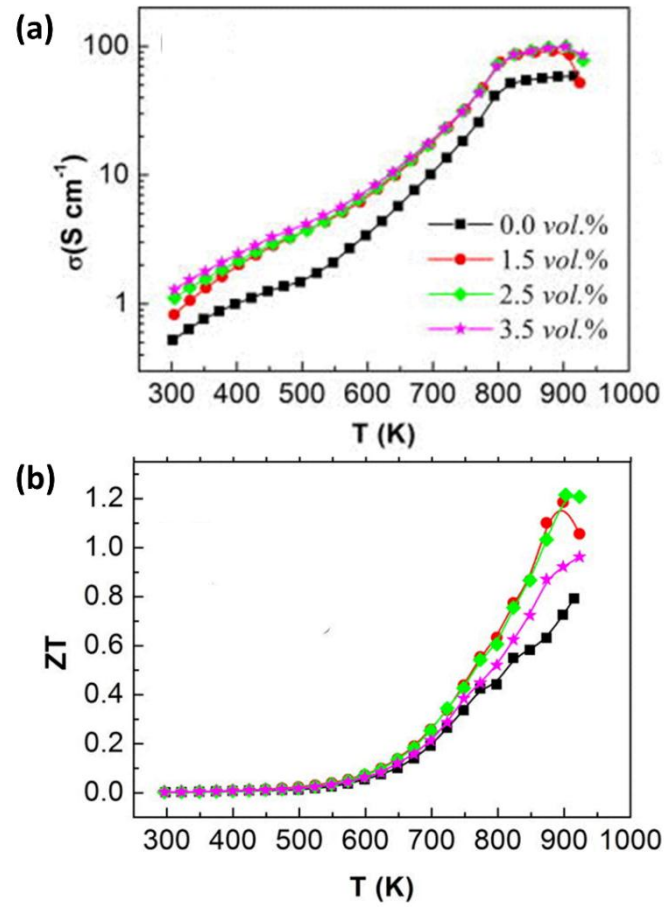


Fig. 2. 24. Temperature dependent electrical conductivity (a) and ZT values (b) of SnSe based composites with carbon black nano-inclusions. [33]

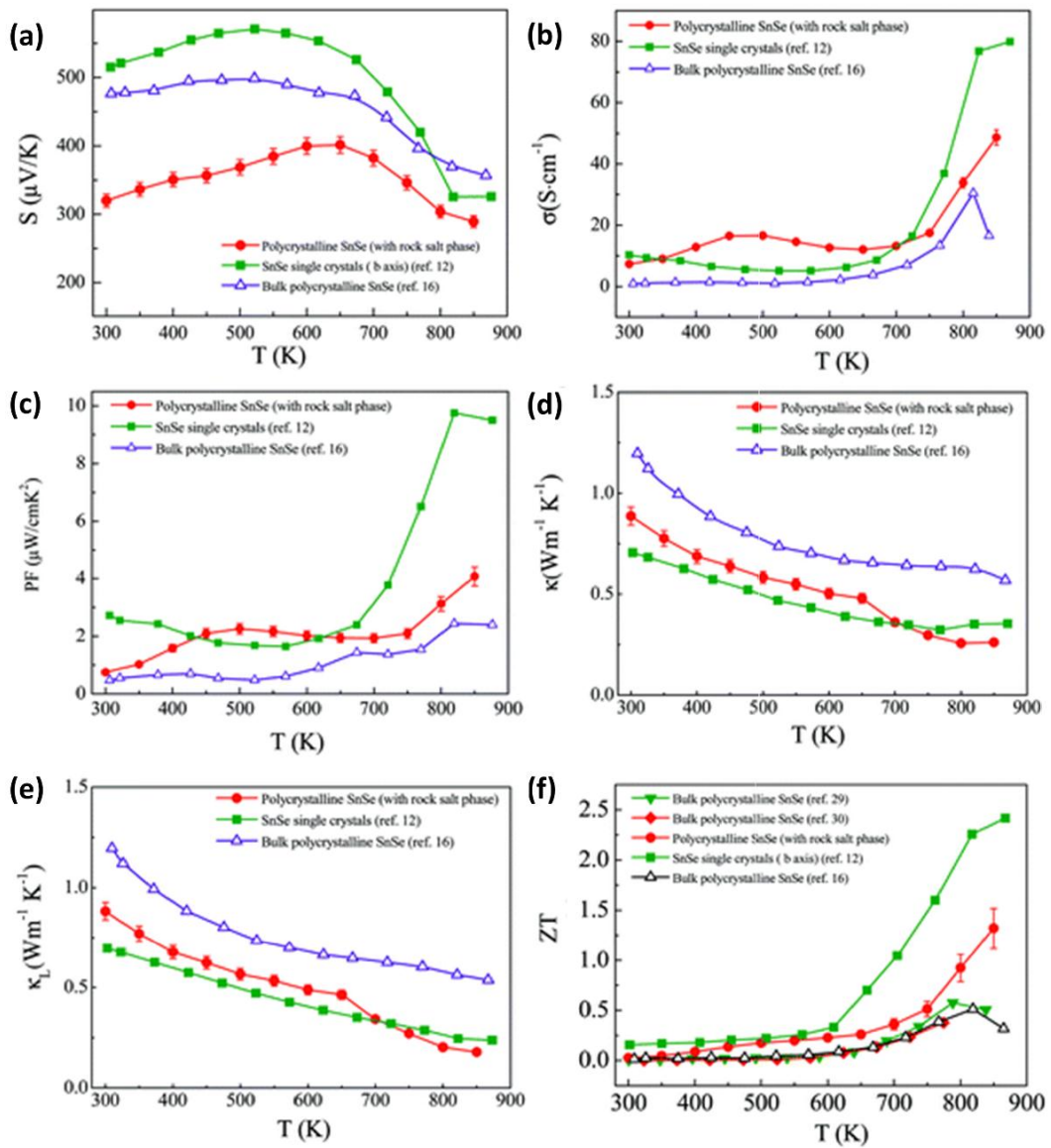


Fig. 2. 25. Temperature dependent thermoelectric transport parameters (a - e) and ZT values

(f) of rock-salt-type nanoprecipitates un-doped polycrystalline SnSe. [27]

b. n-type SnSe

SnSe is fairly hard to be doped. There are limited publications in n-type SnSe as listed in table 4. We have reported Bi-doped n-type SnSe single crystal with ZT value of 2.2 at 733 K [8]. Polycrystalline n-type SnSe have been reported with smaller ZT values of 0.6, 0.7, 1.0, and 1.2 for Tl, BiCl₃, S-I, and Br-Pb doped, respectively. Figure 2.26 shows temperature dependent thermoelectric transport properties of Bi-doped n-type SnSe single crystal [8]. Anisotropic thermoelectric transport properties of SnSe single crystal still remains in Bi-doped SnSe. Maximum power factor of n-type Bi-doped SnSe single crystal, $12 \mu\text{W}/\text{cmK}^2$, was obtained along b -axis, which is higher than that of un-doped SnSe single crystal $10.1 \mu\text{W}/\text{cmK}^2$ [6]. Thermal conductivity remains ultralow. The optimized carrier density (10^{19}cm^{-3}) was obtained around 733 K, leading to the peak of ZT value of 2.2 at 733 K as shown in Fig. 2.27. By STM studies we found that Bi atoms substitute to Sn sites and act as donor impurities lead to the n-type characteristic of our samples, which is confirmed by DFT calculation (Fig. 2.28). Interestingly, the presence of Bi eliminated Sn vacancies (Fig. 2.29), indicating that Bi atoms not only substituted in to Sn sites but also acted as flux for crystal growth. The highest ZT value of n-type polycrystalline SnSe has been reported in Br and P doped SnSe [38]. The electrical conductivity and Seebeck coefficient increased with temperature, while thermal conductivity remains ultralow and decreased with temperature for both Br doped and Br-Pb alloying system, leading to a peak of ZT value of 1.2 at 773 K as shown in Fig. 2.30 and Fig. 2.31.

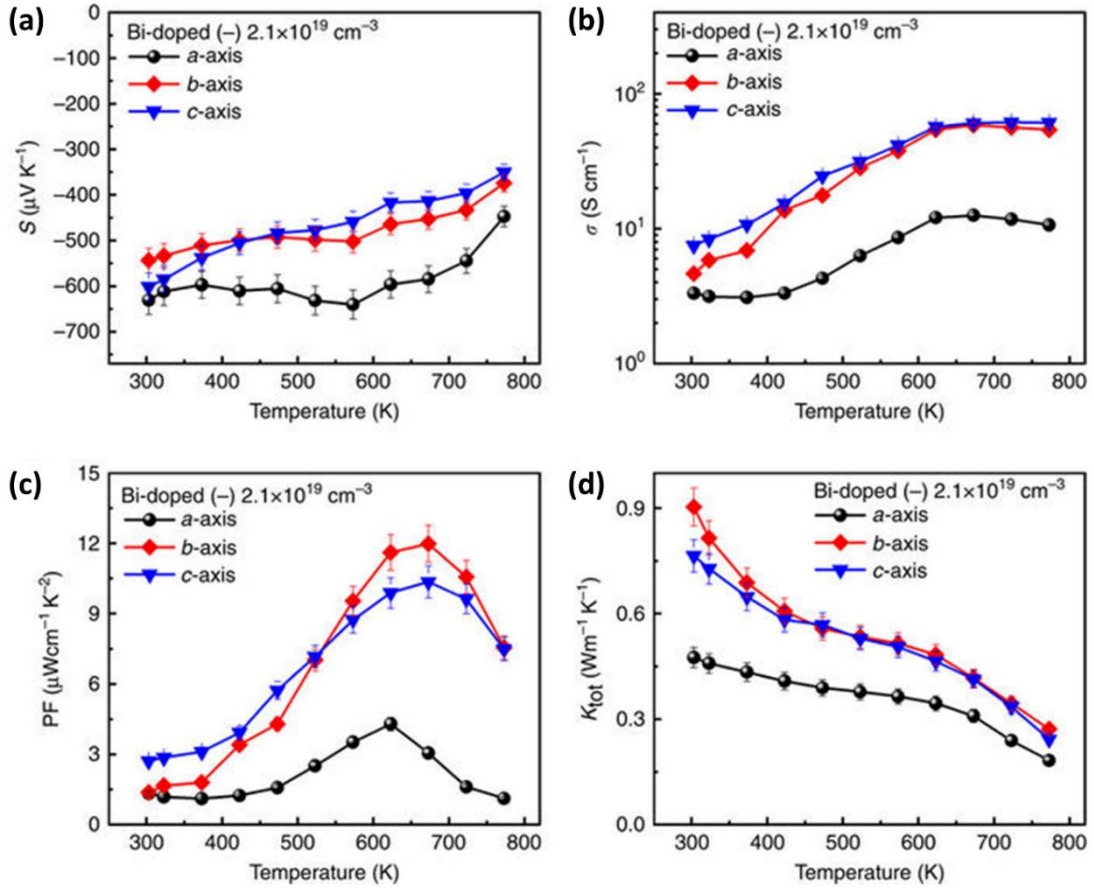


Fig. 2. 26. (a – d) Thermoelectric transport parameters as a function of temperature of Bi-doped n-type SnSe with carrier concentration of $-2.1 \times 10^{19} \text{ cm}^{-3}$ at 773 K along *a*, *b*, and *c*-axes. [8]

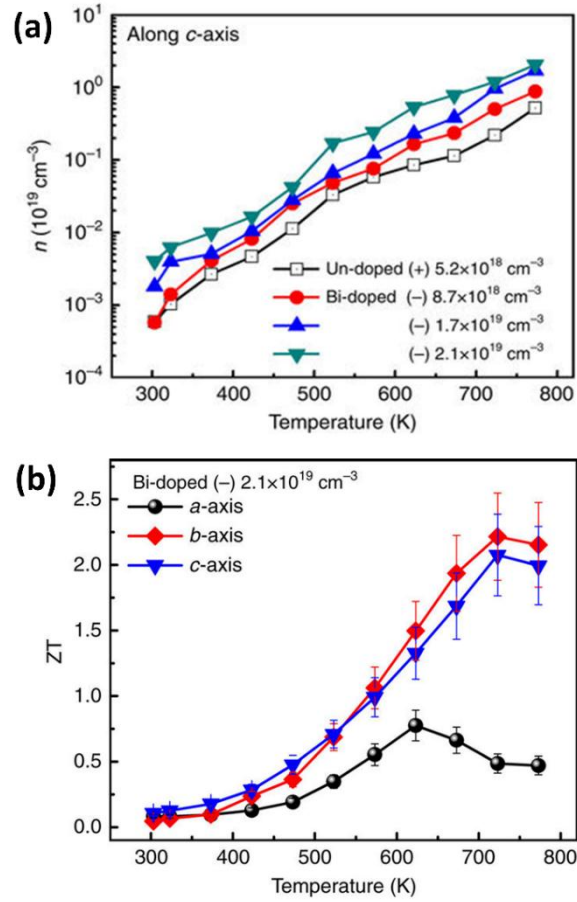


Fig. 2. 27. Temperature dependence of (a) Carrier density of various doping levels of Bi-doped n-type SnSe single crystal along c -axis and (b) ZT values of the highest doping level sample along a , b , and c – axes. [8]

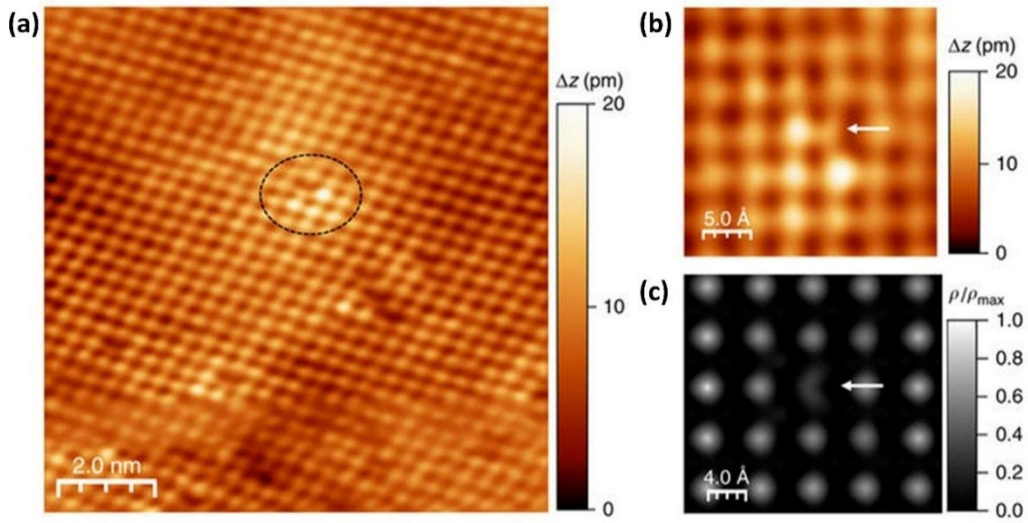


Fig. 2. 28. (a) STM topographic image of Bi-doped SnSe, where the Bi dopant is indicated by dotted ellipse, (b) High resolution STM image taken from the circled areas in (a), (c) Simulated STM image of SnSe supercell with Bi dopant at Sn site. ρ in the color bar represents charge density ($e/\text{\AA}^{-3}$). Both experiment and calculation indicate the substitution of Bi atoms in to Sn site. All STM images were taken with $V_b = -1.8$ V and $I_t = 30$ pA. [8]

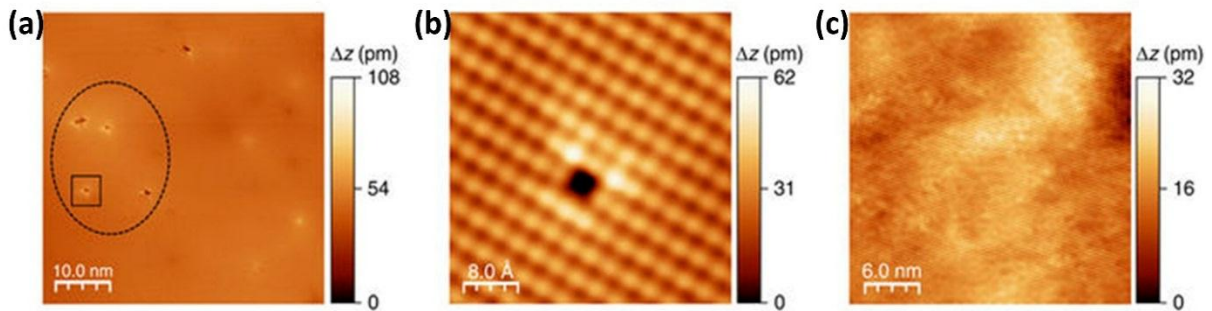


Fig. 2. 29. (a) STM topographic image on the b - c plane of un-doped p-type SnSe with carrier concentration of $5.2 \times 10^{18} \text{ cm}^{-3}$ at 773 K, where Sn vacancies are indicated by dotted ellipse, (b) High resolution STM image taken from black box in (a). (c) STM topographic image on the b - c plane of Bi-doped n-type SnSe with carrier concentration of $-8.7 \times 10^{18} \text{ cm}^{-3}$ at 773 K. The STM scanning conditions: (a), (b) sample bias $V_b = -1.5$ V, tunneling current $I_t = 30$ pA, (c) $V_b = -2.0$ V, $I_t = 18$ pA. [8]

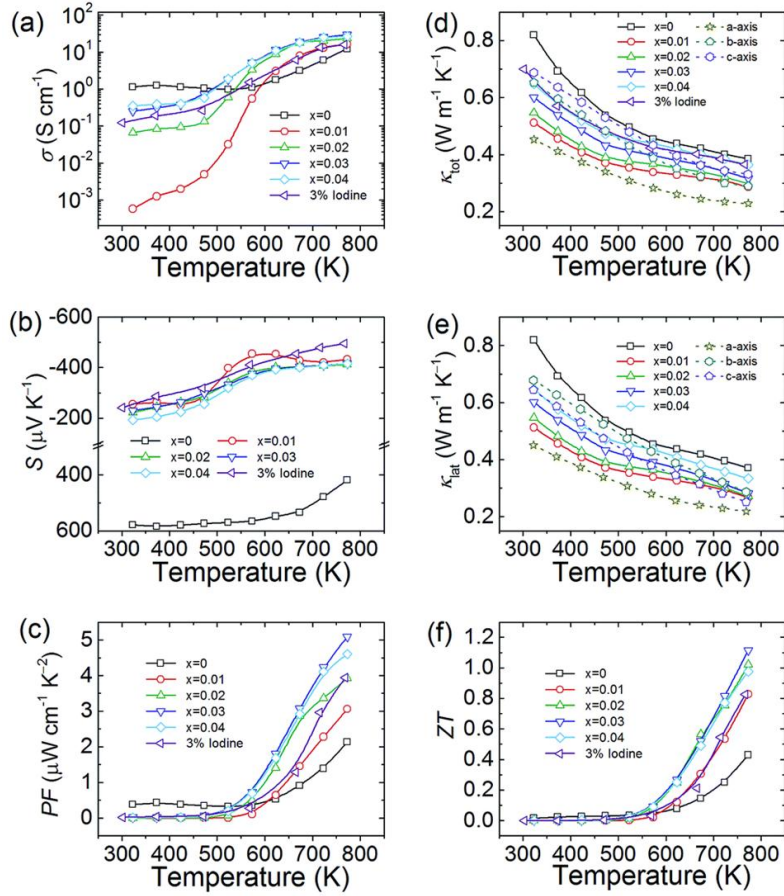


Fig. 2. 30. Thermoelectric transport parameters (a – f) and ZT values (f) as a function of temperature along the pressing direction for $\text{SnSe}_{1-x}\text{Br}_x$ ($x = 0, 0.01, 0.02, 0.03, \text{ and } 0.04$) in compare with those of I-doped SnSe and single SnSe crystals. [39]

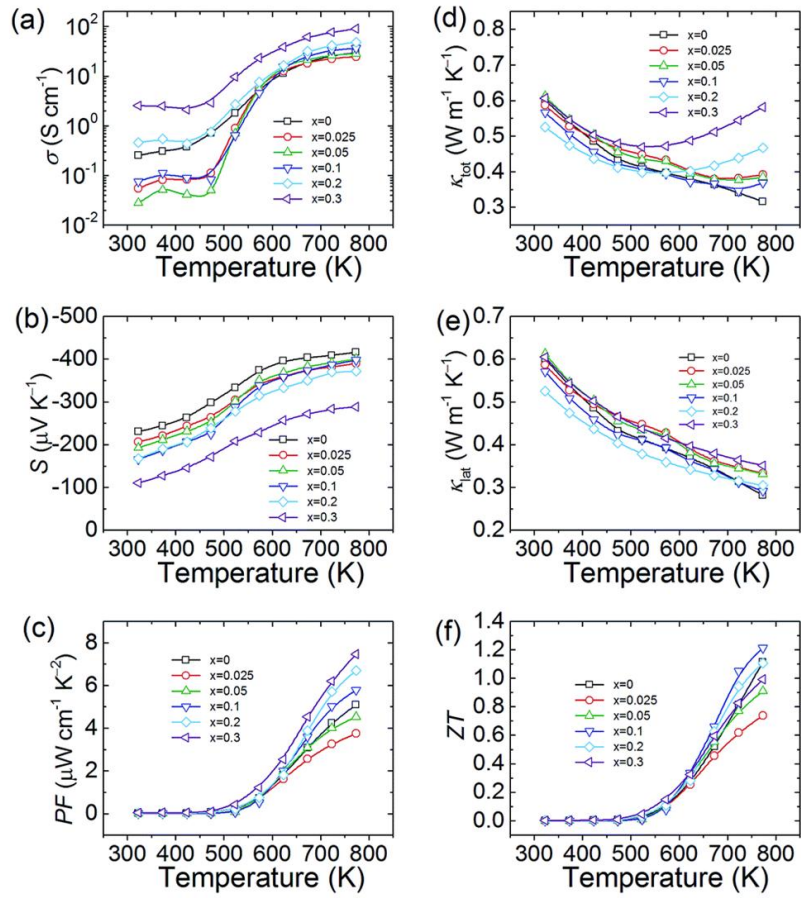


Fig. 2. 31. Thermoelectric transport parameters (a – e) and ZT values (f) as a function of temperature along the pressing direction for $\text{Sn}_{1-x}\text{Pb}_x\text{Se}_{0.97}\text{Br}_{0.03}$ ($x = 0-0.3$). [39]

c. Some issues concerning SnSe

Thermoelectric figure of merit ZT is an indirect measured parameter which depends on electrical conductivity, Seebeck coefficient, and thermal conductivity. Thermal conductivity is typically determined by multiplication of specific heat, mass density, and thermal diffusivity which can be directly measured. The mass density of SnSe is still on debate. The reported value by Zhao *et al.* 5.43 g/cm^3 in un-doped p-type SnSe, was 88% to the value by neutron diffraction studies (6.18 g/cm^3). In recent brief communications, Wei *et al.* [39] argued that good single crystal materials should show densities that close to 100% of the theoretical density, thus, the ultralow thermal conductivity and figure of merit of SnSe presented in [6] are not intrinsic. Zhao *et al.* replied that different values may be due to preparation and handling or measurement errors (around 15% – 20%). [39] In order to clarify the density of SnSe, we have grown un-doped SnSe single crystals using temperature gradient method. Interestingly, the mass density was 5.8~5.9 g/cm^3 , which are also much smaller than that of theoretical value (6.18 g/cm^3). Note that in Bi-doped n-type SnSe, the density was 6.06 g/cm^3 . The reported all values in single crystal are smaller than that of theoretical one, which are needed to be clarified.

2.4 References

- [1] https://en.wikipedia.org/wiki/Seebeck_coefficient.
- [2] H. J. Goldsmid, “thermoelectric refrigeration” the General Electric Company Ltd. Hirst Research Centre Wembley, Middlesex, England, (1964).
- [3] https://en.wikipedia.org/wiki/Thermoelectric_effect#Thomson_effect.
- [4] G. J. Snyder and E. S. Toberer, *Nat. Mater.*, **7**, 105-114 (2008).
- [5] D. R. Merrill, D. B. Moore, S. R. Bauers, M. Falmbigl and D. C. Johnson, *Materials*, **8**, 2000-2029 (2015).
- [6] L. D. Zhao, S. H. Lo, Y. S. Zhang, H. Sun, G. Tan, C. Uher, C. Wolverton, V. P. Dravid, M. G. Kanatzidis, *Nature* **508**, 373 (2014).
- [7] L. D. Zhao, G. Tan, S. Hao, J. He, Y. Pei, H. Chi, H. Wang, S. Gong, H. Xu, V. P. Dravid, C. Uher, G. J. Snyder, C. Wolverton, M. G. Kanatzidis, *Science* **351**, 141 (2016).
- [8] A.T. Duong, V.Q. Nguyen, G. Duvjir, V.T. Duong, S. Kwon, J.Y. Song, J.K. Lee, J.E. Lee, S.D. Park, T. Min, J.W. Lee, J. Kim, S. Cho, *Nat. Commun.* **7**, 13713 (2016).
- [9] <https://ocw.mit.edu/courses/materials-science-and-engineering/3-091sc-introduction-to-solid-state-chemistry-fall-2010/crystalline-materials/19-point-and-line-defects/>
- [10] V.Q. Nguyen and S. Cho, *J. Korean Phys. Soc.* **72**, 841 (2018).
- [11] S. Kim, A. T. Duong, S. Cho, S.H. Rhim, J. D. Kim, *Surf. Sci.* **651**, 5–9 (2016).
- [12] C. D. Zhang, J. C. Lian, W. Yi, Y. H. Jiang, L. W. Liu, H. Hu, W. D. Xiao, S. X. Du, L. L. Sun, and H. J. Gao, *J. Phys. Chem. C* **113**, 18823 (2009).

- [13] G. Shi, E. Kioupakis, J. Appl. Phys. **117**, 065103 (2015).
- [14] Y. Huang, C. Wang, X. Chen, D. Zhou, J. Du, S. Wang and L. Ning, RSC Adv. **7**, 27612 (2017).
- [15] M. Parenteau, C. Carlone, Phys. Rev. B **41**, 5227 (1990).
- [16] K. Kutorasinski, B. Wiendlocha, S. Kaprzyk, and J. Tobola, Phys. Rev. B **91**, 205201 (2015).
- [17] Y. Xiao, C. Chang, Y. Pei, D. Wu, K. Peng, X. Zhou, S. Gong, J. He, Y. Zhang, Z. Zeng, and L-D. Zhao, Phys. Rev. **94**, 125203(2016).
- [18] D. T. Morelli, V. Jovovic, and J. P. Heremans, Phys. Rev. Lett. **101**, 035901 (2008).
- [19] M. D. Nielsen, V. Ozolins and J. P. Heremans, Energy. Environ. Sci. **6**, 570 (2013).
- [20] G. Duvjir, T. Min, T. T. Ly, T. Kim, A. T. Duong, S. Cho, S. H. Rhim, J. Lee, and J. D. Kim, Appl. Phys. Lett. **110**, 262106 (2017).
- [21] C. G. V. Walle, and J. Neugebauer, J. App. Phys. **95**, 3851 (2004).
- [22] M. Jin, H. Shao, H. Hu, D. Li, J. Xu, G. Liu, H. Shen, J. Xu, H. Jiang, J. Jiang, J. Crys. Growth **460**, 112 (2017).
- [23] K. Peng, X. Lu, H. Zhan, S. Hui, X. Tang, G. Wang, J. Dai, C. Uher, G. Wang, and X. Zhou, Energy Environ. Sci. **9**, 454 (2016).
- [24] S. Sassi, C. Candolfi, J. B. Vaney, V. Ohorodniichuk, P. Masschelein, A. Dauscher, and B. Lenoir, Appl. Phys. Lett. **104**, 212105 (2014).

- [25] C. L. Chen, H. Wang, Y. Y. Chen, T. Day, and G. J. Snyder, *J. Mater. Chem. A* **2**, 11171 (2014).
- [26] G. Tang, Q. Wen, T. Yang, Y. Cao, W. Wei, Z. Wang, Z. Zhang and Y. Li, *RSC Adv.* **7**, 8258 (2017).
- [27] Y. M. Han, J. Zhao, M. Zhou, X. X. Jiang, H. Q. Leng, and L. F. Li, *J. Mater. Chem. A* **3**, 4555 (2015).
- [28] T. R. Wei, C. F. Wu, X. Zhang, Q. Tan, L. Sun, Y. Pan, and J. F. Li, *Phys. Chem. Chem. Phys.* **17**, 30102, (2015).
- [29] J. H. Kim, S. Oh, Y. M. Kim, H. S. So, H. Lee, J. S. Rhyee, S. D. Park, and S. J. Kim, *J. Alloys Compd.* **682**, 785 (2016).
- [30] J. C. Li, D. Li, X. Y. Qin, and J. Zhang, *Scripta Materialia* **126**, 6 (2017).
- [31] Y. Zhang, S. Hao, L-D. Zhao, C. Wolverton and Z. Zeng, *J. Mater. Chem. A* **4**, 12073 (2016).
- [32] J. C. Li, D. Li, W. Xu, X. Y. Qin, Y. Y. Li, and J. Zhang, *Appl. Phys. Lett.* **109**, 173902 (2016).
- [33] N. K. Singh, S. Bathula, B. Gahtori, K. Tyagi, D. Haranath, A. Dhar, *J. Alloys Compd.* **668**, 152 (2016).
- [34] Y. Li, F. Li, J. Dong, Z. Ge, F. Kang, J. He, H. Du, B. Lia and J. F. Li, *J. Mater. Chem. C* **4**, 2047 (2016).
- [35] Y. Fua, J. Xub, G. Q. Liub, J. Yang, X. Tan, Z. Liub, H. Qinb, H. Shao, H. Jiang, B. Liang,

and J. Jiang, *J. Mater. Chem. C* **4**, 1201 (2016).

[36] E. K. Chere, Q. Zhang, K. Dahal, F. Cao, J. Mao, and Z. Ren, *J. Mater. Chem. A* **4**, 1848 (2016).

[37] Y. X. Chen, Z. H. Ge, M. Yin, D. Feng, X. Q. Huang, W. Zhao, and J. He, *Adv. Funct. Mater.* **26**, 6836 (2016).

[38] C. Chang, Q. Tan, Y. Pei, Y. Xiao, X. Zhang, Y. X. Chen, L. Zheng, S. Gong, J. F. Li, J. He and L. D. Zhao, *RSC Adv.* **6**, 98216 (2016).

[39] P. C. Wei, S. Bhattacharya, J. He, S. Neeleshwar, R. Podila, Y. Y. Chen and A. M. Rao, *Brief communications arising, Nature* **539**, (2016).

CHAPTER 3: EXPERIMENTS

3.1 Temperature controlling

For any commercial effusion cell or furnace beside the safety and economic issue, the most important requirement is precise controlling and stability of temperature which requires a good temperature controller. This section briefly introduces about a Proportional-Integral-Derivative (PID) temperature controller and an impedance matching. There are many controllers have been used over the time, but the PID controller is one of the best choices for this purpose which has become industry standard due to its simplicity and good performance. In order to maximize the power transferred from power supply to load circuit, the impedance of furnace should be match with that of power supply. On the other hand, to precisely control temperature of a furnace, heating and cooling should be applied simultaneously. Therefore, it is very important to understanding impedance matching and heat transferring.

3.1.1 PID temperature controller

The PID controller can be used to control any measurable variable quantity which can be affected by manipulating other process variable quantities [1]. For example, motor control, control of temperature, pressure, speed, force, etc. The principle is that the controller reads the system state (*PV*) by a sensor (thermocouple for temperature controller). After that, the set point (*SP*) is subtracted to the *PV* to get the error value.

$$e = SP - PV \quad (3.1)$$

This error will be used in three purposes; i) to handle the present via the proportional term, ii) recover the errors from the past via the integral term, and iii) to avoid the future errors via derivative term. Figure 3.1 shows the PID controller close loop and working principle, where K_p , T_i , and T_d are the time constants of proportional, integral, and derivative terms.

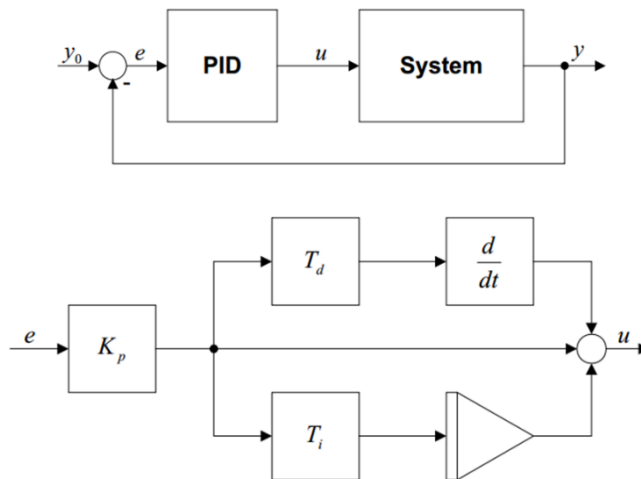


Fig. 3. 1. A control loop (up) and a schematic (down) of PID controller.

A controller using PID program can operate using a single term (P, I, D), couple terms (PI, PD) or all PID terms. However, the single and couple terms have many weak points such as: the P controller cannot eliminate the steady state error, large D leads to sensitivity of system to noises, PI controller may make large overshoot and low response. The best performance of controller can be gained when these terms P, I, and D are used together, called PID controller. The PI controller eliminates the steady state error of the P controller, the PID controller improve the PI controller by eliminates the overshoot and faster the response. The step response of P, PI, and PID controller is represented in Figure 3.2. The figure shows the best response and stability of PID controller compare to the others.

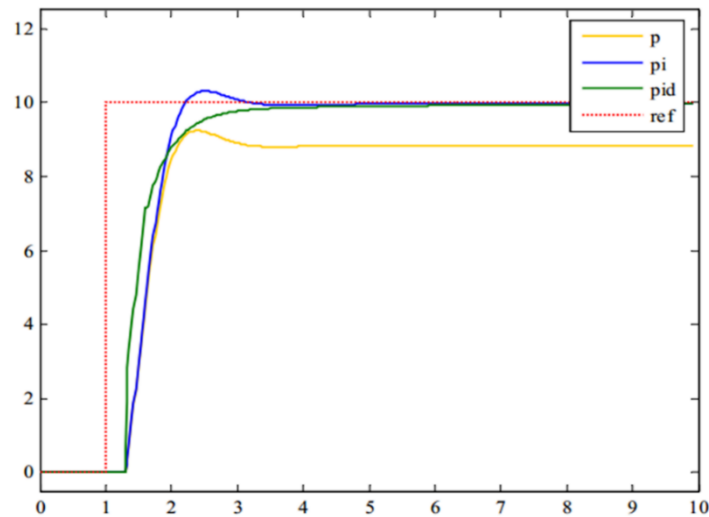


Fig. 3. 2. Step response of P, PI, and PID controller.

3.1.2 Impedance matching

The maximum Power of a given electrical source is the multiplicity of its maximum voltage and maximum current [2]. However, the maximum power transfer is different from the maximum power of the source. This difference happens when the voltage reaches the limit (maximum voltage of the source) while current is still small (too large load's impedance) and vice versa (too small load's impedance). This section describes how to maximize the power transfer extracted from the source to the load in simple case when the load and the source are pure resistance, or the source is an DC one. Impedance matching is adjusting the internal impedance of a source and the impedance of a load circuit to minimize signal reflection or maximize power transfer from the source to the load.

In the case of a complex source impedance Z_S and load impedance Z_L , maximum power transfer is obtained when the complex source impedance is equal to the complex conjugate of load impedance.

$$Z_S = Z_L^* \quad (3.2)$$

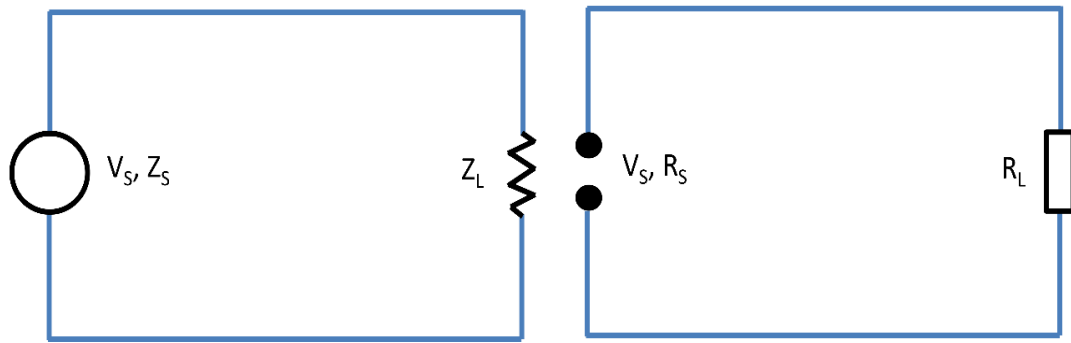


Fig. 3. 3. Electrical circuit consists of source and load in case of reactive circuit (left) and pure resistive circuit (right).

The minimum reflection is obtained when

$$Z_S = Z_L \quad (3.3)$$

In case the source is DC (direct current) source or small frequency or the case of purely resistive load and source. The power is transferred from the source with a voltage V and current I , with the source resistance R_s , load resistance R_L . The relationship between V and I is given by Ohm's law

$$I = \frac{V}{R_s + R_L} \quad (3.4)$$

The dissipated power P_L in the load is calculated by

$$P_L = I^2 R_L = \frac{V^2}{(R_s + R_L)^2} R_L = \frac{V^2}{R_s^2 / R_L + 2R_s + R_L} \quad (3.5)$$

The power reaches maximum value when the denominator reaches its minimum, when

$$\frac{d}{dR_L}(R_S^2 / R_L + 2R_S + R_L) = 1 - \frac{R_S^2}{R_L^2} = 0 \quad (3.6)$$

$$\Leftrightarrow R_S = \pm R_L$$

The values of these resistances are positive therefore the solution above is positive both side.

Note that the second derivative

$$\frac{d^2}{dR_L^2}(R_S^2 / R_L + 2R_S + R_L) = 2\frac{R_S^2}{R_L^3} > 0 \quad (3.7)$$

Therefore, the power transfer is a maximum at

$$R_S = R_L \quad (3.8)$$

Here we conclude that the source resistance must be set equal to the load resistance for maximum power transfer. Note that, the maximize power transfer does not mean the maximize efficiency of the circuit. For perfect case, the source resistance should be zero. As an example, a 100 Volt source with an internal resistance of 10 Ω connected to a 10 Ω load will deliver 250 W to that load. If the load resistance is different from 10 Ω the load power is smaller than 250 W (e.g. $R_L = 40 \Omega$, $P_L = 160 \text{ W}$; $R_L = 6$, $P_L = 234.4 \text{ W}$). Make the source resistance 0 Ohms and the Load Power jumps to 1000 W.

3.1.3 Heat transfer mechanism

In order to efficiently use heat and precisely control temperature, it is necessary to understand the movement of heat and how it is transferred between substances and locations. There are three main ways that heat can transfer between objects: conduction, convection, and radiation. First, we define the conduction of heat is the direct transfer of heat from one object to the other. The heat conduction is dependent on thermal conductivity of materials. We can classify materials in to heat conductor and heat insulator. Metals are very good heat conductors with

very high thermal conductivity (thermal conductivity at 300 K of Cu = 400 W/m-K), while wood and fiberglass are very good heat insulators. Due to the heat insulators just slow down the heat transfer, there is still heat lost from our house or furnace by heat conduction. Second, the heat can be transferred within gases or fluids such as air or water even they are good heat insulators. The mechanism for this transferring is called convection phenomena in which heat is transferred by a current flowing from hot-side to cold-side of the fluid or gas. The conduction and convection usually occur at any temperature when there is a connection between objects or a present of gas (fluid), respectively. The third way of heat transferring, which occurs at any temperature greater than absolute zero especially at high temperature in any transparent medium (vacuum, fluid, gas...), is heat radiation transferring. It is a transfer of heat energy by means of photons in electromagnetic waves. The electromagnetic radiations can carry energy away from the surface. The rate of transfer of radiant energy is described by Stefan-Boltzmann equation. In case of an object in vacuum

$$Q = \varepsilon\sigma T^4 \quad (3.9)$$

For the net of radiation loss rate

$$Q = \varepsilon\sigma(T_a^4 - T_b^4) \quad (3.10)$$

where, Q is the heat flux which is thermal energy radiated by an object per second per unit area, σ is Stefan-Boltzmann coefficient, ε is the emissivity (= 1 for an idea radiator), and T is absolute temperature (K or °C). A typical example for heat radiation is the radiation from the sun. We can produce heat or power from the sun radiation.

3.2 Molecular epitaxy beam MBE for thin film growth

Molecular beam epitaxy (MBE) is one of the most powerful method in physical vapor deposition (PVD) technique, which is used to grow high quality thin film in ultra-high vacuum (UHV). MBE was first introduced in 1970 by A. Y. Cho. Compare to the other conventional vapor deposition method, MBE has many advantages which made it be the most powerful thin film deposition method as follows:

- Sample is grown in UHV (the typical base pressure is 10^{-10} Torr) which is very important condition to produce high purity epitaxial thin film with controllable composition. This UHV condition of MBE is also suitable to integrate of many in-situ characterization tools such as: reflection high energy electron diffraction (RHEED) or low energy electron diffraction (LEED)...

- The sample can be grown with very low growth rate ($0.1 - 3 \text{ \AA/s}$) and growth temperature. The evaporation of element is separated. These features enable MBE to precisely control of epilayers at atomic scale and produce very sharp interface of superlattices as well as multilayers.

However, there are some disadvantages of MBE such as: very complicate system, very expensive (10^6 \$/MBE chamber).

This section introduces some basic knowledge about vacuum levels, vacuum components, vacuum pumps, our home-built MBE set up and the calibration to get precise temperature and growth rate.

3.2.1 Ultra-high vacuum

Vacuum levels

MBE works under UHV condition, the most important condition to produce high quality thin film. To define UHV, it is necessary to know about vacuum levels. The typical unit for vacuum is Torr, and the conversion of vacuum unit is as following:

$$1 \text{ atm} = 1013 \text{ mbar} = 1.013 \times 10^5 \text{ Pa} = 760 \text{ Torr}$$

$$1 \text{ Torr} = 133.3 \text{ Pa}; 1 \text{ Pa} = 7.50 \times 10^{-3} \text{ Torr}$$

Based on the value of pressure inside a chamber, vacuum is classified in to seven levels: atmospheric pressure, low vacuum, medium vacuum, high vacuum, ultrahigh vacuum, extreme high vacuum, outer space, and perfect vacuum. A list of vacuum levels in Torr and Pa is presented in table 3.1. Note that British and German standards define UHV as pressure below 10^{-8} Torr.

Table 3. 1. A list of vacuum levels and the corresponding pressure in Torr, Pa, and Atmosphere.

Vacuum level	Torr	Pa	Atmosphere
Atmospheric pressure	760	1.013×10^5	1
Low vacuum	760 to 25	1×10^5 to 3×10^3	1 to 0.03
Medium vacuum	25 to 1×10^{-3}	3×10^3 to 1×10^{-1}	
High vacuum	1×10^{-3} to 1×10^{-9}	1×10^{-1} to 1×10^{-7}	
Ultra-high vacuum	1×10^{-9} to 1×10^{-12}	1×10^{-7} to 1×10^{-10}	
Extremely high vacuum	$< 1 \times 10^{-12}$	$< 1 \times 10^{-10}$	
Outer space	1×10^{-6} to $< 1 \times 10^{-17}$	1×10^{-4} to $< 3 \times 10^{-15}$	
Perfect vacuum	0	0	0

Why MBE need ultra-high vacuum?

Ultra-high vacuum is a key difference of MBE compare to the other deposition techniques. To understand why the MBE needs ultra-high vacuum, we need to clarify the following parameters:

The first parameter is the root mean square speed of molecules in gas at temperature T. The equation for the root mean square speed of molecules is derived from kinetic theory of gases using Maxwell–Boltzmann distribution function. The higher the temperature, the greater the mean velocity will be. This works well for both nearly ideal, atomic gases like helium and for molecular gases like diatomic oxygen. This can also be written in terms of the Boltzmann constant (k) as

$$v_{rms} = (3k_B T/m)^{1/2} \quad (3.11)$$

where, m is the mass of one molecule of the gas. Table 3.2 shows examples of root mean square speed of some gases molecule at 300 K.

Table 3. 2. Root mean square speed of some gases molecule at 300 K.

Molecule	v_{rms} (m/s)
H ₂	1700
N ₂	450
Ar	380

The second parameter is mean free path of a gas molecule. Molecule travels in gas and collides with other molecular. The average distance between two nearest collisions of molecule is called mean free path. Mean free path of a molecule is dependent on pressure

$$\lambda = \frac{1}{\sqrt{2}\pi d^2 n} \quad (3.12)$$

where, λ is mean free path, d is diameter of a molecule, and n is number of molecule per unit volume which depends on pressure ($n = N_A P/RT$). For the air at 300 K the mean free path in centimeter can be calculated from pressure in Torr as (see table 3.3)

$$\lambda = \frac{5 \times 10^{-3}}{P} \quad (3.13)$$

Table 3. 3. Room temperature (300 K) mean free path of air at different pressure.

Pressure (Torr)	Mean free path (cm)
760	6.7×10^{-6}
1	5×10^{-3}
10^{-3}	5
10^{-6}	5×10^3
10^{-9}	5×10^6

The third parameter we need to consider is the time forming of a single layer of gas on a surface which relates to the purity of thin films. This time can be calculated using the following equation

$$t_m = \frac{4}{n v_{rms} d^2} \quad (3.14)$$

where, t_m is time to form a monolayer (s), n is number of molecules per unit volume, d is diameter of a molecule. In case of the air at room temperature, we can express this time as

$$t_m = \frac{1.86 \times 10^{-6}}{P} \quad (3.15)$$

where, P is pressure in Torr. Table 3.4 lists the time to form a monolayer under some typical vacuum levels.

Table 3. 4. Time to form a monolayer at different pressure.

Pressure (Torr)	t_m
760 (1 atm)	$2 \cdot 10^{-9}$ seconds
10^{-6}	2 seconds
10^{-9}	31 minutes
10^{-10}	5.1 hours
10^{-11}	51 hours

We can see that the mean free path in UHV condition is very long compare to the size of chamber. That mean the molecules do not occur any collision during the growth in UHV condition. The time to form a monolayer in UHV is quite long compare to the time to grow 1 sample (typically 2 hours). These features ensure MBE to produce high quality thin film. These are the reasons why we need UHV for MBE.

Vacuum gauges: To create the UHV condition for MBE, an important component is vacuum detection, called vacuum gauge. There are two typical vacuum gauges used in MBE: hot cathode and cold cathode vacuum gauges. In principle the vacuum detections are indirect measurements, which comprise of two processes: ionized gas molecules and measure electric current by collecting positive ions inside the gauge.

- The hot cathode gauge:

Electrically heated filament to emit electrons. These electrons travel and ionize the gas molecules. Ions are collected at collector and create electric current which proportions to the pressure. Working pressure of the hot cathode gauges is in range from 10^{-3} Torr to 10^{-10} Torr and can be extended to 10^{-11} Torr. The hot-cathode gauges can be damaged or lose their calibration if they are exposed to atmospheric pressure or even low vacuum and get error at

high temperature. The high temperature of filament may induce some out-gassing which is harmful to vacuum.

- The cold cathode gauges

Using crossed electric and magnetic fields (2-6 kV; 1-2 kG) to trap electrons plasma in circulating movement. The electron plasma originates from the random release of an electron at the cathode (caused by a cosmic ray, field emission, a photon, radio-activity....). During movement electrons ionize the gas molecules and create ions current which proportions to the pressure. Working pressure of the cold cathode gauges is in range from 10^{-2} Torr to 10^{-9} Torr and can be extended to 10^{-11} Torr. The cold cathode gauges do not generate heat then do not generate out-gassing. However, with the presence of the magnetic field it may affect to the electron beam from RHEED gun or any in-situ equipment using electron beam.

3.2.2 Vacuum pumps

Vacuum pump is a device which can remove gas molecules from a sealed chamber to leave inside a low-pressure medium called vacuum. To make UHV for MBE from atmosphere, we have to use some kinds of vacuum pump for each vacuum level. Based on the working pressure range we classify vacuum pump in to: low vacuum pump, high and ultrahigh vacuum pump. Low vacuum pump consists of rotary pump, roots pump, and sorption pump etc. High and ultra-high vacuum consists of diffusion pump, turbo-molecular pump, cryo-pump, sputter ion pump, and sublimation pump etc. In this section, I briefly introduce about structure and working principle of some typical vacuum pumps used in MBE like: rotary vane pump, turbo-molecular pump, ion pump, and cryopump.

- Rotary vane pump or mechanical pump [3]

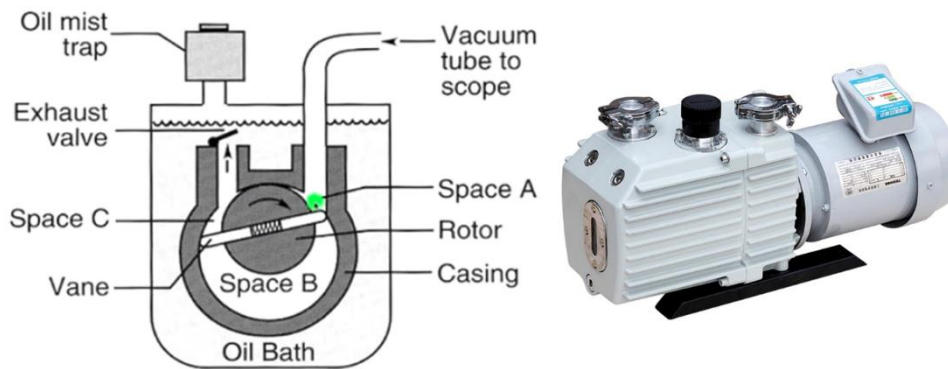


Fig. 3. 4. Schematic illustration working principle (left) and a photo of rotary vane pump (right).

Rotary vane pump was invented by Charles C. Barnes of Sackville, New Brunswick in 1874. This is a positive displacement pump which consists of vanes with a variable length (a spring is located at the middle of the vanes for this purpose) to keep contact with the wall (as shown in Fig. 3.4(a)). These vanes are mounted to a rotor that rotates inside of a casing. A one-way valve is used at the exhaust. When the rotor rotates in the direction of the black arrow, vanes are followed and always sealed on the wall of chamber due to their variable length. As the vanes rotate, the gas in space B is removed. If the pump is connected to a closed chamber, vacuum is generated inside. This pump uses oil for cooling and increase efficiency of removing gases. Figure 3.4(b) is a current rotary pump with three stages, enable it to make vacuum with high speed (up to 605 liter/minute). Due to the presence of oil, the pump is not good for vacuum when the equilibrium state is reached. At equilibrium state a significant concern is contaminations of the entire system by molecular oil back-streaming. The working pressure range of rotary vane pump is from atmosphere to 10^{-3} Torr.

- Turbo-molecular pump

Turbo-molecular pump is a device that can create high vacuum 10^{-7} - 10^{-9} Torr even ultra-high vacuum 10^{-11} Torr from medium vacuum (0.1 - 10^{-3} Torr), based on the principle of rolling the residual gas molecules in the vacuum environment by primary collision with a motor spinning at high speed (jet engine - turbo engine).

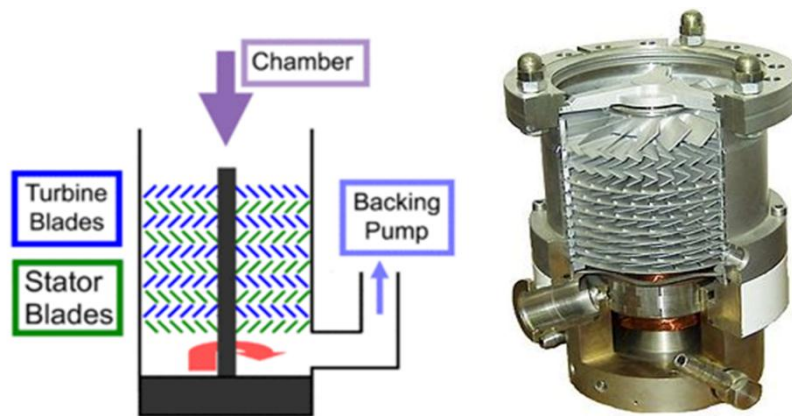


Fig. 3. 5. Schematic illustration working principle (left) and a side view photo of turbo molecular pump (right).

The turbo-molecular pump uses multiple stages, each consists of a high-speed rotating rotor blades and stationary stator blades pair as shown in Fig. 3.5. Gas is captured by the stages and compressed to the inlet of baking pump (i.e. A rotary vane pump is connected in series with turbo-molecular pump at the exhaust). The blades in each stage made an appropriate angle with the pump's principle axis which is very important for high vacuum working environment. When a gas molecular enters the inlet, it is hit by the blades and gain energy from mechanical energy of these blades. The gas molecules with that new momentum will enter the gas transfer holes in the stator and go to the next stages. This process is continued, finally the gas molecules are put out through the exhaust.

An important question is that “why turbo-molecular pump can only work from medium vacuum?”. The answer is come from the its operating principle and structure. A turbo-molecular pump can work only when gas molecules hit by the moving blades reach the stationary blades before colliding with other molecules on their way. To archive that requirement, the distance between moving blades and stationary blades must be smaller than the mean free path of gas molecules. In the turbo-molecular pump that distance is limited about 1 mm. Therefore, the working pressure must be in range of medium vacuum where the mean free path of gas molecules is from 0.7 mm to 5 cm (see table 3.3).

- Ion pump

The ion pump is a device which can make and maintain ultra-high vacuum or even extremer high vacuum (down to 10^{-12} Torr). Ion pump can start working from high vacuum level (10^{-4} Torr). Operating ion pump at higher pressure may lead to shorten of pump’s life. Ion pump consists of many short (stainless steel) cylinders (anodes) sandwiched between two metals (Titanium, or Tantalum) plates (cathodes) placed inside vacuum chamber as shown in Fig. 3.6. Cathodes are placed at ground potential and anodes are placed at high positive voltage 3-7 kV. A strong magnetic field (~ 0.12 T) aligned parallel to the cylinder axis is created by magnets placed outside of the vacuum chamber. When the ion pump is operated, free electrons move in long helical trajectories through the anode tubes. The cylinder anodes act as a penning trap. The long electron paths increase the probability of collision with gas molecules. The gas molecules are ionized to create positive ions and electrons. These secondary electrons can be used for the next ionization of the gas atoms or molecules. The positive ions are accelerated in the strong field to very high speed toward one of the cathodes where they are buried inside the cathode or sputter and react with cathode material to become stable compound placed

elsewhere in the pump's chamber. By that way, ion pump created UHV inside the chamber. The pumping rate is dependent on the specific gas and the absorbance of the cathode material. After many years using, there are holes in the cathodes and dirt inside the chamber. Therefore, we need to replace the cathodes and clean the chamber. One big advantage of ion pump is no moving part involved, therefore, it is able to operate 24/24 hours. However, due to the strong magnet involved it may harmful to the in-situ equipment which use electron beam such as LEED or RHEED etc.

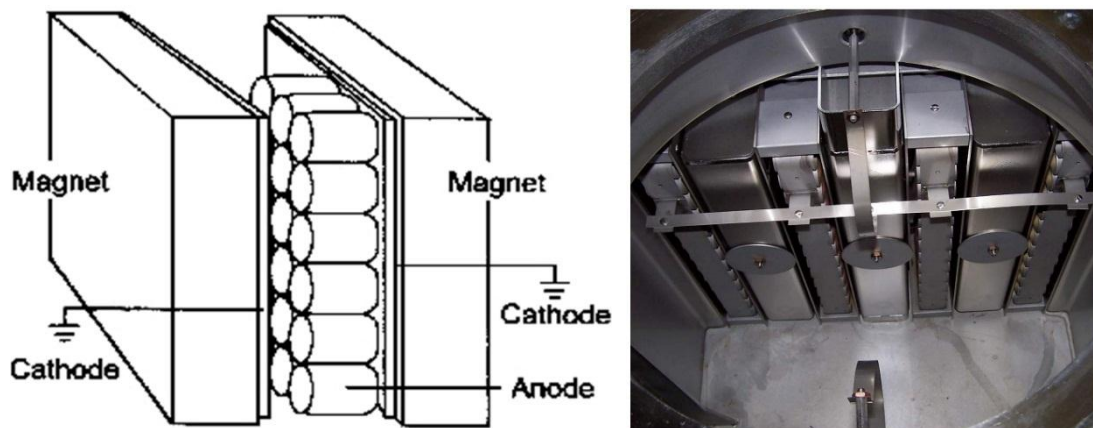


Fig. 3. 6. Schematic illustration (left) and a picture of internal structure of ion pump (right).

- Cryopump or cryogenic pump

A cryopump or a "cryogenic pump" is a vacuum pump that traps gases and vapors by condensing them on a cold surface. However, it is only effective with some gases. The effectiveness depends on the freezing and boiling points of the gas relative to the cryopump's temperature. The cold surface of cryogenic pump will increase the resident time of gas molecules without actual freezing. Liquid He is common used in cryogenic pump. In MBE we usually use liquid N₂ for cryogenic to assist ion pump during the growth. The working pressure range of cryogenic pump is from high or ultra-high vacuum.

3.2.3 MBE setup

MBE is one of the most powerful methods in PVD techniques, which is used to grow high quality thin film in UHV condition. Figure 3.7 shows our home-built MBE set-up and RHEED pattern of SnSe thin film on a MgO (100) substrate. Our MBE system consists of three main chambers: the load lock chamber, the store chamber, and the growth chamber. An oblique configuration was used in our MBE system as shown in Fig. 3.7. A magnetic transfer bar is used to move sample. A high vacuum up to 10^{-6} Torr is created in load lock chamber using diaphragm pump and turbo-molecular pump. The store and growth chamber are kept at UHV (10^{-10} Torr) condition by ion pump (not show in the figure). During the growth we run liquid N₂ in cryo-panel. Water is used to cool down the growth chamber near effusion cells. Shutters with a linear configuration are used and can be controlled by computer through a relay box, which open/close states can be changed within 0.1 second. The sample manipulator can rotate. A K-type thermocouple is used to determine temperature near the sample holder. Real substrate temperature is calibrated based on melting point of some typical metals (In, Sn, Bi, etc.). The in-situ RHEED is used to monitor sample and substrate surface. By looking at RHEED pattern we may know whether the film is epitaxial or not and its surface quality. A shutter is placed in front of the fluorescent screen to protect it from the deposition of materials. To verify the growth rate and estimate the film's thickness we use a thickness monitor with a quartz crystal, placed near substrate. In order to protect the heater of sample manipulator and substrate surface during rate checking, a shutter is used.

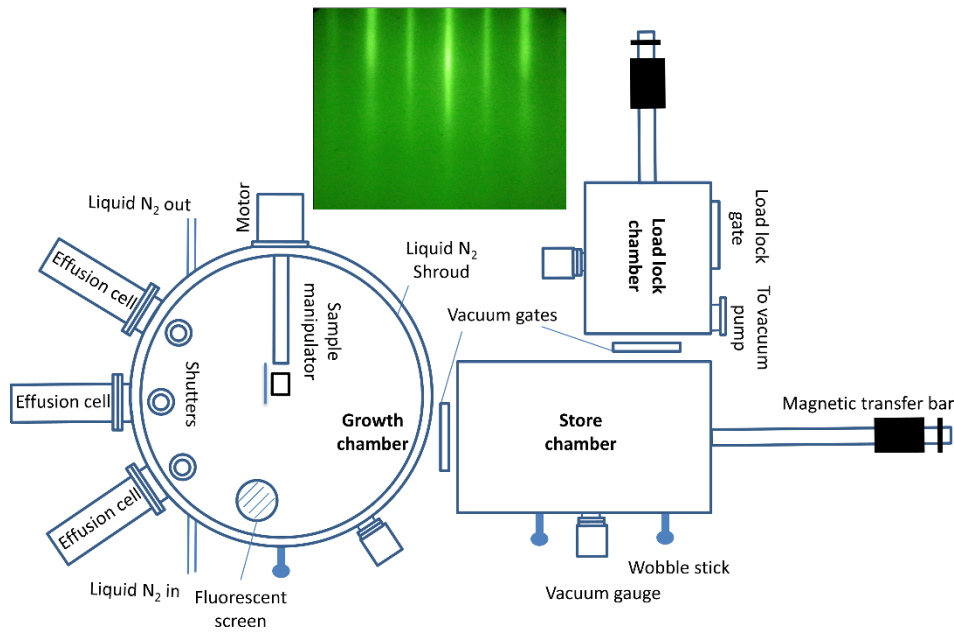


Fig. 3. 7. Diagram of our MBE system and RHEED pattern of SnSe thin film grown on MgO (100) substrate.

3.2.4 Calibrations: substrate temperature, growth rate

Substrate temperature calibration: in our MBE system, we used a bare K-type thermocouple to determine the substrate temperature. A calibration of substrate temperature is needed because of many factors. The thermocouple is placed 1~3 mm from substrate (including thickness of sample holder and some distances). Therefore, a temperature gradient between reading and real temperature of substrate is expected. On the other hand, there are many factors affect to this temperature gradient such as; conduction from sample manipulator, heat radiation from sample holder surface, some displacement of thermocouple. In this work, we calibrated the substrate temperature by measuring the melting temperature of three materials: In (156.3 °C), Sn (231.9 °C), and Bi (271.3 °C). The result of calibration is shown in Fig. 3.8. The temperature is read at each melting point of these materials to create three data points. The reading temperature is a linear function of real temperature. The linear function is given in the Fig. 3.8 (left).

Growth rate also need to calibrate due to: the difference positions, difference sticking coefficients of thickness monitor and substrate, and difference crystal between substrate and thickness monitor. To calibrate the growth-rate we can used SEM cross section or AFM to determine the actual thickness of the film. On the other hand, it is impossible to detect a very low rate using thickness monitor. To solve this problem, we check the rates at high temperature and deduce the rates at low temperature because the plot of the rate as a function of temperature is a linear curve in logarithm scale. As shown in Fig. 3.8 (right) is the growth rate of Bi cell.

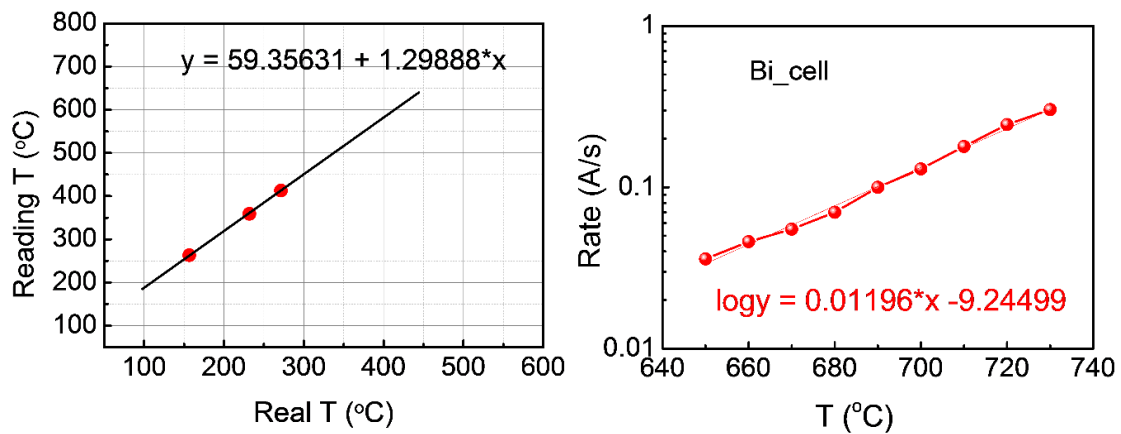


Fig. 3. 8. Calibration of substrate temperature (left) and growth rate of Se cell (right).

3.3 Bulk growth

As shown in chapter 2, single Sn vacancies are the main source of p-type characteristic of SnSe, which affects robustly to the electrical properties and therefore thermoelectric performance of SnSe. The formation of this defect is strongly dependent on the growth condition as well as growth technique. This indicates that the growth technique is a very important factor to optimizing thermoelectric performance of materials, especially of 2D layered materials. This section describes in detail about typical growth techniques for single crystal, and polycrystal of SnSe thermoelectric materials such as; Bridgman, temperature gradient, spark plasma

sintering (SPS), and hot pressing (HP).

3.3.1 Single crystal growth techniques

To produce high quality single crystal ingot, the techniques to grow sample from its melt was invented. The key concept of these techniques is slowly cooling down the melt across its melting point. The defects in single crystal strongly depend on how well we control temperature. This technique group includes Bridgman-Stockbarger, Czochralski, Kyropoulos, zone melting, and temperature gradient techniques. In this section, I discuss in detail about Bridgman-Stockbarger and temperature gradient techniques.

a. Bridgman technique (Bridgman- Stockbarger technique)

The Bridgman technique (also known as Bridgman-Stockbarger method or the directional freeze method) is one of the oldest techniques used for growing single crystals from the melt. Bridgman (1925) and Stockbarger (1936) used slightly different method. In Bridgman technique, the crucible containing the molten material is placed along the axis of a temperature gradient in a vertical furnace, as shown in Fig. 3.9(a). In principle, the Bridgman technique produces the directional solidification of a melt by translating it from the hot part to the cold part of the furnace. First, the raw materials are weighed with appropriate stoichiometry and loaded into ampoule, evacuated or added with inert atmosphere and sealed. The ampoule is usually made of quartz, Pyrex, alumina, graphite, and the noble metal. After shielding, a hook is fabricated at upper end of the ampoule, connected to a motor via a high melting point wire. After maintaining at high temperature to complete reactions between elements to form compound, the ampoule is then slowly lowered from hot part (above material's melting point) to cold part (below material's melting point) of the furnace so that the solidification starts from the lower sharp tip. Due to the constriction shape (very sharp) of the tip, the single crystal seed

is produced. Single crystal is then grown on the seed. The lowering speed of the ampoule ranges from approximately 1mm day^{-1} to 1cm h^{-1} . The cooling rate of ampoule is dependent on the temperature gradient of furnace and the lowering speed of ampoule. Finally, the ampoule is moved down out of the furnace (cooled down to room temperature) and single crystal ingot is obtained. There are two kinds of Bridgman furnace; horizontal and vertical corresponding to horizontal Bridgman technique and vertical Bridgman technique. Usually, the vertical Bridgman technique provides a higher quality crystal than the horizontal one. Stockbarger technique is a modified Bridgman technique, where the furnace is divided into two zones, often separated by a baffle, producing a steeper temperature gradient between zones, as shown in Fig. 3.9(b) [4]. Note that the temperature gradient here can be adjusted by changing the density of heating element or by employing convection phenomena (for vertical furnace). The Bridgman-Stockbarger technique exhibits many advantages: it does not require a seed to initiate the growth, produces large and high quality single crystal ingot, possibly grows sublimating material's compounds, and the crystal orientation can be controlled by adjusting the orientation of the seed (sharp tip of ampoules). However, there are some disadvantages: it is complicated and hard to produce to industrial scale up, difficult to arrange the temperature and ampoule position precisely due to the fluctuation of ampoule, and in one run only one ampoule can be loaded. As mentioned above to produce good thermoelectric single crystal ingot, we have to control well the defects type and defect density. Using Bridgman-Stockbarger technique we may optimize the amounts of elements loaded in the ampoule, the temperature gradient, and the speed of lowering ampoule.

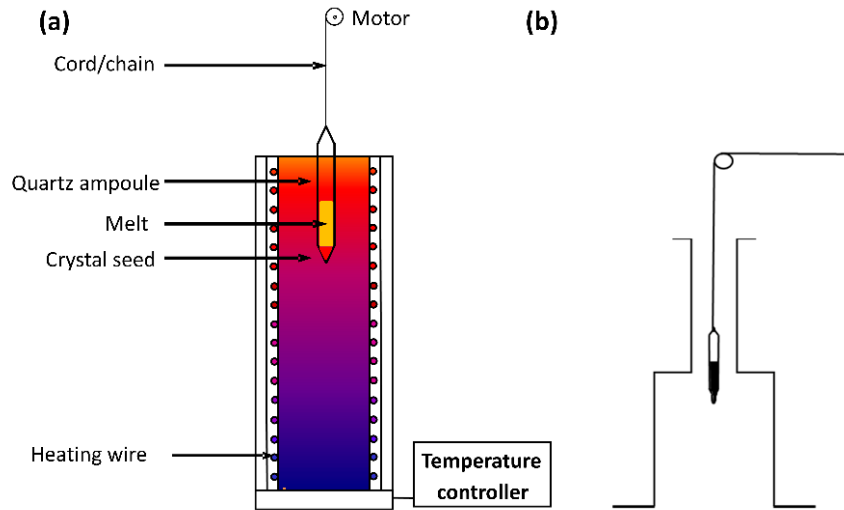


Fig. 3. 9. Diagram of (a) Bridgmann vertical furnace and (b) Stockbarger furnace. [4]

Below is the growth conditions of SnSe single crystal reported by Zhao *et al.* [5]. In this growth, they used Sn chunk (99.999%) and Se shot (99.999%) to fabricate (~20 g) SnSe ingot. First, after sealing the raw materials, the ampoules were slowly heated up to 1223 K within 10 h, maintained at this temperature for 6 h, and then cooled down to room temperature. To fabricate SnSe single crystal, the obtained ingot was crushed in to powders and loaded in to quartz tubes again. The ampoules were heated up to 1223 K within 9.5 h in a vertical Bridgman furnace, and then slowly cooled down to room temperature with the sample's moving rate of 2 mm/h.

b. Temperature gradient technique.

Using the same concept from the melt, the temperature gradient technique has been used to produce 2D single crystal semiconductors. This technique creates the temperature gradient using convection phenomena and heating element density difference. Figure 3.10(a) shows a schematic diagram of vertical furnace. Without moving ampoule, the gradient temperature is only used for the single crystal growth. The temperature was precisely controlled by an AC or DC power supply and PID temperature controller. Inside the furnace, heating wire is uniformly

wounded or more wounded at the upper part around an alumina or quartz. Due to the transparent property of quartz tube, heat radiation can easily conduct heat from wire to ampoule and create a homogeneous cross-sectional temperature. A thermocouple is placed inside the furnace near ampoule for precisely reading temperature at sample position. The following is the details of growing process. First the raw materials were weighted in an expected stoichiometry. Stoichiometric amounts of elements were mixed and sealed in an evacuated thick quartz ampoule with a very sharp tip at the bottom. The ampoule was then sealed in another evacuated bigger quartz ampoule to prevent the sample from oxidation by air when the inner ampoule is broken owing to the different thermal expansion coefficient between the crystal and quartz. If the thermal expansion coefficients are not much different, a single ampoule can be used. The ampoules were then slowly heated up to high temperature above the melting point of materials. During heat-up process raw materials interact to form a compound. To complete this reaction, the ampoule was maintained at high temperature for long time. After that the ampoule is slowly cooled down across the melting point of the compound. Solidification occurs at the bottom part of ampoule first and a single crystal seed is created. As temperature continuously decreases, single crystal grows on the seed. Finally, single crystal ingot is produced. Note that the residual elements are floating at the top part of the ampoule. Figure 3.10(c) shows our SnSe single crystal grown by temperature gradient technique. There are many advantages of this technique over Bridgman technique: there are no moving parts, many ampoules can be loaded together in a running, and it is very simple and easy to operate. Using temperature gradient technique, we have successfully fabricated excellent SnSe single crystal [6]. In this growth, we have used high purity (99.999%) of Sn and Se powders. The powders were weighed in appropriate ratio with a total amount of 20 g, mixed in a quartz tube, evacuated at 10^{-4} Torr, and flame sealed. The ampoules were then loaded in to a vertical furnace.

The temperature was slowly raised up from room temperature to 930 °C (10 °C/h), maintained at 930 °C for 10 h, followed by slowly cooled down (1 °C/h) from 930 to 700 °C across the melting point of SnSe and then from 700 °C to room temperature (20 °C/h).

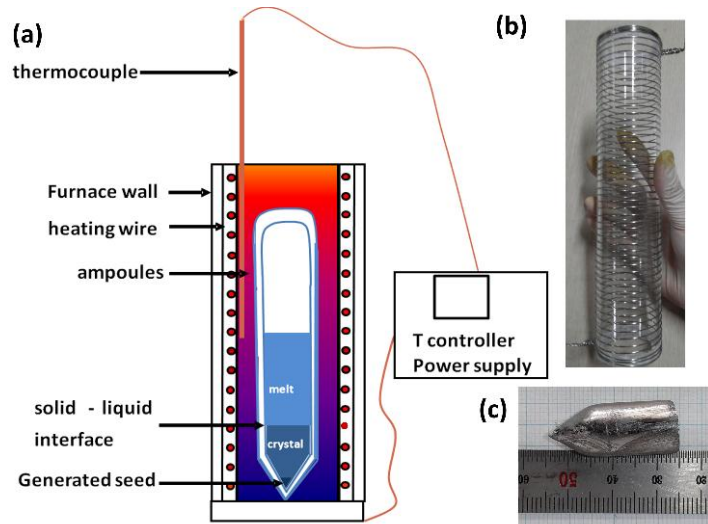


Fig. 3. 10. Diagram of (a) our temperature gradient vertical furnace, (b) vertical furnace's heater, and (c) single crystal ingot of SnSe grown by temperature gradient technique.

3.3.2 Polycrystalline growth techniques

a. Spark plasma sintering (SPS) technique

The Spark plasma sintering (SPS), also known as field assisted sintering technique (FAST) or pulsed electric current sintering (PECS), is a novel sintering technique, known as the best technique to fabricate polycrystalline thermoelectric materials. A schematic of the SPS process is shown in Fig. 3.11 (a). This process allows us to fabricate bulk materials from powders with very high heating rate (1000 °C/min), high density, shorter sintering time (0-10 min), and finer grain size than other conventional sintering method [7, 8]. The most suitable materials can be produced by SPS are functionally grade materials (FGMs), inter-

metallic compounds, fiber reinforce ceramics (FRCs), metal matrix composites (MMCs), and nano-crystalline materials [7].

In principle, SPS is a sintering pressure method by applying simultaneously a high electric pulse current on electrodes and mechanical pressure. Powder is loaded in to a mold with two punches. The powder can be conducting or insulating. For the case of conducting powder an insulating mold (or a conducting mold with insulating material) is used. For the case of insulating powder, the mold should necessarily be electrically conducting to ensure the electrically closed circuit. The punches which play as electrodes should be conducting for the same reason (stainless steel, copper, graphite, etc.). The chosen material of the mold and punches affects to the maximum mechanical pressure (e.g. graphite mold limits the pressure level to 100 MPa). During SPS process, when a high electric pulsed current is applied on electrodes, microscopic electrical discharges are produced in the gaps between particles generating plasma and causing sintering. When a spark discharge appears in the gap of particles, the local temperature can be very high of several ten thousand centigrade [7]. If the local temperature is high enough, a localized melting is occurred [9]. After that the molten liquid was sputtered at high velocity to the surface of neighboring particles, leading to connections between them. Once the connections are formed, the condition for discharge is loosened. After that micro-discharge is stopped, the local temperature decreases very fast, leading to the partially melted microstructure between particles [8]. The cooling rate can be reached up to 50 °C/min; with additional active cooling under gas flow quenching rates of 400 °C/min can be reached [10]. If the local temperature is close to the melting point of powder, sintering necks are formed around the contact between particles as shown in Fig. 3.11 (b). Figure 3.12 shows the evident observations of the melted microstructure, the sputtered microstructure and the necks formed on the surface of Cu particles [8]. The high sintering efficiency of SPS is due to

the spark plasma and spark impact pressure, which can generate high temperature sputtering phenomenon, eliminate adsorptive gas and any impurities, and use Joule heating and plastic deformation effects, etc. [7, 8].

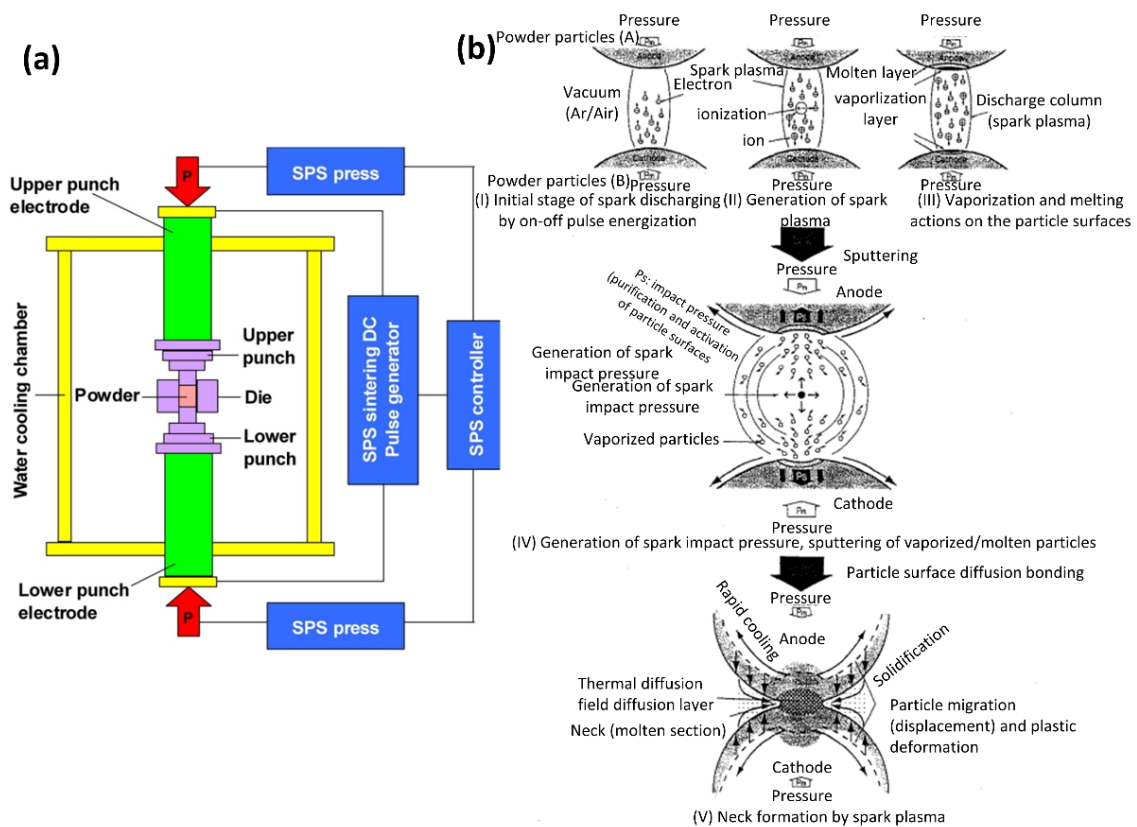


Fig. 3. 11. (a) the structure configuration of SPS system [8] and (b) the basic mechanism of neck formation by SPS. [7]

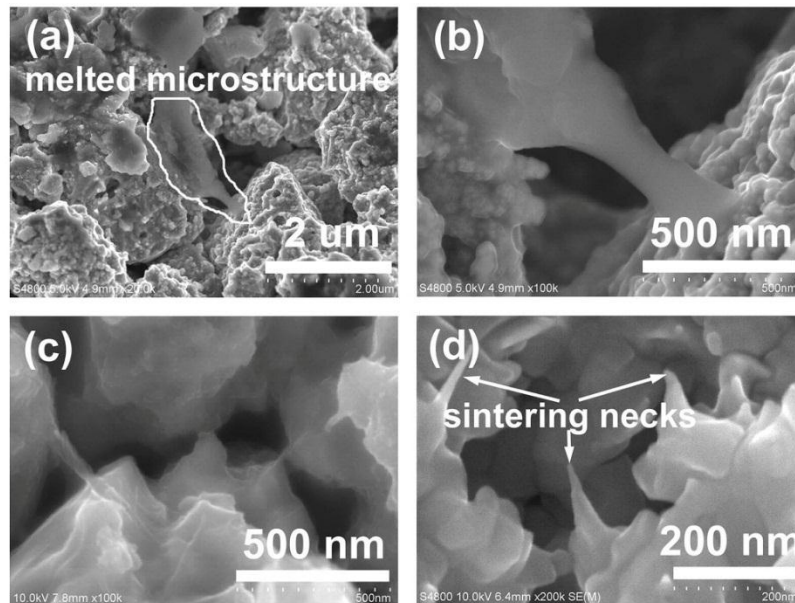


Fig. 3. 12. SEM images of the fracture surfaces of the ultrafine SPS copper sample sintered at 600 °C: (a) partially melted microstructure between two copper particles, (b) the magnification of the melted and sputtered microstructure of copper, (c) the formation of sintering necks on the surface of the copper particles, and (d) the magnification of sintering necks. [8]

b. Hot pressing (HP) technique

Hot pressing is a conventional technique used to fabricate dense polycrystalline materials. In this technique the powder is loaded in a mold, which is heated up by Joule heating ($P = I^2R$) at a temperature high enough to induce sintering and creep processes and the flow of materials due to pressure [7]. The working principle of HP is somewhat similar to that of SPS by applying heat and mechanical pressure simultaneously. In HP process, Joule heating can be generated by two ways; induction heating and resistance heating. The induction heating is the process of heating by high frequency electromagnetic field. When an alternating current (AC) is applied

to an induction coil, the rapidly alternating electromagnetic field penetrates the object, generating eddy currents inside the conductor and producing Joule heating. In ferromagnetic materials, heat can be generated by magnetic hysteresis. The advantages of this induction heating are the independence between heating and pressing and the possibility for powder or liquid phases even in low pressure. The disadvantages are non-uniform heat distribution when the mold is placed off-center and heating rate is low, which is also affected by induction characteristics of material and thermal conductivity of mold.

In the indirect resistance heating technology, the mold is heated by heating element via radiation and convection phenomena. The advantages of this technique are high temperature which is independent on the conductivity of the mold and the interconnection between heating and pressing. The disadvantage is slow heating rate, leading to some unwanted interaction between powders and mold materials. Figure 3.13 shows our mini-hot pressing apparatus employing the indirect heating technology [11]. A cylinder heater is used to heat up chamber. Water cooling is used for easy temperature control as well as increasing cooling rate ability of apparatus. The apparatus can work under various levels of vacuum (low, medium, high) or high pressure of inner gas.

Both HP and SPS are suitable to fabricate high quality of polycrystalline thermoelectric materials. According to the working principles described above, the primary difference between two methods is the way that thermal energy is transferred to the powder. In case of SPS the specimen and pressing tools act as heating element and contribute to direct heating of sintering powder, while in case HP process pressing tool is placed inside a heating chamber and transferring heat by radiation and convection. A direct comparison between two techniques has been reported by Langer *et.al* using submicron alumina samples [12]. He showed that the

densification mechanism for both methods was grain boundary diffusion. The grain size was found to be insensitive to the sintering technology. At a given sintering temperature, HP technique requires more sintering time to produce the same final density of sample prepared by SPS technique.

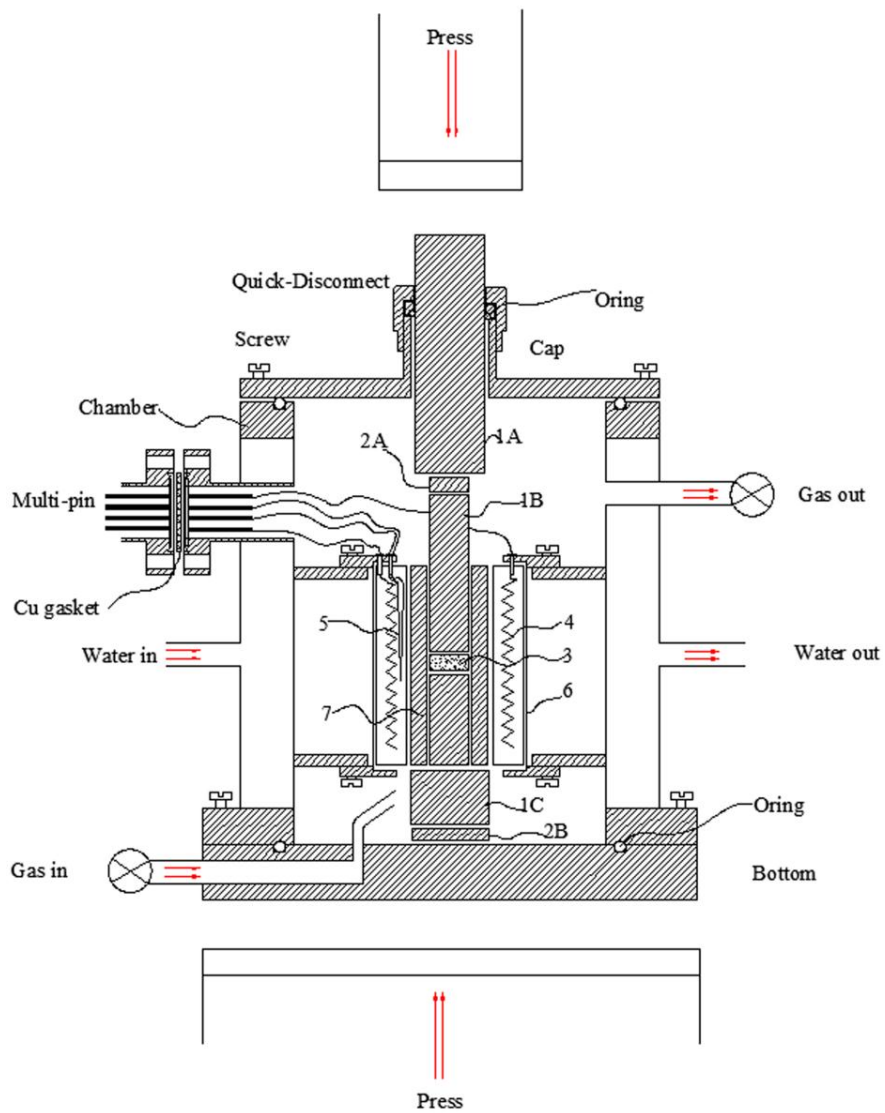


Fig. 3. 13. Entire structure of our mini hot pressing system. [10]

3.4 Transport properties measurement systems in our lab

To determine Seebeck coefficient, electrical conductivity, magneto-resistance and carrier density in our lab we have built our low- and high-temperature transport measurement systems. The low temperature measurement system allows us to measure these parameters in temperature range from 15 to 410 K (extent to 450 K). The high temperature measurement systems allow us to measure these transport parameters from 100 to 1000 K. This section briefly represents about background of four-probe method to measure resistance, Hall effect, and detail about design of our measurement systems.

3.4.1 The Two and Four probe method for resistance measurement

a. The two-point probe configuration

To measure resistance of a conductor, the convention way is using Ohm-meter with a two-point probe as shown in Fig. 3.14. However, this method does not give accurate result. The measured resistance value includes of contacts resistance, cables resistance, and the contribution thermal voltage.

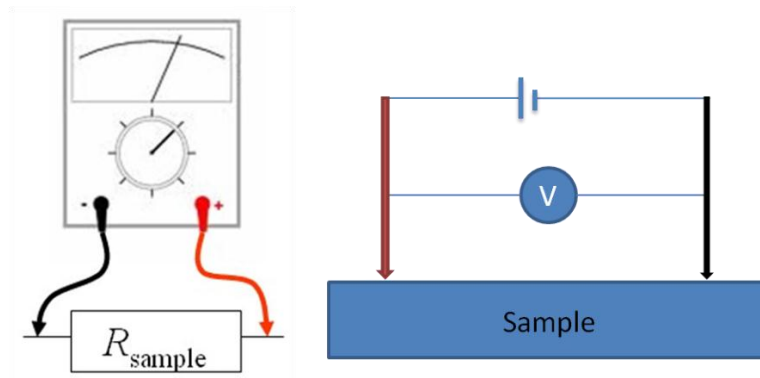


Fig. 3. 14. The two-point probe configuration to measure resistance.

b. The four-point probe configuration

To overcome this problem, a four-point probe technique was developed. This method is commonly used to measure either bulk or thin film resistance and Hall effect with very high accuracy. The collinear four-points probe is preferred for bulk resistance measurement, while 4 points at corner of a cube shape is preferred for thin film resistance measurement (see Fig. 3.15). Let's consider the collinear 4 probe configuration. The inter-distance between points is S . A constant current is passed through the outer probes (1 and 2) and the potential drop V across the middle two probes (3 and 4) is measured. To measure accurately resistance using this configuration the distance between (1-2) should be no smaller than 2 times of that between (3-4).

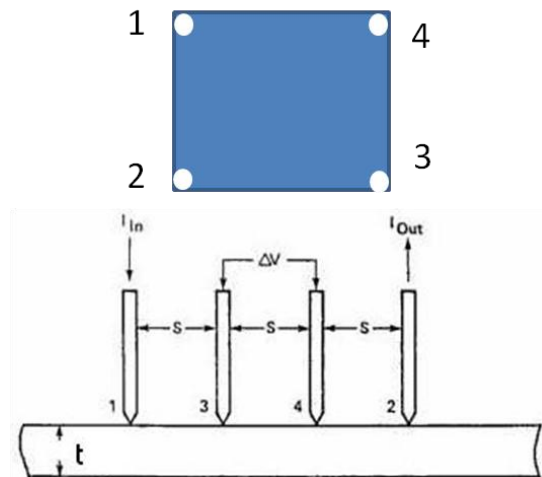


Fig. 3. 15. Square (up) and collinear (down) four-point probe configuration.

c. How to remove contacts and wires resistances

In the two-point probe method, the current is generated by a battery. The circuit is equivalent to a series circuit consists of contacts, wires, and sample. We have

$$I = I_{spl} = I_c = I_w \quad (3.16)$$

The voltmeter measures electrical potential difference between two sides of entire circuit. Therefore, the measured voltage is

$$V = V_{spl} + V_c + V_w \quad (3.17)$$

where, V is measured voltage. V_{spl} , V_c , and V_w are potentials dropt between sample, contacts, and wires, respectively. Based on the Ohm's law, the measured resistance is

$$R = \frac{V}{I} = \frac{V_{spl} + V_c + V_w}{I} = R_{spl} + R_c + R_w \quad (3.18)$$

In the four-point probe method, the circuit is also equivalent to a series circuit includes wires, contacts, and sample. However, the voltmeter only measures electrical potential dropped at the sample. The measured voltage is exactly the voltage between two sides of sample

$$V = V_{spl} \quad (3.19)$$

The measured resistance is calculated beyond Ohm's law as

$$R = \frac{V}{I} = \frac{V_{spl}}{I} = R_{spl} \quad (3.20)$$

In conclusion, the key concept that makes the high accuracy of the four-point probe technique is the equally current of the series circuit.

d. How to remove thermal voltage

The steady state is not an idea one. The sample's temperature is not perfectly uniform, leading to a thermal voltage developed across the sample. The measure voltage always included of thermal voltage in any measurement method. The measure resistance is included of the resistance uncertainty induced by thermal voltage. In case of four-point probe method

$$V = V_{spl} \pm V_{th} \quad (3.21)$$

If each measurement is measured twice with an applied current in direction from probe 1 to probe 2 and reverse from probe 2 to probe 1. The thermal voltage appeared in opposite sign in each time of measurement. To eliminate it we take average the values from each time

$$\left. \begin{array}{l} V_1 = V_{spl} + V_{th} \\ V_2 = V_{spl} - V_{th} \end{array} \right\} \Rightarrow \frac{V_1 + V_2}{2} = V_{spl} \quad (3.22)$$

By this way we can measure accurately the sample's resistance.

3.4.2 The convention Hall effect

The Hall effect was discovered by Edwin Hall in 1879. When a current carrying conductor is placed in a perpendicular magnetic field, a potential voltage difference is generated in the conductor in direction perpendicular to both current and magnetic field. The current consists of the movement of charge carriers (electrons, ions, holes or all of them). With the presence of the magnetic field, the charge carriers are affected by a Lorentz force which is perpendicular to both the current and the magnetic field. Under the action of the Lorentz force, both the positive and negative charge carriers move to one side of the conductor thus they accumulate on one face of the conductor and leave an equal of opposite charges on the other side. This separation of charge induces an electric field which is in opposite direction to the migration of further charge. The more movement of charge carriers, the bigger induced electric field is. The induced electric field increases until steady state is established. As long as the charge is flowing, a steady electric potential difference between two sides of conductor is built up, called Hall voltage.

Consider a rectangular conductor of height w , thickness t in XY plane as shown in the Fig.

3.16. A constant current generator (CCG) is used to generate a constant current I along x axis. A magnetic field B is applied along z axis. The current density is given by

$$J_x = \frac{I}{wt} \quad (3.23)$$

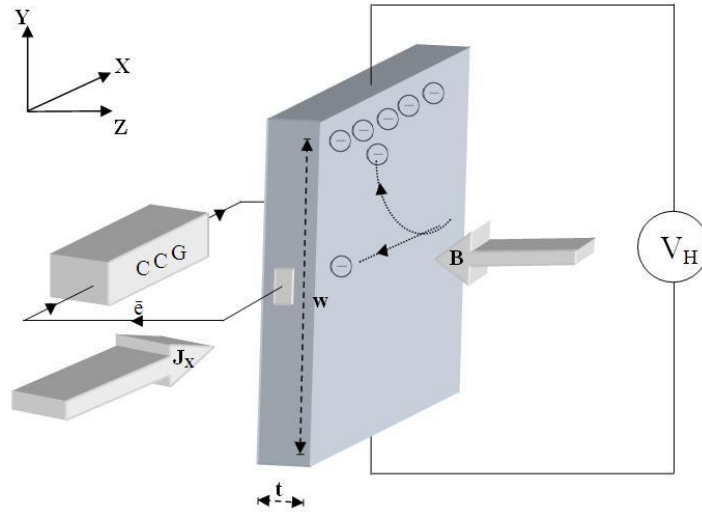


Fig. 3. 16. Schematic representation of Hall Effect in a conductor.

The Lorentz force moves the charge carriers along y axis toward to the top (left hand rule) and expressed by

$$F = e(v \times B) \quad (3.24)$$

Since the charges cannot escape from the material, a vertical charge imbalance is built up. In steady state, the magnetic force on each electron in the y -axis direction (evB) is cancelled out by a y -axis electrical force due to the buildup of charges (eE)

$$eE = evB \Rightarrow E = vB \quad (3.25)$$

where 'ewhere, e is the electric charge, E the hall electric field developed, B the applied magnetic field and ' v ' is the drift velocity of charge carriers. Current I can be expressed as,

$$I = neAv \Rightarrow v = \frac{I}{neA} \quad (3.26)$$

where, n is the carrier density, A is cross section of the conductor $A = wt$. Using (1) and (2) the Hall voltage V_H can be written as

$$V_H = Ew = vBw = \frac{IB}{net} = R_H \frac{IB}{t} \quad (3.27)$$

where, R_H is Hall coefficient

$$R_H = \frac{V_H t}{IB} = \frac{1}{ne} \quad (3.28)$$

In semiconductor, charge carriers are electrons and holes. When a current is applied to a semiconductor, the holes move in the direction of current and the electrons move in opposite direction with current. With the presence of magnetic field, both the electrons and the holes charge carriers are forced to move and accommodate in one side of semiconductor. At equilibrium, a voltage appears at the semiconductor edges.

For moderate magnetic fields the Hall coefficient is

$$R_H = \frac{p\mu_h^2 - n\mu_e^2}{e(p\mu_h + n\mu_e)^2} = \frac{p - nb^2}{e(p + nb^2)} \quad (3.29)$$

$$b = \frac{\mu_e}{\mu_h}$$

where, n is the electron concentration, p is the hole concentration, μ_e is the electron mobility, μ_h is the hole mobility and e the elementary charge.

Applications: The Hall effect measurements using the van der Pauw configuration allows determination of:

- Charge carrier type (n or p-type)
- Charge carrier density (cm^{-3})
- Relevant Hall mobility (cm^2/Vs)

Sample preparation: To ensure the accurate measurement, there are some requirements for the sample preparation as the following:

- The sample must have a flat shape of uniform thickness.
- The sample must not have any isolated holes.
- The sample must be homogeneous and isotropic.
- All four contacts must be located at the edges of the sample.
- The area of each contact should be at least an order of magnitude smaller than that of the entire sample.
- The sample thickness should be much smaller than the width and length of the sample.
- It is preferable that the sample is symmetrical.

The four contacts must be ohmic and be placed on the boundary of sample. Contacts would ideally be infinitely small. Practically, they must be as small as possible; any errors given by their nonzero size will be of the order D/L , where D is the average diameter of the contact and L is the distance between the contacts.

Combine with the electrical conductivity from the four-probe method described above, we may calculate the Hall mobility of dominant charge carrier (electron or hole)

or

$$\begin{aligned} \mu_e &= \frac{\sigma}{ne} \\ \mu_h &= \frac{\sigma}{pe} \end{aligned} \quad (3.30)$$

3.4.3 Low temperature measurement system

To measure electrical conductivity, Hall effect, magneto-resistance, and Seebeck coefficient in temperature range from 15 to 410 K, we have built our home-made low temperature transport measurement system (TPMS) as shown in Fig. 3.17. The measurement system consists of vacuum chamber, rotary pump, electro-magnet, cryostat system, Keithley source-meters. The rotary pump allows us to maintain the system under low vacuum range $\sim 10^{-3}$ Torr. The cryostat (*cryo* means *cold*, *stat* means *stable*) system includes of Lake Shore model 331 temperature controller, displax (DE-202S, Advanced Research Systems, Inc.), heater, and temperature sensors (Silicon diode or resistance temperature detectors RTDs). Heater is designed after considering the impedance matching with the temperature controller and minimized its induced magnetic field. We used Keithley model 2400 series for this measurement system. The Keithley can be used as voltage source (from 5 μ V - 200 V), voltmeter (1 μ V – 20 V), and source of current (50 pA – 0.1 A). The electro-magnet (Walker LDJ Scientific Inc., USA) was used which can generate magnetic field up to 1Tesla (10000 Gauss).

With this measurement system we can measure simultaneously 2 samples for resistance, Hall, and magneto-resistance measurements using four-point probe configuration. While Seebeck coefficient measurement using two probe method allows 1 sample for each time running. Figure 3.18 shows the schematic drawing of these measurements. In Seebeck coefficient measurement, the ambient temperature is kept stable by temperature controller. The temperature gradient (0.1 ~ 7 K) is generated by a heater ($\sim 170 \Omega$) integrated in a cooper block. A K-type differential thermocouple is used to measure the temperature gradient. The thermoelectric voltage can be expressed by

$$\Delta V = S\Delta T + b(\Delta T)^2 + \dots \quad (3.31)$$

We measure the thermoelectric voltage at the steady state for very small intervals of gradient temperature to eliminate the spurious thermal voltage within the circuit and ignore the high order terms of ΔT . The Seebeck coefficient was determined by take the slope of ΔV vs. ΔT curve.

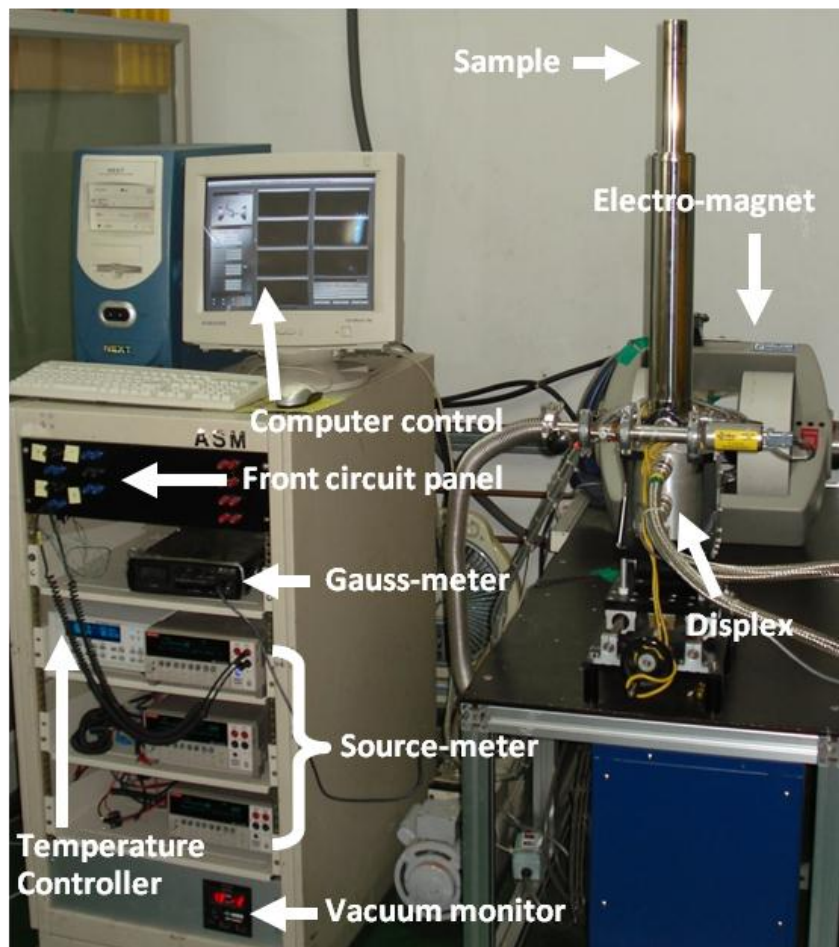


Fig. 3. 17. Our home-build low temperature transport properties measurement system (TPMS).

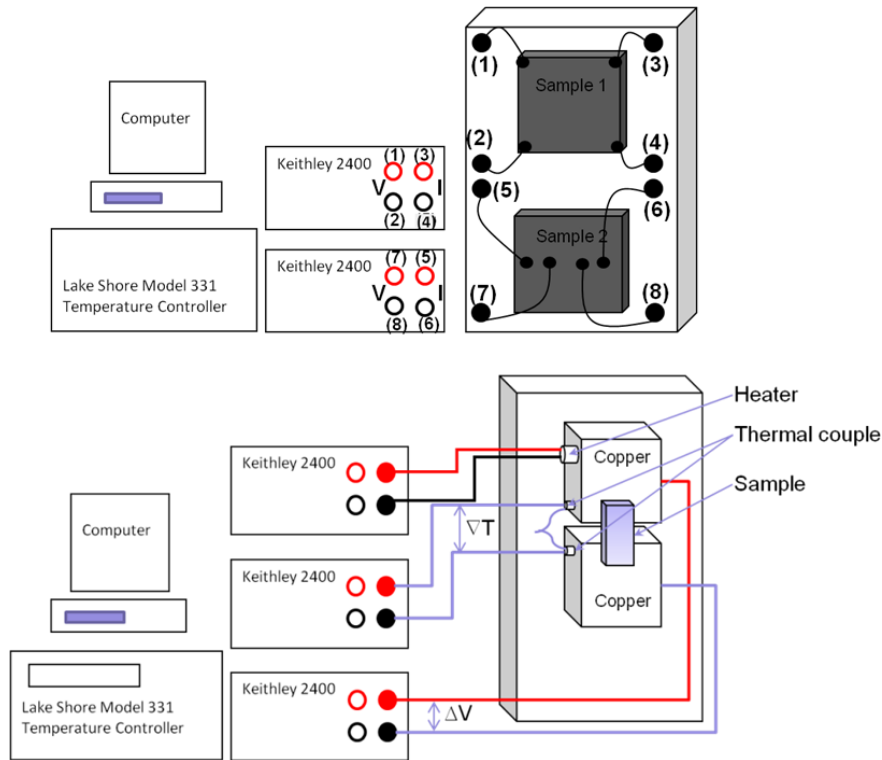


Fig. 3. 18. Schematic illustration of our low temperature measurement system.

3.4.4 The high temperature measurement system

In order to measure the above measurements in temperature range up to 1000 K, we designed and built up our high temperature measurement systems. The first high temperature measurement system is designed to simultaneously measure Seebeck coefficient and electrical conductivity from 77 to 1000 K, and the second one is designed for electrical conductivity, magneto-resistance, and Hall effect measurements from 300 to 1000 K.

3.4.4.1 The 100 to 1000 K range electrical resistivity and Seebeck coefficient measurement system

We designed and built up a combination of low and high temperature range electrical resistivity and Seebeck coefficient measurement system with various features to minimize typical sources of error [13]. Common sources of temperature and voltage measurement errors which may

impact to the accurate measurement are identified and solved. Our low and high temperature electrical resistivity and Seebeck coefficient measurement system employs a colinear four-point geometry with the working temperature range from 100 up to 1000K. Our design is simple to operate, easy to change sample, stable contact, and is suitable for both thin film and bulk samples with a broad range of physical types and shapes. Figure 3.19 shows the photograph of whole system and main internal components. The measurement's principle was described above.

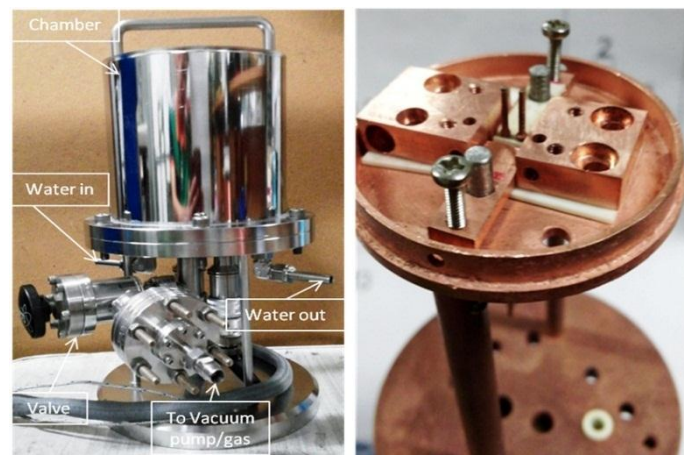


Fig. 3. 19. A photo (a) internal components of our home-built high temperature transport measurement system.

3.4.4.2 The 300 to 1000 K range transport measurement system

Another set up is (300 – 1000 K) transport measurement system. The entire system is placed in a vacuum chamber which also allows us to apply high pressure of inert gas or vacuum. The body of system is made of cooper (high thermal conductivity 400 W/m-K at 300 K) and fixed by two support rods. Heater is made with special design to eliminate the induced magnetic field by current. A magnetic shielding sheet is used which also plays as a heat radiation shielding. A K-type thermocouple is used to determine temperature of sample. Figure 3.20 is a

photograph of the measurement system. A computer and two Keithleys model 2400 series are used for these measurements as described above for low temperature measurement systems. This apparatus allows us to measure simultaneously 2 samples in 1 time running. A magnet with magnetic field up to 10000 Gauss is used to measure magnetoresistance and Hall effect. The main body of the system allow us to integrate with a Seebeck coefficient measurement part as shown in Fig 3.20.

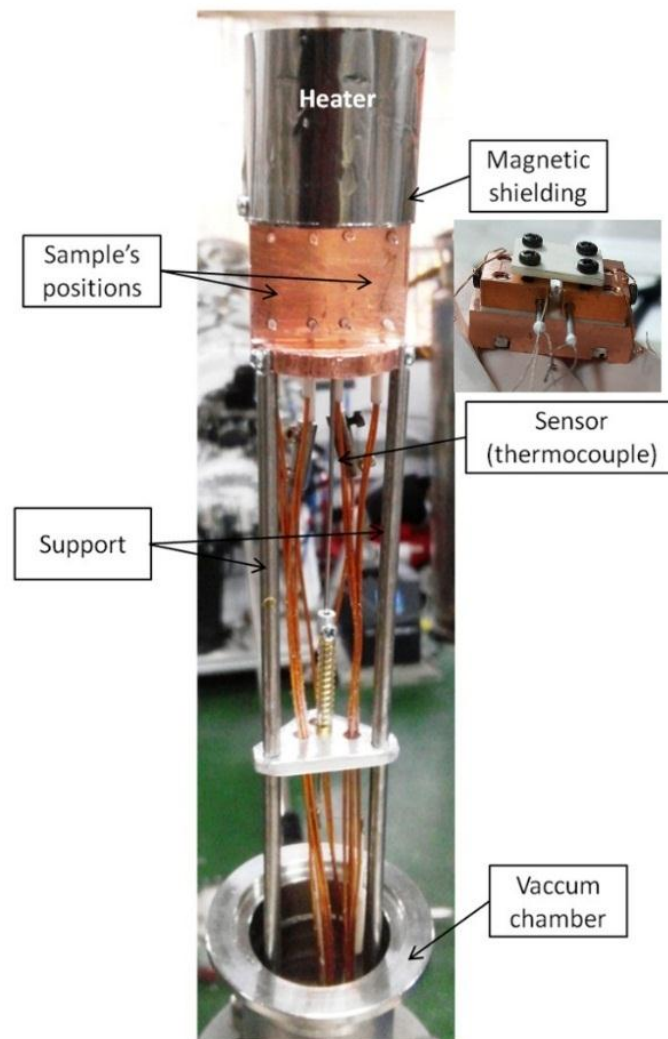


Fig. 3. 20. Photograph of 30 -1000 K of our home-build transport measurement system with a special design of heater.

3.5 Characterizations

3.5.1 X-ray diffraction XRD

The crystal quality of our samples was examined by X-ray diffraction XRD experiments using Cu $K\alpha 1$ radiation (0.154056 nm). The θ - 2θ scan was used to investigate the out of plane orientation and lattice constants of the samples. Rocking curve, ω scan was used to determine the sample's crystallinity by analyze the FWHM of the rocking curves. Azimuth scan (Φ -scan) was used to determine the in-plane orientation of samples.

In principle, XRD θ - 2θ scan, a diffraction peak appears when the incident beam satisfies two conditions: the diffraction plane has to perpendicular to the crystallographic plane, and the Bragg condition

$$2d \sin \theta = m\lambda \quad (3.32)$$

where, d is inter-planar distance, λ is wave length of X-ray beam, and θ is the incident angle (angle between incident beam and crystallographic plane). The position of peak (2θ) is dependent on d , while the intensity of peak is dependent on many factors: Structure factor (include form factor), Lorentz, polarization, multiplicity, temperature factors. The XRD peak's intensity is calculated as

$$I(hkl) = |S(hkl)|^2 \times M_{hkl} \times LP(\theta) \times TF(\theta) \quad (3.33)$$

where, $S(hkl)$ is structure factor, M_{hkl} is multiplicity factor, $LP(\theta)$ is Lorentz and Polarization factors, $TF(\theta)$ is temperature factor (displacement parameter).

To perform the rocking curve, ω scan, first we find out the peak position (2θ), after that incline the sample and measure the intensity. XRD Φ -scan is used to see the in-plane orientation of sample. It can only scan the incline plane with the sample surface (azimuth scan). To perform

this measurement, first the peak position (2θ and ω) of sample's crystallographic plane are found out by θ - 2θ and ω scans. Second, the θ angle is changed to the position of incline plane which we want to scan. Third, the sample is tilted an angle χ (angle between incline plane and surface) and rotate it about the Φ -axis (normal to the surface at incident point).

3.5.2 Reflection high energy electron diffraction (RHEED)

The RHEED is a useful technique to characterize the surface of crystalline materials during and after MBE growth. RHEED gun uses a high voltage 0-30 kV to accelerate electron from filament. A phosphor screen is used to detect the diffraction pattern. The RHEED gun, phosphor screen, and substrate are positioned to create a small angle 1 - 2° between incident electron beam and sample surface. This very small angle ensures that the penetration depth of electron beam is only 1-2 atomic layers. That is reason why RHEED only provides the surface information of the sample. There are some main kinds of RHEED pattern with corresponding information reflecting the growth mode and surface morphology. Streaky RHEED pattern indicates the smooth surface with the layer by layer growth mode. Spotty RHEED pattern indicates the rough surface and the three-dimensional growth mode. Ring pattern indicates the growth of polycrystalline thin film. RHEED oscillation can be used to determine the layer by layer growth mode of the film. On the other hand, by measuring the line spacing in streaky patterns, we can determine the lattice constant of the film (provide that the lattice constant of substrate is known) with the error of 0.1%. The line spacing is inverse proportion to the lattice constant.

$$a \sim \frac{1}{d} \quad (3.34)$$

where, a is lattice constant, and d is line spacing in the streaky RHEED pattern.

3.5.3 Thermal diffusivity and thermal conductivity: LFA, ZEM 3

Thermal conductivity (κ W/m-K) describes the transport of energy – in the form of heat – through a body of mass as the result of a temperature gradient. Determining thermal conductivity is an indirect measurement. The thermal conductivity of a material is proportion to its thermal diffusivity. The thermal diffusivity (D with the unit mm^2/s) is a material-specific property for characterizing unsteady heat conduction. This value describes how quickly a material reacts to a change in temperature. In this work, this measurement was performed by Netzsch LFA457. The thermal conductivity is calculated by

$$\kappa = D\rho C_p \quad (3.35)$$

where, D is thermal diffusivity, ρ is mass density, and C_p is specific heat.

The mass density can be determined by measuring weight (m) and volume (V) by the following formula

$$\rho = \frac{m}{V} \quad (3.36)$$

To minimize the errors, an Archimere method was used to determine mass density of material with any shape. To do that we measure weight of sample in air and in DI water (mass density = 1000 kg/m^3). The mass density of sample is determined by

$$\rho_0 = \frac{m_0}{m_0 - m} \rho_{DI} \quad (3.37)$$

where, ρ_0 is mass density of sample in air, ρ_{DI} is mass density of DI water, m is weight of sample in DI water, and m_0 is weight of sample in air. The main source of error is bubbles on the surface of sample. To conduct measurement accurately we need smooth surface and large

enough sample.

3.6 Measurement's errors

In science, the word “error” means the “uncertainty” which accompanied in any measurement. We cannot measure any sort without error and cannot avoid it by carefully handle the measurement. The experimenter can only try to ensure the errors are as small as possible and estimate how large they are. There are two main types of error: Systematic error and random error which are belong to the precision and accuracy. First, the systematic error is related to the equipment errors (incorrect calibration) or the error of measurement's theory. To minimize this error, first we can do calibrate the equipment or develop the theory of measurement. Second, the random error is related to operator's skill (e.g. reading errors), or some factors from ambient environment leading to the different values between measurements. To minimize this kind of error, we may repeat the experiment many times and take average by appropriate equations of statistics.

In this work, we used the home build high temperature transport measurement system and UlvacRiko ZEM-3 instrument to measure Seebeck coefficient and electrical conductivity. The thermal diffusivities were measured by lase fash analysis LFA instrument (model: LFA-457, NETZSCH, Germany). The standard uncertainties of UlvacRiko ZEM-3 were reported by company: 5% for Seebeck coefficient and electrical conductivity; and about 15% for power factor. The LFA-457 instrument gave an uncertainty of thermal conductivity of 5% (estimated value). The uncertainties of our home build high temperature transport measurement system were calculated and reported [6]. This section represents the calculation for these uncertainties.

3.6.1 Electrical conductivity measurement error

The electrical conductivity can be calculated by

$$\sigma = \frac{1}{\rho} = \frac{l}{Rab} \quad (3.38)$$

where, ρ is electrical resistivity, R is electrical resistance, l is length (distance between two voltage probes in the collinear 4 probe configuration mentioned above), and a and b are the width and thickness of sample. Take natural logarithm both sides of this equation we have

$$\begin{aligned} \sigma &= \frac{1}{\rho} = \frac{l}{Rab} \\ \ln \sigma &= \ln l - \ln R - \ln a - \ln b \end{aligned} \quad (3.39)$$

Take derivative both sides

$$\begin{aligned} d(\ln \sigma) &= d(\ln l) - d(\ln R) - d(\ln a) - d(\ln b) \\ \frac{d\sigma}{\sigma} &= \frac{dl}{l} - \frac{dR}{R} - \frac{da}{a} - \frac{db}{b} \end{aligned} \quad (3.40)$$

Use the letter “ Δ ” instead of letter “ d ”, at average values of quantities, consider only maximum value, we have

$$\frac{\Delta\sigma}{\bar{\sigma}} = \frac{\Delta l}{\bar{l}} + \frac{\Delta R}{\bar{R}} + \frac{\Delta a}{\bar{a}} + \frac{\Delta b}{\bar{b}} \quad (3.41)$$

Here, we neglected the uncertainty of resistance given by Keithley model 2400 (less than 0.1%).

The typical sample size used for our home build measurement system is $l = 2 \text{ mm}$, $a = 2 \text{ mm}$, and $b = 0.3 \text{ mm}$. The uncertainty of rulers is $\Delta l = \Delta a = \Delta b = 0.01 \text{ mm}$. We have

$$\frac{\Delta\sigma}{\bar{\sigma}} = \frac{0.01}{2} + \frac{0.01}{2} + \frac{0.01}{0.3} = 0.043 = 4.3\% \quad (3.42)$$

The error for electrical conductivity is 4.3%.

3.6.2 Seebeck coefficient measurement's error

For this measurement, we used the repeating measurement method to determine the error at room temperature [6]. The reference material is Bismuth (Bi) polycrystalline. The measurement was repeated 18 times and was analyzed using fitting data technique as shown in the Fig. 3.21. We determined Seebeck coefficients from the linear slope of ΔV vs. ΔT curves. The measured Seebeck coefficient of polycrystalline Bi is $-57.7 \pm 0.76 \mu\text{V/K}$. Standard error from the linear fitting is 1.3% . Note that the Seebeck coefficient of Bi single crystal is $-51.4 \mu\text{V/K}$ along perpendicular to the three-fold axis and $-102.7 \mu\text{V/K}$ along parallel to the three-fold axis. The Seebeck coefficient of the reported polycrystalline Bi is $-60 \mu\text{V/K}$ at 300 K. The slight difference between the measured and reported values is due to the sample quality such as grain size, purity, etc.

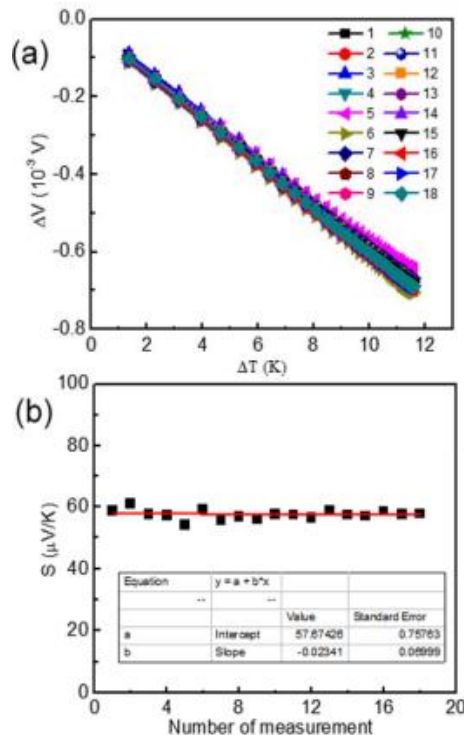


Fig. 3. 21. a) ΔV vs. ΔT at 300 K of polycrystalline Bi and b) measurement' error.

3.6.3 Thermal conductivity measurement error

The laser flash analysis (LFA) Netzsch LFA 457 measurement system was used to determine thermal diffusivity of samples. The reported error for this system is $\pm 3\%$.

3.6.4 Power factor's error

Power factor is calculated from Seebeck coefficient and electrical conductivity as

$$PF = S^2 \sigma \quad (3.43)$$

The uncertainty of power factor is calculated using the rules of indirect measurement's error calculation.

$$\begin{aligned} PF &= S^2 \sigma \\ \ln PF &= 2 \ln S + \ln \sigma \\ \frac{\Delta PF}{PF} &= 2 \frac{\Delta S}{S} + \frac{\Delta \sigma}{\sigma} = 2 \times 0.013 + 0.043 = 0.069 = 6.9\% \end{aligned} \quad (3.44)$$

3.6.5 Figure of merit's error

The thermoelectric figure of merit is calculated by

$$\begin{aligned} ZT &= \frac{PF}{\kappa} T \\ \ln ZT &= \ln PF + \ln T - \ln \kappa \\ \frac{\Delta ZT}{ZT} &= \frac{\Delta PF}{PF} + \frac{\Delta \kappa}{\kappa} = 0.069 + 0.03 = 0.099 = 9.9\% \end{aligned} \quad (3.45)$$

Here, κ is thermal conductivity, and T is absolute temperature (the uncertainty of T is neglected).

3.6.6 Errors of ZEM 3

Apart of samples in this work, the electrical resistivity and Seebeck coefficient were measured using an Ulvac Riko ZEM-3 instrument under a helium atmosphere from room temperature to 923 K. The uncertainty for Seebeck coefficient, electrical conductivity, and ZT are 5%, 10% and 20%, respectively.

3.7 References

- [1] <http://www.digikey.com/en/pdf/a/atmel/avr221-discrete-pid-controller-on-tinyavr-and-megaavr-devices>.
- [2] https://en.wikipedia.org/wiki/Impedance_matching.
- [3] https://en.wikipedia.org/wiki/Rotary_vane_pump
- [4] D. R. Lovett, semimetals and narrow band gap semiconductors, p. 28-30 London Pion limited (1977).
- [5] L.D. Zhao, S.H. Lo, Y.S. Zhang, H. Sun, G. Tan, C. Uher, C. Wolverton, V.P. Dravid, M.G. Kanatzidis, *Nature* **508**, 373 (2014).
- [6] A.T. Duong, V.Q. Nguyen, G. Duvjir, V.T. Duong, S. Kwon, J.Y. Song, J.K. Lee, J.E. Lee, S.D. Park, T. Min, J.W. Lee, J. Kim, S. Cho, *Nat. Commun.* **7**, 13713 (2016).
- [7] M. Tokita, Mechanism of spark plasma sintering, in Proceedings of the International Symposium on Microwave, Plasma and Thermochemical Processing of Advanced Materials, ed S. Miyake and M. Samandi. JWRI, Osaka Universities Japan, 69 (1997).
- [8] Z. H. Zhang, Z-F. Liu, J. F. Lu, X. B. Shen, F. C. Wang, and Y. D. Wang, *Scripta Materialia* **81**, 56 (2014).
- [9] S. Diouf, A. Molinari, *Powder Technol.* **221**, 220 (2012).
- [10] O. Guillon, J. G. Julian, B. Dargatz, T. Kessel, G. Schierning, J. Räthel, M. Herrmann, *Adv. Eng. Mater.* **16**, 830 (2014).
- [11] Mini hot press apparatus, The Korean Intellectual Property Office WO 2017043910 A1

(2017).

[12] J. Langer, M. J. Hoffmann, O. Guillon, *Acta Materialia* **57**, 5454 (2009).

[13] “77 K to 1000 K range electrical resistivity and Seebeck coefficient measurement system”,
The Korean Intellectual Property Office, No 10-1726498, (2017).

CHAPTER 4: ENGINEERING DEFECTS IN SnSe SINGLE

CRYSTAL

(TO BE SUBMITTED)

SnSe is a layered semiconductor with orthorhombic structure whose excellent thermoelectric property has been reported with a huge ZT value of 2.6 in p-type and 2.2 in Bi doped n-type SnSe. Anharmonic bonding is assigned to the cause of the ultralow thermal conductivity of SnSe, also makes this material becomes hard to be doped. The p-type characteristic of SnSe is attributed to single Sn vacancies, suggesting a possibility to control carrier concentration of SnSe without doping by controlling vacancies concentration which strongly depends on growth condition. In this work, we have fabricated SnSe and controlled type and number of vacancies by changing cooling rate during the growth. The average mass density was 5.95 g/cm^3 . STM images showed a sudden increase number of defects with cooling rate and the change of dominant defect type from single Sn vacancy to multi-vacancies. The single Sn vacancy seems to be disappeared when the cooling rate was exceeded $1 \text{ }^\circ\text{C/h}$. The decrease number of single Sn vacancy leading to decrease hole concentration and electrical conductivity with cooling rate. The thermal conductivities were not ultralow and were not depend on the intrinsic defects. This may due to the presence of small amount of SnSe₂ phase in our samples. Maximum ZT values were achieved in sample at cooling rate of $0.5 \text{ }^\circ\text{C/h}$; 0.55 , 0.71 , and 1.2 at 873 K along a , b , and c -axes, respectively.

4.1 Introduction

Thermoelectric (TE) converter which can directly convert waste heat in to electricity and vice versa is a good candidate for alternative source of sustainable energy. These TE devices exploit

the thermoelectric effects; Seebeck - Peltier effects and consist of both n and p-type TE materials. Their conversion efficiency can be evaluated by the dimensionless figure of merits, $ZT = S^2\sigma T/\kappa$, where S is Seebeck coefficient, T is absolute temperature, σ is electrical conductivity, and κ is total thermal conductivity. A high ZT material should exhibits high Seebeck coefficient (S), high electrical conductivity (σ), and low thermal conductivity (κ)[1]. In principle, the ZT value of a substance can be increased to infinity, however, enhancing ZT value is still a great challenge to scientists due to the interdependence of σ , S , and κ through the carrier concentration. So far, efforts have been done to enhance ZT by: enhancing power factor, lowering total thermal conductivity or both simultaneously. Power factor can be enhanced through carrier concentration optimization, mixed phase structure[2–4], band engineering[5–7]. Lower thermal conductivity can be achieved by increase phonon scattering centers and adding number of interfaces such as in superlattices, alloys, nano wires, and nano tube, nano structured[6]. On the other hand, finding out nontoxic and earth abundant TE materials is another important mission.

Recently, SnSe has been reported with excellent thermoelectric performance $ZT = 2.62$ along b -axis at 923 K[8]. It is well known as p-type semiconductor with an indirect band gap $E_g = 0.829$ eV at 300 K and direct band gap $E_g = 0.464$ eV above 813 K[9]. SnSe exhibits 2D layered structure with the layer's stacking along a -axis by a weak Van der Waals force, leading to a strong anisotropic transport and weak mechanical properties. The high ZT value of SnSe is attributed to its ultralow intrinsic thermal conductivity (the lowest lattice thermal conductivities known for any crystalline materials (< 0.4 W m⁻¹ K⁻¹ at 923 K)) due to strong anharmonicity of the chemical bonds[10]. This anharmonic bonding also makes SnSe becomes fairly hard to be doped[2]. To date, two experimental studies about doped SnSe single crystal with $ZT = 0.7 - 2.0$ at 300 - 773 K and $ZT = 2.2$ at 733 K have been reported in p-type Na-doped and n-type

Bi-doped SnSe, respectively[11,12]. Unfortunately, the doping efficiency of SnSe was very low. For applications, polycrystalline SnSe has been focused. Many studies focused on thermoelectric properties of polycrystalline SnSe have been reported. However, the ZT values for un-doped, n-type, and p-type doped polycrystalline SnSe are much smaller than that of single crystal, in range from 0.5 to 1.3 for SnSe un-doped, and doped with Ag, I, BiCl₃, S, Na-Te, Te, In, Zn, and Br[1–4,13–20]. The most common method to fabricate single crystal SnSe and/or SnSe compound is Bridgman technique. By this method, the mixed raw materials are heated up to appropriate temperature and then slowly cooled down to room temperature by pulling down the ampoule. However, there are no systematically studies on the crystal imperfections induced by the growth condition. All experiments have been done without clearly understand about microscopic nature of SnSe.

Our idea comes from the previous work, where we have first experimentally showed that the p-type characteristic of SnSe is originated from single Sn vacancy[21]. Zhao et al. has also argued that a large amount of vacancies was presented in his samples. Ibrahim *et al.*[22] has also suggested an experimentally confirm the role of vacancies to the lattice thermal conductivity of SnSe. In this work, SnSe have grown by temperature gradient technique. The vacancies concentration was successfully controlled by changing the cooling rate in the temperature range across melting point of SnSe (861 °C). We observed a change of dominant defect type from single Sn vacancy to multi-vacancies when cooling rate is greater than 1 °C/h. The hole concentration and electrical conductivity decreased with cooling rate. Thermal conductivities were found to vacancies independent and were not ultralow. The highest ZT values were achieved in sample at cooling rate of 0.5 °C/h; 0.55, 1.2, and 0.71 at 873 K along a , b , and c -axes, respectively. These low ZT values may due to the presence of SnSe₂ phase in our samples.

4.2 Experiment

4.2.1 Raw materials

Sn powder (99,99% Alfa Aesar) and Se powder (99,98% Alfa Aesar)

4.2.2 Temperature gradient growth

SnSe single crystal ingots (20 g) have been fabricated by temperature gradient technique. The raw materials of Sn and Se were first calculated in atomic ratio of 1:1 and weighed using balance with a resolution of 10^{-4} g. Stoichiometric amounts of elements were dried at 100 °C for 10 minutes, mixed and sealed in an evacuated ($< 10^{-4}$ Torr) thick quartz ampoule. The ampoule was then sealed in another evacuated bigger quartz ampoule, to prevent the sample from oxidation by air when the inner ampoule is broken owing to the different thermal expansion coefficients between the crystal and quartz and the volume expansion of SnSe at transition temperature from *Cmcm* to *Pnma* phase (~500 °C). These ampoules were slowly heated up over a period of 30 h up to 600 °C. It was maintained at this temperature for 10 min and then continuously heated up to 950 °C within 35 h. To complete reaction between Sn and Se we maintained the ampoules at this temperature for 15 h. After that the ampoules were slowly cooled down to 800 °C (below melting point of SnSe 861 °C) with the cooling rate of 0.5, 1.0, 2.0, 3.0, 4.0, and 5.0 °C/h, following by slowly cool down to 400 °C at 5 °C/h and then to room temperature at 15 °C/h. Excellent ingots were obtained.

4.2.3 Thermoelectric transport measurements

The samples were cut in to $10\text{ mm} \times 2\text{ mm} \times 2\text{ mm}$ bars, which were used to measure simultaneously the electrical resistivity and Seebeck coefficient using an Ulvac Riko ZEM-3 instrument under a helium atmosphere from room temperature to 923 K. In order to prevent the sample evaporation and protect the instrument, the samples were coated with a thin layer

of boron nitride (BN). The uncertainty of Seebeck coefficient and electrical conductivity measurements is 5%, leading to an uncertainty of 15% for power factor.

4.2.4 Crystal structure measurements

X-ray diffraction (XRD) measurements, field emission scanning electron spectroscopy (FE-SEM), and transmission electron microscopy (TEM) were employed to investigate the crystal structure of samples.

4.2.5 Hall measurements

High-temperature Hall resistance as a function of magnetic field measurement was taken with a home-made high-temperature apparatus. The samples were cut in to dimensions $5\text{ mm} \times 5\text{ mm} \times 0.5\text{ mm}$ for this measurement. A low vacuum (10^{-3} Torr) environment was used to prevent the samples from oxidation at high temperature.

4.2.6 Thermal conductivity measurements

The thermal diffusivities were measured with a Netzsch LFA 457 instrument and analyzed using Cowan model with pulse correction. To measure thermal diffusivity, we cut the samples in to dimensions $8\text{ mm} \times 8\text{ mm} \times 1\sim 2\text{ mm}$. A thin layer of graphite was coated on surface of samples to minimize errors from the emissivity of the material. The total thermal conductivity was calculated from $\kappa_{tot} = DC_p\rho$, where D is thermal diffusivity, C_p is specific heat which was taken from Ref. 8, and ρ is mass density of sample which was calculate by measure dimensions and mass of the samples. The uncertainty of the thermal conductivity is estimated to be within 5%, considering the uncertainties for D , C_p , and ρ .

4.2.7 Scanning Tunneling Microscopy (STM) measurements

For STM study, a single-crystal SnSe sample was transferred into the home-built low

temperature STM system and cleaved in-situ to obtain clean surfaces. Tungsten tips were prepared by electro-chemical etching and cleaned with electron beam heating for STM measurements as described elsewhere[12].

4.2.8 Transmission electron microscopy (TEM) measurement

The sample was cut cross-sectional (perpendicular to the cleaved plane) by focused ion beam (model Helios Nanolab 450 F1) with an in-situ lift out technique. After that transmission electron microscope investigation was conducted with a Titan Double Cs corrected TEM (model Titan cubed G2 60-300).

4.3 Results

4.3.1 Structural analyses

A picture of sample is shown in Fig. 4.1(a) which is easily to be cleaved along (*bc*) plane. Field emission scanning electron microscopy (FE-SEM) indicated the layered structure of our sample as shown in Fig. 4.1(b). The room temperature XRD pattern of this cleaved SnSe sample is shown in Fig. 4.1(c), which can be indexed base on orthorhombic SnSe phase (space group *Pnma*). As being shown in the figure, only the (*h00*) peaks are observed indicates that the cleaved plane of SnSe is perpendicular to the *a*-axis. However, there is a small amount of SnSe₂ phase present in our samples which is indicated in powder XRD patterns in Fig. 4.1(d). The average *a*, *b*, and *c*-axes lattice constants calculated from XRD data are 11.52, 4.46, and 4.18 Å, respectively. These lattice constants are consistent with previous reports for SnSe. Energy dispersive spectroscopy (EDS) and electron probe micro analysis (EPMA) measurements indicated the presence of exceed Se amount in our samples leading to the ratio $Sn/Se = 48/52$ (supplementary figure S4.1), in consistent with this presence of SnSe₂ phase. Note that, both SnSe and SnSe₂ are 2D layered materials. Our observation suggested that the layers of SnSe

and SnSe₂ are stacked parallel each other with a much dominance of SnSe phase. Due to the micrometers scale penetration depth of X-ray beam, we expect that the thickness of SnSe layer is larger than 1 μm, and the cleaved planes always are SnSe layers, therefore, the XRD patterns of the cleaved planes show only SnSe peaks.

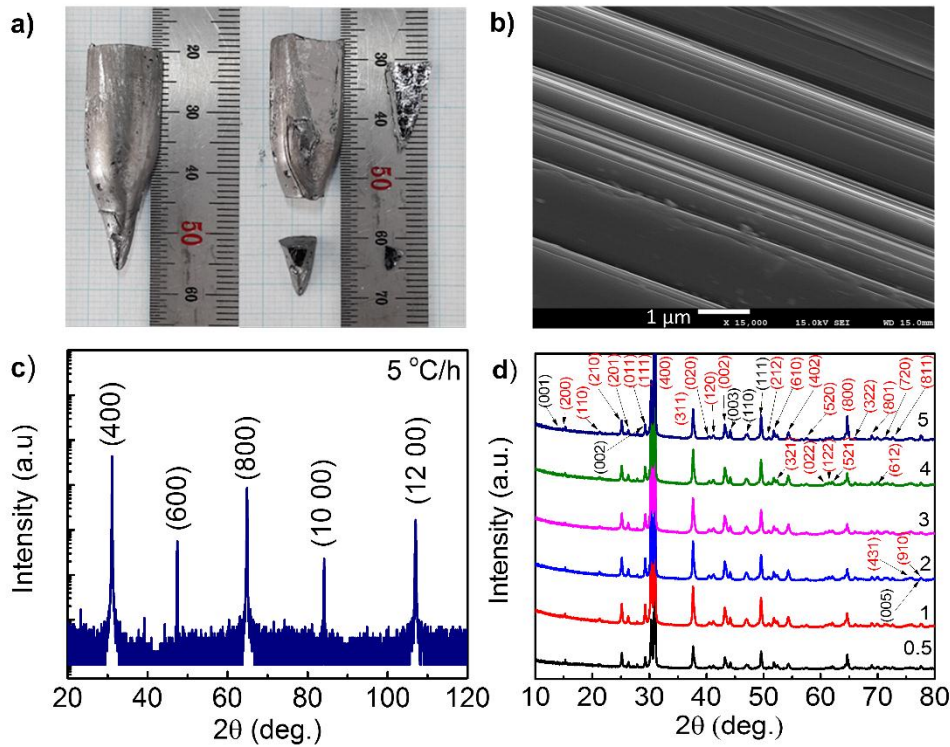


Fig. 4. 1. (a) A picture of SnSe ingot, (b) FE-SEM image of SnSe confirms the layered structure, (c) XRD pattern of SnSe single crystal with cooling rate of 5.0 °C/h. The samples with other cooling rate show the same XRD pattern (supplementary figure S4.4), and (d) PXRD patterns of all samples show the existence of SnSe₂ phase, where SnSe and SnSe₂ peaks are denoted in red and black colors, respectively. The average lattice constants of SnSe calculated from XRD are $a = 11.52$, $b = 4.46$, and $c = 4.18$ Å.

Figure 4.2 shows the cross-sectional TEM image of sample at cooling rate of 0.5 °C/h. Excellent crystallinity SnSe was observed. The estimated average lattice constants of SnSe

from TEM image are $a = 11.87 \text{ \AA}$ and $b = 4.59 \text{ \AA}$, in consistent with the XRD data. Unfortunately, the presence of SnSe₂ layers was not observed in the image. There are two possible reasons for this absence of SnSe₂ phase in the TEM images. First, the thickness of SnSe layer may larger than FIB penetration depth ($\sim 5 \text{ \mu m}$). Second, we missed the interfaces between two phases during the TEM scanning.

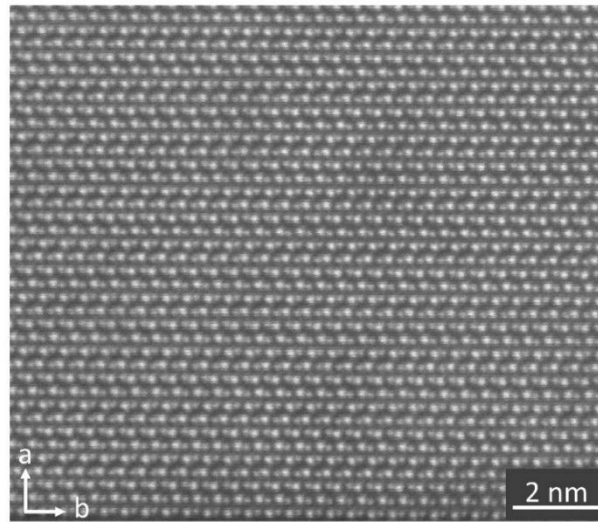


Fig. 4. 2. Cross-sectional transmission electron microscopy (TEM) image of sample SnSe 0.5 °C/h. The SnSe₂ phase exists somewhere which is difficult to be recognized. The average lattice constants obtained from TEM image are $a = 11.87$ and $b = 4.59 \text{ \AA}$.

4.3.2 Evidences of defects engineering

Hall resistance as a function of magnetic field H and the calculated carrier concentration of all samples near room temperature are shown in Fig. 4.3. The carrier concentrations are calculated from the slope of R_H vs. H curves using the formula, $R_H = \frac{1}{ned}H$, where $R_H = \frac{V_H}{I}$ is Hall resistance, V_H is Hall voltage, I is applied current, n is carrier concentration, d is sample's thickness, and e is electrical charge. Positive slope of R_H vs. H curves indicated the p-type characteristic of our samples. The calculated carrier concentration of samples decreased with

cooling rate and nearly saturate at cooling rate above 2 °C/h. Unfortunately, we could not measure carrier concentration at higher temperature due to the Hall effect is not clear in this temperature range, leading to the irreversible of R_H vs. H curves.

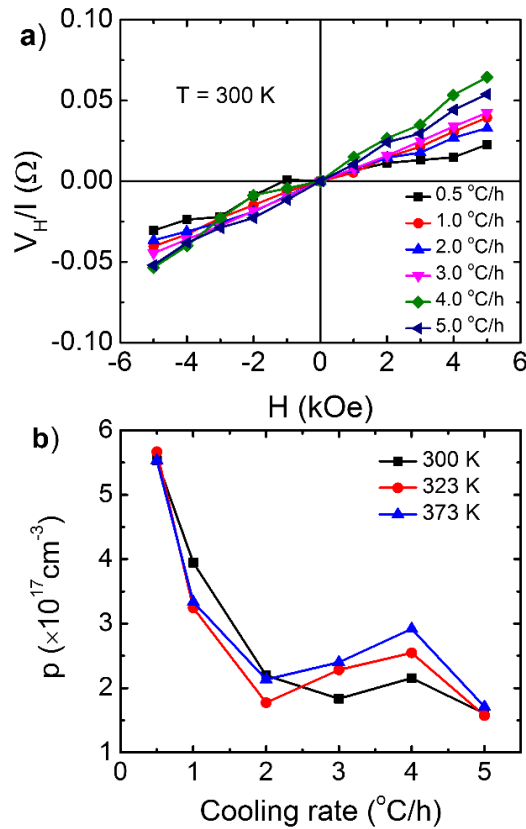


Fig. 4. 3. (a) The plots of V_H/I vs. H of all samples at 300 K with positive slopes indicate the p-type characteristic of our samples, and (b) Carrier density as a function of cooling rate at some critical temperatures.

To investigate the microscopic structure and defects of the samples we carried out the scanning tunneling microscope STM experiments for samples with cooling rate of 0.5, 1.0, 2.0 and 5.0 °C/h at 77 K is shown in Fig. 4.4 The images conditions including samples bias, tunneling current, and dimensions are shown in the figure. The images showed only SnSe cleaved plane as expected from XRD data. The bright spots indicate rows of Sn atoms, while Se atoms located

in dark regions are not visible[21]. The measured lattice constants from STM images are $b=4.44 \text{ \AA}$ and $c = 4.15 \text{ \AA}$, in agreement with those obtained from XRD and TEM data. As shown in the figure, a large number of defects were observed. The defects consist of single Sn vacancy, Se vacancy, Se-Sn-Se vacancy (described elsewhere[21]), multi vacancies (supplementary figure S4.2), and other minority unidentified defects. On the other hand, the number of defects increased with cooling rate. As shown in Fig. 4.4(a) and (b), single Sn vacancy is dominant defect in sample with cooling rate of 0.5 and $1.0 \text{ }^\circ\text{C/h}$. A high resolution STM image taken from one of single Sn vacancies (solid circles) is shown in Fig. 4.4(c). The size of this defect is $2b \times 2c$, indicated the missing of a single Sn atom. However, due to the limitation of scanning area of STM experiments, it is hard compare the single Sn vacancy concentration between these samples. It was reported that single Sn vacancy is the main source of p-type characteristic of SnSe[21]. If a sample contains higher acceptor defects concentration, it has higher carrier concentration and vice versa. Based on the carrier concentration calculated above, we may conclude that the acceptor defects concentration is larger in sample with cooling rate of $0.5 \text{ }^\circ\text{C/h}$ than that in sample $1 \text{ }^\circ\text{C/h}$. As the cooling rate increased, the number of defects suddenly increased. We found that multi-vacancies are dominant defects in sample at cooling rate of 2.0 and $5.0 \text{ }^\circ\text{C/h}$; such as two Sn, or five Sn vacancies (supplementary figure S4.2). Due to the Se atoms are invisible from the STM images we could not count the number of Se missing atoms in these multi vacancies. On the other hand, we could not see any single Sn vacancy in these samples, indicating that multi vacancies also contributed hole carriers to the crystal. As mentioned above, the carrier concentrations in these samples are nearly same. That means some multi vacancies may contribute charge carrier to the crystal, but some may not. A further study is needed to clarify this issue in detail. Our observations of decrease single Sn vacancy and increase multi-vacancies with cooling rate are completely natural as the effects of cooling rate

to the crystal grown from its melt. These observations provided a visible evidence for our success on controlling defects as well as carrier concentration of SnSe. This change of defect type and concentration take a strong effect to the thermoelectric transport properties of samples as following.

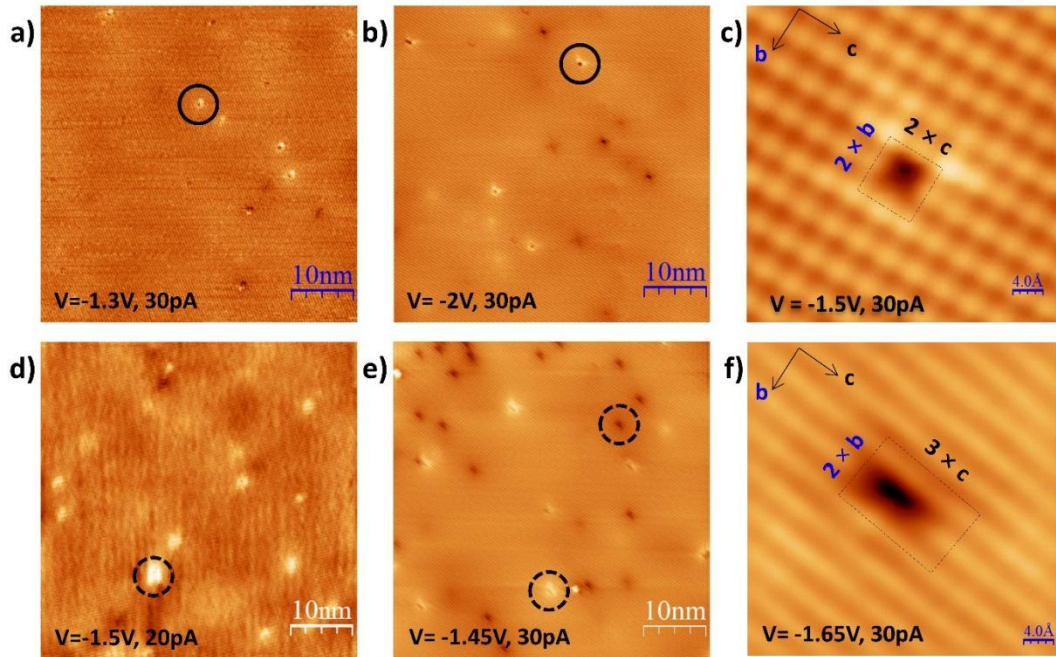


Fig. 4. 4. STM topographic images of samples (a) $0.5\text{ }^{\circ}\text{C/h}$, (b) $1\text{ }^{\circ}\text{C/h}$, (d) $2\text{ }^{\circ}\text{C/h}$, (e) $5\text{ }^{\circ}\text{C/h}$. (c), (f) High resolution STM images taken from single Sn vacancy (solid circles) and one of multi-vacancies (dotted circles) in (a, b) and (d, f), respectively. Here $b = 4.44\text{ \AA}$ and $c = 4.15\text{ \AA}$. The given numbers at the bottom are sample's bias and tunneling current. The detail number of Sn missing atom in each vacancy is shown in supplementary figure S4.2.

4.3.3 Thermoelectric transport properties

Figure 4.5 shows the temperature dependent electrical conductivities, Seebeck coefficients, and power factors along b -axis which showed the highest ZT [8]. The temperature dependent electrical conductivity curves showed the same trend for all samples which is consistent with

results reported by Zhao *et al.*[8] (Fig. 5(a)). In the temperature range from 300 to 523 K, the electrical conductivity decreases with temperature indicating the metallic transport behavior. It shows semiconducting behavior from 523 K to 872K, after that the electrical conductivity slightly decreased. The transition at 523 K is attributed to the thermal excitation of carriers while the transition at 873 K is attributed to the phase transition from *Pnma* to the *Cmcm* space group of SnSe[9]. The decrease of electrical conductivity above 823 K is due to the increase electron-phonon scattering. The Seebeck coefficients vs. temperature curves are shown in Fig. 4.5(b) which are consistent with the electrical conductivity-temperature curves. The values of Seebeck coefficients are positive, indicating the p-type characteristic of our samples. Seebeck coefficients increased with temperature, reached the maximum values at 523 K and then decreased with temperature due to the bipolar conduction. Figure 4.5(c) showed the temperature dependence of thermoelectric power factors (*PFs*) at all cooling rates. Higher *PFs* were achieved in high temperature range correspond to the *Cmcm* phase of SnSe. The highest *PF* value of $11.23 \mu\text{W cm}^{-1} \text{K}^{-2}$ was achieved at 873 K in sample at cooling rate of $0.5 \text{ }^\circ\text{C/h}$ which is 12.3% higher than that reported by Zhao *et al.*[8].

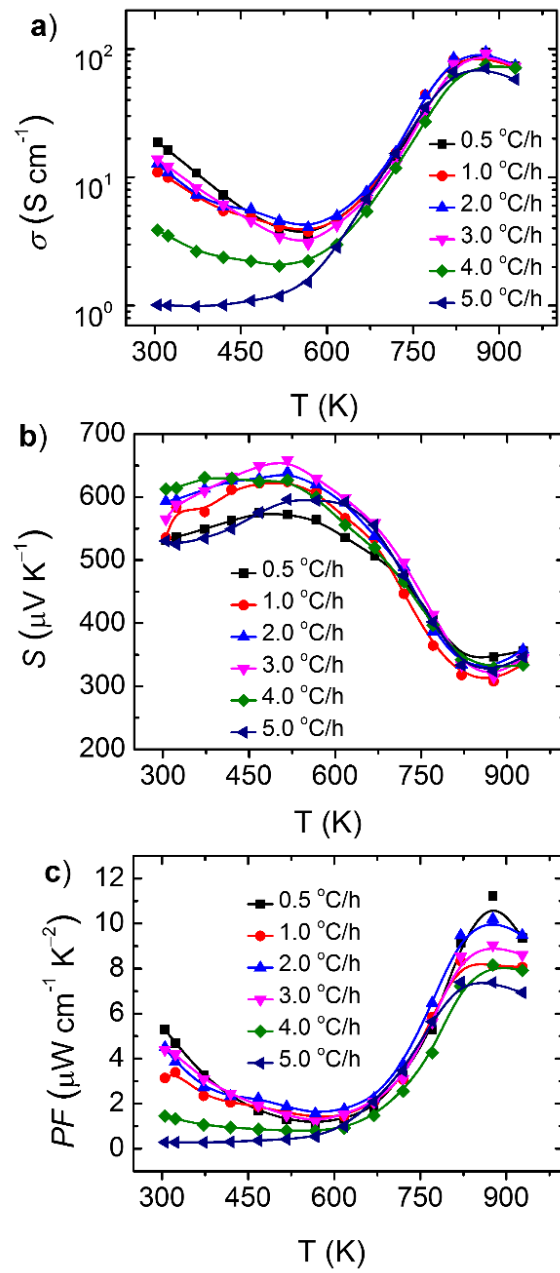


Fig. 4. 5. The temperature dependent (a) electrical conductivities, (b) Seebeck coefficients, and (c) thermoelectric PFs of SnSe single crystal along b-axis of samples with cooling rate of 0.5, 1.0, 2.0, 3.0, 4.0, and 5.0 °C/h. All samples exhibited p-type characteristic in consistent with Hall data.

The cooling rate took a strong effect to the transport properties of samples. As shown in Fig. 4.6, the electrical conductivity, Seebeck coefficient, and power factor were plotted as a function of cooling rate. In the whole range of cooling rate, the transport parameters decreased with cooling rate with a kink at $1\text{ }^{\circ}\text{C/h}$ due to the change in dominant defects whose contributions to the carrier concentration and carrier's mobility are different. The kink was confirmed by the reproducibility of thermoelectric transport data for 5 times measurements using 5 pieces cut along b -axis from 5 different ingots (in 5 synthesis batches) of samples at cooling rate of $1\text{ }^{\circ}\text{C/h}$ (supplementary figure S4.4). In the following, we discuss the thermoelectric transport behavior of samples in two regions with the dominance of single Sn vacancy and multi-vacancies as defined by STM study mentioned above. Note that, SnSe occurs the phase transition from $Pnma$ to $Cmcm$ at about 800 K. First, in region (I), at below 800 K, Seebeck coefficient increased, while the electrical conductivity decreases with cooling rate due to the decrease of carrier concentration. The PF increased with cooling rate. Above 800 K, Seebeck coefficient and electrical conductivity decreased with cooling rate. As a result, PF decreased. Second, in region (II), Seebeck coefficient, electrical conductivity and power factor decreased with cooling rate which is assigned to the decrease of carrier's mobility. The decrease of carrier's mobility with cooling rate is due to the increase number of defects which act as scattering centers.

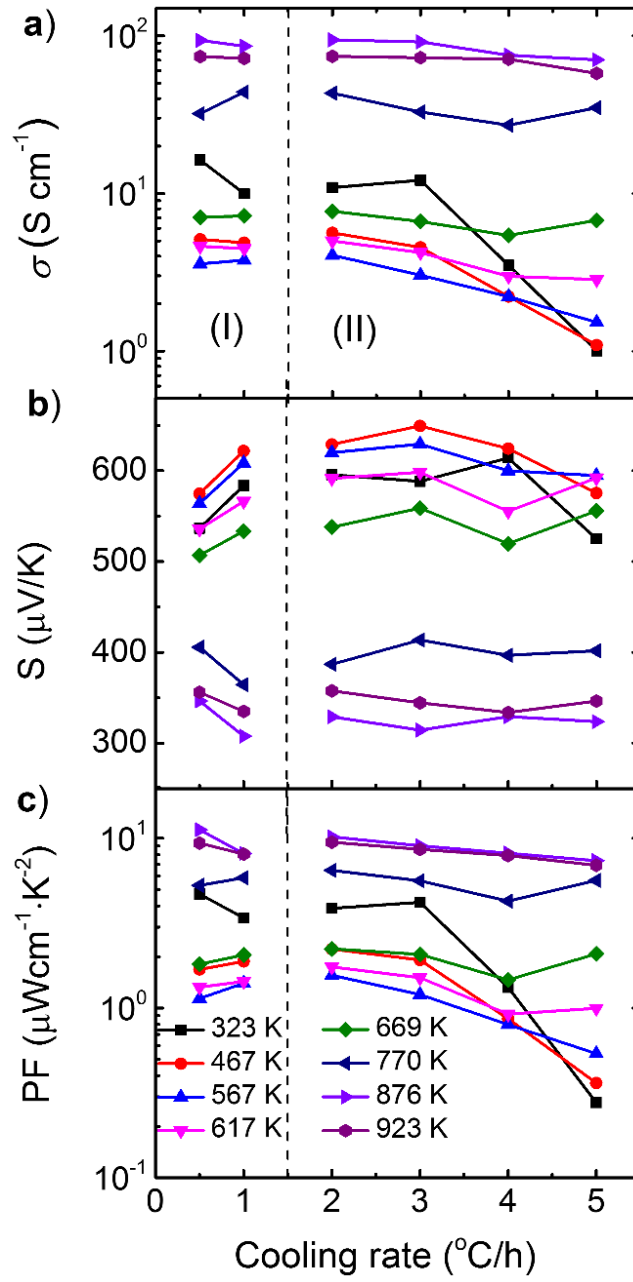


Fig. 4. 6. Cooling rate dependent (a) electrical conductivities, (b) Seebeck coefficients, and (c) thermoelectric power factors (*PFs*) of SnSe single crystal along b-axis of samples at some typical temperatures.

4.3.4 Thermal conductivity and thermoelectric figure of merit ZT

Figure 4.7 showed the temperature dependent thermal conductivity and thermoelectric figure of merit ZT for all samples along b -axis. Temperature dependent thermal conductivity (Fig. 4.7(a)) show the nearly same thermal conductivity values for all samples, indicating the independence of thermal conductivity on intrinsic defects (supplementary figure S4.6). Similar defect chemistry in doped SnS and SnTe does not strongly affect to the lattice thermal conductivity, although it takes strong effect to the transport properties of these materials[23,24]. At 300 K the thermal conductivities are in range from 1.5 to 2.1 $\text{W m}^{-1} \text{K}^{-1}$ which are between two and three times larger than those reported for p-type un-doped and n-type Bi doped SnSe[8,12]. The thermal conductivity decreased with temperature, reached minimum value at 750 K (0.59 $\text{W m}^{-1} \text{K}^{-1}$), and then raised up to 0.83 $\text{W m}^{-1} \text{K}^{-1}$ at 823 K due to the $Pnma$ to $Cmcm$ phase transition, finally it slightly decreased again as temperature increase from 800 - 923 K due to the increase electron-phonon scatterings. Our results are comparable to those reported for SnSe single crystal[22,25–28], and for SnSe polycrystalline samples[1,2,29].

Now we turn to discuss about possible reasons for the high thermal conductivity in our SnSe single crystal and some prior reports. One possible reason for the high thermal conductivity was suggested by Zhao *et al.*[11] as the surface oxidation of samples due to the air exposure. Another reason for the high thermal conductivity is micro-crack in the samples which may double the thermal conductivity of SnSe[30]. The third reason for the high thermal conductivity of our samples is the nearly fully dense of our samples (96.3% of the theoretical density from XRD; 6.18 g/cm^3). Finally, we recall here that our powder XRD data showed the existence of SnSe₂ phase in our samples. The presence of SnSe₂ phase may be the main reason for the change of mass density as well as thermal conductivity of the samples. Based on our data we first

experimentally concluded that intrinsic defects do not play a prominent role in the lattice thermal conductivity of SnSe and there always presence of SnSe₂ phase when SnSe single crystal is grown. We suggest a further systematically study about the role of SnSe₂ phase to thermoelectric properties of single crystal grown under Sn rich and Se rich conditions. We also suggest a study on the growth and thermoelectric properties of SnSe and SnSe₂ together which is known as misfit layer compound and its subset, fere-crystal (almost crystal).

Figure 4.7(b) shows the ZT values along b -axis of all samples. ZT values increased with temperature and decreased with cooling rate. The highest value $ZT = 1.2$ at 873 K was achieved in sample at cooling rate of 0.5 °C/h. This ZT value is two times smaller than that reported by Zhao *et al.*[8] due to the higher thermal conductivity.

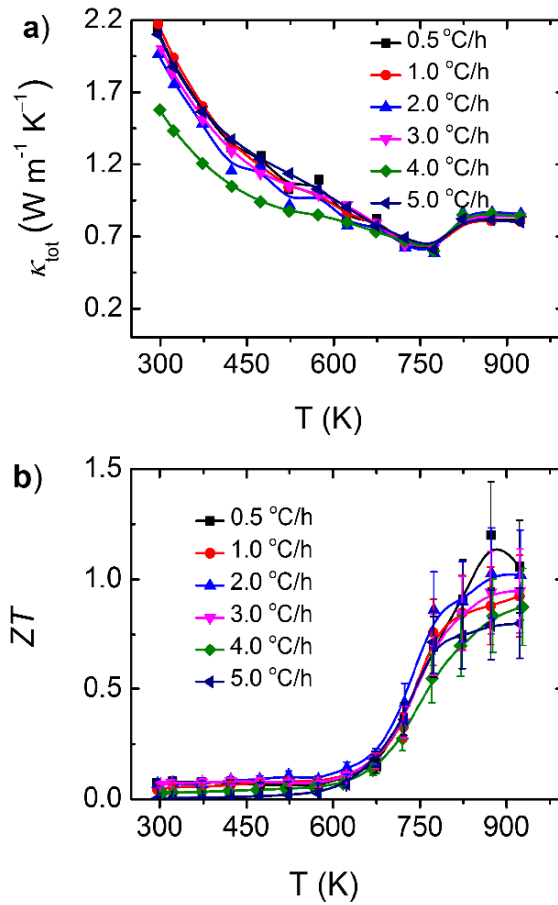


Fig. 4. 7. (a) Thermal conductivity and (b) thermoelectric figure of merit (ZT) as a function of temperature along b-axis for all samples. Thermal conductivities are independent on cooling rate, while thermoelectric figure of merit increased with decreased cooling rate.

4.3.5 Anisotropic thermoelectric transport properties

The temperature dependent electrical conductivities, Seebeck coefficients, PFs , and thermal conductivities along a , b , and c -axes of the best sample at cooling rate of 0.5 °C/h are shown in Fig. 4.8. Anisotropic thermoelectric transport properties were clearly observed. The electrical and thermal conductivities are much higher along b and c -axes than those along a -axis while Seebeck coefficients are nearly crystallographic direction independent. The obtained

highest PF values are much different 2.23, 11.23, and 7.33 $\mu\text{W}\cdot\text{cm}^{-1}\text{K}^{-2}$ at 873 K along a , b , and c -axes, respectively. Figure 4.9 showed the anisotropic of ZT values for this sample. The highest ZT of 1.2 was achieved along b -axis at 873 K, while those along a and c -axes were much smaller 0.55 and 0.71 at 873 K. These anisotropic trends are similar to the data reported by Zhao *et al.*[8].

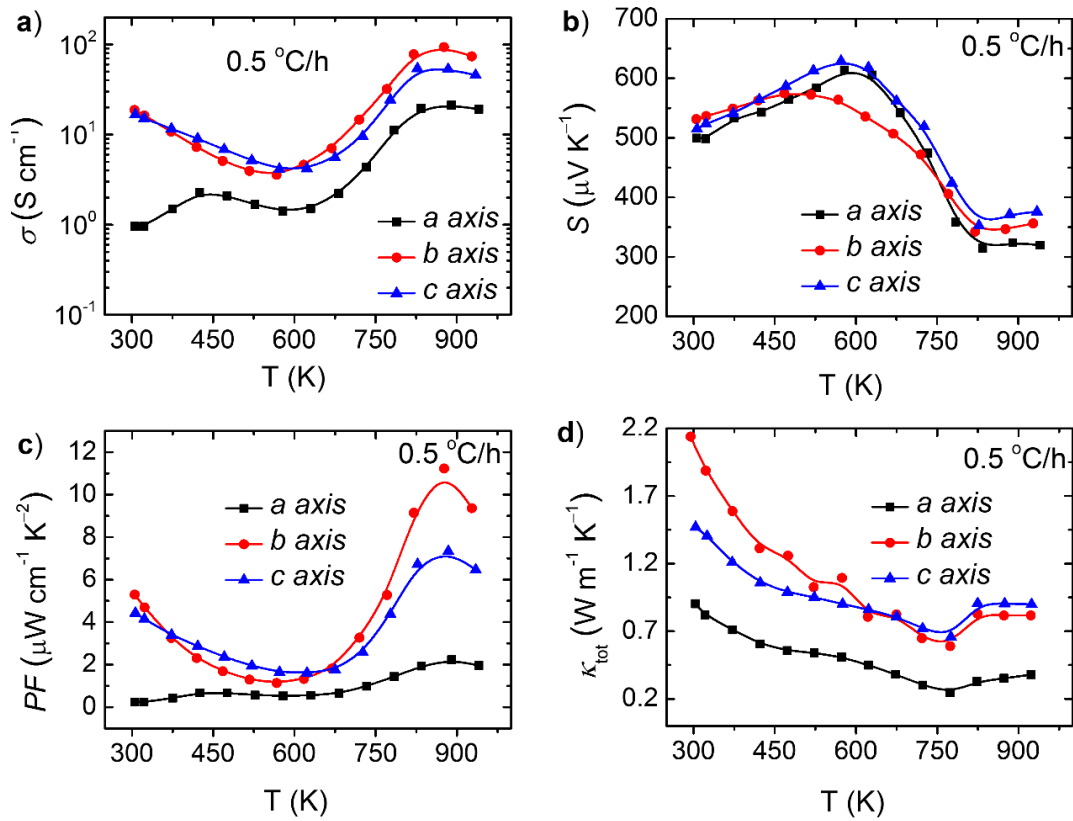


Fig. 4. 8. Anisotropic thermoelectric transport properties of sample 0.5 °C/h. Temperature dependent (a) electrical conductivities, (b) Seebeck coefficients, (c) thermoelectric power factors (PFs), and (d) total thermal conductivities along a , b , and c -axes.

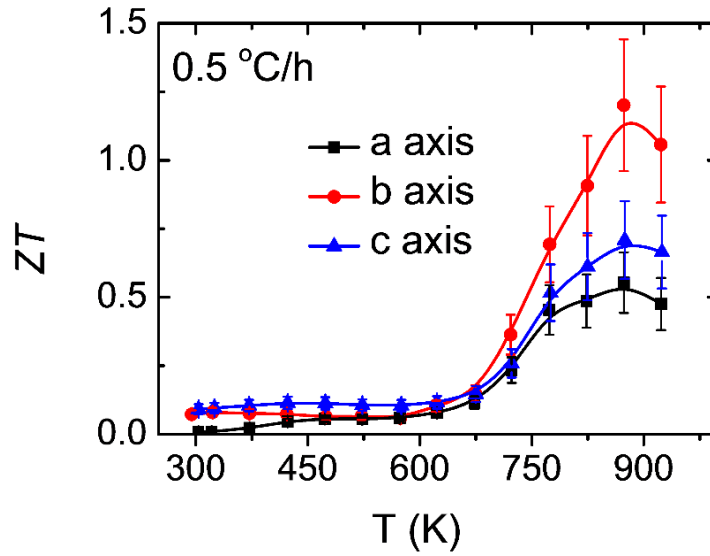


Fig. 4. 9. Anisotropic thermoelectric figure of merit of sample $0.5\text{ }^{\circ}\text{C/h}$. Maximum ZT values are 0.55 , 1.2 , and 0.71 at 873 K along a , b , and c -axes, respectively.

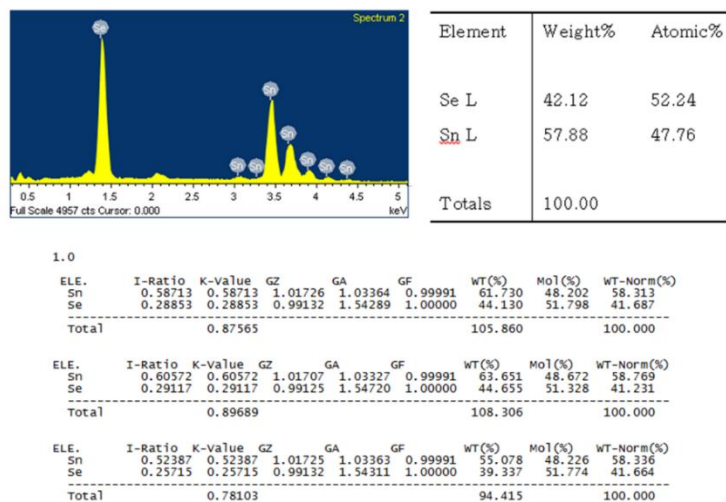
4.4 Conclusion

The p-type semiconductors SnSe with tunable defects were successfully fabricated by temperature gradient technique by changing cooling rate. We observed the increase of defects concentration with cooling rate and a change of dominant defect type from single Sn vacancy in slow cooling samples to multi-vacancies in rapid cooling samples. Different from previous works not only single Sn vacancy but also other defects contributed to the p-type characteristic of SnSe single crystal. Electrical conductivity, Seebeck coefficient, and therefore PF were strongly dependent, while thermal conductivity was not dependent on cooling rate. Small ZT values were achieved due to the high thermal conductivities which are highly attributed to the presence of minority secondary SnSe₂ phase in crystal. The other possible reasons for these high thermal conductivities have also been discussed. In particular, based on the difference in mass density and lattice thermal conductivity of SnSe reported by different groups with a highly possible fluctuation of Sn and Se amounts, a systematically study about thermal

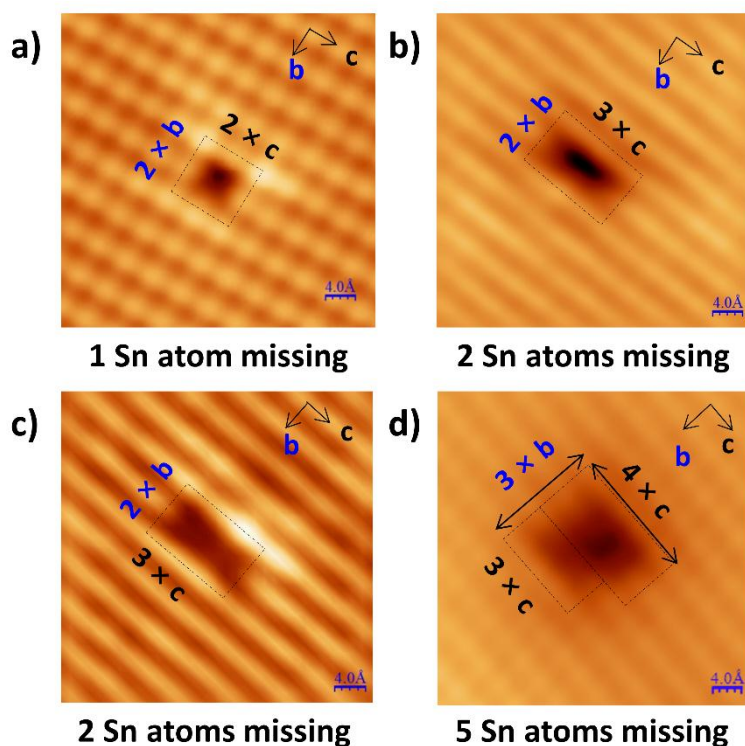
transport properties of SnSe under different growth condition is needed to produce the high ZT SnSe. Also, it is necessary to develop technique to cut not only SnSe samples but also other layered materials without any induced micro-crack or oxidation which helpful to reduce number of variant thermal conductivity studies.

4.5 Supplementary figures

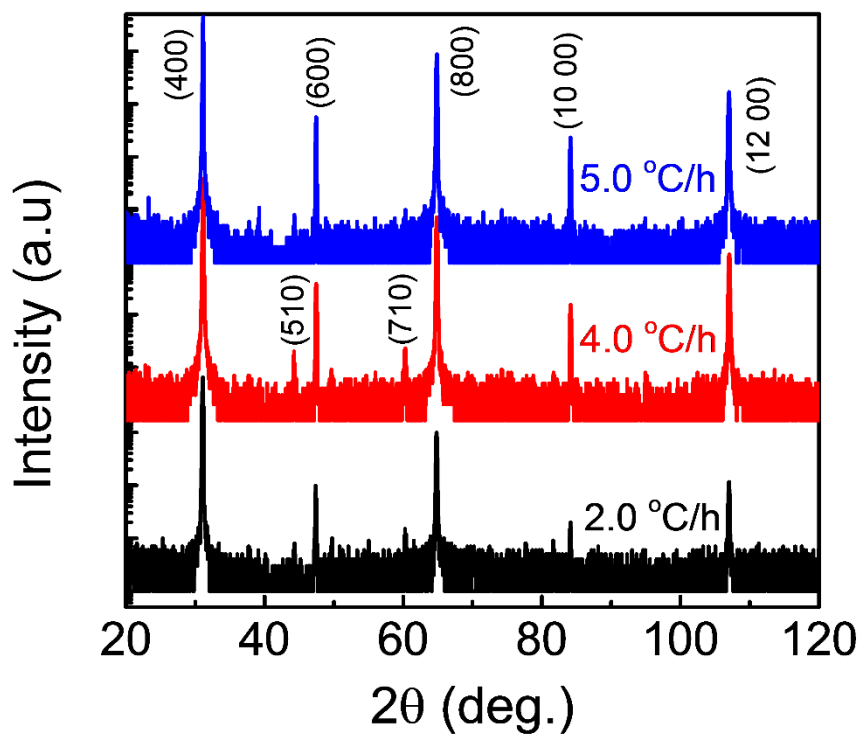
Supplementary Fig. 4. 1. Composition determinations by EDX and EPMA.



Supplementary Fig. 4. 2. STM images showed detail of (a) single Sn vacancy and (b-d) multi-vacancies. Note that only the missing of Sn atoms is visibly to be counted.

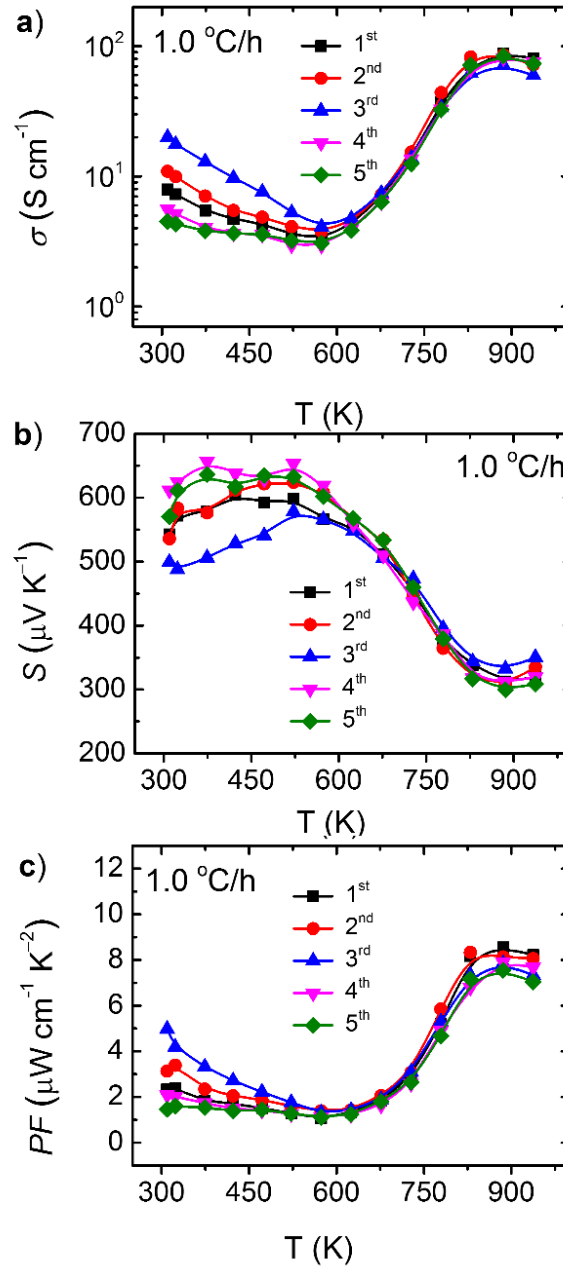


Supplementary Fig. 4. 3. XRD patterns of some samples with different cooling rate, where the extra peaks come from the bending or fragment of layers induced by cleaving process.

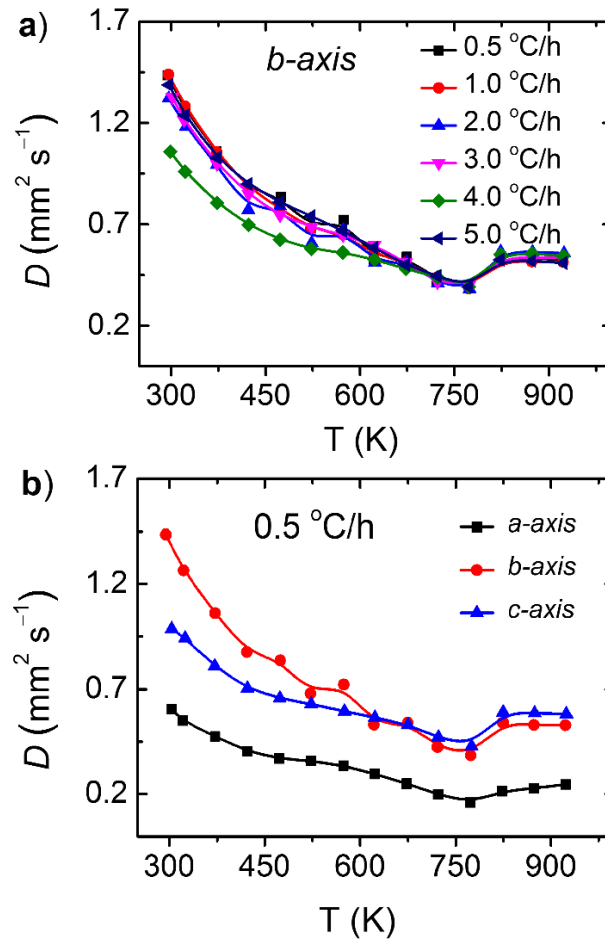


Supplementary Fig. 4. 4. Reproducibility data of sample at cooling rate of 1 °C/h.

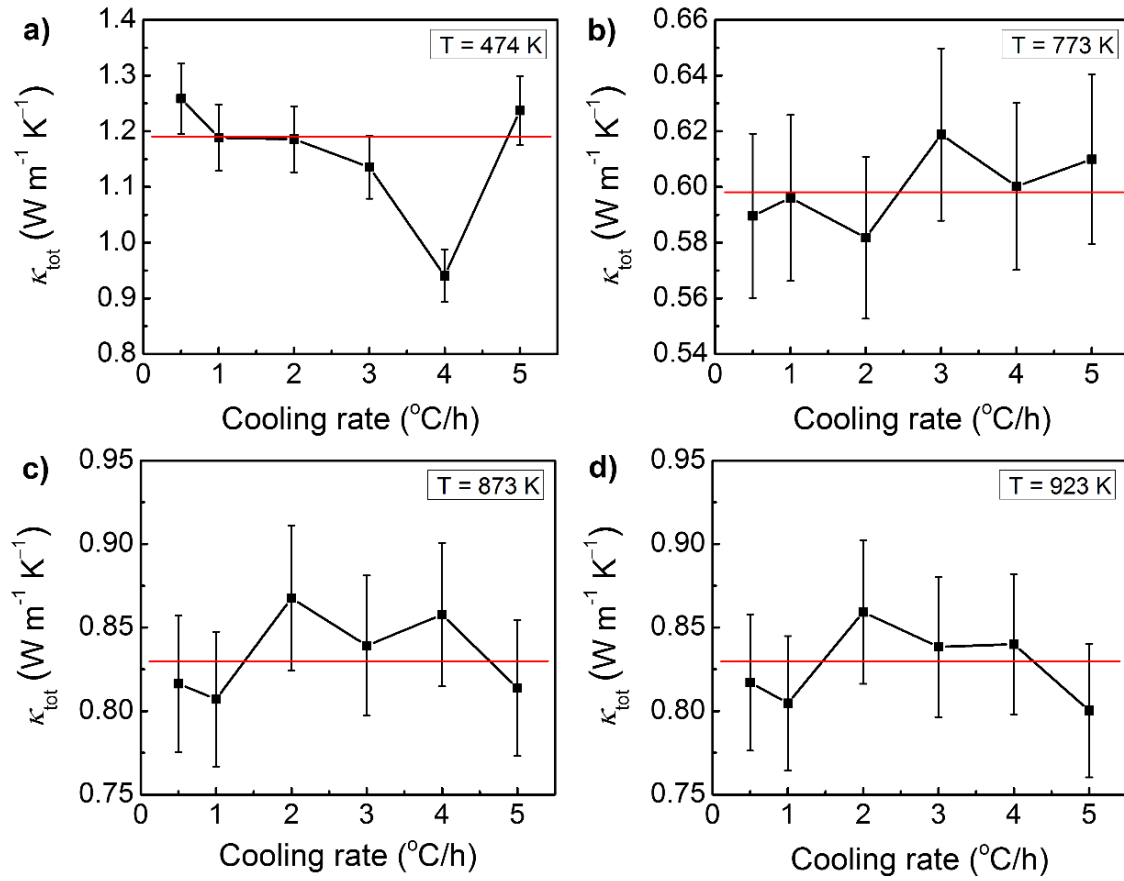
Temperature dependent (a) electrical conductivities, (b) Seebeck coefficients, and (c) PFs obtained from five pieces cut from five different ingots along *b*-axis.



Supplementary Fig. 4. 5. (a) Thermal diffusivity of all samples along *b*-axis and (b) thermal diffusivity of sample at cooling rate of 0.5 °C/h along *a*, *b*, and *c*-axes.



Supplementary Fig. 4. 6. The independence of total thermal conductivity on cooling rate at some critical temperatures.



4.6 References

- [1] S. Sassi, C. Candolfi, J.B. Vaney, V. Ohorodniichuk, P. Masschelein, A. Dauscher, B. Lenoir, Assessment of the thermoelectric performance of polycrystalline p -type SnSe, *Appl. Phys. Lett.* 104 (2014) 0–4. doi:10.1063/1.4880817.
- [2] C.L. Chen, H. Wang, Y.Y. Chen, T. Day, G.J. Snyder, Thermoelectric properties of p-type polycrystalline SnSe doped with Ag, *J. Mater. Chem. A.* 2 (2014) 11171–11176. doi:10.1039/C4TA01643B.
- [3] Q. Zhang, E.K. Chere, J. Sun, F. Cao, K. Dahal, S. Chen, G. Chen, Z. Ren, Studies on Thermoelectric Properties of n-type Polycrystalline SnSe_{1-x}S_x by Iodine Doping, *Adv. Energy Mater.* 5 (2015) 1–8. doi:10.1002/aenm.201500360.
- [4] G. Tang, Q. Wen, T. Yang, Y. Cao, W. Wei, Z. Wang, Z. Zhang, Y. Li, Rock-salt-type nanoprecipitates lead to high thermoelectric performance in undoped polycrystalline SnSe, *RSC Adv.* 7 (2017) 8258–8263. doi:10.1039/C7RA00140A.
- [5] W. Liu, X. Tan, K. Yin, H. Liu, X. Tang, J. Shi, Q. Zhang, C. Uher, Convergence of conduction bands as a means of enhancing thermoelectric performance of n-type Mg₂Si_{1-x}Sn_x solid solutions, *Phys. Rev. Lett.* 108 (2012) 1–5. doi:10.1103/PhysRevLett.108.166601.
- [6] Y. Pei, X. Shi, A. Lalonde, H. Wang, L. Chen, G.J. Snyder, Convergence of electronic bands for high performance bulk thermoelectrics, *Nature.* 473 (2011) 66–69. doi:10.1038/nature09996.
- [7] S.N. Girard, J. He, X. Zhou, D. Shoemaker, C.M. Jaworski, C. Uher, V.P. Dravid, J.P. Heremans, M.G. Kanatzidis, High performance Na-doped PbTe-PbS thermoelectric materials: Electronic density of states modification and shape-controlled nanostructures, *J. Am. Chem.*

Soc. 133 (2011) 16588–16597. doi:10.1021/ja206380h.

[8] L.-D. Zhao, S.-H. Lo, Y. Zhang, H. Sun, G. Tan, C. Uher, C. Wolverton, V.P. Dravid, M.G. Kanatzidis, Ultralow thermal conductivity and high thermoelectric figure of merit in SnSe crystals, *Nature*. 508 (2014) 373–377. doi:10.1038/nature13184.

[9] G. Shi, E. Kioupakis, Quasiparticle band structures and thermoelectric transport properties of p-type SnSe, *J. Appl. Phys.* 117 (2015). doi:10.1063/1.4907805.

[10] S. Lee, K. Esfarjani, T. Luo, J. Zhou, Z. Tian, G. Chen, Resonant bonding leads to low lattice thermal conductivity, *Nat. Commun.* 5 (2014) 1–8. doi:10.1038/ncomms4525.

[11] L. Zhao, G. Tan, S. Hao, J. He, V.P. Dravid, C. Uher, G.J. Snyder, Ultrahigh power factor and thermoelectric performance in hole-doped single-crystal SnSe, *Science* (80-.). 351 (2016) 141–144. doi:10.1126/science.aad3749.

[12] A.T. Duong, V.Q. Nguyen, G. Duvjir, V.T. Duong, S. Kwon, J.Y. Song, J.K. Lee, J.E. Lee, S. Park, T. Min, J. Lee, J. Kim, S. Cho, Achieving $ZT=2.2$ with Bi-doped n-type SnSe single crystals, *Nat. Commun.* 7 (2016) 1–6. doi:10.1038/ncomms13713.

[13] X. Wang, J. Xu, G. Liu, Y. Fu, Z. Liu, X. Tan, H. Shao, H. Jiang, T. Tan, J. Jiang, Optimization of thermoelectric properties in n-type SnSe doped with BiCl₃, *Appl. Phys. Lett.* 108 (2016) 1–6. doi:10.1063/1.4942890.

[14] Y.-M. Han, J. Zhao, M. Zhou, X.-X. Jiang, H.-Q. Leng, L.-F. Li, Thermoelectric performance of SnS and SnS–SnSe solid solution, *J. Mater. Chem. A*. 3 (2015) 4555–4559. doi:10.1039/C4TA06955B.

[15] T.R. Wei, C.F. Wu, X. Zhang, Q. Tan, L. Sun, Y. Pan, J.F. Li, Thermoelectric transport properties of pristine and Na-doped SnSe_{1-x}Te_x polycrystals, *Phys. Chem. Chem. Phys.* 17

(2015) 30102–30109. doi:10.1039/C5CP05510E.

[16] Y. Li, X. Shi, D. Ren, J. Chen, L. Chen, Investigation of the anisotropic thermoelectric properties of oriented polycrystalline SnSe, *Energies*. 8 (2015) 6275–6285. doi:10.3390/en8076275.

[17] S. Chen, K. Cai, W. Zhao, The effect of Te doping on the electronic structure and thermoelectric properties of SnSe, *Phys. B Condens. Matter*. 407 (2012) 4154–4159. doi:10.1016/j.physb.2012.06.041.

[18] J.H. Kim, S. Oh, Y.M. Kim, H.S. So, H. Lee, J.S. Rhyee, S.D. Park, S.J. Kim, Indium substitution effect on thermoelectric and optical properties of $\text{Sn}_{1-x}\text{In}_x\text{Se}$ compounds, *J. Alloys Compd.* 682 (2016) 785–790. doi:10.1016/j.jallcom.2016.04.308.

[19] J.C. Li, D. Li, X.Y. Qin, J. Zhang, Enhanced thermoelectric performance of p-type SnSe doped with Zn, *Scr. Mater.* 126 (2017) 6–10. doi:10.1016/j.scriptamat.2016.08.009.

[20] C. Chang, Q. Tan, Y. Pei, Y. Xiao, X. Zhang, Y.-X. Chen, L. Zheng, S. Gong, J.-F. Li, J. He, L.-D. Zhao, Raising thermoelectric performance of n-type SnSe via Br doping and Pb alloying, *RSC Adv.* 6 (2016) 98216–98220. doi:10.1039/C6RA21884A.

[21] G. Duvjir, T. Min, T. Thi Ly, T. Kim, A.T. Duong, S. Cho, S.H. Rhim, J. Lee, J. Kim, Origin of p-type characteristics in a SnSe single crystal, *Appl. Phys. Lett.* 110 (2017). doi:10.1063/1.4991003.

[22] D. Ibrahim, J.B. Vaney, S. Sassi, C. Candolfi, V. Ohorodniichuk, P. Levinsky, C. Semprinoschnig, A. Dauscher, B. Lenoir, Reinvestigation of the thermal properties of single-crystalline SnSe, *Appl. Phys. Lett.* 110 (2017). doi:10.1063/1.4974348.

[23] Q. Tan, L.-D. Zhao, J.-F. Li, C.-F. Wu, T.-R. Wei, Z.-B. Xing, M.G. Kanatzidis,

Thermoelectrics with earth abundant elements: low thermal conductivity and high thermopower in doped SnS, *J. Mater. Chem. A.* 2 (2014) 17302–17306. doi:10.1039/C4TA04462B.

[24] G. Tan, F. Shi, S. Hao, H. Chi, L.D. Zhao, C. Uher, C. Wolverton, V.P. Dravid, M.G. Kanatzidis, Codoping in SnTe: Enhancement of thermoelectric performance through synergy of resonance levels and band convergence, *J. Am. Chem. Soc.* 137 (2015) 5100–5112. doi:10.1021/jacs.5b00837.

[25] K. Peng, X. Lu, H. Zhan, S. Hui, X. Tang, G. Wang, J. Dai, C. Uher, G. Wang, X. Zhou, Broad temperature plateau for high ZT s in heavily doped p-type SnSe single crystals, *Energy Environ. Sci.* 9 (2016) 454–460. doi:10.1039/C5EE03366G.

[26] D.P. Spitzer, Lattice thermal conductivity of semiconductors: A chemical bond approach, *J. Phys. Chem. Solids.* 31 (1970) 19–40. doi:10.1016/0022-3697(70)90284-2.

[27] J.D. Wasscher, W. Albers, C. Haas, Simple evaluation of the maximum thermoelectric figure of merit, with application to mixed crystals $\text{SnS}_{1-x}\text{Se}_x$, *Solid State Electron.* 6 (1963) 261–264. doi:10.1016/0038-1101(63)90083-2.

[28] M. Jin, H. Shao, H. Hu, D. Li, J. Xu, G. Liu, H. Shen, J. Xu, H. Jiang, J. Jiang, Single crystal growth of $\text{Sn}_{0.97}\text{Ag}_{0.03}\text{Se}$ by a novel horizontal Bridgman method and its thermoelectric properties, *J. Cryst. Growth.* 460 (2017) 112–116. doi:10.1016/j.jcrysgro.2016.12.087.

[29] S. Sassi, C. Candolfi, J.B. Vaney, V. Ohorodniichuk, P. Masschelein, A. Dauscher, B. Lenoir, *Mater. Today Proc.* 2 (2015) 690–698. doi:10.1016/j.matpr.2015.05.093.

[30] L.-D. Zhao, C. Chang, G. Tan, M.G. Kanatzidis, *Energy Environ. Sci.* 9 (2016) 3044–3060. doi:10.1039/C6EE01755J.

**CHAPTER 5: LAYERS' ROTATION AND
THERMOELECTRIC TRANSPORT PROPERTIES OF SnSe
EPITAXIAL THIN FILMS
(TO BE SUBMITTED)**

We have investigated the effects of Se/Sn flux ratio on the growth and thermoelectric transport properties of (h00) oriented SnSe thin films on MgO (100) substrate using MBE. All films were epitaxially grown at 294 °C with various Se/Sn flux ratios of 0.8, 0.9, 1, 3, 5, and 7. The crystal structure of the obtained SnSe thin films was orthorhombic (Pnma space group) with a-axis (h00) orientation. We observed a rotation of layers in our samples. A bi-layer structure consists of 0° and 90° rotated layers was observed in sample with Se/Sn ratios of 0.8, 0.9, and 1, while additional 45° rotated layers were simultaneously observed in samples with higher Se/Sn ratio of 3, 5 and 7. Especially, 135° rotated layers were observed in sample with Se/Sn ratio of 7. Interestingly, the best crystalline film was obtained at the Se/Sn ratio of 1. Thermoelectric and transport properties of films were also strongly affected by the flux ratio. The highest power factor, $8.51 \mu\text{W cm}^{-1} \text{K}^{-2}$ was obtained at 650 K in sample at flux ratio of 0.8. TEM images showed very good crystallinity in consistent with the high resistivity. Our results suggest a possibility to reduce thermal conductivity of SnSe thin film along a-axis by the layer's rotations.

5.1 Introduction

SnSe is an orthorhombic layered semiconductor with the layered stacking along a-axis. It has been studied for widely applications such as electronic devices due to the high hole's mobility or as active layer for optoelectronic devices. [1] At 750 K, SnSe occurs a structure transition

from Pnma to Cmc_m. Low temperature orthorhombic Pnma SnSe phase ($a = 11.490 \text{ \AA}$, $b = 4.440 \text{ \AA}$, and $c = 4.135 \text{ \AA}$) has an indirect band gap $E_g = 0.86\text{-}1 \text{ eV}$ at 300 K and high temperature Cmc_m phase has a direct band gap $E_g = 0.464 \text{ eV}$. [2, 3, 4] Recently, p-type SnSe has received considerable attention on thermoelectricity due to its very high $ZT = 2.6$ at 923 K in single crystal. [5] In the recent work, we have reported the $ZT = 2.2$ in Bi-doped n-type SnSe single crystal at 733 K. [6] These high ZT values of SnSe are mainly assigned to its low lattice thermal conductivity due to resonance bonding which causes optical phonon softening, strong anharmonic scattering and large phase space for three-phonon scattering processes. [7]

In thin film form, SnSe has been studied for many applications such as memory switching devices, cathode materials in lithium intercalation, batteries, sensor, laser materials, thin film polarizer, optoelectronic, photovoltaic devices and candidates for solar cell applications. [8, 9] A systematically study about effect of substrate on the growth of SnSe epitaxial thin film has been reported. [1] However, there was no report about thermoelectric transport properties of SnSe epitaxial thin films. Chemical vapor deposition, [8] spray pyrolysis technique, [9] electro-deposition, flash evaporation, [10] solid state reactions, [11] thermal evaporation, [12] pulse laser deposition, [1, 13, 14] and molecular beam epitaxy [15] techniques have been used to grow SnSe thin films.

Considering its thin film applications, we need to address and control the defects in SnSe, which is common issue in 2D layered materials. Recently, we carried out microscopic study on un-doped (p-type) and Bi-doped (n-type) SnSe using low temperature scanning tunneling microscope (STM) operated at 79 K under ultra-high vacuum environment ($< 10^{-11}$ Torr). Sn and Se vacancies are widely distributed, indicating that only Sn vacancies are dominant p-type native defects in SnSe. [16] On the other hand, Se is a high vapor pressure element like S and

Te. Generally speaking, we sublimate more S or Se than other elements during the growth. Therefore, a systematic study about the influence of Se/Sn flux ratio to the growth and thermoelectric transport properties of SnSe thin film is needed. Molecular beam epitaxy (MBE) is one of the best choices for this purpose where the evaporation rate of material can be easily controlled by effusion cell and monitored by thickness monitor and the film can be grown at quite low temperature and low deposition rate.

Here, we report on systematic study about the influence of Se/Sn flux ratio to the growth and thermoelectric transport properties of SnSe thin film on MgO (100) substrate. We found that all films were epitaxially grown with various Se/Sn flux ratios of 0.8, 0.9, 1, 3, 5, and 7. The 0° , 45° , 90° , and 135° rotated layers were observed in our samples. Thermoelectric transport properties of the films were strongly affected by Se/Sn flux ratio. We achieved high power factor value; $8.51 \mu\text{W cm}^{-1} \text{K}^{-2}$ at 650 K in sample at flux ratio of 0.8 which is 2.84 times larger than that of bulk. Interestingly, the best crystalline film was obtained at the flux ratio of 1 with a 90° rotated bi-layer structure. The rotations of layers may a very important manner to optimize thermoelectric properties of not only SnSe but also of any layered materials thin films.

5.2 Experiment

SnSe thin films were epitaxially grown on MgO (100) substrates by MBE. We considered MgO as substrate for SnSe growth because the lattice constants of MgO ($a = 4.219 \text{ \AA}$) is quite close to those of orthorhombic SnSe ($a = 11.490 \text{ \AA}$, $b = 4.440 \text{ \AA}$, $c = 4.135 \text{ \AA}$). The corresponding lattice mismatches are 9.2%, -5.0%, and 2.0% along a , b , and c -axis, respectively. The cleaned MgO (100) substrate was loaded into the vacuum chamber and pre-heating at 600°C for 30 minutes in ultra-high vacuum in order to remove the residual impurities. After that the substrate was cooled down to 294°C , which was experimentally determined for epitaxial SnSe growth.

The base pressure of the growth chamber was $\sim 10^{-10}$ Torr. The films were grown by the co-deposition of Sn and Se using effusion cells. The evaporation rates of Sn and Se were independently determined using a quartz crystal thickness monitor. The thickness of SnSe thin films was 200 nm. Six films were grown with different Se/Sn flux ratio of 0.8, 0.9, 1, 3, 5, and 7. The detail of deposition rates and times are shown in table 5.1.

Table 5. 1. The detail of deposition rates of Sn and Se elements, growth rates and times of SnSe samples.

Se/Sn flux ratio	Rate Se ($\text{\AA}/\text{s}$)	Rate Sn ($\text{\AA}/\text{s}$)	SnSe growth rate ($\text{\AA}/\text{s}$)	SnSe growth time (s)
0.8	0.16	0.2	0.32	6250
0.9	0.18	0.2	0.36	5555
1	0.22	0.22	0.44	4545
3	0.5	0.17	0.34	5882
5	0.5	0.1	0.2	10000
7	0.5	0.07	0.14	14286

The quality of the substrate and the films was monitored by in-situ reflection high energy electron diffraction (RHEED). The crystal structure of the samples was characterized by Raman scattering and X-ray diffraction (XRD) measurements. The crystallinity was evaluated by XRD ω -scans. We used XRD Φ -scan to confirm the stacking of the films on substrate. Optical band gap of film was determined using UV-Vis absorption spectra. Transmission electron microscopy (TEM) was employed to visualize the cross-sectional structure of thin films. Electrical resistivities were measured using four-probe Van de Pauw method. Seebeck coefficients were measured by differential method. The thermal voltage was measured by

creating a small gradient temperature along sample. The relation between ΔV and ΔT was $\Delta V = S\Delta T$, where the higher order of ΔT was ignored. The Seebeck coefficient was determined from the slope of linear part of ΔV vs. ΔT curve. Power factor was calculated by multiply electrical conductivity with square Seebeck coefficient.

The SnSe single crystal was grown by temperature gradient technique which is described elsewhere. [6]

5.3 Results

The RHEED patterns of MgO substrate along [001] azimuth and SnSe thin films with various Se/Sn flux ratio are shown in Fig. 5.1. The cleaned MgO (100) substrate after pre-heating showed a streaky RHEED pattern, indicating the clean and flat surface as shown in the inset of Fig. 5.1(a). For SnSe thin films, at the first few minutes, the patterns were smeared out from those of substrate, after that the lines appeared, and finally we recorded the patterns at the end of the growth (Fig. 5.1). All RHEED patterns indicated the epitaxial growth of our samples without any surface reconstruction. However, the flux ratio strongly affects to the film's growth mode. Streaky RHEED patterns were observed in samples with flux ratio of 0.8, 0.9, 1, 3, and 5, indicating the 2D layer-by-layer growth mode. Among them, better streaky patterns were obtained in samples with flux ratio of 0.8, 0.9, 1 and 3, indicating smooth surfaces. While, weak ring pattern was observed in the sample with flux ratio of 7, indicating the rough film surface. Note that the RHEED pattern of polycrystalline films is sharp and strong rings.

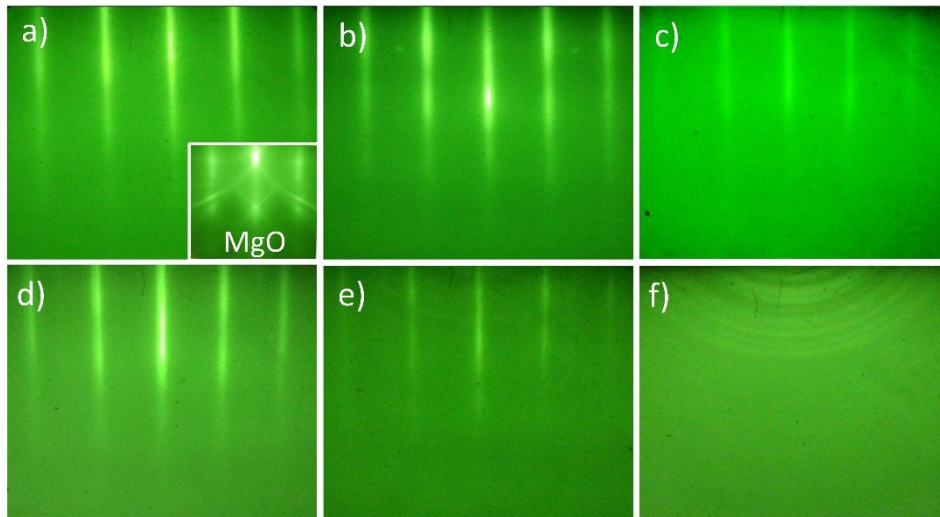


Fig. 5. 1. RHEED patterns along [001] azimuth of SnSe thin film with various flux ratio Se/Sn of (a) 0.8; (b) 0.9; (c) 1; (d) 3; (e) 5; and (f) 7. The inset of (a) is that of MgO (100) substrate after preheating. Streaky RHEED patterns were obtained indicating the epitaxial growths with very smooth surfaces, except the sample with flux ratio of 7.

The out-of-plane θ - 2θ scan X-ray diffraction patterns of the films and SnSe single crystal grown by temperature gradient method are shown in Fig 5.2(a). The patterns show only (h00) peaks of SnSe and MgO substrate. All diffraction peaks of SnSe can be indexed based on the orthorhombic (Pnma space group). The a-axis lattice constant calculated using (400) peaks is 11.52 Å for all samples. Compared to that of single crystal 11.50 Å our films exhibited a slight compressive strain 0.17%. No any secondary phases were observed, indicating the indeed SnSe stoichiometry of our films which was also confirmed by electron probe microscopic analysis (EPMA) and Raman spectra (supplementary Fig 5.1). Now we discuss about the growth and orientation of the films. In general, it is possible to grow a film on a substrate when the lattice mismatch between them is smaller than 10%. According to the lattice mismatches calculated in the experimental section, there are three possible ways for SnSe to grow on MgO (100) substrate in; (ab), (ac), and (bc) planes. The smallest lattice mismatch plane is (bc) plane. Thus, the samples prefer to grow with the (bc) plane on MgO (100), leading to a-axis orientation,

which is usually advantageous for electronic device applications.

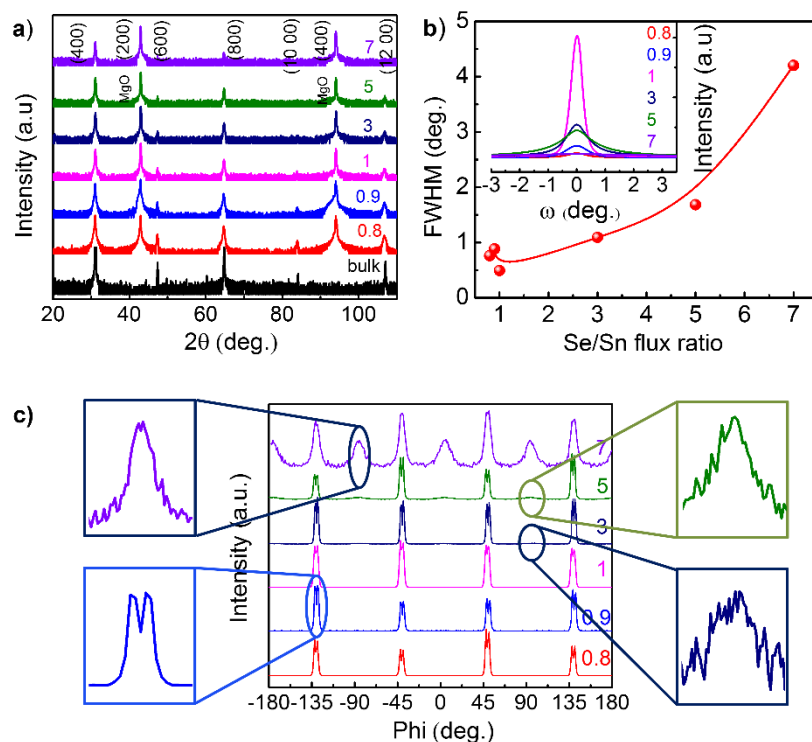


Fig. 5. 2. (a) X-ray diffraction patterns of SnSe/MgO (100) thin films and SnSe single crystal.

The calculated average a-axis lattice constants are the same 11.52 Å for all thin film, and 11.50 Å for bulk. (b) Se/Sn flux ratio dependent FWHM fitted from XRD omega scan curves for symmetrical (400) reflection of all samples. The inset is the corresponding rocking curves. (c) Φ -scan using (111) plane of all films in linear scale. The insets are magnified of the splitting peaks in linear scale (left) and of the small peaks in log scale (right).

In order to investigate the influence of Se/Sn flux ratio to the crystallinity of samples, we performed the XRD ω -scan at (400) position. Full width at half maximum (FWHM) of rocking curves as a function of Se/Sn flux ratio is shown in Fig 5.2(b). The inset figure shows the rocking curves of all samples. It is cleared that the higher Se rate shows the broader of the peak, indicating the poorer crystallinity. The sample with flux ratio of 1 exhibits the sharpest peak, indicating the nearly parallel arrangement of atomic planes, i.e., the highest crystallinity film.

The lowest crystallinity is observed in sample with flux ratio of 7 due to its biggest FWHM, which is consistent with the RHEED patterns.

Figure 5.2(c) represents a 360° Φ -scan (azimuth scan - in linear scale) with $2\theta = 30.4541^\circ$ (the SnSe (111) Bragg angle) and the scattering vector titled $\chi = 75.2218^\circ$ (the (400) vs (111) inter-planar angle) in the diffraction plane with respect to the surface normal. For all samples, the Φ -scan patterns show 4 major peaks. Each peak is split in to two peaks with an interval of about 3σ (see the inset (bottom left)). Interestingly, in the samples at Se/Sn flux ratios of 3, 5, and 7, we observed additional peaks with much smaller intensity, located at interstitial positions between the major peaks (see the insets (right) - in log scale). Especially, in sample at flux ratio of 7, these additional peaks are also split in to two peaks (see the inset (top left)).

To interpret the Φ -scan data, we take schematic illustrations of the Φ -scan measurement as shown in Fig 5.3. Figure 5.3(a) shows the processes of the Φ -scan measurement for orthorhombic SnSe using (111) plane. The XRD Φ -scan data provide us the in-plane orientation of the sample. During the measurement, the sample is rotated about the axis perpendicular to the sample's surface (Φ -axis), therefore, the crystalline planes, parallel to the surface will provide a straight line in the Φ -scan pattern. Due to this reason, we must choose a plane inclined with respect to the surface and rotate the sample around the axis perpendicular to the surface, here we chose (111) plane. The important task here is finding out the right diffraction conditions (idea position) for the (111) plane. Note that, the conditions of diffraction are the Braggs condition ($2d\sin\theta = \lambda$) and that the diffraction plane has to perpendicular to the crystal plane. The processes of the Φ -scan measurement are follow. First, we find out the idea position for the (100) plane (we use this plane in the schematic illustration due to it belong to the same family with the (400) plane) by fixing the Φ angle, varying the θ , χ , and ω angles until

get the diffraction peak from (100) plane (Fig 5.3(a) left). Second, we set the $2\theta = 30.4541^\circ$ (the SnSe (111) Bragg angle). And then, the sample is tilted from the original sample's surface by an angle of 75.2218° (Fig 5.3(b) right). Finally, we fix all the angles and rotate the sample around Φ -axis (perpendicular to the current sample's surface) until we get the diffraction peak from (111) plane. Continue to rotate the sample about the Φ -axis, we get a set of four Φ -scan peaks. Figure 5.3(b) shows the simulation and experimental Φ -scan peaks for SnSe single crystal. The intervals are about 94° between the first and the third peaks and about 86° between the second and the fourth peak due to the two-fold symmetry of orthorhombic crystal. Note that, these angles may slightly different in strained films due to the lattice constants are slightly changed.

Now we turn to interpret the splitting peaks in the Φ -scan data. The splitting of the peaks can be explained by the rotation of layers. By this argument, the splitting of the major peaks is due to the presence of bi-layer structure. This bi-layer structure consists of the first layers (0° rotated layers) and the second layers, rotated 90° with respect to the first layers (90° rotated layers). These layers provide their own set of four peaks with the interchange intervals, i.e., $94^\circ - 86^\circ - 94^\circ$ and $86^\circ - 94^\circ - 86^\circ$. The sum of these peaks results in the splitting peaks, as illustrated in Fig 5.3(c). Similarly, the observations of the additional peaks located at interstitial positions between major peaks in sample at flux ratio of 3, 5, and 7 represent the existence of 45° rotated layers with respect to the 0° rotated layers in these samples. Finally, the splitting of these additional peaks in sample at flux ratio of 7 represents the existence of 90° rotated layers with respect to the 45° rotated layers (i.e., 135° rotated with respect to the 0° layers). Similar explanation is applied for these layer's rotations. The rotation of layers is a very important observation which is expected to reduce thermal conductivity of SnSe.

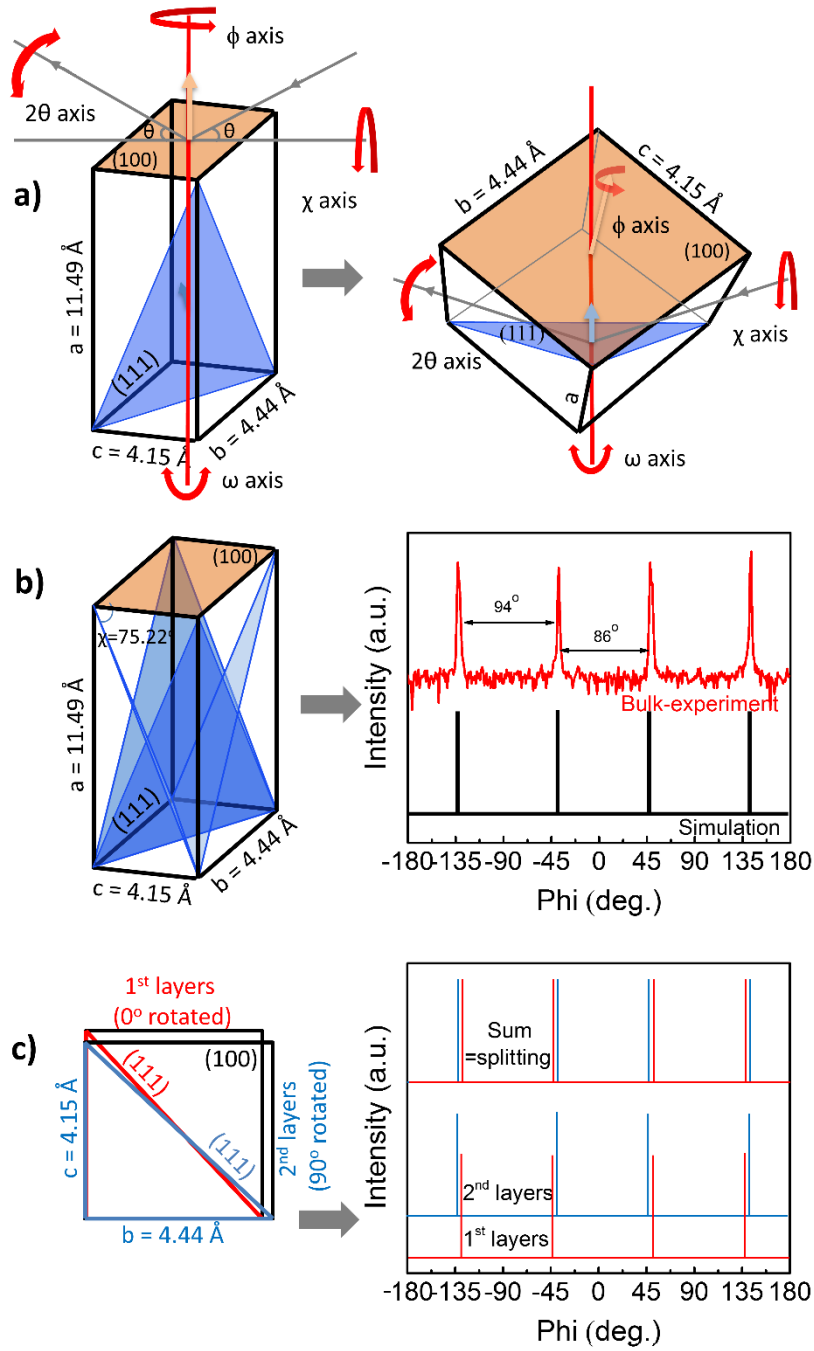


Fig. 5. 3. (a) Φ -scan using (111) plane of orthorhombic SnSe measurement processes. (b) simulation and experimental Φ -scan peaks of SnSe single crystal using (111) plane. (c) Simulation Φ -scan peaks of SnSe single crystal in case of 0° and 90° rotated layers.

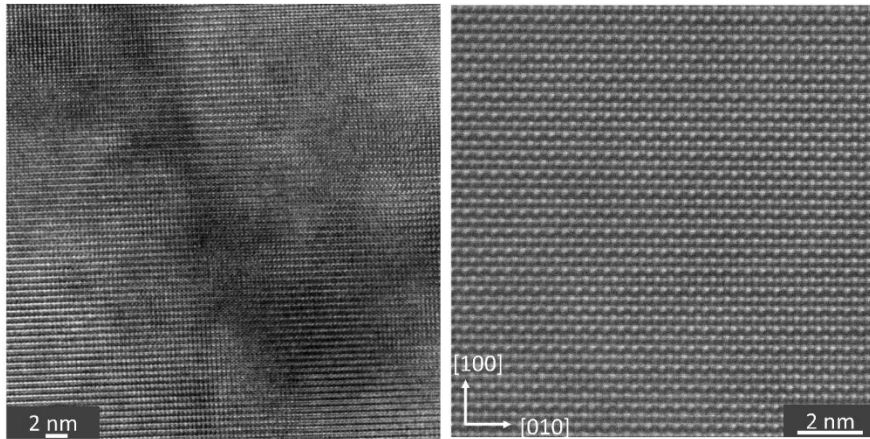


Fig. 5. 4. Cross-sectional TEM images of samples at $Se/Sn = 3$ in large scale (left) and magnified (right). The average lattice constants were $a = 11.8 \text{ \AA}$ and $b = 4.4 \text{ \AA}$.

To visualize the rotations of layers in the films, we took the TEM cross-sectional images cut along (001) plane for samples with flux ratio of 3 which consists of 0° , 45° , and 90° rotated layers, as shown in Fig 5.4. The cross sectional was created by focused ion beam (FIB) with in-situ lift-out technique. The TEM image shows very high crystallinity SnSe crystal. The average lattice constants obtained from TEM image are $a = 11.80 \text{ \AA}$ and $b = 4.40 \text{ \AA}$, in agreement with those from XRD data. Unfortunately, we could not see the sign of layer's rotations in the image. There are reasons for this problem. First, the atomic arrangement between 0° and 90° rotated layers is the same Sn-Se-Sn-Se with the distance between Sn(Se) atoms is b or c . The very close values of b and c -axes lattice constants make them hard to be distinguished. Note that, the b and c -axes lattice constants in strain films on a cubic substrate should have closer value than in bulk. Second, the atomic arrangement in 45° rotated layers is Sn-Sn-Se-Se-Sn-Sn-Se-Se. Therefore, the sign of 45° rotated layers is possible to be distinguished from 0° and 90° rotated layers. However, we might miss the sign of 45° rotated layers due to the much dominance of other rotated layers (0° and 90°) in the sample.

The rotations of layers strongly affect to the thermoelectric transport properties of our films as shown in as shown in Fig. 5.5. Temperature dependent electrical resistivity curves of all films are shown in Fig. 5.5(a). A semiconducting behavior was observed in all films. Crossovers were observed at 540 K and 668 K in sample with flux ratio of 1, as shown in the inset of Fig. 5.5(a), reproducible as shown in supplementary Fig 5.3, indicating the existence of at least two types of defects located at different energy levels in this sample. The defects' energy levels in semiconductors can be estimated from activation energies which are determined from the slopes of $\ln\rho$ vs $10^3/T$ curves as shown in Fig. 5.5(b), based on the formula for temperature dependent resistivity of semiconductors:

$$\rho = \rho_0 e^{\frac{E_A}{k_B T}} \quad (1)$$

where, E_A is activation energy, k_B is Boltzmann constant, and T is absolute temperature. The calculated activation energy values are about 0.19, 0.21, 0.31, 0.14, 0.21, 0.28 eV for samples with Se/Sn flux ratio of 0.8, 0.9, 1, 3, 5, and 7 at low temperature part, respectively. These large values of activation energy indicated the deep defect's energy levels in our films in consistent with the high crystallinity shown in rocking curves and TEM image. In overall, the activation energy decreases with decrease crystallinity and reflects the order of resistivity. The highest activation energy is found in sample with flux ratio of 1 in consistent with its highest crystallinity. Interestingly, the activation energy reaches the lowest value in sample with flux ratio of 3 and then increases again in samples with flux ratio of 5 and 7. Note that according to our previous work the main source of p-type characteristic of SnSe is single Sn vacancy. [16] This behavior may due to the increase single Sn vacancy concentration in the sample with flux ratio of 3 (under Se rich condition). Exert Se amounts induce more layers' rotations (reduce crystallinity) but reduce single Sn vacancy concentration (larger vacancies may be

energetically formed) leading to increase electrical resistivity in the samples with flux ratio of 5 and 7.

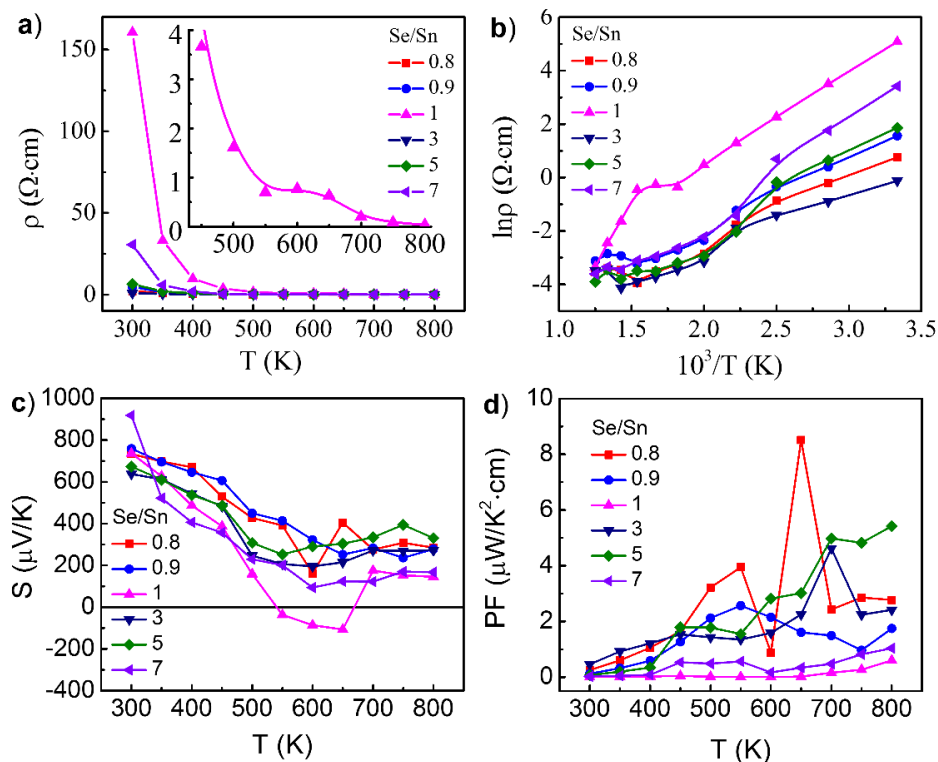


Fig. 5.5. (a) Temperature dependent resistivity, (b) the plot of $\ln\rho$ vs $10^3/T$, (c) and (d) temperature dependent Seebeck coefficient and power factor of all samples.

Figure 5.5(c) shows the temperature dependent Seebeck coefficient of our samples. As shown in the figure, Seebeck coefficient decreased with temperature, indicating bipolar transport in our sample. This bipolar transport occurs from room temperature, which is earlier than bulk above 525 K [5]. This behavior once again affirms that defects (acceptor) in our samples are located at deeper energy levels, leading to higher Fermi level from valence band edge than those in bulk. Especially, temperature dependent Seebeck coefficient curve of samples with flux ratio of 1 showed a p to n-type transition at about 540 K after that it showed an n to p-type transition again at 668 K. This p-n-p type transition is consistent with the change of its

resistivity in three temperature regions, mentioned above. The first transition from p to n-type is assigned to the bipolar transport. In bipolar transport regime, Seebeck coefficient is contributed by electrons and holes and can be calculated by the following formula

$$S = \frac{p\mu_p S_p - n\mu_n S_n}{n\mu_n + p\mu_p} \quad (2)$$

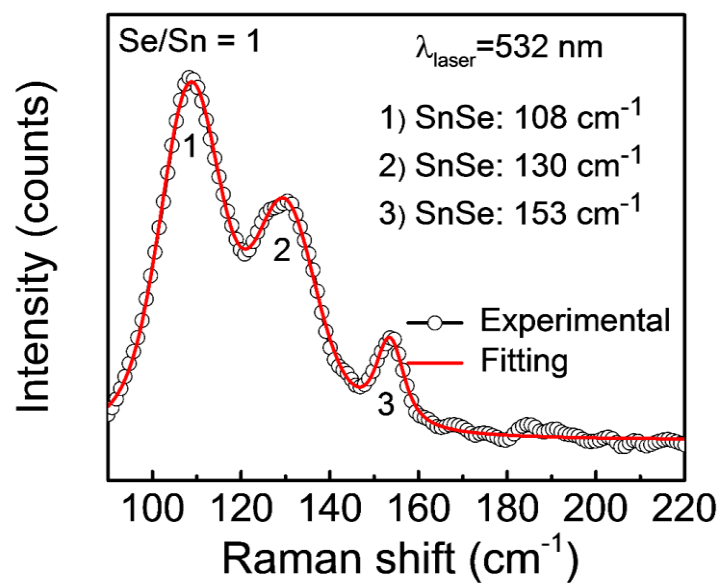
where, p and n are hole and electron concentration, μ_p and μ_n are hole and electron mobility, S_p and S_n are contribution of hole and electron to Seebeck coefficient, respectively. Due to the increase probability of electron in conduction band the electron concentration increases with higher mobility than hole. The contribution of electron to Seebeck coefficient is dominant, negative Seebeck coefficient (n-type) is achieved. However, as temperature continuously increased, holes are generated from deeper energy level defects. This make the hole contribution to Seebeck coefficient increased and become dominant albeit the bipolar transport also increased with temperature, leading to the second n- to p-type transition at 668 K. Temperature dependence of thermoelectric power factor (PF) is shown in Fig. 5.5(d). PF values of thin films are smaller than those of bulk due to the high electrical resistivity. Maximum PF value of $8.51 \mu\text{W cm}^{-1} \text{K}^{-2}$ is achieved in the sample with flux ratio of 0.8 at 650 K which is 2.84 times larger than that of bulk. This data is reproducible as shown in supplementary Fig. 5.2. Our results addressed optimum growth condition for SnSe thermoelectric thin film with high PF at moderate temperature range. With the rotations of layers, we expect that thermal conductivity of sample also significantly reduced.

5.4 Conclusion

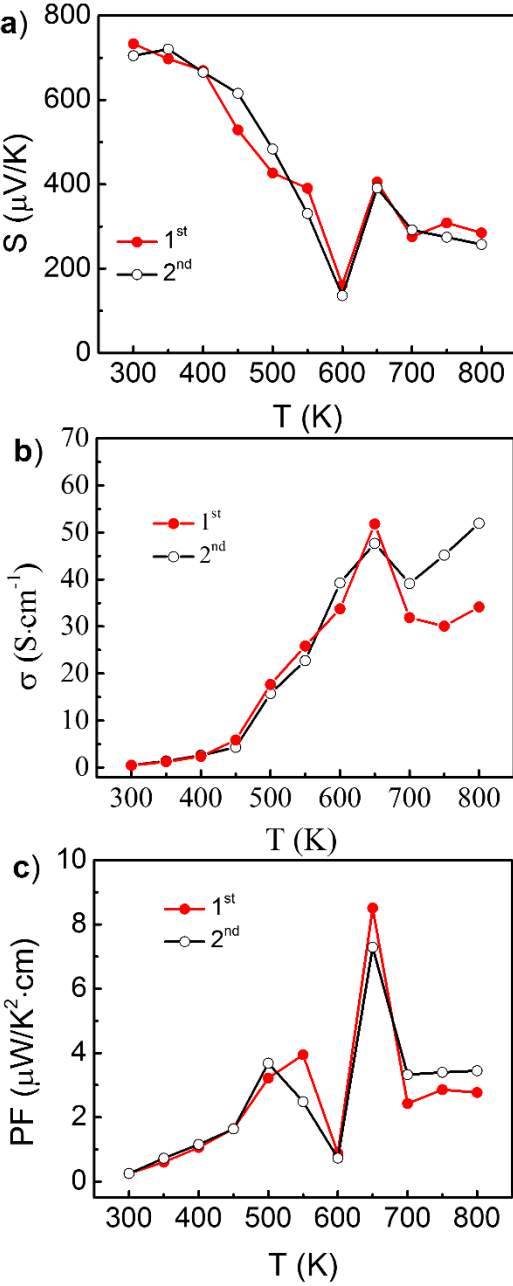
In conclusion, we have reported on the influence of Se/Sn flux ratio to the growth and thermoelectric transport properties of (h00) oriented SnSe thin films on MgO (100) substrate using MBE. All films were epitaxially grown at 294 °C with Se/Sn flux ratios of 0.8, 0.9, 1, 3, 5, and 7 with orthorhombic crystal structure. The best crystallinity was achieved in sample with flux ratio of 1. We observed a 90° rotated domain in all samples. Beside that a second 45° rotated domain was observed sample with flux ratio of 5 and 7 while a third 135° rotated domain was observed only in sample with flux ratio of 7. Sample at flux ratio of 0.8 was expected to have good thermoelectric performance due to its high power-factor value; $0.851 \mu\text{W cm}^{-1} \text{K}^{-2}$ at 650 K. Our results also suggest a possibly to reduce thermal conductivity of SnSe along *a*-axis by controlling layer's orientation.

5.5 Supplementary figures

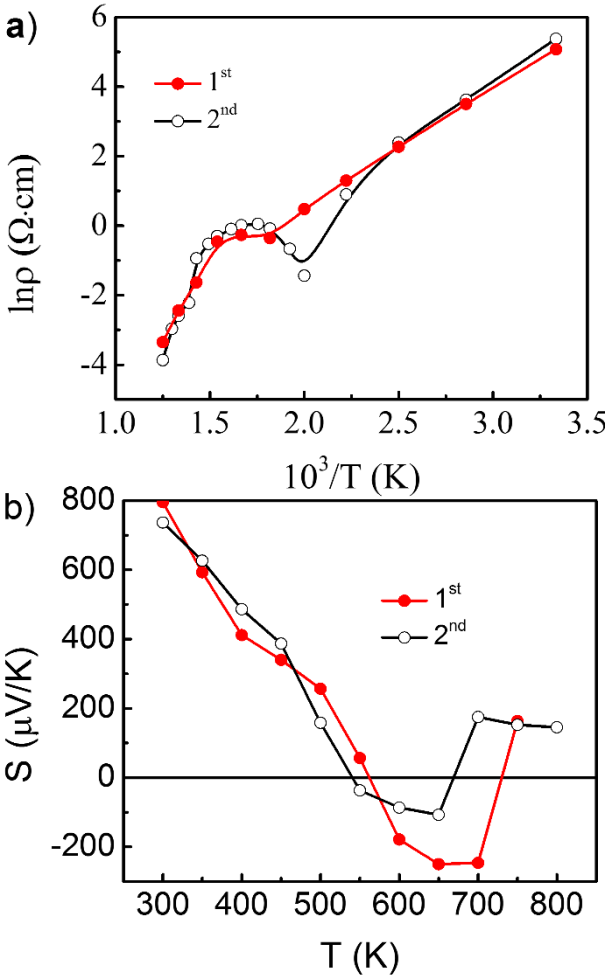
Supplementary Fig. 5. 1. Room temperature raman spectra of SnSe/MgO (100) thin films with flux ratio of 1. There are 3 raman peaks at 108 cm^{-1} corresponds to B_{3g} mode, 130, and 153 cm^{-1} correspond to A_g modes. No secondary phases were observed.



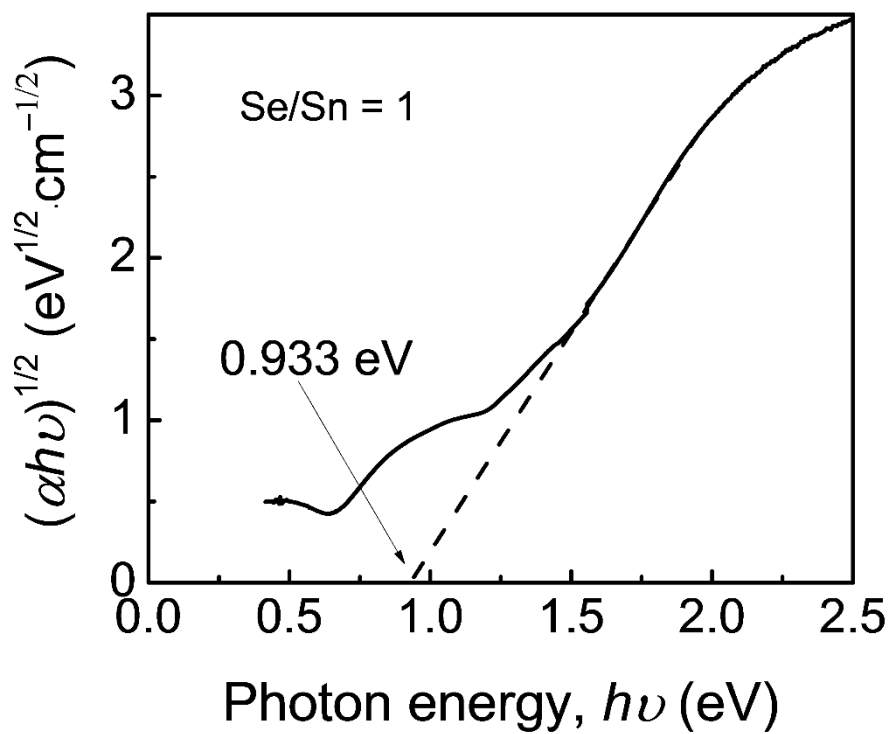
Supplementary Fig. 5. 2. Reproducibility. Temperature dependent a) Seebeck coefficient, b) electrical conductivity, and c) PF of sample at flux ratio of 0.8.



Supplementary Fig. 5. 3. Reproducibility. Temperature dependent a) electrical resistivity and b) Seebeck coefficient for sample at flux ratio of 1.



Supplementary Fig. 5. 4. Re-plot of absorption spectra obtained from UV-vis measurement for sample with flux ratio of 1. The determined indirect optical band gap is 0.933 eV in agreement with other report.



5.6 References

- [1] T. Inoue, H. Hiramatsu, H. Hosono, T. Kamiya, *J. Appl. Phys.* **118**, 205302 (2015).
- [2] B. Subramaniana, C. Sanjeevirajaa, M. Jayachandran, *J. Crystal Growth* **234**, 421 (2002).
- [3] M. Parenteau, C. Carlone, *Phys. Rev. B* **41**, 5227 (1990).
- [4] G. Shi, E. Kioupakis, *J. Appl. Phys.* **117**, 065103 (2015).
- [5] L. D. Zhao, S. H. Lo, Y. S. Zhang, H. Sun, G. Tan, C. Uher, C. Wolverton, V. P. Dravid, M. G. Kanatzidis, *Nature* **508**, 373 (2014).
- [6] A. T. Duong, V. Q. Nguyen, G. Duvjir, V. T. Duong, S. Kwon, J. Y. Song, J. K. Lee, J. E. Lee, S. D. Park, T. Min, J. W. Lee, J. Kim, S. Cho, *Nat. Commun.* **7**, 13713 (2016).
- [7] S. Lee, K. Esfarjani, T. Luo, J. Zhou, Z. Tian, G. Chen, *Nat. Commun.* **5**, 3525 (2014).
- [8] N. D. Boscher, C. J. Carmalt, R. G. Palgrave, I. P. Parkin, *Thin Solid Films* **516**, 4750 (2008).
- [9] D. M. Escobar, M. Ramachandran, A. S. Juárez, J. S. N. Rios, *Thin Solid Films* **535**, 390 (2013).
- [10] G. H. Chandra, J. N. Kumar, N. M. Rao, S. Uthanna, *J. Crystal Growth* **306**, 68 (2007).
- [11] D. T. Quan, *Thin Solid Films* **149**, 197 (1987).
- [12] N. Kumar, V. Sharma, N. Padha, N. M. Shah, M. S. Desai, C. J. Panchal, I. Y. Protsenko, *Cryst. Res. Technol.* **45**, 53 (2010).
- [13] R. Teghil, A. G. Guidoni, A. Mele, S. Piccirillo, G. Pizzella, V. Marotta, *Thin Solid Films* **241**, 126 (1994).

- [14] R. Teghil, A. Santagata, V. Marotta, S. Orlando, G. Pizzella, A. G. Guidoni, A. Mele, *Appl. Sur. Sci.* **90**, 505 (1995).
- [15] Z. Wang, J. Wang, Y. Zang, Q. Zhang, J. A. Shi, T. Jiang, Y. Gong, C. L. Song, S. H. Ji, L. L. Wang, L. Gu, K. He, W. Duan, X. Ma, X. Chen, Q. K. Xu, *Adv. Mater.* **27**, 4150 (2015).
- [16] G. Duvjir, T. Min, T. T. Ly, T. Kim, A. T. Duong, S. Cho, S. H. Rhim, J. Lee, J. Kim, *Appl. Phys. Lett.* **110**, 262106 (2017).

CHAPTER 6: THERMOELECTRIC PROPERTIES OF HOT PRESS Bi-DOPED N-TYPE POLYCRYSTALLINE SnSe

(ACCEPTED – Nanoscale Research Letters)

We report on the successful preparation of Bi-doped n-type polycrystalline SnSe by hot press method. We observed anisotropic transport properties due to the (h00) preferred orientation of grains along the pressing direction. The electrical conductivity perpendicular to the pressing direction is higher than that parallel to the pressing direction; 12.85 and 6.46 S cm⁻¹ at 773 K for SnSe:Bi 8% sample, respectively. While thermal conductivity perpendicular to the pressing direction is higher than that parallel to the pressing direction; 0.81 and 0.60 Wm⁻¹K⁻¹ at 773 K for SnSe:Bi 8% sample, respectively. We observed a bipolar conducting mechanism in our samples leading to n to p-type transition, whose transition temperature increases with Bi concentration. Our work addressed a possibility to dope polycrystalline SnSe by a hot-pressing process, which may be applied to module applications.

6.1 Introduction

Thermoelectric materials can directly convert waste heat into electricity, which is one of the most important global sustainable energy solutions or can be used as solid-state Peltier coolers. These thermoelectric devices have exhibited many advantages such as no involvement of moving part, small size, light weight, no noise, no pollution, and long-life service, etc. However, their applications are still limited by the economical reasons and low energy conversion efficiency, which is evaluated by the dimensionless thermoelectric figure of merit, $ZT = S^2\sigma T/\kappa$, where S is Seebeck coefficient, T is absolute temperature, σ is electrical conductivity, and κ is thermal conductivity. The good thermoelectric material should have high Seebeck coefficient,

high electrical conductivity, and low thermal conductivity. However, these three transport coefficients are inter-dependent [1]. There are two main ways to enhance ZT ; enhancing power factor ($PF, S^2\sigma$) or lowering total thermal conductivity. Electrical conductivity and Seebeck coefficient are inversely related each other in most materials, which limit the thermoelectric power factor. Lower thermal conductivity can be achieved by increasing phonon scattering center or adding a number of interfaces in materials such as superlattices, alloys, nanowires, and nanotubes, etc. Bi_2Te_3 and PbTe are two traditional thermoelectric materials, whose ZT s are much improved; 1.8 at 320 K for $\text{Bi}_{0.5}\text{Sb}_{1.5}\text{Te}_3$ [2] and 2.2 at 915 K for $\text{PbTe}+2\%\text{Na}+4\%\text{SrTe}$ [3]. However, there are many disadvantages for the systems because Bi and Te elements are rare on the earth, resulting in increase of costs with the development of LED industry, [4] and the lead is toxic element. Therefore, it is necessary to explore economical and non-toxic (lead-free) alternative materials for thermoelectric applications.

IV-VI compound semiconductor SnSe is a robust candidate for thermoelectric conversion applications, which has been recently reported with high thermoelectric performance; $ZT = 2.6$ at 923 K in un-doped p-type and $ZT = 2.0$ at 773 K in intentionally hole-doped SnSe single crystal [5, 6]. Recently, we achieved $ZT = 2.2$ in n-type Bi-doped SnSe single crystal [7]. These high ZT values are attributed to the ultralow intrinsic thermal conductivity due to the long-range interaction along $\langle 100 \rangle$ direction caused by resonant bonding, leading to optical phonon softening, strong anharmonic scattering and large phase space for three-phonon scattering processes [8]. Bulk SnSe belongs to orthorhombic $Pnma$ space group ($a = 11.49 \text{ \AA}$, $b = 4.44 \text{ \AA}$, $c = 4.14 \text{ \AA}$) with an indirect band gap energy of $E_g = 0.829 \text{ eV}$ at 300 K. When temperature is increased it changes to orthorhombic $Cmcm$ space group ($a = 11.71$, $b = 4.31$, and $c = 4.32 \text{ \AA}$) with a direct band gap of $E_g = 0.464 \text{ eV}$ around 807 K [9]. SnSe exhibits a two-dimensional (2D) layered structure, where each Sn atom is surrounded by a highly distorted octahedron of

Se atoms to form a zigzag structure. Along b-c plane, there is a strong Sn-Se covalent bonding and along a-axis, there is a weak van der Waals force, which gives a strong anisotropic transport and very weak mechanical properties. The most common technique to fabricate single crystal SnSe is Bridgman technique which is quite specific and hard to produce in industry scale-up [1]. Considering the large-scale applications and the poor mechanical properties in layered material, polycrystalline SnSe is a possible solution.

Recently, un-doped p-type polycrystalline SnSe has been reported with $ZT = 0.5$ at 823 K, $ZT = 1.3$ at 850 K for rock-salt SnSe and doped p-type SnSe have been reported with the highest $ZT = 0.6$ at 750 K for Ag dopant [1, 10, 11]. Polycrystalline n-type SnSe have been reported with the ZT range from 0.6 to 1.2 for Te, I, BiCl₃, and Br dopants [4, 12, 13, 14]. Hot pressing and spark plasma sintering (SPS) are the most general techniques used to fabricate a polycrystalline of un-doped and doped SnSe.

Here we report on the successful preparation of Bi-doped n-type polycrystalline SnSe by hot press method. We observed anisotropic transport properties due to the (h00) preferred orientation of grains along pressing direction. We also observed a bipolar conducting mechanism in our samples leading to n to p-type transition, whose transition temperature increases with Bi concentration.

6.2 Experiment

The aim of this paper is fabricating and investigating thermoelectric properties of n-type Bi-doped SnSe polycrystalline with various Bi concentrations (0, 2, 4, 6, and 8%). The doping process is fulfilled by mixing and hot-pressing SnSe with Bi powders. The details of fabrications and characterizations of the samples are as below;

6.2.1 Fabrication of SnSe compound by temperature gradient technique

We fabricated SnSe compound using temperature gradient technique. The high purity (99.999%) of Sn and Se powders were weighed in an atomic ratio of 1:1 using a balance with a resolution of 10^{-4} g. The powders were mixed and sealed in an evacuated ($< 10^{-4}$ Torr) quartz ampoule. The ampoule was then sealed in another evacuated bigger quartz ampoule in order to prevent the sample from oxidation by air in the case when the inner ampoule is broken owing to the difference of thermal expansion between the crystal and quartz. The ampoules were slowly heated up to 600 °C for 30 h. It was maintained at this temperature for 1 h and then continuously heated up to 950 °C for 35 h. To complete the reaction between Sn and Se we maintained the ampoules at this temperature for 16 h and then slowly cooled down to room temperature. Excellent SnSe compound with dimensions of 13 mm diameter \times 25 mm length was obtained.

6.2.2 Fabrication of n-type Bi-dope SnSe polycrystalline samples by hot-press technique

The obtained ingots above were ground into powders and mixed with various Bi (0, 2, 4, 6, and 8%) amounts for 1 hour using a mixing machine. The mixed powder was loaded into 13 mm diameter mold and then hot pressed at 800 °C using 30 MPa pressure in Ar environment for 30 minutes to form a dense pellet with 13 mm diameter and 15 mm length.

6.2.3 Characterizations

The samples were analyzed by X-ray diffraction (XRD) in both parallel and perpendicular to the pressing direction. Field emission scanning electron microscopy (FE-SEM) was used to observe the microscopic image in fractured surface of the samples. To probe the anisotropic transport and thermoelectric properties, the samples were cut into $2 \times 1.5 \times 8$ mm bars for transport and $13 \times 13 \times 1.5$ mm for thermal diffusivity measurements along both parallel (//)

and perpendicular (\perp) directions using a diamond saw. Electrical conductivity and Seebeck coefficient were simultaneously collected from room temperature to 773 K with a collinear four probe configuration under an Ar atmosphere to prevent oxidation and evaporation of sample. The laser flash diffusivity method (model: LFA-457, NETZSCH, Germany) was used to determine thermal diffusivity from room temperature to 773 K. Mass density was determined by measuring sample's dimensions and mass. Heat capacity was taken from Sassi's work for polycrystalline SnSe [1]. Thermal conductivity was calculated by the relationship $\kappa = DC_p\rho$, where D , C_p , and ρ are thermal diffusivity, the heat capacity, and the mass density, respectively.

6.3 Results

The room temperature XRD patterns of sample SnSe:Bi 4 % in both \perp and \parallel directions are shown in Fig. 6.1, which are indexed based on the orthorhombic SnSe phase (space group $Pnma$). In the patterns, there are several small peaks, which are identified as rhombohedral Bi. This dominant Bi secondary phase indicates that SnSe does not decompose at 800 °C and other phases such as BiSnSe or Bi₂Se₃ are not formed. The average lattice parameters estimated from XRD patterns were $a = 11.469$, $b = 4.435$, and $c = 4.143$ Å, in good agreement with the previous reports [1, 4]. The patterns also showed strong (400) peak intensities in the plane parallel to the pressing direction, indicating that grains have preferentially aligned along [h00] direction due to the layered structure of SnSe.

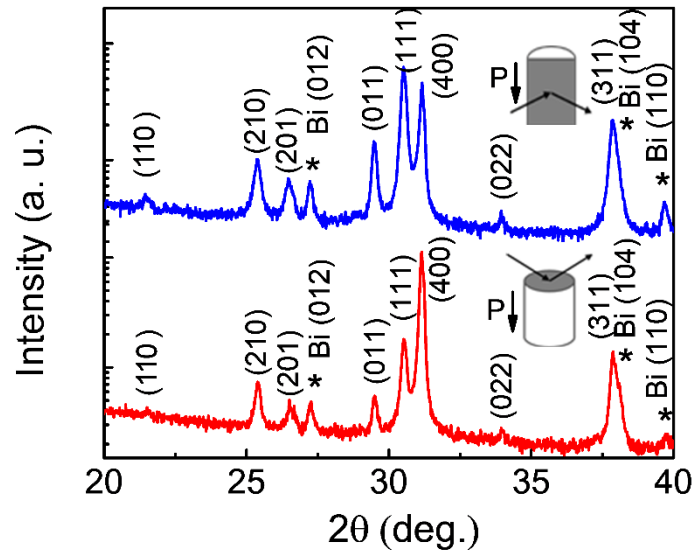


Fig. 6. 1. Room temperature XRD patterns for SnSe:Bi 4% along perpendicular (red color) and parallel (blue color) to the pressing direction as illustrated in the inset. The figure showed the orthorhombic structure and the presence of rhombohedral Bi phase.

The surface SEM images of the fractured SnSe:Bi 4% (a and b) and SnSe:Bi 6% (c and d) samples are shown in Fig. 6.2, which were taken on the plane parallel to the pressing direction as defined in the Fig. 6.2. As shown in the figure, our samples exhibited the layered structure with the fragments of layers tending to lie on the plane. Some tilted layers were seen in Fig. 6.2(b) and (c). On the other hand, when the Bi doping content increased from 4% to 6%, the estimated grain size increased from 3 to 10 μm . This observation indicated that Bi was not only substituted for Sn but also played as a flux leading to the increase in grain size.

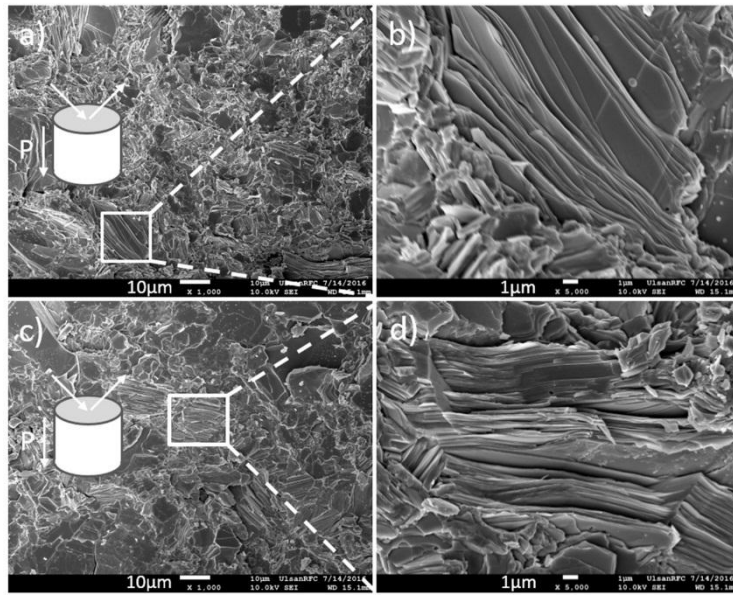


Fig. 6. 2. FE-SEM images of the fractured surfaces along the \perp direction of sample SnSe:Bi 4% (a and b) and SnSe:Bi 6% (c and d). FE-SEM images showed the layered structure and the dominant layers on the plane perpendicular to the pressing direction.

Temperature dependent Seebeck coefficient (S), electrical conductivity, and power factor of samples for \perp and \parallel directions are shown in Fig. 6.3. The figure showed the anisotropic transport properties, which are dependent on pressing directions. The electrical conductivity along the \perp direction is higher than that along the \parallel direction due to the preferred orientation of hot-pressed sample as mentioned above. Considering n-type samples, along the \perp direction, the electrical conductivity increased with Bi content, while along the \parallel direction it reached to the maximum value in the SnSe:Bi 6% sample and then decreased in the SnSe:Bi 8% sample. The electrical conductivities in all samples along both directions rise with temperature, indicating a typical semiconductor behavior as shown in Fig. 6.3(a) and (d). There was no metallic behavior above 700 K in our data, which is different from the previous reports due to the re-evaporation of Se at high temperature [1, 13]. This behavior confirmed the stability of our samples with the measured temperature range under Ar atmosphere.

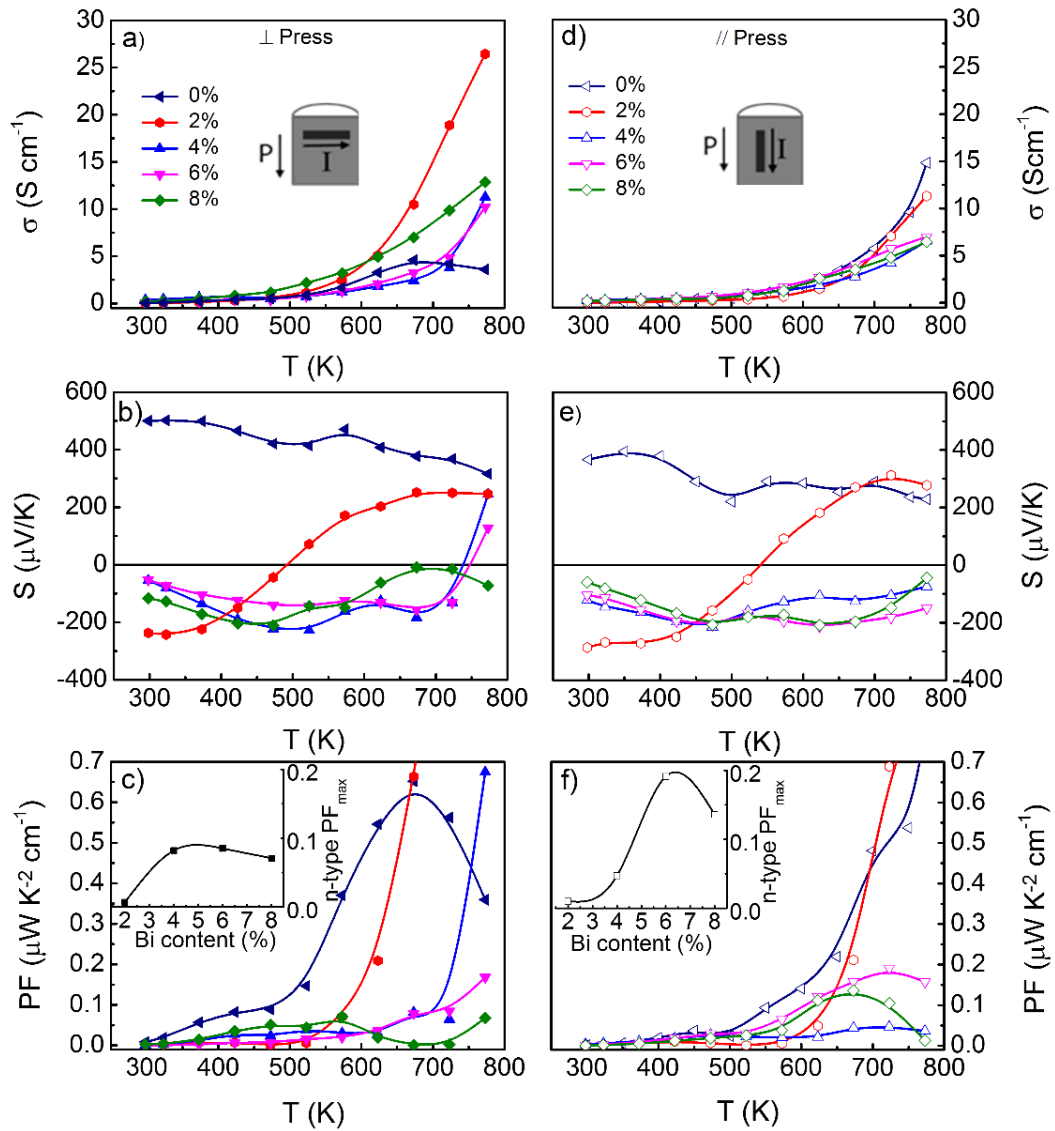


Fig. 6.3. Temperature dependence of electrical conductivity (a, d), Seebeck coefficient (b, e), and power factor (c, f) of samples with various Bi contents along \perp and \parallel directions as defined in the inset of (a) and (d), where the black arrows indicated the press direction P. The n-type maximum power factor as a function of Bi content is shown in the inset of (c) and (f). A small anisotropy in Seebeck coefficient was observed as shown in Fig. 6.3(b) and (e). Positive Seebeck coefficient was observed in the undoped sample, while negative Seebeck coefficients were observed in Bi-doped samples, indicating the substitution of Bi into Sn site.

The temperature dependent Seebeck coefficient curves of Bi-doped samples showed n to p-type transitions. Along the \perp direction, the transition temperatures were 492, 730, and 762 K for SnSe:Bi 2, 4, and 6% samples, respectively, while no transition was observed for SnSe:Bi 8% sample. Along the \parallel direction, the transition was observed at 541 K only for SnSe:Bi 2% sample. The absence of the n to p-type transitions in some samples may be due to higher transition temperatures than our maximum measured temperature, 773 K. These n to p-type transitions are related to bipolar conducting mechanism in our samples. The substituted Bi provided electrons to the conduction band and the Sn vacancies, played as the acceptors, generated holes in the valence band. As the temperature increases from 300 K, the donor impurities are activated and then n-type conduction is dominant. As a result, negative S is achieved. When the temperature is above a critical point, electrons in the valence band gain enough thermal energy to elevate to the acceptor levels and then holes are generated. When the hole becomes dominant charge carrier, positive S is achieved. The contribution of the electrons and the holes to S compensated each other and decreased S. Since, S can be calculated by the following formula for semiconductor;

$$S = \frac{p\mu_p S_p - n\mu_n S_n}{n\mu_n + p\mu_p} \quad (1)$$

where, S is the total Seebeck coefficient, n and p are the electron and the hole concentrations, μ_p and μ_n are the electron and the hole mobility, S_p and S_n are contributions of the electron and the hole to S. As shown in Fig. 6.3(b) and (e), the n to p-type transition temperature along the \perp direction is lower than that along the \parallel direction. This observation can be easily understood due to the higher electrical conductivity, indicating the higher mobility of charge carriers along the \perp direction than that along the \parallel direction. As shown in Fig. 6.3(a), (b), (d) and (e), below the transition temperature, electron carrier is dominant and its mobility along the \perp direction is

larger than that of electron along the // direction. However, above the transition, hole carrier is dominant with much higher hole mobility along the \perp direction. Thus, Seebeck coefficient transition along the \perp direction occurs first. This transition temperature also increases with Bi content, indicating the substitution of Bi for Sn in SnSe lattice. As a result of the small Seebeck coefficient and electrical conductivity, very small power factor values are achieved (Fig. 6.3(c) and (f)). The inset of Fig. 6.3(c) and (f) showed maximum power factors of n-type samples as a function of the Bi content. These values of power factor are higher along the // direction than those along the \perp direction. The power factor reached maximum value of $0.19 \mu\text{W}/\text{cm}\cdot\text{K}^2$ in SnSe:Bi 6% sample along the // direction.

Figure 6.4 shows the temperature dependence of heat capacity (C_p), thermal diffusivity (D), and thermal conductivity (κ) of polycrystalline SnSe:Bi 6% and SnSe:Bi 8% samples along both directions, which exhibited higher power factors. The lowest thermal conductivity of $0.544 \text{ W}/\text{m}\cdot\text{K}$ is obtained along the // direction at 723 K SnSe:Bi 6% sample (Fig. 6.4c). The thermal conductivities along both directions are comparable with other reports for polycrystalline SnSe [1, 9-13] and lower than that of single crystal SnSe:Na [6]. However, these values are higher than that of un-doped p-type SnSe [5] and Bi-doped n-type SnSe single crystal [7]. Note that the thermal conductivity is proportional to mass density, heat capacity, and thermal diffusivity of material. Polycrystalline samples are expected to have similar or even lower thermal conductivity values due to the additional phonon scatterings by grain boundaries. One possible reason for this high thermal conductivity was suggested by Zhao *et al.* [6] as the surface oxidation of samples due to the air exposure. However, Ibrahim *et al.* [15] disagreed with this opinion. Another reason for the high thermal conductivity is micro-crack in the samples, which may double the thermal conductivity of SnSe suggested by Zhao *et al.* [16]. This micro-crack may come from the cutting and polishing processes during the sample preparation for thermal

diffusivity measurements. In this work, we took the heat capacity values from Sassi's work [1] for polycrystalline SnSe, which are higher than that for single crystalline SnSe in [5, 7] as shown in the Fig. 6.4(a). Note that we have linearly extrapolated Sassi's temperature dependent heat capacity from 300 to 773 K. The measured thermal diffusivity was higher along perpendicular and comparable along parallel direction compared to that along b-axis for Bi-doped n-type SnSe single crystal (Fig. 6.4(b)). The mass densities were comparable with n-type Bi-doped SnSe single crystalline samples [7]; 6.11 and 6.09 g/cm^3 for sample SnSe:Bi 6% and 8%, respectively. Therefore, we conclude that the higher thermal conductivity in our polycrystalline samples than in single crystalline samples comes from the higher values of thermal diffusivity and specific heat.

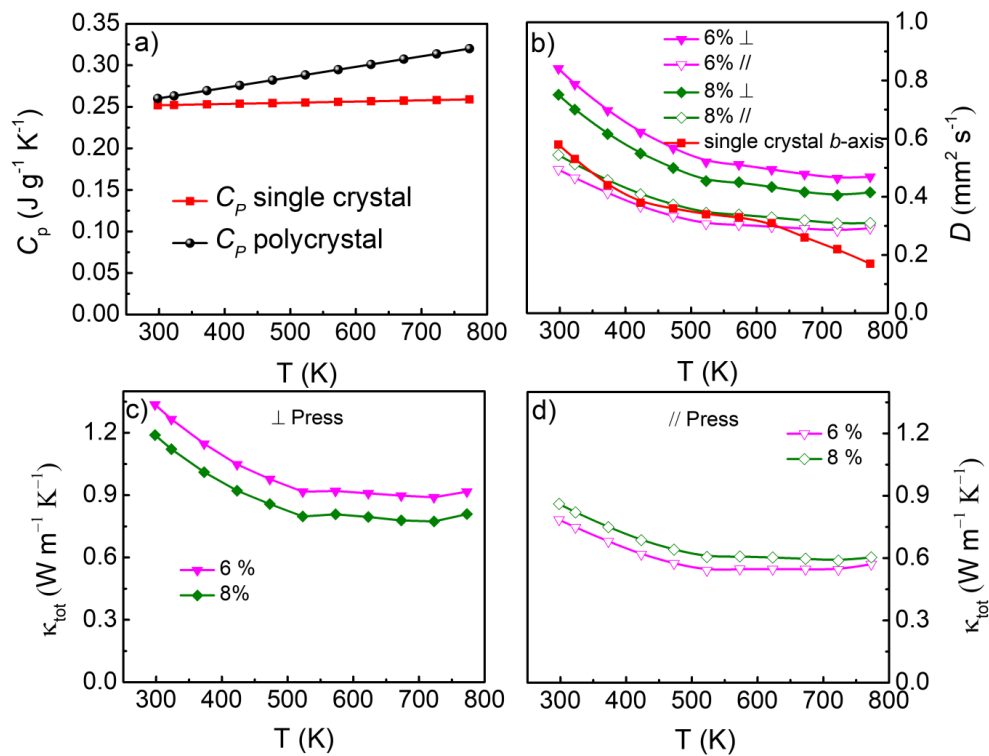


Fig. 6. 4. Temperature dependence of heat capacity (C_p) taken from [1] (a), thermal diffusivity (D) (b), and thermal conductivity (κ) of SnSe:Bi 6% and SnSe:Bi 8% samples along both \perp and \parallel directions in compare with Bi doped n-type SnSe single crystal [7] (c, d).

The dimensionless figure of merit ZT values as a function of temperature for these samples along both directions are shown in Fig. 6.5. The highest ZT of 0.025 is obtained at 723 K along the // direction for SnSe:Bi 6% sample, which seems to optimal doping content. Due to the small electrical conductivity, the total thermal conductivity is mostly attributed to the lattice thermal conductivity. Therefore, lower thermal conductivity is obtained along the // direction owing to the weak atomic connections. Consequently, higher ZT values are obtained along the // direction. However, these ZT values are quite small compared to those of single crystal or even other polycrystalline SnSe due to the lower S and σ values.

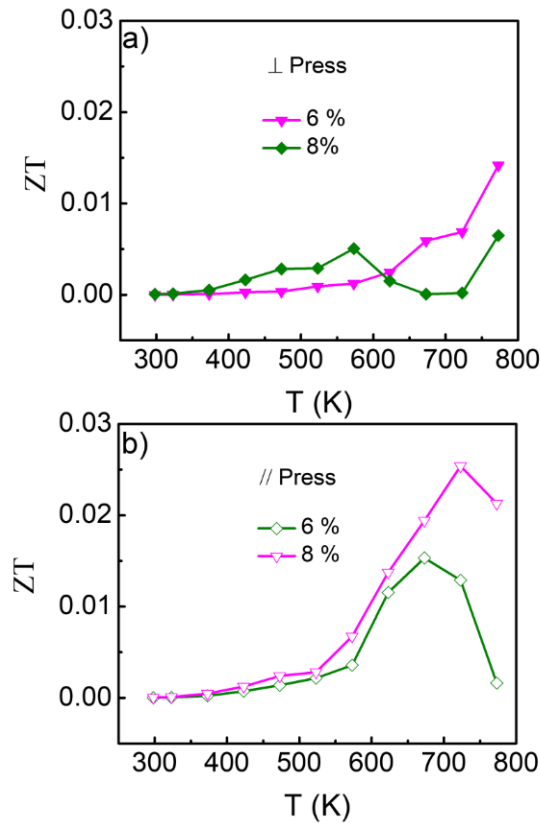


Fig. 6. 5. Temperature dependence of dimensionless thermoelectric figure of merit of polycrystalline SnSe:Bi 6% and SnSe:Bi 8% samples along both \perp (a) and $//$ (b) directions.

6.4 Conclusion

In conclusion, polycrystalline SnSe has been doped with various Bi concentrations by hot press method. The samples exhibited the layered structure with a preferential (h00) orientation. An anisotropic transport and thermoelectric properties have been observed. The electrical conductivities perpendicular to the pressing direction (12.85 S cm^{-1}) are higher than that parallel to the pressing direction (6.46 S cm^{-1}) at 773 K for SnSe:Bi 8% sample. While thermal conductivities perpendicular to the pressing direction ($0.81 \text{ Wm}^{-1} \text{ K}^{-1}$) are higher than those parallel to the pressing direction ($0.60 \text{ Wm}^{-1} \text{ K}^{-1}$) at 773 K for SnSe:Bi 8% sample. We observed a bipolar conducting mechanism in our samples leading to n to p-type transition, whose temperature increases with Bi concentration. The optimum Bi doping concentration was 6% with the highest ZT value of 0.025 at 723 K. This ZT value is quite low due to the low electrical conductivity and Seebeck coefficient. Our work addressed a possibility to dope polycrystalline SnSe by a hot-pressing process, which may be applied to module applications.

6.5 References

- [1] S. Sassi, C. Candolfi, J. B. Vaney, V. Ohorodniichuk, P. Masschelein, A. Dauscher, and B. Lenoir, *Appl. Phys. Lett.* **104**, 212105 (2014).
- [2] S. I. Kim, K. H. Lee, H. A. Mun, H. S. Kim, S. W. Hwang, J. W. Roh, D.J. Yang, W. H. Shin, X. S. Li, Y. H. Lee, G. J. Snyder, and S. W. Kim, *Science* **348**, 109 (2015).
- [3] K. Biswas, J. He, I. D. Blum, C. I. Wu, T. P. Hogan, D. N. Seidman, V. P. Dravid, and M. G. Kanatzidis, *Nature* **489**, 414 (2012).
- [4] S. Chen, K. Cai, W. Zhao, *Physica B* **407**, 4154 (2012).
- [5] L. D. Zhao, S. H. Lo, Y. Zhang, H. Sun, G. Tan, C. Uher, C. Wolverton, V. P. Dravid, and M. G. Kanatzidis, *Nature* **508**, 373 (2014).
- [6] L. D. Zhao, G. Tan, S. Hao, J. He, Y. Pei, H. Chi, H. Wang, S. Gong, H. Xu, V. P. Dravid, C. Uher, G. J. Snyder, C. Wolverton, and M. G. Kanatzidis, *Science* **351**, 141 (2016).
- [7] A. T. Duong, V. Q. Nguyen, G. Duvjir, V. T. Duong, S. Kwon, J. Y. Song, J. K. Lee, J. E. Lee, S. D. Park, T. Min, J. W. Lee, J. Kim, and S. Cho, *Nat. Commun.* **7**, 13713 (2016).
- [8] S. Lee, K. Esfarjani, T. Luo, J. Zhou, Z. Tian, and G. Chen, *Nat. Commun.* **5**, 3525 (2014).
- [9] Y. Li, X. Shi, D. Ren, J. Chen, and L. D. Chen, *Energies* **8**, 6275 (2015).
- [10] G. Tang, Q. Wen, T. Yang, Y. Cao, W. Wei, Z. Wang, Z. Zhang, and Y. Li, *RSC. Adv.* **7**, 8258 (2017).
- [11] C. L. Chen, H. Wang, Y. Y. Chen, T. Day, and G. J. Snyder, *J. Mater. Chem. A* **2**, 11171 (2014).
- [12] Q. Zhang, E. K. Chere, J. Sun, F. Cao, K. Dahal, S. Chen, G. Chen, and Z. Re

n, *Adv. Eng. Mater.* **5**, 1500360 (2015).

[13] X. Wang, J. Xu, G. Liu, Y. Fu, Z. Liu, X. Tan, H. Shao, H. Jiang, T. Tan, and J. Jiang, *Appl. Phys. Lett.* **108**, 083902 (2016).

[14] C. Chang, Q. Tan, Y. Pei, Y. Xiao, X. Zhang, Y. X. Chen, L. Zheng, S. Gong, J. F. Li, J. Hec, and L. D. Zhao, *RSC Adv.* **6**, 98216 (2016).

[15] D. Ibrahim, J. B. Vaney, S. Sassi, C. Candolfi, V. Ohorodniichuk, P. Levinsky, C. Semprimoschnig, A. Dauscher, and B. Lenoir, *Appl. Phys. Lett.* **110**, 032103 (2017).

[16] L. D. Zhao, C. Chang, G. Tan, and M. G. Kanatzidis, *Energy Environ. Sci.* **9**, 3044 (2016).

CHAPTER 7: SYNTHESIS AND CHARACTERIZATION

MICROSTRUCTURE AND THERMOELECTRIC

PROPERTIES OF SnSe-SnSe₂ COMPOSITES

(TO BE CONTINUED)

In the previous work (chapter 4), we showed that SnSe crystal usually contains an amount of SnSe₂ secondary phase. In this work, we present the synthesis, microstructure, and thermoelectric properties of mixed phase SnSe-SnSe₂ using temperature gradient technique with various Sn:Se atomic ratio. The samples show apparent coexistence of SnSe and SnSe₂ phases. With increase Se amount, SnSe₂ phase increase and become dominant, confirmed by XRD measurements. Optical microscopic images show the parallel slab microstructure of phases in the samples. The volume fraction of SnSe₂ phase increases with Se amount. TEM images show sharp and coherent interfaces between two phases. Seebeck coefficient decreases and changes from p-type to n-type characteristic with increase Se amount. Electrical conductivity also decreases, while thermal diffusivity increases with increase Se amount. Anisotropic thermoelectric properties and ZT values of these samples will be discussed since this work is not finished, yet.

7.1 Introduction

Thermoelectric (TE) devices which can directly convert waste heat into electrical energy is a good sustainable solution for the global energy crisis. Each TE device consists of both n- and p-type pair TE materials. The TE device's efficiency is proportion to these material's TE figure of merit $ZT = S^2\sigma T/\kappa$, where, S is Seebeck coefficient, σ and κ are electrical and thermal conductivity, and T is absolute temperature. Since these transport parameters are inter-

dependence, ZT value can only be improved by optimizing them. So far, band engineering [1-3], nanostructure, superlattices, alloys, nanowires, nanotubes [2], etc. have been made to enhance ZT . It is predicted that a two dimensional (2D) layered material exhibits comparable properties to the artificial superlattices [4]. Layered material is comprised of a 2D arrangement of atoms or slabs (i.e. several layers of atoms such as transition metal dichalcogenides...), where the intralayer bonding (e.g. covalent bonding) is much stronger than interlayer bonding (e.g. van der Waals bonding) [5]. These layered materials are of interest due to the electrons in layers behave as quasi-two dimensional. The interactions between layers can be easily modulated by introducing intercalations of foreign atoms. Followed up this idea, misfit layer compounds which introduce interfaces between different layered materials (multiple constituents) are potential TE material to improve ZT through both enhanced phonon scattering at interfaces and electronic interaction between constituents [6]. On the other hand, with the presence of turbostratic disorder, this material has shown extremely low cross-plane thermal conductivities and very low in-plane thermal conductivities. Misfit layer chalcogenide compounds consist of two types of slab, where the intralayer bonding is much stronger than interlayer bonding. The general formula for misfit chalcogenide layer compounds is $(MX_{1+\delta})_m-(TX_2)_n$, where, M is Sn, Pb, Sb, Bi, or a rare earth, T is Ti, B, Nb, Ta, or Cr, and X is Se or S. The bonding between constituents (interfaces) in the misfit layer compound, related to its stability is puzzle. There are there suggestions for this bonding. The first suggestion is that the bonding between constituents is a weak van der Waals bonding. The second suggestion is based on the lack of charge transfer in X-ray photoelectron spectroscopy (XPS) [7] and band structure calculation [8], leading to a covalent bonding. However, XPS, XAS (X-ray absorption spectroscopy), and EELS (electron energy loss spectroscopy) study showed that the charge transfer is a common feature [9], leading to the possibility of an ionic interaction between layers.

The misfit chalcogenide compound contains both “electron-crystal” term, provided by TX₂ layers with high carrier mobility and “phonon-glass” term, provided by MX layer. Due to the charge transfer from MX to TX₂ constituents, it is possible to optimize carrier concentration of TX₂ layer without affecting its high mobility. On the other hand, it is also possible to investigate magnetic properties of the misfit chalcogenide compound if T is a magnetic element such as Mn, Cr, Co, etc. To date, many reports about TE, magnetic, and superconducting properties of the misfit chalcogenide compounds. A typical evidence of controlling carrier concentration via charge transfer from MX to TX₂ constituents has been reported in [(PbSe)_{1.14}]_m(NbSe₂)₁ [10]. Ultra-low total thermal conductivities were obtained, (Yb_{0.95}S)_{1.24}NbS₂ (0.80 WK⁻¹m⁻¹ at 300 K) [11], (LaS)_{1.20}CrS₂ and (LaS)_{1.14}NbS₂ (1.2 and 1.5 WK⁻¹m⁻¹ at 300 K) [12], and Bi₂[AE]₂Co₂O_y (AE = Ca, Ca_{0.5}Sr_{0.5}, Sr, and Ba) (0.2–0.28 WK⁻¹m⁻¹ at 300 K along cross plane direction) [13]. A magnetic anisotropy has been observed in (BiSe)_{1.23}CrSe₂ and (BiSe)_{1.22}(Cr_{1.2}Se₂)₂ [14]. A superconducting behavior with tunable Curie temperature has been found in (PbSe)_{1.14}(NbSe₂)_n [15]. Recently, layered Bi₂Te₃-In₂Te₃ composites has been reported with tunable TE properties via controlling interface density [16]. SnSe is a p-type semiconductor with excellence thermoelectric performance $ZT = 2.6$ at 923 K [17]. While SnSe₂ is an n-type semiconductor. In the previous work (chapter 4), we showed that a small amount of SnSe₂ secondary phase is always exist in SnSe single crystals. The presence of SnSe₂ secondary phase may the main reason for the difficult reproducibility of high ZT SnSe. However, there is no report about the structure as well as TE properties of SnSe-SnSe₂ composites. In this work we investigate the synthesis, microstructure, and TE properties of SnSe-SnSe₂ composites. The SnSe₂ phase has been successfully controlled by varying atomic ratio $x = \text{Se}/\text{Sn}$, $x = 1, 1.2, 1.5, 1.75, \text{ and } 2$ which is temporarily used as the name of samples. XRD data show the co-existence of both the SnSe and the SnSe₂ phases in our samples which

is also confirmed by TEM image with sharp and coherent interfaces. With the increase of x , the SnSe_2 phase increases and then becomes dominant. The volume fraction of SnSe_2 phase increases with x . Seebeck coefficient decreases and changes from p-type to n-type characteristics with x increase. Electrical conductivity decreases, while thermal diffusivity increases with x . Anisotropic thermoelectric properties and ZT values of these samples will be discussed.

7.2 Experiment

7.2.1 Raw materials

Sn powder (99,99% Alfa Aesar) and Se powder (99,98% Alfa Aesar)

7.2.2 Temperature gradient growth and characterizations

The ingots (20 g) have been fabricated by temperature gradient technique as described in chapter 4. The raw materials of Sn and Se were first calculated in various atomic ratio $x = \text{Se/Sn}$ of 1, 1.2, 1.5, 1.75, and 2 which is temporary name of samples. After that we weighed the amounts of elements using balance with a resolution of 10^{-4} g. Stoichiometric amounts of elements were dried, mixed, and sealed in an evacuated thick quartz ampoule. These ampoules were slowly heated up to 950 °C and maintained for 15 h. After that the ampoules were cooled down to 900 °C at the rate of 5 °C/h and then slowly cooled down to 800 °C with the cooling rate of 0.5°C/h, following by cool down to room temperature.

In order to characterize electrical resistivity and Seebeck coefficient using an Ulvac Riko ZEM-3 instrument under a helium atmosphere from room temperature to 923 K, samples were cut in to $10 \text{ mm} \times 2 \text{ mm} \times 2 \text{ mm}$ bars. The samples were protected by BN coating layer. The uncertainties of measurements are 5%, 5% and 15% for Seebeck coefficient, electrical conductivity and power factor, respectively. X-ray diffraction (XRD) measurements were

carried out to investigate the crystal structure and phase of samples. Optical microscopy and transmission electron microscopy (TEM model Titan cubed G2 60-300) were used to investigate the microstructure of samples. To conduct the optical microscopic measurements, we cut cross-sectional and polished the samples using SiC papers up to the grit size of 1200 with 0.3 μm Al_2O_3 powder suspension. Focus ion beam (FIB) technique was used to prepare for TEM cross-section measurement. A Netzsch LFA 457 instrument and analyzed using Cowan model with pulse correction was used to measure thermal diffusivity of samples which were cut in to dimensions $8\text{ mm} \times 8\text{ mm} \times 1\sim 2\text{ mm}$. A thin layer of graphite was coated on surface of samples to minimize errors from the emissivity of the material.

7.3 Results

Figure 1 shows the XRD patterns taken from cleave planes and powder XRD of all samples. Diffraction peaks of orthorhombic SnSe and hexagonal SnSe₂ are apparently observed, indicating the coexistent of both constituents. The calculated lattice constants from XRD data of SnSe are $a = 11.54$, $b = 4.45$, and $c = 4.18\text{ \AA}$ and these of SnSe₂ are $a = 3.81$ and $c = 6.19\text{ \AA}$, in agreement with other reports. The major peaks in cleave XRD data and the prefer orientation in PXRD indicate the parallel arrangement of slab of SnSe and SnSe₂ constituents. The data also show the increase of SnSe₂ phase with x.

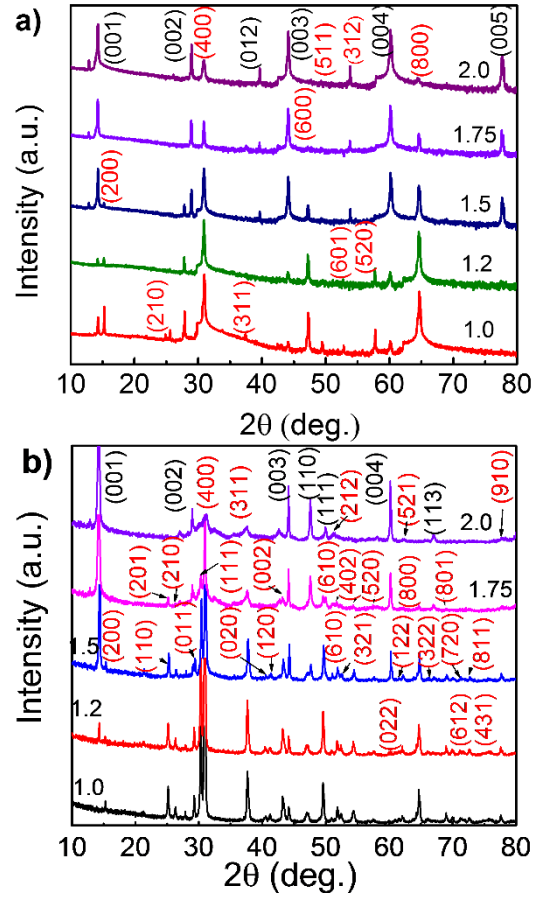


Fig. 7. 1. (a) XRD patterns taken from cleave plane and (b) powder XRD patterns of all samples, $x = 1, 1.2, 1.5, 1.75,$ and 2 . The red numbers indicate the Miller indices of SnSe and the black numbers indicate those of SnSe₂.

To investigate the microstructure of samples, we take the cross-sectional TEM images of sample $x = 1.75$ as shown in Fig. 7.2. The image shows the apparent observation of the coexistence of both SnSe and SnSe₂ constituents with a sharp and coherent interface. The calculated average lattice constants from TEM image of SnSe are $a = 11.44$ and $c = 4.14$ Å and those of SnSe₂ are $a = 3.81$ and $c = 6.04$ Å, in agreement with XRD data. The thickness of SnSe slab is nearly $5 \mu\text{m}$ (which need to be characterized more). The image also indicates the parallel arrangement of SnSe and SnSe₂ slabs. The cross-sectional plane determined from TEM image of SnSe is (100) and that of SnSe₂ is (120). Note that, here the a -axis of SnSe is

parallel to the c -axis of SnSe_2 and are set along with the z -axis.

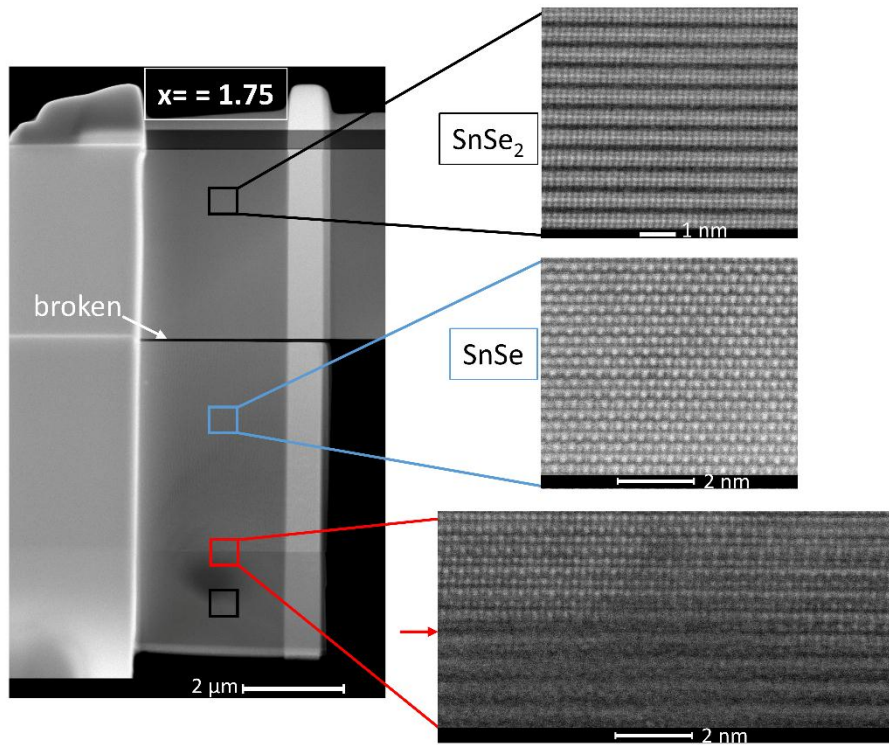


Fig. 7. 2. TEM cross-sectional images of sample $x = 1.75$.

Figure 7.3 shows optical microscopic images of all samples taken after polishing cross-sectional samples using SiC papers with grit size up to number 1200, with $0.3 \mu\text{m}$ Al_2O_3 powder suspension. The images show low quality of polishing with a lot of scratches, but enough to distinguish the two constituents by contrast (which need to be confirmed by composition analyses). The image of sample $x = 1$ show only SnSe phase due to its much dominance compare to SnSe_2 phase which cannot be observed under microscopy resolution. The images of samples $x = 1.2, 1.5,$ and 1.75 show apparent dark and bright parallel slabs, assigned to SnSe (bright) and SnSe_2 (dark) phases (which need to be confirmed by composition analyses). The volume fraction of SnSe_2 phase increases with x , in agreement with observations in the XRD data and the TEM image. Finally, sample $x = 2.0$ shows only SnSe_2 phase (dark) due to its

much dominance compare to SnSe phase which cannot be observed under microscopy resolution. Here, one question is arisen that why the cleave XRD can detect both constituents. Note that, the spot size of X-ray beam is about millimeters and the penetration depth of X-ray beam is about $1\ \mu\text{m}$ which is smaller than the thickness of the slabs. The possible reason is due to the cleaved surfaces may contain many ladders where both constituents are exposed. Due to the thicknesses of the slabs are not confirmed yet, there is possible reason that the thicknesses of the slabs are smaller than XRD penetration depth. Another possible reason is that both phases may laterally exist (which need to be confirmed).

These above conclusions are deduced from combination of all of my current data, better polishing will be made for scanning electron microscopy (SEM) and energy dispersive spectroscopy (EDS) experiments in the future. The lateral (in-plane) information will be examined by STM.

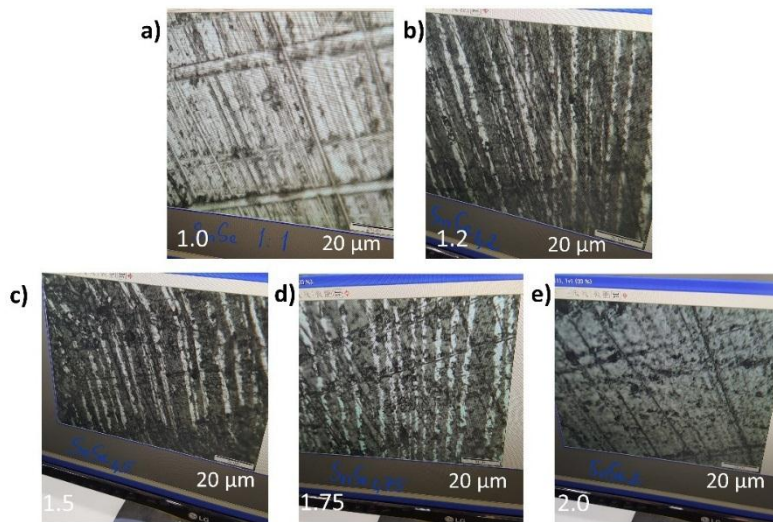


Fig. 7. 3. Cross-sectional optical microscopy images of all samples after rough polishing with maximum SiC paper grit size of 1200 with, with $0.3\ \mu\text{m}\ \text{Al}_2\text{O}_3$ powder suspension.

Temperature dependent Seebeck coefficient, electrical conductivity, power factor, and thermal diffusivity of all samples taken along in-plane are shown in Fig. 7.4. Of all samples, the Seebeck coefficient, S decreases with x and decreases with temperature. Positive S was observed in sample $x = 1$. A transition of S from p- to n-type were observed in samples $x = 1.2$, 1.5, and 1.75 and finally S became negative in sample $x = 2$, as shown in Fig. 7.3(a). Note that, SnSe is a p-type semiconductor while SnSe₂ is an n-type semiconductor. Our observations are reasonable due to the increase of SnSe₂ amount with x , as shown above. With the dominance of SnSe the samples show positive S , and negative S is achieved with the dominance of SnSe₂. A transition from p- to n-type is expected when the SnSe₂ amount becomes comparable to the SnSe. The electrical conductivity also decreases with x and increase with temperature as shown in Fig. 7.4(b). This observation may due to the increase number of interface with x , leading to decrease carrier mobility. Hall measurements will be taken to confirm this argument. On the other hand, the joints of p-type SnSe and n-type SnSe₂ semiconductors generate p-n junctions in our samples which may play an important role in the thermoelectric transport properties. The power factor, PF also decreases with x , where maximum $PF = 11.23 \mu\text{W}/\text{cm}\cdot\text{K}^2$ was achieved in sample $x = 1$ at 876 K as shown in Fig. 7.4(c). Thermal diffusivity increases with x , as shown in Fig. 7.4(d) due to the increase of SnSe₂ amount which showed higher thermal diffusivity [18]. To calculate thermal conductivity and TE figure of merit values, mass density and specific heat of all samples will be determined.

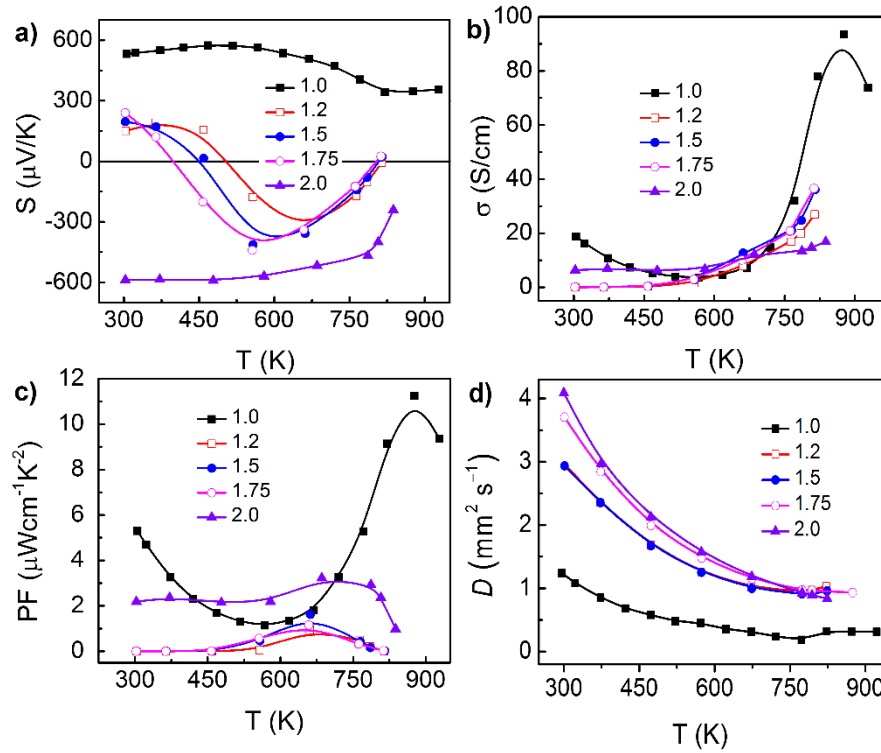


Fig. 7. 4. Temperature dependent (a) Seebeck coefficient, (b) electrical conductivity, (c) power factor, and (d) thermal diffusivity of all samples.

7.4 Conclusion

In conclusion, we have successfully fabricated SnSe-SnSe₂ composite and investigated its microstructure and thermoelectric transport properties. Based on our current observation, the both constituents coexist in the samples with parallel slabs. The volume fraction of SnSe₂ phase increase with Se amount. The Seebeck coefficient, electrical conductivity, and power factor decrease while the thermal diffusivity increases with Se amount. More detail about thermoelectric properties of these samples will be discussed. By this work, we temporarily conclude that it is always possibility to obtain SnSe₂ phase in SnSe single crystal which is harmful to the TE performance of the sample.

7.5 References

- [1] W. Liu, X. Tan, K. Yin, H. Liu, X. Tang, J. Shi, Q. Zhang, C. Uher, Convergence of conduction bands as a means of enhancing thermoelectric performance of n-type $\text{Mg}_2\text{Si}_{1-x}\text{Sn}_x$ solid solutions, *Phys. Rev. Lett.* **108** (2012) 1–5. doi:10.1103/PhysRevLett.108.166601.
- [2] Y. Pei, X. Shi, A. Lalonde, H. Wang, L. Chen, G.J. Snyder, Convergence of electronic bands for high performance bulk thermoelectrics, *Nature*. **473** (2011) 66–69. doi:10.1038/nature09996.
- [3] S.N. Girard, J. He, X. Zhou, D. Shoemaker, C.M. Jaworski, C. Uher, V.P. Dravid, J.P. Heremans, M.G. Kanatzidis, *J. Am. Chem. Soc.* **133**, 16588 (2011).
- [4] Y. Zhou and L-D. Zhao, *Adv. Mater.* **29**, 1702676 (2017).
- [5] G.A. Wiegers, *Prog. Solid State Chem.* **24**, 1 (1996).
- [6] D. R. Merrill, D. B. Moore, S. R. Bauers, M. Falmbigl, and D. C. Johnson, *Materials* **8**, 2000 (2015).
- [7] A. Ettema and C. Haae, *J. phys. Condens. Matter.* **5**, 3817(1993).
- [8] C. M. Fang, A. Ettema, C. Hass, G. A. Wiegers, H. Leuken, and R. A. Groot, *Phys. Rev. B* **52**, 2336 (1995).
- [9] M. Hangyo, T. Nishio, S. Nakashima, Y. Ohno, T. Terashima, and N. Kojima, *Jpn. J. Appl. Phys. Pt.* **32**, 581 (1993).
- [10] M. B. Alemayehu, G. Mitchson, J. Ditto, B. E. Hanken, M. Asta, and D. C. Johnson, *Chem. Mater.* **26**, 1859 (2014).
- [11] Y. Miyazaki, H. Ogawa, and T. Kajitani, *Jpn. J. Appl. Phys.* **43**, L1202 (2004).

- [12] P. Jood, M. Ohta, H. Nishiate, A. Yamamoto, O. I. Lebedev, D. Berthebaud, K. Suekuni, and M. Kunii, *Chem. Mater.* **26**, 2684(2014).
- [13] L. Li, X. J. Yan, S. T. Dong, Y. Y. Lv, X. Li, S. H. Yao, Y. B. Chen, S. T. Zhang, J. Zhou, H. Lu, M. H. Lu, and Y. F. Chen, *Appl. Phys. Lett.* **111**, 033902 (2017).
- [14] S. M. Clarke and D. E. Freedman, *Inorg. Chem.* **54**, 2765 (2015).
- [15] C. Grosse, M. B. Alemayehu, M. Falmbigl, A. Mogilatenko, O. Chiatti, D. C. Johnson, and S. F. Fischer, *Sci. Rep.* **6**, 33457 (2016).
- [16] D. Liu, X. Li, P. M. C. Borlido, S. Botti, R. Schmechel, and M. Rettenmayr, *Sci. Rep.* **7**, 43611 ((2017).
- [17] L. D. Zhao, S. H. Lo, Y. Zhang, H. Sun, G. Tan, C. Uher, C. Wolverton, V. P. Dravid, and M. G. Kanatzidis, *Nature* **508**, 373 (2014).
- [18] P. Xu, T. Fu, J. Xin, Y. Liu, P. Ying, X. Zhao, H. Pan, and T. Zhu, *Sci. Bull.* **xx**, xxx (2017).

CHAPTER 8: CONCLUSIONS

In conclusion, the engineering defects study in SnSe single crystal, polycrystal, and thin film were carried out using temperature gradient, hot press, and molecular beam epitaxy techniques. It has been shown that the number and type of defect can be easily controlled during the solidification of the crystals. Single Sn vacancy was found to be the main source of the p-type characteristic of SnSe. The resistance of sample increases when the number of single Sn vacancy decreases, especially in SnSe thin film grown by MBE where sample is nearly defect free. These intrinsic defects do not affect to the thermal conductivity of samples. We also found that Bi can be doped in to SnSe polycrystal just by hot press process. However, the doping concentration and therefore, thermoelectric performance are quite low. In all bulk SnSe grown by the temperature gradient technique, there is small amount of SnSe₂ secondary phase which is harmful to the TE performance of samples. When we increase the amount of Se to grow samples, the SnSe₂ phase becomes comparable to the SnSe phase. Such kind of material is called misfit layer compounds which is a promising TE material. I will continue this work not only for Sn-Se but also other layered systems in the next steps of my research. Also optimizing growth condition to get high TE performance for SnSe thin film is a necessary future work.

APPENDIX 1: ANTIFERROMAGNETIC INTERFACES IN CoFe₂O₄/Fe₃O₄ SUPERLATTICES (TO BE SUBMITTED)

We report the influences of antiferromagnetic interfaces on the transport and magnetic properties of [CoFe₂O₄(*x*Å)/Fe₃O₄(*x*Å)]_{*n*} superlattices which have been epitaxially grown on MgO (100) substrate using molecular beam epitaxy. The strong antiferromagnetic ordering formed at the interfaces is due to the exchange coupling between two oxides. An open of other loop is observed in high field part of magnetization curves, assigned to a combination of magnetizations of antiferromagnetic interfaces and ferrimagnetic layers. This behavior becomes more obvious, when the superlattice's wave length decreases due to a dominance of interfaces. Anomalous anisotropic magneto-resistance (MR) is also observed due to the presence of interfaces.

9.1 Introduction

Magnetite, Fe₃O₄, is a ferrimagnet with a cubic inverse spinel structure, exhibits a metal-insulator, Verwey, transition at about 120 K[1] which could be potentially used in resistive random access memories (ReRAMs) applications. It is predicted to possess as half-metallic nature and 100% spin polarization. Cobalt ferrite is one of the most important members of the ferrite family, which is characterized by its high coercivity, moderate magnetization and very high magneto-crystalline anisotropy. Both of them have very high Curie temperature, above 800 K, therefore, they viable for technological applications up to high temperature. There are many publications about physical properties of this family. Some researchers focus on exchange coupling at interface between these oxides in their bi-layer system[1–4]. However, less studies about their multi-layers and superlattices (SLs) have been reported, where an

artificial periodicity of ultrathin films made of Fe_3O_4 (FO) and CoFe_2O_4 (CFO) is created. The properties of this SL are governed by the interplay of a number of quantum effects such as quantum confinement, tunneling effect, and many physical phenomena come from interfaces such as the exchange interaction where the spins in adjacent layers are oriented with respect to one another. The SL configuration brings many interesting phenomena compare to the single thin film such as enhance Seebeck coefficient, bi-stable magneto-resistance switching, possibility to study about exchange bias effect, exchange spring magnet, and TMR, GMR experiments due to the role of interfaces, etc. Recently, Ana V. Ramos *et al.*[1,2] reported that the CFO/FO bi-layers present an unusual exchange-coupled system whose properties are due to the nature of the oxide-oxide super-exchange interactions at the interface. He observed a shoulder in magnetization M-H curve assigned to the superposition of soft and hard magnetizations. Z. He *et al.*[5] reported that SLs $\text{Co}_x\text{Fe}_{3-x}\text{O}_4$ exhibited the resistance switching and the negative differential resistance feature during perpendicular transport measurements, which could be used in resistive random access memories (ReRAMs)[3]. Ferrimagnetic-ferrimagnetic oxide SLs $\text{Fe}_3\text{O}_4/\text{Mn}_3\text{O}_4$ (FO/MO) and ferromagnetic-ferromagnetic oxide SL $\text{La}_{0.7}\text{Sr}_{0.3}\text{MnO}_3/\text{SrRuO}_3$ (LSMO/SRO) have also been reported with a very strong antiferromagnetic (AF) coupling at interfaces[6–8]. However, these SLs contain low T_C material which limited their applications within low temperature range.

The molecular beam epitaxy (MBE) is one of the best methods to produce epitaxial SLs due to the low growth temperature to prevent the inter-diffusion of elements. To the best of our knowledge this is the first study about CFO/FO superlattices. Two SLs $25\text{\AA}/25\text{\AA}$ ($[\text{CFO}(25\text{\AA})/\text{FO}(25\text{\AA})]_{40}$) and $100\text{\AA}/100\text{\AA}$ ($[\text{CFO}(100\text{\AA})/\text{FO}(100\text{\AA})]_{10}$) were fabricated on MgO (100) substrate at 400 °C. The sample quality and characterization were investigated by in-situ RHEED and ex-situ HR-TEM measurements and will be discussed in part A. Interfaces

between layers play an important role in magnetic and transport properties of samples. Part B presents about magnetic properties of SLs. A strong antiferromagnetic ordering was formed at the interfaces and strongly affected to the M-H curves of SLs, leading to an open of other loop at high field parts. The effects of interfaces increase when SL's wave length decreases due to the dominance of interfaces. We took a schematic illustration magnetization of superlattices where they were considered as a ferrimagnetic SLs. The interfaces also played as scattering centers which strongly affected to temperature dependent electrical resistivity and anisotropic magneto-resistance (MR) which will be discussed in part C.

9.2 Experiment

The SLs CFO/FO were epitaxially grown on MgO (100) by molecular beam epitaxy (VG Semicon, Inc.). The MBE system was equipped with the standard effusion cell for Co, Fe and oxygen cracker cell for oxygen supply. The MgO (100) substrate was initially cleaned with methanol then immediately loaded into growth chamber. After preheating at 600 °C for 30 minutes to completely remove the residual impurities the substrate was cooled down to 400 °C which was maintained during the growth. The base pressure before apply oxygen was in range of 10^{-9} Torr. Atomic oxygen gas was then applied using an oxygen cracking cell. The films were grown by the co-deposition of Co and Fe using effusion cells under an oxygen partial pressure of 10^{-6} Torr. Two samples of SLs $[\text{CFO}(25\text{\AA})/\text{FO}(25\text{\AA})]_{40}$ and $[\text{CFO}(100\text{\AA})/\text{FO}(100\text{\AA})]_{10}$ were grown MgO (100) substrate, where the numbers inside bracket are CFO and FO well thickness and outside bracket are number of SL's period. We call these samples as 25Å/25Å and 100Å/100Å, respectively. Our MBE system further allowed for *in-situ* reflection high energy electron diffraction (RHEED) in order to examine the quality of the deposited layers where the total thicknesses of the samples were 200 nm. TEM cross-sectional

measurement was taken to evaluate the SLs configuration. Electrical resistivity and magnetoresistance MR of SLs were measured using a four-probe Van der Pauw configuration and magnetic field up to 7.5 kOe. Magnetic behavior of SLs has been investigated using superconducting quantum interference device (SQUID) magnetometer (Quantum Design, Inc.) with a magnetic field up to 70 kOe. The majority of the measurements were performed with various temperatures from 300 K down to 80 K which is below the Verwey transition temperature (120 K) of magnetite with the magnetic field aligned parallel to the films surface.

9.3 Results

9.3.1 Thin films growth and characterization

Figure 9.1 shows RHEED patterns of SLs performed after the growths. The inset of figure 1(a) shows a RHEED pattern of MgO (100) substrate along [111] azimuth after preheating at 600 °C. Streaky RHEED pattern with apparent Kikuchi lines was obtained, indicating the clean and flat surface. Figure 9.1 (a) shows a RHEED pattern obtained from 40 periods of CFO/FO/MgO (100) SL with the well thickness of 25 Å CFO and 25 Å FO. The diffraction streaks are sharp with apparent Kikuchi lines, representing the epitaxial with layer-by-layer Frank-Vander Merwe growth mode of the sample. It also indicates a very smooth surface and interface between layers. RHEED pattern obtained from 10 periods of CFO/FO/MgO (100) with the well thickness of 100 Å CFO and 100 Å FO is shown in Fig. 9.1 (b). The spotty RHEED pattern indicates rough surfaces and interfaces of this sample. The roughness of surfaces and interfaces strongly affect to the sample's properties, especially transport properties which will be discussed.

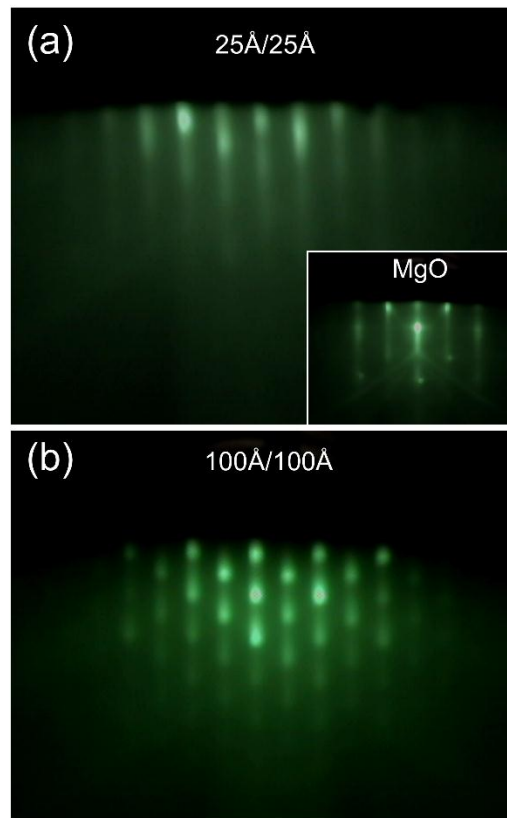


Fig. 9. 1. RHEED patterns of $\text{CoFe}_2\text{O}_4/\text{Fe}_3\text{O}_4$ SLs (a) 40 periods of $\text{CoFe}_2\text{O}_4/\text{Fe}_3\text{O}_4/\text{MgO}(100)$ SL with the well thickness of 25 Å CoFe_2O_4 and 25Å Fe_3O_4 and (b) 10 periods of $\text{CoFe}_2\text{O}_4/\text{Fe}_3\text{O}_4/\text{MgO}(100)$ with the well thickness of 100 Å CoFe_2O_4 and 100 Å Fe_3O_4 . The inset of Fig. 8.1 (a) is that of MgO substrate.

A schematic illustration of the configuration of SLs grown on MgO (100) substrate is shown in Fig. 9.2(a), where d is the well thickness (25 Å and 100 Å), n is SL period (40 and 10) for sample 25Å/25Å and 100Å/100Å, respectively. The growths were started with deposition of FO layer on MgO (100) substrate, after that CFO layer was deposited continuously to perform the first period of SL. The deposition of layers was fulfilled by open and close shutters located in front of effusion cells and can be controlled by computer. The iron cell and oxygen cracking cell were always open during growth. The Co cell was opened after the deposition of FO layer and was closed the deposition of CFO layer, and so on... When sample was completely

deposited, all shutters were closed simultaneously. In order to experimentally evaluate the SLs configuration, we have chosen the sample $25\text{\AA}/25\text{\AA}$ to take the TEM cross-sectional measurement as shown in Fig. 9.2(b). The white arrows indicate the well thicknesses of CFO and FO layers. However, there is no visible delimitation either in contrast or atomic arrangement between two layers. This observation can be interpreted by the nearly identical in structure and chemistry of these ferrites. Both layers are same cubic spinel structure, the substitution of Co with nearly similar atomic radius into Fe sites (135 and 140 pm) hardly take affects to the lattice parameter of this system. Therefore, there is no expectation of any significant strain or defects in the SLs. The same situation has also been reported in bi-layer system[1]. The continuity in whole range of sample without any delimitation also indicates the high quality epitaxial growth of our SL. The lacking in contrast between two layers is due to the proximity in atomic masses of Co and Fe. The possibility of Co inter-diffusion into Fe_3O_4 layers may not be investigated base on this technique. However, we believe that the growth temperature of $400\text{ }^\circ\text{C}$ is low enough to prevent the inter-diffusion of Co into Fe_3O_4 layers. Note that, electron energy loss spectroscopy (EELS) analysis of bi-layer system grown at $450\text{ }^\circ\text{C}$ [1] indicated no interdiffusion of Co into the Fe_3O_4 . The sign of SL configuration may be revealed in magnetic and transport properties which are presented below.

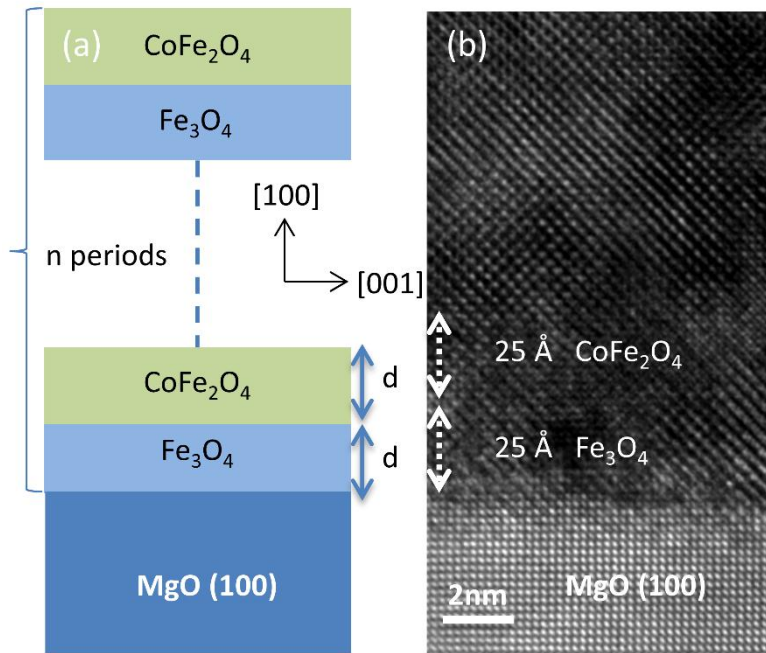


Fig. 9. 2. (a) Schematic showing the configuration of SLs grown on MgO (100) substrate with $d = 25$ and 100 \AA , $n = 40$ and 10 periods for SL $25\text{\AA}/25\text{\AA}$ and $100\text{\AA}/100\text{\AA}$. (b) TEM cross-sectional image of sample $25\text{\AA}/25\text{\AA}$.

9.3.2 Magnetic property

Figure 9.3 shows in-plane magnetization curves of SLs at some temperatures in compare with that of single thin films CFO and FO. These curves show anomalous shapes above Verwey temperature, where another loop is opened at the high field part. This open of the loop is often found in antiferromagnetic systems at high field due to the spin-flop transition. The saturation magnetization increases with SL's wavelength; from 239 to 322 emu/cm^3 at 300 K , from 250 to 343 emu/cm^3 at 220 K , from 255 to 336 emu/cm^3 at 160 K , and from 253 to 360 emu/cm^3 at 80 K for sample $25\text{\AA}/25\text{\AA}$ and $100\text{\AA}/100\text{\AA}$, respectively. Coercive field also increases with SL's wave length; from 252 to 302 Oe at 300 K , from 824 to 909 Oe at 220 K , from 2036 to 2143 Oe at 160 K , and from 4768 to 5117 Oe at 80 K for sample $25\text{\AA}/25\text{\AA}$ and $100\text{\AA}/100\text{\AA}$,

respectively. Note that in CFO single thin film the saturation magnetization is smaller, while coercive field is bigger than those of FO due to the smaller magnetic moment ($3 \mu_B$) and the higher magneto-crystalline anisotropy of Co compare to Fe. The saturation field of CFO thin film is about 50 kOe. The M-H curves of SLs are not simply a superposition of those of two individual layers which happen in bi-layer system[1,2] and can only be explained by the presence of an exchange coupling at the interfaces and the high magneto-crystalline anisotropy of Co. The exchange coupling forces magnetic moments align anti-parallel to each other at the interfaces. Due to these anti-parallel alignments, the magnetic moments at the interfaces tend to cancel out each other. With the interface dominance the saturation magnetization of sample 25Å/25Å is smaller than that of sample 100Å/100Å. Coercive field of sample 25Å/25Å is also smaller than that of 100Å/100Å due to the presence of thicker CFO layers with high coercive field. Higher coercive field in thicker CFO film was also reported by A. Lisfi *et al.*[9]. Both the saturation magnetizations and coercive fields of SLs are in middle of FO and CFO single layers, indicating the simultaneous presences of FO and CFO layers in the samples.

Now, we discuss in detail the shape of M-H curves of SLs, as shown in Fig. 9.3(a - c). Recently, there are some publications reported about CFO/FO[1–3] and Mn(Zn)Fe₂O₄/CoFe₂O₄[4] bi-layer systems, they observed two inflections in the second and forth quadrant of M-H curves which are assigned to the switch of CFO and (Mn(Zn) Fe₂O₄) or FO due to the exchange coupling at the interface between two layers. The M-H curves of bi-layer system are superposition of those of individual layers. This could also be the case of SL, however, in SL system, the interface is dominant with comparable thickness to the SL's layers. At the interfaces, the spins in adjacent layers are oriented with respect to one another to form a strong anti-ferromagnetic ordering. As shown in the Fig. 9.3(a – c), a dramatic accentuation of anti-ferromagnetic behavior is observed at high applied magnetic field (switching field). The

switching field increases with decreasing temperature, these values are around 3, 5, and 6 kOe at 300, 220, and 160 K, respectively. This switching field is stronger than that of LSMO/SRO SL[7] ($H^* \sim 1.6$ kOe) but weaker than that of FO/MO SL[6] ($H^* \sim 10$ kOe). This is a strong evidence for the presence of a powerful exchange coupling at the interfaces which released a stable and strong anti-parallel magnetic state. However, the M-H curves become normal at below Verwey transition temperature (Fig. 9.3(d)). This behavior is due to the transition from cubic spinel to monoclinic structure of both layers which is confirmed by a rapidly change of coercivities near Verwey transition as shown in the inset of Fig. 9.3(d). This distortion from cubic symmetry may affect the exchange coupling at interfaces of SLs.

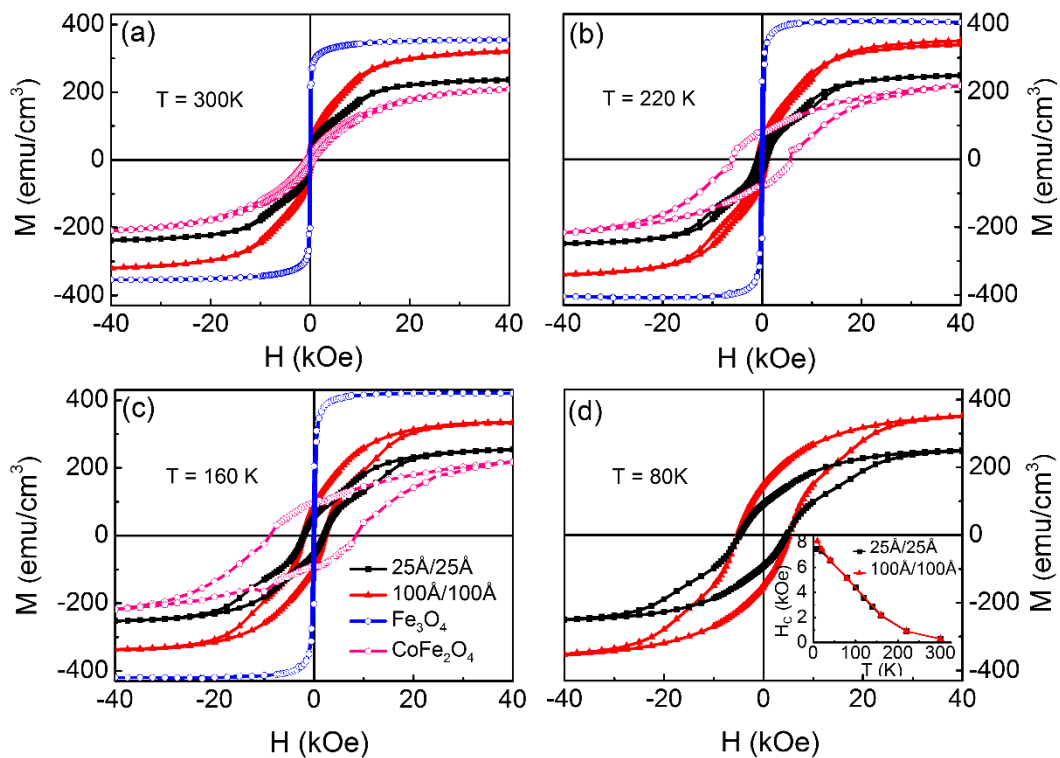


Fig. 9. 3. In-plane magnetization hysteresis loop of SLs in compare with that of 2000 Å CoFe₂O₄ and Fe₃O₄ single thin films at (a) 300 K, (b) 220 K, (c) 160 K, and (d) 80 K. The inset of (d) is temperature dependent coercivity of SLs.

In order to understand the mechanism of switching in M-H curves above Verwey temperature, we take the schematic illustration of magnetization for SLs where we consider the SLs as ferrimagnetic SLs due to the difference magnetic moment between FO ($4\mu_B$) [10] and CFO ($3.4\mu_B$)[11] layer as shown in Fig. 9.4. To the best of our knowledge, there was no theoretical model available to explain this magnetic response, yet. We found that these data are qualitatively similar to the magnetic response of FO/MO SLs[6] which has been explained using the same model for Gd/Fe multilayer system and of LSMO/SRO SL[7] systems. These SLs are typical anti-parallel systems. In this paper, we explain the magnetic behavior of SLs by a model in which we consider the interfaces as AFM layers with comparable thickness to the SL's FM layers (Fig. 9.4(a)). Under an applied magnetic field, ferrimagnetic layers and anti-ferromagnetic interfaces are switched. The M-H curves of SLs are sum of those of FM and AFM layers (Fig. 9.4(b)). Note that, in this model, the relative magnitude of saturation magnetization, coercive fields, and remanences of M-H curves of FM and AFM layers take strong affect to the shape of SLs' M-H curves. The relative magnitudes shown in the Fig. 9.4(b) are just one typical case. All magnetizations are calculated for the whole SL's volume.

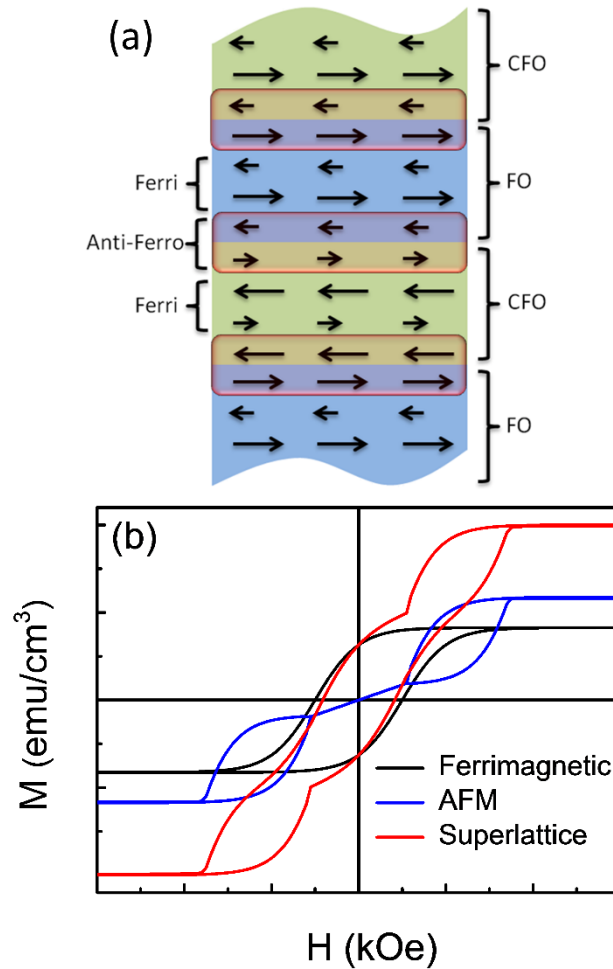


Fig. 9. 4. Schematic illustration of (a) spin ordering of SL where an anti-ferromagnetic layer is formed at the interfaces, (b) M-H curves of SL which is the sum of those of AFM and FM layers.

9.3.3 Transport properties

Figure 9.5(a) shows the temperature dependent electrical resistivity of SLs in compare with CFO and FO single thin films measured using the dc four-probe method in the Van der Pauw configuration. The curves show the apparent Verwey (first order metal-insulator transition) transition in FO thin film around 105 K and the semiconducting behavior in CFO thin film and SLs without Verwey transition. Note that the majority conducting mechanism in Fe_3O_4 is well

known as hopping electron between cations Fe^{2+} and Fe^{3+} . The Verwey transition occurred in this thin film can be explained by a charge ordering (CO) of the Fe^{2+} and Fe^{3+} states on the B sites in alternating layers, although this was not confirmed[12]. For case of CFO, the conducting mechanism is the activation of electron from valance to conduction band, leading to the semiconducting behavior without Verwey transition. The Verwey transition is not observed in SLs which can be easily understood by the presence of both CFO and FO layers. The FO conduction is dominant above Verwey temperature, while CFO conduction is dominant below Verwey temperature. On the other hand, the electrical resistivity of sample $25\text{\AA}/25\text{\AA}$ is smaller than that of sample $100\text{\AA}/100\text{\AA}$. This observation can be explained due to the rough surface of sample $100\text{\AA}/100\text{\AA}$ as shown in RHEED pattern, lead to an enhancement of scattering at the interfaces and increase resistivity.

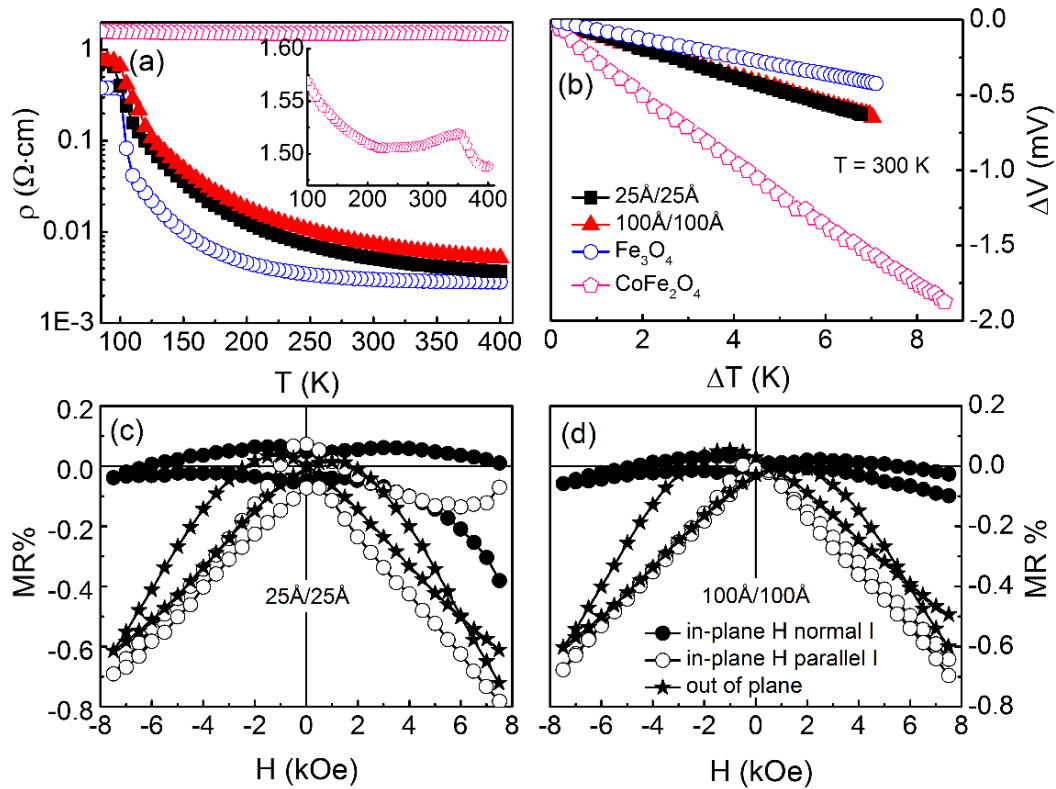


Fig. 9. 5. (a) Temperature dependent electrical resistivity of SLs in compare with that single thin films. The inset is that of CoFe_2O_4 thin film, (b) ΔV vs ΔT curves at 300 K, (c) and (d) Magneto-resistance of SLs $25\text{\AA}/25\text{\AA}$ and $100\text{\AA}/100\text{\AA}$ at 300 K in three directions: out-of-plane and in-plane with magnetic field H parallel and normal to current I .

The role of interfaces was further studied by magneto-resistance (MR) measurements as shown in Fig. 9.5(b) and (c). The MR measurements were taken with an applied magnetic field: out-of-plane (i), in-plane and parallel (ii), in-plane and perpendicular (iii) to the current direction at room temperature. Negative MR values were observed in all cases of measurement as shown in Fig. 9.5(b) and (c). The MR effect is the change of resistance in the presence of applied magnetic field due to Lorentz force and the change of magnetization with magnetic field. The negative MR is usually occurred in ferri/ferromagnetic materials. In these materials, increase (decrease) scattering induced by the presence of applied magnetic field leads to increase

(decrease) resistance, hence, lowering (raising) negative MR or raising (lowering) positive MR of the materials. Usually, ferromagnetic materials present an anisotropic magneto-resistance (AMR) due to the spin-orbit coupling, where the s electron (conduction electrons) are scattered by the unquenched part of angular momentum of 3d electrons. The presence of the applied magnetic field tends to align the magnetic moment of the ferromagnetic material along the field direction. Due to the deformation of 3d electron cloud under the applied magnetic field, the cross-section scattering is higher when the field is parallel than that when the field is perpendicular to the current. As a result, the negative MR is smaller when the field is parallel than that when the field is perpendicular to the current. Here, the field is perpendicular to the current in both cases (i) and (iii). Based on these arguments, it is expected to obtain smaller MR(ii) than MR(i) and MR(iii). To compare MR(i) and MR(iii), we note that in thin films, the easy axes are located in-plane due to the shape anisotropy. The directional orientation of magnetic moment along in-plane is easier than along out-of-plane. Therefore, the cross-section scattering is larger in case (i). As a result, MR(i) is smaller than MR(iii). Hence the expected order of MR values in magnetic thin films is $MR(ii) < MR(i) < MR(iii)$. However, we observed a different order, $MR(iii) < MR(i) < MR(ii)$. This observation can only be explained by the presence of interfaces which induce additional scatterings. Maximum negative MR is achieved in the case (ii), because the charge carriers are weakly affected by Lorentz force and interfaces. In case (i), Lorentz force bends the electrons' trajectories along in-plane, leading to increase scattering and decrease negative MR. In case (iii) the charge carriers are forced to move across the interfaces and undergo much scattering at interfaces. Hence, minimum negative MR is achieved in this case.

9.4 Conclusion

The SLs [CFO(25Å)/FO(25Å)]₄₀ and [CFO(100Å)/FO(100Å)]₁₀ have been fabricated on MgO (100) substrate by molecular beam epitaxy (MBE). The epitaxial growths of SLs were indicated by RHEED patterns and HR-TEM image. The magnetic and transport properties of SLs provided the strong evidences for the presence of SLs configuration. An AFM ordering at the interfaces was observed. The anomalous shape of M-H curves of SLs has been explained as the sum of those of AFM interfaces and FM layers. Interfaces between layers with AFM ordering and the roughness interfaces (surfaces) also released many scattering centers and take a strong affect to transport properties of SLs. Our work showed the role of interfaces on the physical properties in SL systems which is important for spintronic applications.

9.5 References

- [1] A. V. Ramos, J. B. Moussy, M. J. Guittet, M. Gautier-Soyer, C. Gatel, P. Bayle-Guillemaud, B. Warot-Fonrose, and E. Snoeck, *Phys. Rev. B - Condens. Matter Mater. Phys.* **75**, 1 (2007).
- [2] A. V. Ramos, S. Matzen, J. B. Moussy, F. Ott, and M. Viret, *Phys. Rev. B - Condens. Matter Mater. Phys.* **79**, 2005 (2009).
- [3] M. G. Chapline and S. X. Wang, *J. Appl. Phys.* **97**, 10C915 (2005).
- [4] Y. Suzuki, R.B. van Dover, E. M. Gyorgy, J. M. Phillips, and R. J. Felder, *Phys. Rev. B* **53**, 14016 (1996).
- [5] Z. He, J. A. Koza, G. Mu, A. S. Miller, E.W. Bohannon, and J. A. Switzer, *Chem. Mater.* **25**, 223 (2013).
- [6] S. C. Lin, K. M. Kuo, and G. Chern, *J. Appl. Phys.* **109**, 07C116 (2011).
- [7] M. Ziese, I. Vrejoiu, and D. Hesse, *Appl. Phys. Lett.* **97**, 2009 (2010).
- [8] M. Ziese, I. Vrejoiu, E. Pippel, P. Esquinazi, D. Hesse, C. Etz, J. Henk, A. Ernst, I. V. Maznichenko, W. Hergert, and I. Mertig, *Phys. Rev. Lett.* **104**, 1 (2010).
- [9] A. Lisfi and C.M. Williams, *J. Appl. Phys.* **93**, 8143 (2003).
- [10] S. K. Arora, H.C. Wu, R. J. Choudhary, I. V. Shvets, O. N. Mryasov, H. Yao, and W. Y. Ching, *Phys. Rev. B - Condens. Matter Mater. Phys.* **77**, 2 (2008).
- [11] G. A. Sawatzky, F. Van Der Woude, and A. H. Morrish, *J. Appl. Phys.* **39**, 1204 (1968).
- [12] J.P. Wright, J. P. Attfield, and P. G. Radaelli, *Phys. Rev. Lett.* **87**, 2664011 (2001).

APPENDIX 2: TUNING TRANSPORT AND MAGNETIC PROPERTIES OF $\text{Co}_x\text{Fe}_{3-x}\text{O}_4$ THIN FILMS BY Co CONTENT

(SUBMITTED to Journal of Alloys and Compounds)

We systematically investigated the influence of the Co content on the magnetic and transport properties of spinel $\text{Co}_x\text{Fe}_{3-x}\text{O}_4$ ($0 \leq x \leq 1$) thin films on MgO (001) substrates prepared by molecular beam epitaxy. Our films exhibited the spinel structure as expected. The Verwey transition was clearly observed in Fe_3O_4 and $\text{Co}_{0.6}\text{Fe}_{2.4}\text{O}_4$, while it disappeared with higher Co contents. Electrical resistivity increased with the Co content from $0.003 \text{ } \Omega\text{-cm}$ for $x = 0$ to $1.5 \text{ } \Omega\text{-cm}$ for $x = 1$ at 300 K. As expected, magnetization curves show an increase of the coercive fields of the samples with the Co content. In addition, the samples reveal complex magnetic properties that are explained by a reorientation of the anisotropy easy axis from the crystal $\langle 111 \rangle$ directions to the $\langle 100 \rangle$ directions with the Co content.

10.1 Introduction

The first magnetic material, magnetite Fe_3O_4 , discovered and used during Ancient Greece, still attracts attentions because of its puzzling properties. It is a ferrimagnet with an inverse spinel structure (lattice constant, $a = 8.397 \text{ } \text{\AA}$), showing half-metallic nature and high Curie temperature (T_C) up to 850 K. This material has a first order metal-insulator transition at 120 K, called Verwey transition. The inverse spinel crystal structure of Fe_3O_4 can be expressed as $[\text{Fe}^{3+}]_A[\text{Fe}^{2+}\text{Fe}^{3+}]_B\text{O}_4$, where A denoted the tetrahedrally coordinated Fe^{3+} (A-site) and B denoted the octahedral sites (B-site) [1]. The ferrimagnetism in Fe_3O_4 is due to the antiparallel alignment of the magnetic moments between the two B cations and the single A cation. The electrical conduction in ferrite originates from the superposition of two transport mechanisms,

small-polaron (*sp*) band and *sp* hopping conduction [2]. Recently, researchers have focused on mixed ferrite, especially with 3d transition metals such as Co, Mn, Zn, Ni, Cu, and Cr. It has been reported that the di-valences like Cr^{2+} and Mn^{2+} tend to occupy the A sites, while ions Mg^{2+} , Co^{2+} , Ni^{2+} and Cu^{2+} tend to occupy the B sites in the inverse spinel structure [3,4]. Among them, Co has very large magneto-crystalline anisotropy, which is expected to be of interest because the replacements of Fe ions by Co ions will not only affect the transport properties but also the magnetic properties of ferrite. The fraction of divalent cations that reside on the octahedral site was defined as inverse parameter, λ , where $\lambda = 0$ for normal spinel and 1 for inverse spinel; for example, in CoFe_2O_4 , λ ranges from 0.76 to 0.98 [5]; for random distribution between two kinds of site, $\lambda = 0.67$ [4]. Mössbauer spectra of CoFe_2O_4 supported $\lambda = 0.67$ [6] and Rahman *et al.* estimated $\lambda = 0.54$ [7]. This inverse parameter has a strong effect on the electrical and magnetic properties of bulk ferrite[8]. CoFe_2O_4 has been widely used in applications such as magnetic recording, magnetic stress sensors, spin filtering, millimeter-wave filters, telecommunication equipment, and bio-molecular drug delivery [8–11], etc. There were several reports on the influence of Co concentration to the physical properties of ferrite. However, to the best of our knowledge, the systematic study of the effects of large Co content on the transport and magnetic properties of epitaxial $\text{Co}_x\text{Fe}_{3-x}\text{O}_4$ thin films has not been reported.

In this paper, we report on the influence of Co content on the magnetic and transport properties of spinel $\text{Co}_x\text{Fe}_{3-x}\text{O}_4$ ($0 \leq x \leq 1$) thin films. With the increase of Co content the Verwey metal-insulator transition of Fe_3O_4 was shifted to higher temperature and eventually disappeared with large Co content. With increasing Co concentration the electrical resistivity can be tuned over 3 orders of magnitude. Coercive field increased, while saturation magnetization decreased with Co content. More surprisingly a non-zero remanence is observed in the out of plane

magnetization curves. This is attributed to an enhancement of the out of plane magnetic anisotropy due to the strains in the films.

10.2 Experiment

$\text{Co}_x\text{Fe}_{3-x}\text{O}_4$ ($x = 0.0, 0.6, 0.8, \text{ and } 1.0$) thin films were epitaxially grown on MgO (001) substrates by MBE (VG Semicon, Inc.). The MgO substrate was initially cleaned with methanol before being loaded into the vacuum chamber. After pre-heating at 600 °C for 30 minutes in ultra-high vacuum (UHV), the substrate was cooled down to 400 °C, and maintained at that temperature during the growth. The base pressure of the growth chamber was $\sim 10^{-9}$ Torr. Atomic oxygen gas was then applied using an oxygen cracking cell. The films were grown by the co-deposition of Co and Fe using effusion cells under an oxygen partial pressure of 10^{-6} Torr. The evaporation rates were determined using a quartz crystal thickness monitor. The expected film thickness was 200 nm. The quality of the films was monitored by *in-situ* reflection high energy electron diffraction (RHEED). The crystal structure of the samples was characterized by X-ray diffraction (XRD). The composition of films was determined after deposition by electron probe micro-analyzer (EPMA). A four-probe Van der Pauw configuration was employed to measure electrical resistivity. The charge carrier type in the samples was deduced from the slope of ΔV vs ΔT curves using a differential method. The magnetic properties of the films have been examined in-plane and out-of-plane by an alternating gradient field magnetometer (AGFM) and a superconducting quantum interference device (SQUID) magnetometer (Quantum Design, Inc.) with the applied magnetic field up to 25 and 75 kOe, respectively.

10.3 Results

Figure 10.1 shows the RHEED patterns of the $\text{Co}_x\text{Fe}_{3-x}\text{O}_4$ films along the [100] azimuth taken after film growth. The cleaned MgO substrate showed a good RHEED pattern with Kikuchi lines, as shown in the inset of Fig. 10.1 (a). Streaky RHEED patterns were observed in all samples, indicating the epitaxial growth and smooth surface of the samples on MgO substrate.

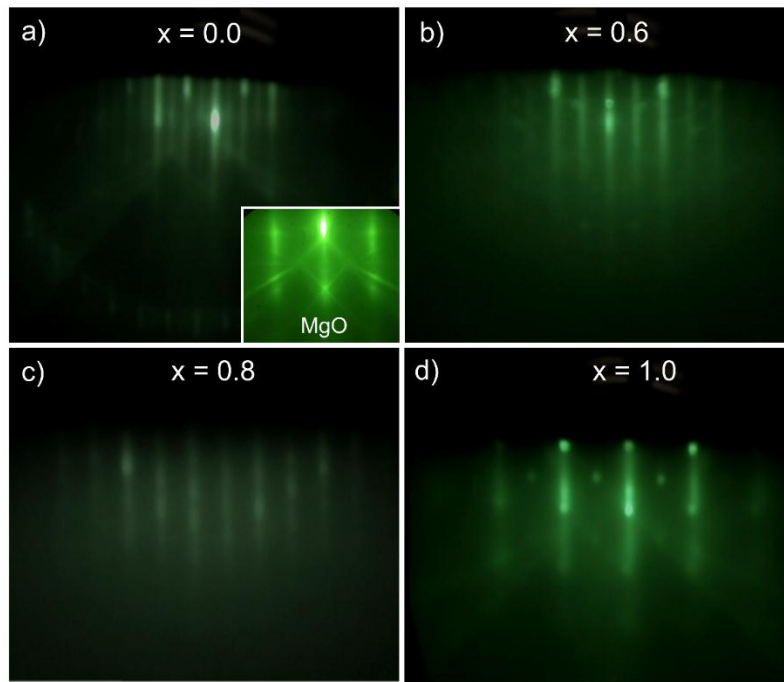


Fig. 10. 1. RHEED patterns of $\text{Co}_x\text{Fe}_{3-x}\text{O}_4$ thin films; (a) $x = 0.0$, (b) $x = 0.6$, (c) $x = 0.8$, and (d) $x = 1.0$. The inset in Fig. 10(a) is that of MgO substrate.

The pattern also indicated a surface reconstruction in our films. The relation between lattice constant of a crystal and its RHEED lines spacing is expressed as

$$a \sim \frac{1}{d} \quad (1)$$

where, a is a -axis lattice constant of the crystal and d is the RHEED lines spacing. Based on the relation (1), we may estimate the lattice constant of the film with standard error of 0.1%.

The lines spacing of MgO is two times larger than that of the films, indicating the double lattice constant of the films compared to that of the substrate in agreement with theoretical values.

The crystalline structures of the $\text{Co}_x\text{Fe}_{3-x}\text{O}_4$ films on MgO (001) substrate were examined by θ - 2θ scan XRD experiment, as illustrated in Fig. 10.2. All films exhibited a single phase with an excellent crystalline quality on MgO (001) substrate, which can be indexed in a spinel structure. With the presence of Co, there is a slight shift of (008) peaks toward to the right. The lattices constants were calculated from (008) peaks; 8.365, 8.357, 8.360, and 8.360 Å for samples $x = 0.0, 0.6, 0.8,$ and $1.0,$ respectively. These values indicated a decrease of lattice constants with the presence of Co. Compared to the bulk values of Fe_3O_4 (8.397 Å) and CoFe_2O_4 (8.388 Å), our films exhibited tensile strains; 0.38% and 0.36% for $x = 0.0$ and $x = 1.0,$ respectively. These observations are consistent with the substitution of Co into Fe site because of the smaller atomic radius of Co (135 pm) compared to the one of Fe (140 pm) [12].

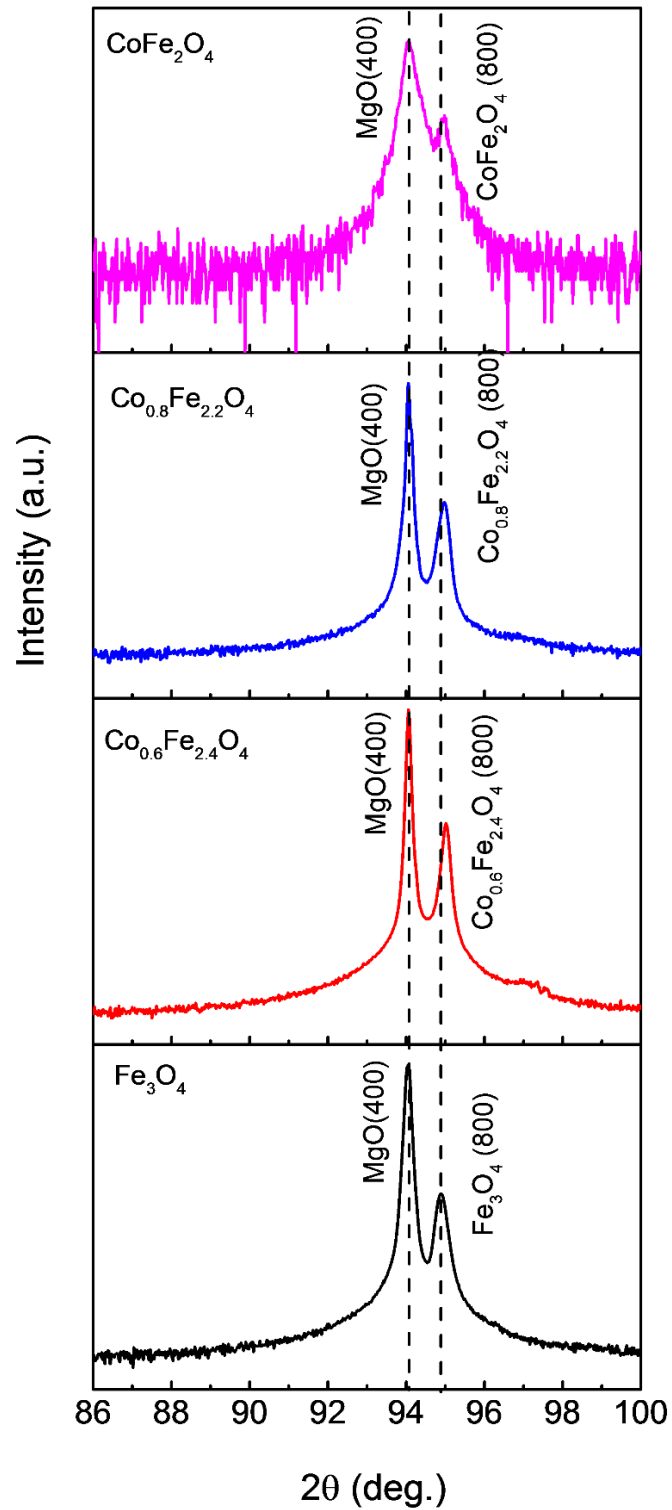


Fig. 10. 2. XRD patterns of $\text{Co}_x\text{Fe}_{3-x}\text{O}_4$ thin films on the MgO (001) substrate at various Co concentrations; $x = 0.0$, $x = 0.6$, $x = 0.8$, and $x = 1.0$. All films show spinel crystal structure.

Figure 10.3(a) shows the effects of Co doping content on the electrical resistivity of $\text{Co}_x\text{Fe}_{3-x}\text{O}_4$ in the temperature range from 410 K down to 85 K, which is below the Verwey transition temperature of Fe_3O_4 . For all samples the electrical resistivity decreased with increasing temperature. The introduction of Co atoms into ferrite shows an increasing electrical resistivity over three orders of magnitude from $0.003 \text{ } \Omega\text{-cm}$ for $x = 0.0$ to $1.5 \text{ } \Omega\text{-cm}$ for $x = 1.0$ at 300 K. A Verwey transition was clearly observed in the Fe_3O_4 at around 105 K in agreement with previous report [13,14]. The observation of a Verwey transition also confirmed the high quality of our un-doped film. With the introduction of small Co content, the Verwey transition temperature increases up to 115 K in the $\text{Co}_{0.6}\text{Fe}_{2.4}\text{O}_4$ film. On the other hand, the Verwey transition was not observed for higher Co contents. The conduction in ferrites can be explained by hopping models, where the electrical conduction of ferrite is dominated by electron hopping between Fe^{2+} and Fe^{3+} cations present at octahedral B sites. Hopping rate increases with temperature due to the increase in thermal energy compared to the hopping barrier height [15]. In contrast, in CoFe_2O_4 electron hopping is not possible anymore and electron conduction can only occur by thermal activation of electrons from the valance band to the conduction band. Therefore, the resistivity mainly depends on the size of band gap. J. A. Moyer *et al.* [5] reported that when doping CoFe_2O_4 with Fe the introduction of Fe^{2+} ions produces an increase of the density of states at the fermi level resulting in a shift of the Fermi level with respect to the top of the valance band. In summary the resistivity measurements show that the replacement of Fe ions by Co ions results in an increase in electrical resistivity originating from the gradual suppression of the electron hopping mechanism, and in a shift and eventually the disappearance of Verwey transition. Interestingly, a transition in the temperature dependent resistivity was observed at 365 K in CoFe_2O_4 as shown in Fig. 10.3(a). Note that in bulk form, CoFe_2O_4 exhibited no transition above room temperature [16]. However, a similar transition has been

reported in the CoFe_2O_4 nanostructures around 330 K [7] and 370 K [17] assigned to a semiconductor to metallic transition. These authors interpreted this transition by the coexistence of cation-anion-cation (c-a-c) and cation-cation (c-c) interaction in rock-salt-structures.

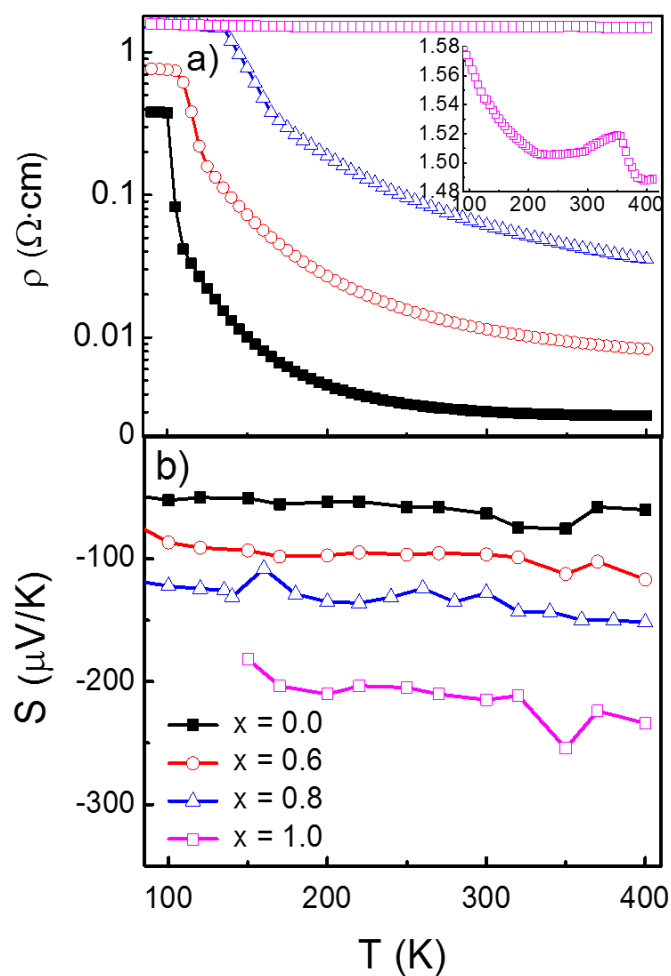


Fig. 10. 3. Temperature dependence of (a) electrical resistivity and (b) Seebeck coefficient with different Co concentrations; $x = 0.0, 0.6, \text{ and } 0.8$, and 1.0 . The inset of Fig. 1(a) is a magnification of temperature dependent resistivity of sample $x = 1.0$.

Figure 10.3(b) shows the temperature dependent Seebeck coefficient. The sign of the Seebeck coefficient was negative, indicating dominant n-type conduction. The Seebeck coefficient

increase with the increase in Co concentration is consistent with the trend in electrical resistivity; from $-63 \mu\text{V/K}$ for $x = 0.0$ to $-215 \mu\text{V/K cm}$ for $x = 1.0$ at 300 K. A peak at 350 K was also observed in sample CoFe_2O_4 that is consistent with the transition already mentioned in the electrical resistivity.

In order to investigate the influence of the Co content on the magnetic properties of the ferrites we have measured the magnetization as a function of magnetic field using an AGFM set up. Figure 10.4 shows room temperature in-plane and out-of-plane M-H curves of our films. However, the AGFM maximum magnetic field is 25 kOe and even if this field was large enough to reach the reversible part of the magnetization processes, it was not possible to fully saturate the magnetization of the samples. Therefore, the AGFM measurements were complemented by SQUID measurements in order to properly evaluate saturation magnetizations. The evolution of saturation magnetization versus Co content is shown in Fig. 10.4(c). Saturation magnetization is decreasing, with the Co content. The decrease of saturation magnetization with the Co content can be interpreted as following. The net magnetization of spinel ferrite can be given by $M = \sum M_{\text{B-sites}} - \sum M_{\text{A-sites}}$, where $\sum M_{\text{A-sites}}$ and $\sum M_{\text{B-sites}}$ are the contributions to the net magnetization by the cations on the tetrahedral A and octahedral B-sites, respectively [16]. The Co^{2+} ions (magnetic moment $3\mu_{\text{B}}$) in the Co-ferrite system tend to replace Fe ions (magnetic moment $4.9 \sim 6.7 \mu_{\text{B}}$) in either the tetrahedral A-sites or octahedral B-sites, resulting in an overall decrease in the total magnetic moment. The Fig. 10.4(c) and (d) also show the evolution of the remnant magnetizations (M_r/M_s) and of the coercive fields as a function of the Co content. It is surprising that the out-of-plane remnant magnetizations and coercive fields are increasing with the Co content and eventually decrease again when $x = 1$. In-plane coercive fields only increase with the Co content. An increase of the coercive fields is expected with the introduction of Co because Co ions provide a strong contribution to the

magneto-crystalline anisotropy. The most likely explanation of the evolution of the out-of-plane remnant magnetizations and coercive fields is that a reorientation of the magneto-crystalline anisotropy takes place with the Co content. Indeed, in bulk Fe_3O_4 the magnetic anisotropy easy axes are along the $\langle 111 \rangle$ directions while in bulk CoFe_2O_4 the magnetic anisotropy easy axes are along the $\langle 100 \rangle$ directions. When a small content of Co is introduced, the anisotropy is enlarged but the Fe_3O_4 magnetic anisotropy directions are not modified. Since the growth direction of the samples is $[100]$, increasing the anisotropy along the $[111]$ direction will result in an out-of-plane contribution of the magnetic anisotropy that overcomes (at least partly) the demagnetizing energy. This explains the increase of the out-of-plane remnant magnetizations and coercive fields until the Co content becomes large enough to allow a reorientation of the magnetic easy axes along the $\langle 100 \rangle$ directions. $\langle 100 \rangle$ directions are situated as well out of the film plane as in the film plane, therefore no out-of-plane contribution should be found and in such case out-of-plane remnant magnetizations and coercive fields should be negligible. Our experimental results show that in agreement with this description the remnant magnetization and out-of-plane coercive field decrease when $x = 1$ but stay however significantly larger than zero. This might be due to an enhancement of the out-of-plane magnetic anisotropy due to the strains in the films that have been discussed in a previous paragraph. It can also be noticed that with the presence of Co, a shoulder is observed in sample $x = 0.6$ and more clearly in sample $x = 0.8$ but disappeared in sample $x = 1.0$. Similar shoulders are observed in $\text{CoFe}_2\text{O}_4/\text{Fe}_3\text{O}_4$ bi-layer systems or in any bi-layer systems which consist of one soft and one hard magnetic layers [11,18–20]. However, we do not think that the observation of a shoulder in the magnetization curves of samples $x = 0.6$ and 0.8 is due to the coexistence of soft and hard magnetic phases since this would require a non-homogeneous distribution of the Co ions into the samples. The observation of this shoulder is probably related

to the complex magnetic anisotropy orientations discussed above that might lead to complex magnetization reversal processes in samples in which canted and/or perpendicular anisotropy directions compete with demagnetizing field.

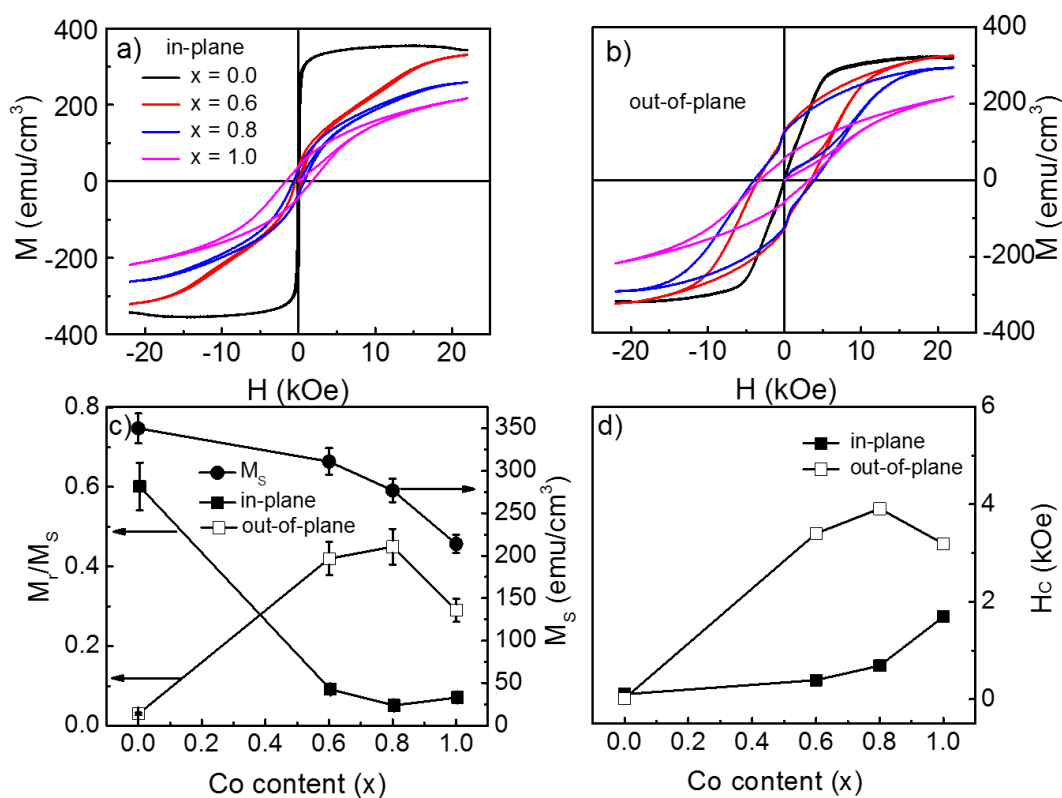


Fig. 10. 4. Room temperature magnetic field dependent magnetization by AGFM for (a) in-plane and (b) out of plane for samples; $x = 0.0, 0.6, 0.8,$ and 1.0 . (c) saturation magnetization taken from SQUID measurements and remnant magnetizations (M_r/M_s) as a function of Co content. (d) in and out-of-plane coercive fields taken from AGFM measurements as a function of Co content.

10.4 Conclusion

Through the Co content we have shown that it is possible to tune the magnetic and transport properties of epitaxial $\text{Co}_x\text{Fe}_{3-x}\text{O}_4$ ($0 \leq x \leq 1$) thin films. The Verwey metal-insulator transition was clearly shown in the samples with $x = 0.0$ and 0.6 but disappeared in the samples with $x = 0.8$ and 1.0 . The electrical resistivity increased with the Co content and can be tailored over more than 3 orders of magnitude. A semiconductor to metallic transition was observed at 365 K in the CoFe_2O_4 film. The samples reveal complex magnetic properties that are explained by a reorientation of the anisotropy easy axis from the $\langle 111 \rangle$ directions to the $\langle 100 \rangle$ directions with the Co content. In summary the magnetic and transport properties of the films can be easily controlled by changing the Co concentration, indicating a possibility to incorporate $\text{Co}_x\text{Fe}_{3-x}\text{O}_4$ films as ferromagnetic electrodes in spintronic devices.

10.5 References

- [1] J. P. Wright, J. P. Attfield, and P. G. Radaelli, *Phys. Rev. Lett.* **87**, 2664011 (2001).
- [2] D. Ihle and B. Lorenz, *J. Phys. C Solid State Phys.* **18**, L647 (1985).
- [3] D. Tripathy, A. O. Adeyeye, C. B. Boothroyd, and S. N. Piramanayagam, *J. Appl. Phys.* **101**, 1 (2007).
- [4] J. D. Dunitz and L. E. Orgel, *J. Phys. Chem. Solids.* **3**, 318 (1957).
- [5] J. A. Moyer, C. A. F. Vaz, E. Negusse, D. A. Arena, and V. E. Henrich, *Phys. Rev. B - Condens. Matter Mater. Phys.* **83**, 1 (2011).
- [6] N. Moumen and M. P. Pileni, *Chemi. Mater.* **4756**, 1128 (1996).
- [7] A. U. Rahman, M. A. Rafiq, S. Karim, K. Maaz, M. Siddique, and M. M. Hasan, *J. Phys. D. Appl. Phys.* **44**, doi:10.1088/0022-3727/44/16/165404 (2011).
- [8] E. V. Gopalan, P. A. Joy, I. A. Al-Omari, D. S. Kumar, Y. Yoshida, and M. R. Anantharaman, *J. Alloys Compd.* **485**, 711 (2009).
- [9] Y. Cedeño-Mattei, O. Perales-Perez, M. S. Tomar, F. Roman, P. M. Voyles, and W. G. Stratton, *J. Appl. Phys.* **103**, 4 (2008).
- [10] T. Saragi, N. Syakir, T.H. Nainggolan, C. Alboin, and Risdiana, *AIP Conference Proceedings* **1554**, 123 (2013).
- [11] A. V. Ramos, J. B. Moussy, M. J. Guittet, M. Gautier-Soyer, C. Gatel, P. Bayle-Guillemaud, B. Warot-Fonrose, and E. Snoeck, *Phys. Rev. B - Condens. Matter Mater. Phys.* **75**, 1 (2007).

- [12] N. Viart, G. Rebmann, G. Pourroy, J. L. Loison, G. Versini, F. Huber, C. Ulhaq-Bouillet, C. Mény, P. Panissod, and L. Saviot, *Thin Solid Films*. **471**, 40 (2005).
- [13] D. Reisinger, P. Majewski, M. Opel, L. Alff, and R. Gross, *Appl. Phys. Lett.* **85**, 4980 (2004).
- [14] E. J. W. VERWEY, *Nature*. **144**, 327 (1939).
- [15] J. Smith and H. P. J. Wijn, *Ferites* NewYork Wiley, 1959, pp 229–234.
- [16] I. C. Nlebedim, E. M. Levin, R. Prozorov, K. W. Dennis, R. W. McCallum, and D. C. Jiles, *IEEE Trans. Magn.* **49**, 4269 (2013).
- [17] A. Arunkumar, D. Vanidha, K. Oudayakumar, S. Rajagopan, and R. Kannan, *J. Appl. Phys.* **114**, 1 (2013).
- [18] M. G. Chapline and S. X. Wang, *J. Appl. Phys.* **97**, 10C915 (2005).
- [19] Y. Suzuki, R. B. van Dover, E. M. Gyorgy, J. M. Phillips, and R. J. Felder, *Phys. Rev. B*. **53**, 14016 (1996).
- [20] A. V. Ramos, S. Matzen, J.B. Moussy, F. Ott, and M. Viret, *Phys. Rev. B - Condens. Matter Mater. Phys.* **79**, 2005 (2009).

APPENDIX 3: SEEBECK COEFFICIENT AND ELECTRICAL

RESISTANCE MEASUREMENT SYSTEM (제벡계수 및

전기저항 측정장치)

등록특허 10-1690427



(19) 대한민국특허청(KR)

(45) 공고일자 2016년12월27일

(12) 등록특허공보(B1)

(11) 등록번호 10-1690427

(24) 등록일자 2016년12월21일

- | | |
|--|---|
| <p>(51) 국제특허분류(Int. Cl.)
 <i>G01R 27/02</i> (2006.01) <i>G01R 1/073</i> (2006.01)
 <i>G01R 27/08</i> (2006.01) <i>H01L 35/28</i> (2006.01)</p> <p>(52) CPC특허분류
 <i>G01R 27/02</i> (2013.01)
 <i>G01R 1/073</i> (2013.01)</p> <p>(21) 출원번호 10-2015-0131434</p> <p>(22) 출원일자 2015년09월17일
 심사청구일자 2015년09월17일</p> <p>(56) 선행기술조사문헌
 JP07324991 A
 KR1020130028377 A
 KR1020150007686 A
 KR1020150037458 A</p> | <p>(73) 특허권자
 울산대학교 산학협력단
 울산광역시 남구 대학로 93(무거동)</p> <p>(72) 발명자
 조성래
 부산광역시 해운대구 해운대해변로 349-25, 101동
 1301호 (중동, 해운대중동두산위브아파트)</p> <p>웬 반 랑
 울산 남구 대학로</p> <p>등 안 투안
 울산 남구 대학로</p> <p>(74) 대리인
 특허법인다나</p> |
|--|---|

전체 청구항 수 : 총 13 항

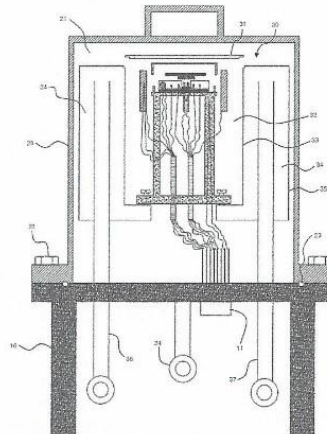
심사관 : 김려원

(54) 발명의 명칭 제벡계수 및 전기저항 측정장치

(57) 요약

본 발명은 제벡계수 및 전기저항 측정장치에 관한 것으로, 특히 77K 내지 1300K의 온도 영역에서 열전 소재의 제벡계수 및 전기저항을 측정하는 장치에 관한 것이다.

대표도 - 도1



(52) CPC특허분류

G01R 27/08 (2013.01)

H01L 35/28 (2013.01)

이 발명을 지원한 국가연구개발사업

과제고유번호 G031590912

부처명 산업통상자원부

연구관리전문기관 한국에너지기술평가원

연구사업명 에너지기술개발사업

연구과제명 전자구조변형과 최적도핑을 통한 ZT=2.5 고효율 전이금속반도체 열전 신물질 개발(1)

기여율 1/1

주관기관 울산대학교 산학협력단

연구기간 2013.12.01 ~ 2014.09.30

명세서

청구범위

청구항 1

밀봉된 내부공간을 갖고, 내부공간에 진공 또는 고압가스 분위기 형성이 가능한 진공챔버;
 진공챔버의 내부공간에 설치되는 내통, 내통의 인쪽에 형성되는 제1공간, 내통보다 크기가 크고 내통과 밀봉되도록 연결되는 외통, 내통과 외통 사이에 형성되는 밀봉된 공간으로서 냉각매체를 수용하는 제2공간을 구비하는 냉각챔버;
 냉각챔버의 제2공간과 연결되도록 설치되고, 냉각챔버에 냉각매체가 유입되는 냉각매체 유입관;
 냉각챔버의 제2공간과 연결되도록 설치되고, 냉각챔버로부터 냉각매체가 배출되는 냉각매체 배출관;
 냉각챔버의 제1공간에 설치되는 제1메탈블록;
 냉각챔버의 제1공간에 설치되고, 제1메탈블록과 이격 배치되는 제2메탈블록;
 제1메탈블록 또는 제2메탈블록에 설치되고, 온도 구배를 형성하는 제1히터;
 냉각챔버의 제1공간에 제1메탈블록 및 제2메탈블록을 둘러싸도록 설치되는 제2히터;
 냉각챔버의 제1공간 및 메탈블록 상부에 설치되고, 샘플을 지지하는 샘플홀더;
 제1메탈블록에 형성되는 제1프로브;
 제2메탈블록에 형성되는 제2프로브;
 제1메탈블록 및 제2메탈블록 사이에 형성되는 제3프로브;
 제1메탈블록 및 제2메탈블록 사이에 형성되고, 제3프로브와 이격 배치되는 제4프로브;
 제1메탈블록 및 제2메탈블록 각각에 설치되어 온도 구배를 측정하는 제1열전대 및 제2열전대를 포함하는 제백계수 및 전기저항 측정장치.

청구항 2

제1항에 있어서,
 77K 내지 1300K의 온도 영역에서 열전 소재의 제백계수 및 전기저항을 측정 가능한 것을 특징으로 하는 제백계수 및 전기저항 측정장치.

청구항 3

제1항에 있어서,
 냉각매체는 액체 질소, 고압기체, 또는 물인 것을 특징으로 하는 제백계수 및 전기저항 측정장치.

청구항 4

제1항에 있어서,
 냉각매체 유입관의 출구 및 냉각매체 배출관의 입구는 각각 제2공간의 상단부에 배치되는 것을 특징으로 하는 제백계수 및 전기저항 측정장치.

청구항 5

제1항에 있어서,

제2히터는 중공 원통 형상의 실린더 히터인 것을 특징으로 하는 제백계수 및 전기저항 측정장치.

청구항 6

제1항에 있어서,

제1프로브, 제2프로브, 제3프로브, 제4프로브 중 제1프로브 및 제2프로브는 진류를 인가하고, 나머지 제3프로브 및 제4프로브는 전압을 측정하는 것을 특징으로 하는 제백계수 및 전기저항 측정장치.

청구항 7

제1항에 있어서,

제1열전대 및 제2열전대는 샘플의 온도 구배를 측정하고, 제1프로브 및 제2프로브는 전압을 측정하는 것을 특징으로 하는 제백계수 및 전기저항 측정장치.

청구항 8

제1항에 있어서,

제1열전대 및 제2열전대는 온도 구배를 측정하기 위해 같은 전극으로 직렬 연결되는 것을 특징으로 하는 제백계수 및 전기저항 측정장치.

청구항 9

제1항에 있어서,

제3프로브 및 제4프로브는 상하방향으로 이동 가능한 것을 특징으로 하는 제백계수 및 전기저항 측정장치.

청구항 10

제9항에 있어서,

제3프로브 및 제4프로브를 각각 지지하는 승강판; 및 승강판과 나사결합하고 회전에 의해 승강판을 승강시키는 승강조절나사를 추가로 포함하는 제백계수 및 전기저항 측정장치.

청구항 11

제1항에 있어서,

진공챔버의 하부에 설치되는 제1지지대;

진공챔버와 제1지지대 사이를 밀봉하는 밀봉부재;

진공챔버와 제1지지대를 결합시키는 제1결합부재;

진공챔버와 연결되는 진공펌프;

제1지지대에 설치되고, 각 히터, 프로브 및 열전대와 연결되는 멀티핀을 추가로 포함하는 제백계수 및 전기저항 측정장치.

청구항 12

제1항에 있어서,
 냉각챔버의 제1공간에서 제1메탈블록 및 제2메탈블록의 하부에 설치되는 제2지지대;
 제1메탈블록 및 제2메탈블록과 제2지지대 사이에 설치되는 절연체;
 냉각챔버와 제2지지대를 결합시키는 제2결합부재;
 제2히터 및 제2지지대 각각에 설치되는 제3열전대 및 제4열전대;
 냉각챔버의 상단에 개폐 가능하게 설치되는 제1캡;
 제2지지대의 상단에 개폐 가능하게 설치되는 제2캡을 추가로 포함하는 제백계수 및 전기저항 측정장치.

청구항 13

제12항에 있어서,
 제2지지대 상부에 설치되는 가이드부재;
 제2캡과 샘플홀더 사이에 설치되고, 가이드부재의 상단이 삽입되는 가이드 홀을 구비하며, 샘플홀더를 압축하는 압축부재를 추가로 포함하는 제백계수 및 전기저항 측정장치.

발명의 설명

기술분야

[0001] 본 발명은 제백계수 및 전기저항 측정장치에 관한 것으로, 특히 77K 내지 1300K의 온도 영역에서 열전 소재의 제백계수 및 전기저항을 측정하는 장치에 관한 것이다.

배경기술

[0002] 제백(Seebeck)효과는 열전 소재의 양단에 온도차를 부여하면 기전력이 발생하는 현상이다. n형 반도체의 경우, 양단간의 온도차가 발생하면, 고온단에 있는 전자들은 저온단에 있는 전자들에 비해 보다 높은 운동에너지를 갖게 된다. 이러한 열적 구동력에 의해, 고온단에 있는 전자들이 에너지를 낮추기 위해 저온단으로 확산하게 된다. 전자들이 고온단에서 저온단으로 이동함에 따라, 고온단은 (+)로, 저온단은 (-)로 대전되어 양단간에 전위차가 발생하게 된다. 이러한 상태가 되면, 다시 고온단으로 전자를 되돌려 보내려는 기전력이 발생하게 되며, 열적 구동력과 기전력이 평형을 이룰 때까지 캐리어의 이동이 진행된다. 이러한 기전력은 소자 양단의 온도차에 비례하게 된다. 한편, p형 반도체의 경우 정공이 주요 캐리어이므로, 기전력의 방향은 n형과 반대가 된다. 이와 같은 열전 소재의 특성을 평가하기 위해 제백계수(Seebeck coefficient)가 사용되며, 제백계수는 다음과 같은 식으로 정의될 수 있다.

[0003] [수학식 1]

[0004]
$$S = \Delta V / \Delta T$$

[0005] 즉, 제백계수(S)는 전압(V)의 변화에 비례하고, 온도(T)의 변화에 반비례함을 알 수 있다. 따라서 열전 소재의 제백계수를 측정하기 위한 방법으로는, 열전 소재의 어느 한 축을 가열하고, 가열원에서 서로 다른 이격거리를 갖는 한 쌍의 포인트의 온도와 전압을 각각 측정하는 방법이 보편화되어 있다.

[0006] 그러나, 기존 제백계수 측정장치는 상온 및 고온 범위에서 측정하는 장치와 저온에서 측정하는 장치로 구분되어 있었다.

발명의 내용

해결하려는 과제

[0007] 본 발명의 목적은 고온 범위뿐만 아니라 저온 범위에서도 열전 소재의 제백계수 및 전기저항을 측정할 수 있는 장치를 제공하는 것이다.

과제의 해결 수단

[0008] 본 발명은 상술한 목적을 달성하기 위해, 밀봉된 내부공간을 갖고, 내부공간에 진공 또는 고압가스 분위기 형성이 가능한 진공챔버; 진공챔버의 내부공간에 설치되는 내통, 내통의 안쪽에 형성되는 제1공간, 내통보다 크기가 크고 내통과 밀봉되도록 연결되는 외통, 내통과 외통 사이에 형성되는 밀봉된 공간으로서 냉각매체를 수용하는 제2공간을 구비하는 냉각챔버; 냉각챔버의 제2공간과 연결되도록 설치되고, 냉각챔버에 냉각매체가 유입되는 냉각매체 유입관; 냉각챔버의 제2공간과 연결되도록 설치되고, 냉각챔버로부터 냉각매체가 배출되는 냉각매체 배출관; 냉각챔버의 제1공간에 설치되는 제1메탈블록; 냉각챔버의 제1공간에 설치되고, 제1메탈블록과 이격 배치되는 제2메탈블록; 제1메탈블록 또는 제2메탈블록에 설치되고, 온도 구배를 형성하는 제1히터; 냉각챔버의 제1공간에 제1메탈블록 및 제2메탈블록을 둘러싸도록 설치되는 제2히터; 냉각챔버의 제1공간 및 메탈블록 상부에 설치되고, 샘플을 지지하는 샘플홀더; 제1메탈블록에 형성되는 제1프로브; 제2메탈블록에 형성되는 제2프로브; 제1메탈블록 및 제2메탈블록 사이에 형성되는 제3프로브; 제1메탈블록 및 제2메탈블록 사이에 형성되고, 제3프로브와 이격 배치되는 제4프로브; 제1메탈블록 및 제2메탈블록 각각에 설치되어 온도 구배를 측정하는 제1열전대 및 제2열전대를 포함하는 제백계수 및 전기저항 측정장치를 제공한다.

[0009] 본 발명에 따른 제백계수 및 전기저항 측정장치는 77K 내지 1300K의 온도 영역에서 열전 소재의 제백계수 및 전기저항을 측정 가능한 것을 특징으로 한다.

[0010] 본 발명에서 냉각매체는 액체 질소, 고압기체, 또는 물일 수 있다.

[0011] 본 발명에서 냉각매체 유입관의 출구 및 냉각매체 배출관의 입구는 각각 제2공간의 상단부에 배치될 수 있다.

[0012] 본 발명에서 제2히터는 중공 원통 형상의 실린더 히터일 수 있다.

[0013] 본 발명에서 전기저항을 측정하기 위해, 제1프로브, 제2프로브, 제3프로브, 제4프로브 중 제1프로브 및 제2프로브는 전류를 인가하고, 나머지 제3프로브 및 제4프로브는 전압을 측정할 수 있다.

[0014] 본 발명에서 제백계수를 측정하기 위해, 제1열전대 및 제2열전대는 샘플의 온도 구배를 측정하고, 제1프로브 및 제2프로브는 전압을 측정할 수 있다.

[0015] 본 발명에서 제1열전대 및 제2열전대는 온도 구배를 측정하기 위해 같은 전극으로 직렬 연결될 수 있다.

[0016] 본 발명에서 제3프로브 및 제4프로브는 상하방향으로 이동 가능하다.

[0017] 본 발명에 따른 장치는 제3프로브 및 제4프로브를 각각 지지하는 승강판; 및 승강판과 나사결합하고 회전에 의해 승강판을 승강시키는 승강조절나사를 추가로 포함할 수 있다.

[0018] 본 발명에 따른 장치는 진공챔버의 하부에 설치되는 제1지지대; 진공챔버와 제1지지대 사이를 밀봉하는 밀봉부재; 진공챔버와 제1지지대를 결합시키는 제1결합부재; 진공챔버와 연결되는 진공펌프; 제1지지대에 설치되고, 각 히터, 프로브 및 열전대와 연결되는 멀티핀을 추가로 포함할 수 있다.

[0019] 본 발명에 따른 장치는 냉각챔버의 제1공간에서 제1메탈블록 및 제2메탈블록의 하부에 설치되는 제2지지대; 제1메탈블록 및 제2메탈블록과 제2지지대 사이에 설치되는 절연체; 냉각챔버와 제2지지대를 결합시키는 제2결합부재; 제2히터 및 제2지지대 각각에 설치되는 제3열전대 및 제4열전대; 냉각챔버의 상단에 개폐 가능하게 설치되는 제1캡; 제2지지대의 상단에 개폐 가능하게 설치되는 제2캡을 추가로 포함할 수 있다.

[0020] 본 발명에 따른 장치는 제2지지대 상부에 설치되는 가이드부재; 제2캡과 샘플홀더 사이에 설치되고, 가이드부재의 상단이 삽입되는 가이드 홀을 구비하며, 샘플홀더를 압축하는 압축부재를 추가로 포함할 수 있다.

발명의 효과

[0021] 본 발명에 따른 장치는 냉각챔버 및 실린더 히터를 구비하여 고온 범위뿐만 아니라 저온 범위에서도 열전 소재의 제백계수 및 전기저항을 측정할 수 있다.

도면의 간단한 설명

[0022] 도 1은 본 발명에 따른 제백계수 및 전기저항 측정장치의 전체 구성을 나타내는 단면도이다.

도 2는 본 발명에 따른 제백계수 및 전기저항 측정장치의 냉각챔버 내부에 설치되는 내부 부품들을 일측에서 나타내는 단면도이다.

도 3은 본 발명에 따른 제백계수 및 전기저항 측정장치의 냉각챔버 내부에 설치되는 내부 부품들을 다른 일측에서 나타내는 단면도이다.

도 4는 본 발명에 따른 제백계수 및 전기저항 측정장치의 냉각챔버 내부에 설치되는 내부 부품들을 위에서 바라본 평면도이다.

도 5는 본 발명에 따라 측정된 온도 변화 대 전압 변화의 그래프이다.

도 6은 본 발명에 따라 측정된 전류 대 전압의 그래프이다.

발명을 실시하기 위한 구체적인 내용

- [0023] 이하, 첨부도면을 참조하여 본 발명을 상세하게 설명한다.
- [0024] 도 1은 본 발명에 따른 제백계수 및 전기저항 측정장치의 전체 구성을 나타내는 단면도이고, 도 2는 본 발명에 따른 제백계수 및 전기저항 측정장치의 냉각챔버 내부에 설치되는 내부 부품들을 일측에서 나타내는 단면도이며, 도 3은 본 발명에 따른 제백계수 및 전기저항 측정장치의 냉각챔버 내부에 설치되는 내부 부품들을 다른 일측에서 나타내는 단면도이고, 도 4는 본 발명에 따른 제백계수 및 전기저항 측정장치의 냉각챔버 내부에 설치되는 내부 부품들을 위에서 바라본 평면도이다.
- [0025] 도 1 내지 4를 참고하면, 본 발명에 따른 제백계수 및 전기저항 측정장치는 제1지지대(10), 멀티핀(11), 진공챔버(20), 내부공간(21), 제1결합부재(22), 밀봉부재(23), 진공펌프(24), 냉각챔버(30), 제1캡(31), 제1공간(32), 내통(33), 제2공간(34), 외통(35), 냉각매체 유입관(36), 냉각매체 배출관(37), 제2지지대(40), 제2결합부재(41), 제3열전대(42), 제2캡(43), 제2히터(50), 제4열전대(51), 제1메탈블록(60), 제2메탈블록(61), 제1히터(62), 절연체(63), 제1프로브(70), 제2프로브(71), 제3프로브(72), 제4프로브(73), 승강판(74), 승강조절나사(75), 샘플홀더(80), 샘플(81), 제1열전대(82), 제2열전대(83), 압축부재(90), 가이드부재(91) 등으로 구성될 수 있다. 모든 부품들은 저온 및 고온 범위에 적합하고 안정된 재료로 제작될 수 있다.
- [0026] 제1지지대(10)는 진공챔버(20)의 하부에 설치되어 진공챔버(20)를 지지하는 역할을 한다. 제1지지대(10)는 도면에 예시된 바와 같이 상판과 이를 받치는 복수의 다리로 구성될 수 있다.
- [0027] 멀티핀(11)은 제1지지대(10)에 설치되고, 각 히터(50, 62), 프로브(70, 71, 72, 73) 및 열전대(42, 51, 82, 83)와 전선을 통해 연결되어 이들을 외부와 연결하는 역할을 한다.
- [0028] 진공챔버(20)는 제1지지대(10) 상부에 설치되고, 밀봉된 내부공간(21)을 갖는다. 내부공간(21)에는 진공 형성이 가능하다. 한편, 일부 소재는 고온 측정으로 인해 증발될 수 있는데, 증발 온도를 증가시키기 위해 또는 다른 목적을 위해, 진공챔버(20) 내부에 고압을 갖는 비활성 가스 분위기를 형성할 수도 있다. 진공챔버(20)에 진공을 형성할 경우, 냉각효율을 개선하여 냉각속도를 빠르게 할 수 있다.
- [0029] 제1결합부재(22)는 제1지지대(10)와 진공챔버(20)를 결합시키는 역할을 하며, 예를 들어 나사결합부재 등을 사용할 수 있다.
- [0030] 밀봉부재(23)는 제1지지대(10)와 진공챔버(20)를 밀봉시키는 역할을 하며, 예를 들어 고무 오링 등을 사용할 수 있다.
- [0031] 진공펌프(24)는 진공챔버(20)와 연결되어 진공챔버(20)의 내부공간(21)에 진공을 형성할 수 있다.
- [0032] 냉각챔버(30)는 진공챔버(20)의 내부공간(21)에 설치되고, 제1캡(31), 제1공간(32), 내통(33), 제2공간(34), 외통(35) 등으로 구성될 수 있다.
- [0033] 제1캡(31)은 냉각챔버(30)의 상단에 개폐 가능하게 설치될 수 있다. 제1캡(31)은 외부로의 열복사를 차단하는 역할도 할 수 있다.
- [0034] 제1공간(32)은 내통(33)의 안쪽에 형성되는 내통(33)의 내부공간으로서, 제1캡(31)에 의해 밀폐될 수 있다.
- [0035] 내통(33)은 예를 들어 원통형으로 구성될 수 있다. 내통(33)의 상부는 개방될 수 있고, 제1캡(31)에 의해 밀폐될 수 있다.

- [0036] 외통(35)은 내통(33)보다 크기(직경)가 크고 내통(33)과 밀봉되도록 연결될 수 있다. 외통(35)은 예를 들어 원동형으로 구성될 수 있다.
- [0037] 제2공간(34)은 내통(33)과 외통(35) 사이에 형성되는 밀봉된 공간으로서 냉각매체를 수용할 수 있다.
- [0038] 내통(33)과 외통(35)의 하부 중앙에는 전선 등을 외부에 연결하기 위한 홀이 형성될 수 있고, 홀은 제2지지대(40)에 의해 밀폐될 수 있다.
- [0039] 냉각매체 유입관(36)은 냉각챔버(30)를 관통하여 냉각챔버(20)의 제2공간(34)과 연결되도록 설치되고, 이를 통해 냉각챔버(30)에 냉각매체가 유입될 수 있다.
- [0040] 냉각매체 배출관(37)은 냉각챔버(30)를 관통하여 냉각챔버(20)의 제2공간(34)과 연결되도록 설치되고, 이를 통해 냉각매체가 냉각챔버(30)로부터 배출될 수 있다.
- [0041] 냉각매체 유입관(36)의 출구 및 냉각매체 배출관(37)의 입구는 도 1에 도시된 바와 같이 각각 제2공간(34)의 상단부에 배치될 수 있고, 이에 따라 냉각매체가 냉각챔버(30)에 머무는 체류시간을 증가시켜 냉각효율을 개선할 수 있다. 냉각매체 유입관(36) 출구 및 냉각매체 배출관(37) 입구의 높이가 낮으면 냉각매체가 냉각챔버(30)에서 얼마 체류하지 못하고 그냥 빠져나올 수 있다.
- [0042] 냉각매체로 액체 질소, 고압 기체, 또는 물 등을 사용할 수 있고, 바람직하게는 액체 질소를 사용할 수 있다. 물을 사용할 경우, 실온에서 고온까지 측정 가능하며, 액체 질소를 사용할 경우 약 77K의 극저온까지 측정 가능하다. 고온으로 가열 시에는 액체질소를 미리 제거할 수 있다.
- [0043] 본 발명에서는 냉각챔버(30)를 설치하고 냉각매체로 액체질소를 사용함으로써, 약 77K의 극저온까지 제백계수 및 전기저항을 측정할 수 있다.
- [0044] 제2지지대(40)는 냉각챔버(30)의 제1공간(32)에 설치될 수 있고, 도면에 예시된 바와 같이 상판과 하판 및 두 판을 연결하는 복수의 다리로 구성될 수 있다.
- [0045] 제2결합부재(41)는 냉각챔버(30)와 제2지지대(40)를 결합시키는 역할을 하며, 예를 들어 나사결합부재 등을 사용할 수 있다.
- [0046] 제3열전대(42)는 제2지지대(40)의 다리 안에 삽입 설치될 수 있고, 주위온도를 측정할 수 있다. 제3열전대(42)로 측정된 온도는 기준 온도로 사용될 수 있다.
- [0047] 제2갭(43)은 제2지지대(40)의 상단에 개폐 가능하게 설치될 수 있다. 제2지지대(40)와 제2갭(43)에 의해 형성되는 밀폐공간에 메탈블록(60, 61) 및 샘플(81) 등이 설치될 수 있다.
- [0048] 제2히터(50)는 냉각챔버(30)의 제1공간(32)에 설치되고, 또한 제1메탈블록(60) 및 제2메탈블록(61) 그리고 샘플(81)을 둘러싸도록 설치된다. 제2히터(50)는 바람직하게는 중공 원통 형상의 실린더 히터일 수 있다. 제2히터(50)를 실린더 히터로 구성함에 따라, 메탈블록(60, 61) 및 샘플(81) 등을 균일하게 가열하여 측정 에러를 줄이고 정확도를 개선할 수 있으며, 가열효율을 개선하여 신속하게 약 1300K의 고온까지 제백계수 및 전기저항을 측정할 수 있다. 제2히터(50)는 주위(ambient) 온도를 높이기 위해 사용될 수 있다.
- [0049] 주위온도를 조절하기 위해, 제2히터(50) 및 냉각챔버(30) 등에 연결되는 PID(Proportional Integral Derivative) 온도 제어기를 설치할 수 있다. 제2히터(50) 및 냉각챔버(30)에 의해 샘플(81)의 가열과 냉각이 동시에 가능하고, 전체 샘플 온도는 PID 온도 제어기에 의해 용이하게 제어될 수 있다.
- [0050] 제4열전대(51)는 제2히터(50)에 설치될 수 있고, 주위온도 및 제2히터(50) 등의 온도를 측정할 수 있다.
- [0051] 제1메탈블록(60)은 냉각챔버(30)의 제1공간(32)에 설치되고, 제2지지대(40)의 상부에 설치될 수 있다.
- [0052] 제2메탈블록(61)은 냉각챔버(30)의 제1공간(32)에 설치되고, 제1메탈블록(60)과 일정 간격으로 이격 배치되며, 제2지지대(40)의 상부에 설치될 수 있다.
- [0053] 제1메탈블록(60) 및 제2메탈블록(61) 각각에는 두 메탈블록(60, 61) 및/또는 샘플(81)의 온도 구배를 측정하는 제1열전대(82) 및 제2열전대(83)가 설치될 수 있다. 제1열전대(82) 및 제2열전대(83)는 각각 제1메탈블록(60) 및 제2메탈블록(61)의 내부에 설치될 수 있고, 또한 온도 구배를 측정하기 위해 같은 전극으로 직렬 연결될 수 있다. 제1열전대 내지 제4열전대는 지지대(40)와 안정되게 연결되어 저온 및 고온 범위에서 온도의 정확한 값을 제공할 수 있다.

- [0054] 제백계수를 측정하기 위해, 제1열전대(82) 및 제2열전대(83)는 샘플의 온도 구배를 측정하고, 제1프로브(70) 및 제2프로브(71)는 전압을 측정할 수 있다.
- [0055] 제1히터(62)는 제1메탈블록(60) 또는 제2메탈블록(61)에 설치되고, 메탈블록(60, 61) 및/또는 샘플(81)에 온도 구배를 형성할 수 있다. 제1히터(62)는 크기와 외부로의 열복사를 최소화하면서 충분히 큰 저항을 갖도록 설계될 수 있고, 메탈블록 내부에 삽입 설치할 수 있다. 제1히터(62)는 열복사를 차단하기 위해 금속 호일 등으로 차폐될 수 있다.
- [0056] 절연체(63)는 제2지지대(40) 및 메탈블록(60, 61) 사이에 설치되어 이들을 절연시키는 역할을 한다. 절연체(63)는 판상으로 구성될 수 있다.
- [0057] 제1프로브(70)는 제1메탈블록(60)에 형성될 수 있고, 제2프로브(71)는 제2메탈블록(61)에 형성될 수 있다.
- [0058] 제3프로브(72)는 제1메탈블록(60) 및 제2메탈블록(61) 사이에 설치될 수 있다.
- [0059] 제4프로브(73)는 제1메탈블록(60) 및 제2메탈블록(61) 사이에 설치되고, 제3프로브(72)와 일정 간격으로 이격 배치될 수 있다.
- [0060] 이와 같이, 본 발명에서는 선형 형태의 4탐침(four-point probe) 및 반 데르 포우(Van der Pauw)법을 이용하여 전기저항을 측정할 수 있다. 구체적으로, 제1프로브(70), 제2프로브(71), 제3프로브(72), 제4프로브(73) 중 제1프로브(70) 및 제2프로브(71)는 전류를 인가하고, 나머지 제3프로브(72) 및 제4프로브(73)는 전압을 측정하며, 전류와 전압으로부터 전기저항을 구할 수 있다.
- [0061] 기존의 2프로브 구조는 접촉강도에 따라 접촉저항이 발생하는 문제가 있으나, 4프로브 구조의 경우 접촉저항을 제거할 수 있는 이점이 있다.
- [0062] 옴 미터를 이용하여 옴 접촉을 먼저 확인한 후, 전류와 전압을 확인할 수 있다. 전류계는 직렬 연결될 수 있고, 전압계는 병렬 연결될 수 있다.
- [0063] 제백계수 측정시에는 제1프로브(70) 및 제2프로브(71)만 이용하고, 제3프로브(72) 및 제4프로브(73)는 이용하지 않을 수 있다. 전기저항 측정시에는 4개의 프로브를 모두 이용할 수 있다.
- [0064] 중앙의 프로브(72, 73)를 분리하거나 외부 접촉을 변경시킴으로써, 4프로브 구조에서 2프로브 구조로 용이하게 변경할 수 있다.
- [0065] 제3프로브(72) 및 제4프로브(73)는 승강판(74) 및 승강조절나사(75)에 의해 상하방향으로 이동 가능하며, 이에 따라 프로브(72, 73)와 샘플(81)의 안정된 접촉 등을 확보할 수 있고, 고온에 의해 영향을 받지 않을 수 있다.
- [0066] 승강판(74)은 제3프로브(72) 및 제4프로브(73)와 체결되어 이들을 각각 지지하고, 승강조절나사(75)에 의해 상하방향으로 승강할 수 있다.
- [0067] 승강조절나사(75)는 승강판(74)과 나사결합하고, 회전에 의해 승강판(74)을 승강시킬 수 있다. 즉, 승강조절나사(75)를 돌려서 승강판(74)을 상하방향으로 승강시킬 수 있다. 승강조절나사(75)는 승강판(74)에 복수 개(75a, 75b)로 설치될 수 있다.
- [0068] 샘플홀더(80)는 냉각챔버(30)의 제1공간(32) 및 메탈블록(60, 61) 상부에 설치되고, 샘플(81)을 지지하는 역할을 한다. 샘플홀더(80)는 절연체로 이루어질 수 있다.
- [0069] 샘플(81)은 메탈블록(60, 61) 상부에 배치되고, 샘플홀더(80)에 의해 지지될 수 있다. 샘플(81)은 측정 장치의 수평방향 기하구조로 인해 매우 용이하게 조립 및 설치될 수 있다.
- [0070] 압축부재(90)는 제2캡(43)과 샘플홀더(80) 사이에 설치되고, 샘플홀더(80)을 압축하여 메탈블록(60, 61) 및 샘플(81)의 접촉을 개선하는 역할을 한다. 압축부재(90)는 가이드 부재(91)와 결합할 수 있고, 이를 위해 가이드 부재(91)의 상단이 삽입되는 가이드 홈을 하부에 구비할 수 있다.
- [0071] 가이드부재(91)는 압축부재(90)와 결합하여 이를 안내하는 역할을 할 수 있다. 가이드부재(91)는 제2지지대(40) 상부에 설치되고, 긴 막대 형상으로 이루어질 수 있으며, 승강판(74)에 복수 개(91a, 91b)로 설치될 수 있다.
- [0072] 또한, 샘플(81)의 두 지점 사이의 열전 전압 및 온도 구배를 측정하기 위해 복수의 전압계(미도시)를 사용할 수 있으며, 각 부품들을 제어하고 측정값의 표시와 저장 및 분석 등을 위해 컴퓨터(미도시)를 사용할 수 있다.
- [0073] 도 5는 본 발명에 따른 장치를 이용하여 측정된 온도 변화 대 전압 변화의 그래프로서, 533K에서 측정된 온도

구배의 함수로서 열전 전압을 나타낸 것이며, 여기서 기울기가 제백계수이다. 기울기가 거의 완전한 직선인데, 이는 측정 에러가 매우 작음을 나타낸다.

[0074] 도 6은 본 발명에 따른 장치를 이용하여 측정된 전류 대 전압의 그래프로서, 300K에서 측정된 전류의 함수로서 전압을 나타낸 것이며, 여기서 기울기가 전기저항이다.

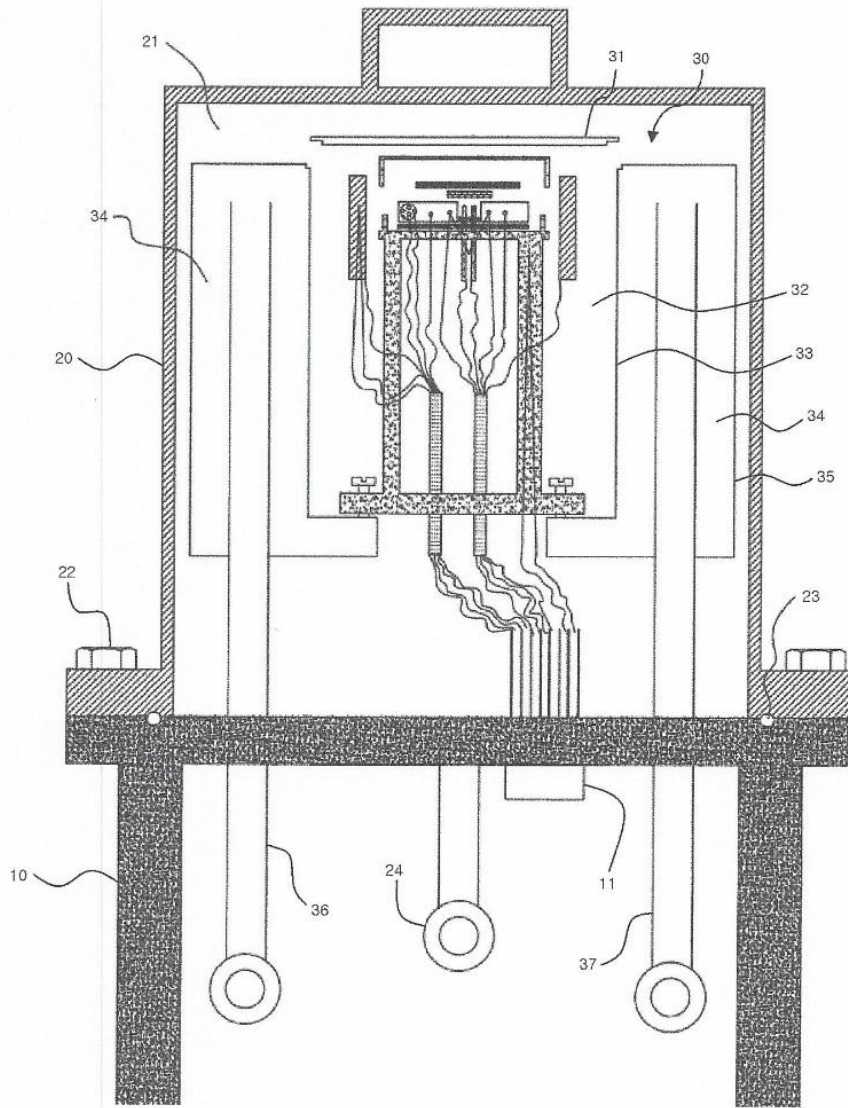
[0075] 본 발명에 따른 장치는 지온 및 고온 범위에서 제백계수 및 전기저항을 측정할 수 있으며, 조작이 간편하고 샘플을 바꾸기가 용이하며, 안정된 접촉을 제공하고 다양한 크기와 형상을 갖는 박막과 벌크 샘플의 측정에 적합하다.

[0076] 본 발명에 따른 장치는 반도체 소재에 적용될 수 있고, 예를 들어 차량 내 시트의 냉각재, 정수기의 냉각재, 반도체 분야 등에 적용될 수 있다. 또한, 기존의 장치는 수평으로 설치되었으나, 본 발명의 장치는 수직으로 설치 가능하다. 또한, 기존 장비는 1억 원 이상의 고가였으나, 본 발명의 장치는 천만 원 이하로 제작될 수 있다.

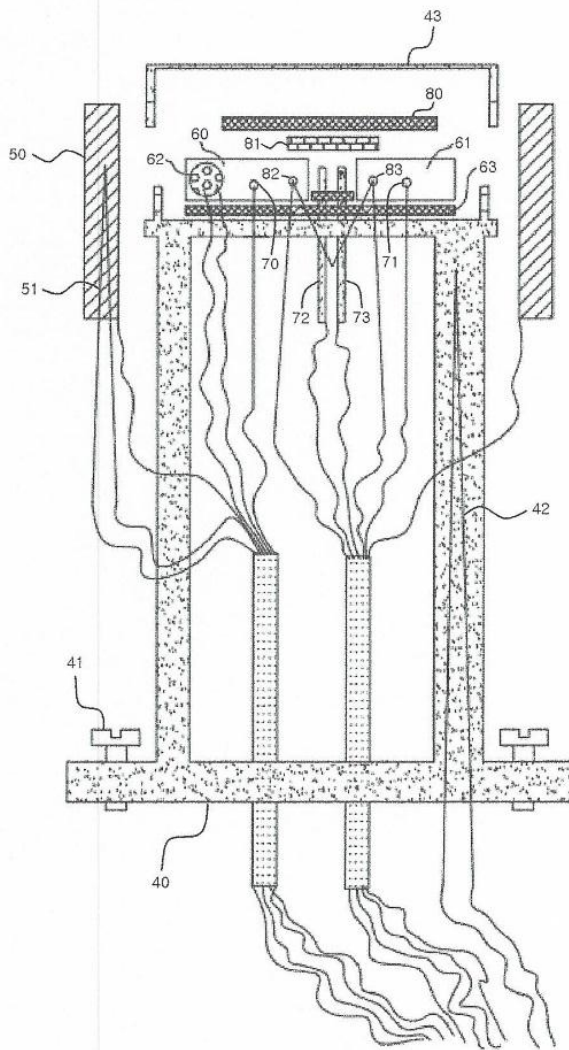
부호의 설명

[0077] 10: 제1지지대, 11: 필터판, 20: 진공챔버, 21: 내부공간, 22: 제1결합부재, 23: 밀봉부재, 24: 진공펌프, 30: 냉각챔버, 31: 제1캡, 32: 제1공간, 33: 내통, 34: 제2공간, 35: 외통, 36: 냉각매체 유입관, 37: 냉각매체 배출관, 40: 제2지지대, 41: 제2결합부재, 42: 제3열전대, 43: 제2캡, 50: 제2히터, 51: 제4열전대, 60: 제1메탈 블록, 61: 제2메탈블록, 62: 제1히터, 63: 절연체, 70: 제1프로브, 71: 제2프로브, 72: 제3프로브, 73: 제4프로브, 74: 승강관, 75: 승강조절나사, 80: 샘플홀더, 81: 샘플, 82: 제1열전대, 83: 제2열전대, 90: 압축부재, 91: 가이드부재

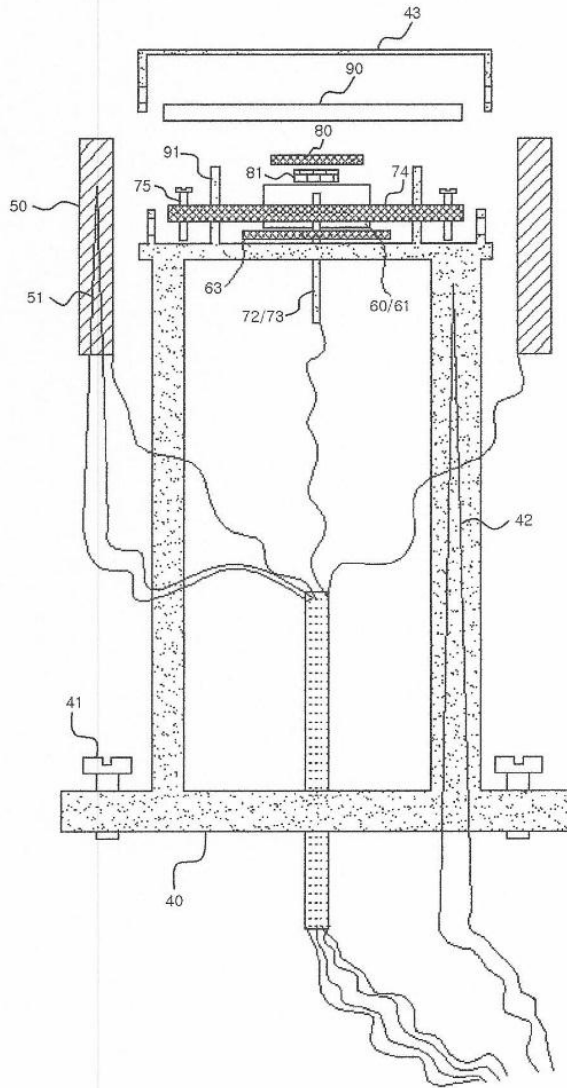
도면
도면1



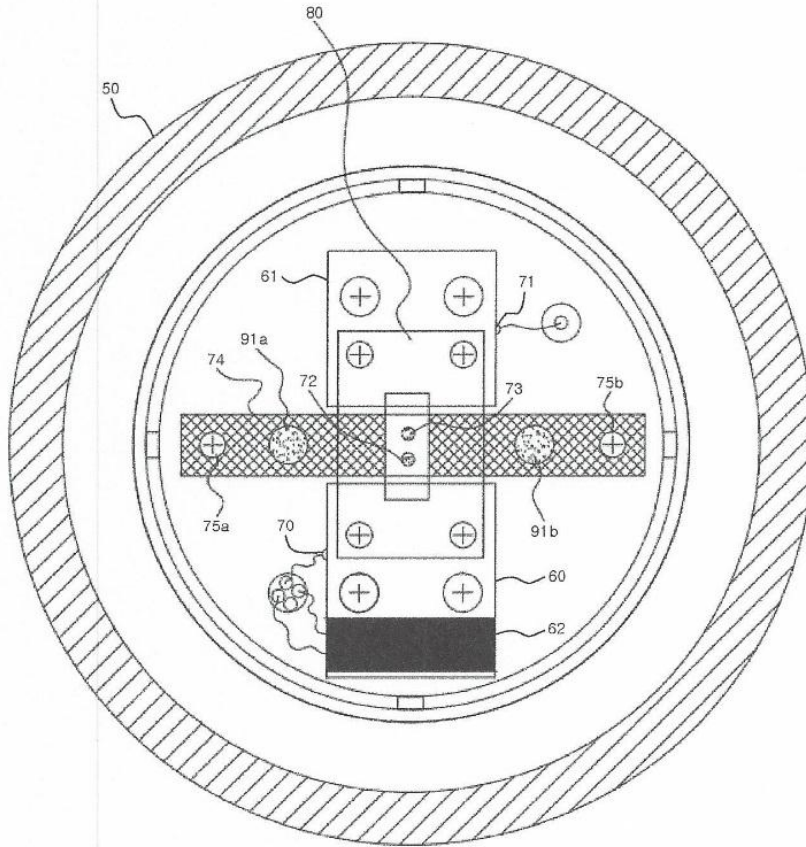
도면2



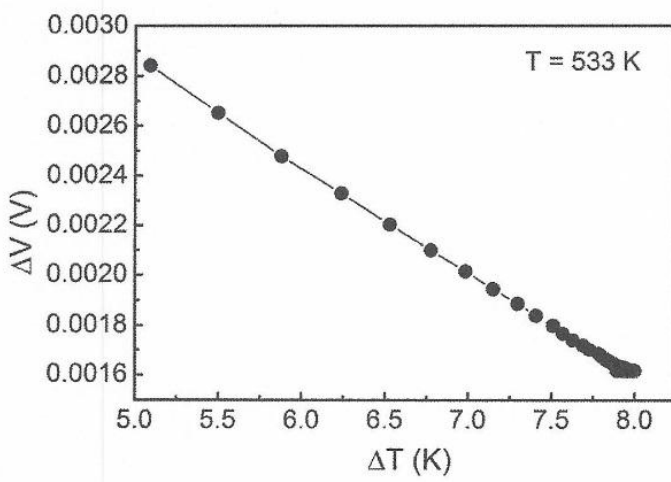
도면3



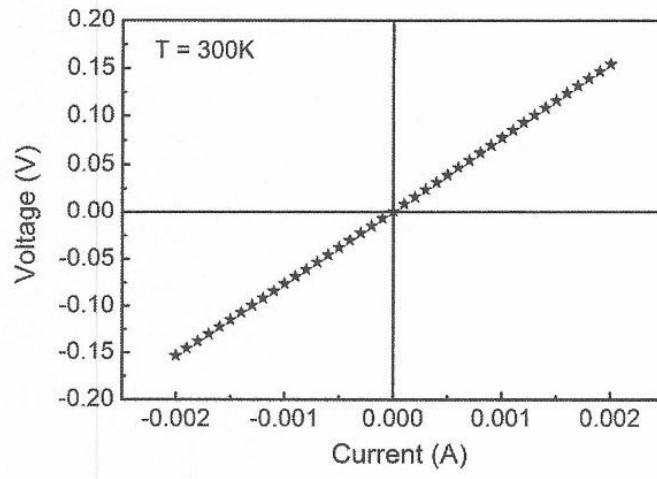
도면4



도면5




도면6



APPENDIX 4: COMPACT HOT PRESS APPARATUS (미니 핫

프레스 장치)

등록특허 10-1753980

	(19) 대한민국특허청(KR) (12) 등록특허공보(B1)	(45) 공고일자 2017년07월06일 (11) 등록번호 10-1753980 (24) 등록일자 2017년06월28일
	(51) 국제특허분류(Int. Cl.) B30B 11/02 (2006.01) B30B 15/02 (2017.01) B30B 15/12 (2006.01) B30B 15/34 (2006.01) (52) CPC특허분류 B30B 11/02 (2013.01) B30B 11/027 (2013.01) (21) 출원번호 10-2015-0128968 (22) 출원일자 2015년09월11일 심사청구일자 2015년09월11일 (65) 공개번호 10-2017-0031436 (43) 공개일자 2017년03월21일 (56) 선행기술조사문헌 JP2646732 B2* JP61199002 A* JP7083959 B2* *는 심사관에 의하여 인용된 문헌	(73) 특허권자 울산대학교 산학협력단 울산광역시 남구 대학로 93(무거동) (72) 발명자 조성래 부산광역시 해운대구 해운대해변로 349-25, 101동 1301호 (중동, 해운대중동두산위브아파트) 권해웅 부산광역시 남구 분포로 111, 139동 504호(용호동, 엘지메트로시티아파트) (덧면에 계속) (74) 대리인 특허법인다나

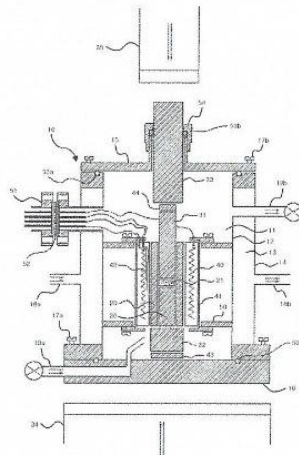
전체 청구항 수 : 총 11 항 심사관 : 김영훈

(54) 발명의 명칭 미니 핫 프레스 장치

(57) 요약

본 발명은 미니 핫 프레스 장치에 관한 것으로, 특히 저진공, 고진공, 초고진공, 고압 가스, 가스 흐름, 심지어는 공기 등과 같은 다양한 주위 환경에서 가압과 가열에 의해 다결정 소재를 만들거나 어닐링 목적으로 사용될 수 있는 장치에 관한 것이다.

대표도 - 도1



- (52) CPC특허분류
B30B 15/022 (2013.01)
B30B 15/12 (2013.01)
B30B 15/34 (2013.01)

- (72) 발명자

웬 반 황

울산 남구 대학로

박은지

울산광역시 남구 옥현로2번길 11, 105호 (무거동)

박은정

울산광역시 남구 옥현로2번길 11, 105호 (무거동)

김말식

경상북도 포항시 북구 양학로34번길 14, 104동
1607호(학잠동, 대림힐타운)

이 발명을 지원한 국가연구개발사업

과제고유번호 G031590912

부처명 산업통상자원부

연구관리전문기관 한국에너지기술평가원

연구사업명 에너지기술개발사업

연구과제명 전자구조변형과 최적도핑을 통한 ZT=2.5 고효율 전이금속반도체 열전 신물질 개발

기여율 1/1

주관기관 울산대학교 산학협력단

연구기간 2014.10.01 ~ 2015.09.30

명세서

청구범위

청구항 1

내통, 내통의 안쪽에 형성되는 제1공간, 내통보다 크기가 크고 내통과 밀봉되도록 연결되는 외통, 내통과 외통 사이에 형성되는 밀봉된 공간으로서 냉각매체를 수용하는 제2공간, 내통과 외통의 상단에 설치되는 캡, 내통과 외통의 하단에 설치되는 바닥판을 구비하는 챔버;

챔버의 제1공간에 설치되고, 내부에 소재를 수용하는 중공 몰드;

중공 몰드 내부에 삽입되고, 소재의 하부에 위치하는 제1로드;

중공 몰드 내부에 삽입되고, 소재의 상부에 위치하는 제2로드;

챔버의 제1공간에서 제1로드의 하부에 위치하는 제3로드;

제2로드의 상부에 위치하고, 챔버의 캡을 관통하도록 설치되어 챔버의 제1공간 및 챔버의 외부에 걸쳐 배치되는 제4로드;

챔버의 제1공간에 중공 몰드를 둘러싸도록 설치되는 히터;

챔버의 외부에 설치되고, 제4로드를 가압하는 프레스를 구비하며,

중공 몰드, 제3로드 및 제4로드는 절연체로 이루어져서 프레스 중 소재의 전기저항 측정이 가능하고, 제1로드 및 제2로드를 전류를 인가하면 자체 발열이 가능한 것을 특징으로 하는 미니 핫 프레스 장치.

청구항 2

제1항에 있어서,

히터는 중공 원통 형상의 실린더 히터인 것을 특징으로 하는 미니 핫 프레스 장치.

청구항 3

제1항에 있어서,

히터의 외부 둘레에 설치되는 열복사 차단재를 추가로 포함하는 미니 핫 프레스 장치.

청구항 4

제1항에 있어서,

중공 몰드 및 히터 사이에 설치되는 열전대를 추가로 포함하는 미니 핫 프레스 장치.

청구항 5

제1항에 있어서,

제2로드와 제4로드 사이 및 제3로드 하부에 각각 설치되는 저열전도판을 추가로 포함하는 미니 핫 프레스 장치.

청구항 6

제1항에 있어서,

챔버의 제2공간과 연결되도록 설치되는 냉각매체 유입구 및 냉각매체 배출구를 추가로 포함하는 미니 핫 프레스 장치.

청구항 7

제1항에 있어서,

챔버의 제1공간과 연결되도록 설치되는 가스 유입구 및 가스 배출구를 추가로 포함하는 미니 핫 프레스 장치.

청구항 8

제7항에 있어서,

가스는 불활성가스, 고압가스, 냉각매체 중에서 선택되는 1종인 것을 특징으로 하는 미니 핫 프레스 장치.

청구항 9

제1항에 있어서,

챔버에는 진공펌프가 연결되어 챔버 내부에 진공이 형성되는 것을 특징으로 하는 미니 핫 프레스 장치.

청구항 10

삭제

청구항 11

제1항에 있어서,

캡과 제4로드의 관통부위에 설치되는 급속-분리 커플링(quick-disconnect coupling), 내통과 외통 및 바닥판 사이, 내통과 외통 및 캡 사이, 캡 및 급속-분리 커플링 사이에 각각 설치되는 오링을 추가로 포함하는 미니 핫 프레스 장치.

청구항 12

제1항에 있어서,

캡과 제4로드의 관통부위에 설치되는 초고진공 벨로우즈(UHV bellows), 내통과 외통 및 바닥판 사이, 내통과 외통 및 캡 사이에 각각 설치되는 구리 가스켓을 추가로 포함하는 미니 핫 프레스 장치.

발명의 설명

기술분야

[0001] 본 발명은 미니 핫 프레스(compact hot press) 장치에 관한 것으로, 특히 저진공, 고진공, 초고진공, 고압가스, 가스 흐름, 심지어는 공기 등과 같은 다양한 주위 환경에서 가압과 가열에 의해 다결정 소재를 만들거나 어닐링 목적으로 사용될 수 있는 장치에 관한 것이다.

배경기술

[0002] 일반적으로 핫 프레스(hot press)란 단순히 뜨거운 상태에서 누른다는 의미로서, 일정한 온도로 가압하여 제품을 성형하는 방법 또는 장치를 일컫는다. 이러한 핫 프레스는 인쇄회로기판(printed circuit board: PCB),

섬유판재, 고급건축자재(장판, 내화벽돌), 자동차용 강판 등의 생산 공정 중 뜨거운 상태에서 가압성형이 필요한 공정에 이용되며, 제시한 응용분야 이외에도 디스플레이(LCD, PDP 등) 산업, 연성인쇄회로 기판 성형 같은 특수한 산업분야에서의 활용이 증가하고 있는 추세이다.

[0003] 기존의 핫 프레스 장치는 일반적으로 큰 크기를 가졌고, 프레스 성형 이외에 다른 기능이 없었다.

발명의 내용

해결하려는 과제

[0004] 본 발명의 목적은 크기가 작고 다양한 기능을 갖는 미니 핫 프레스 장치를 제공하는 것이다.

과제의 해결 수단

[0005] 본 발명은 상술한 목적을 달성하기 위해, 내통, 내통의 안쪽에 형성되는 제1공간, 내통보다 크기가 크고 내통과 밀봉되도록 연결되는 외통, 내통과 외통 사이에 형성되는 밀봉된 공간으로서 냉각매체를 수용하는 제2공간, 내통과 외통의 상단에 설치되는 캡, 내통과 외통의 하단에 설치되는 바닥판을 구비하는 챔버; 챔버의 제1공간에 설치되고, 내부에 소재를 수용하는 중공 몰드; 중공 몰드 내부에 삽입되고, 소재의 하부에 위치하는 제1로드; 중공 몰드 내부에 삽입되고, 소재의 상부에 위치하는 제2로드; 챔버의 제1공간에서 제1로드의 하부에 위치하는 제3로드; 제2로드의 상부에 위치하고, 챔버의 캡을 관통하도록 설치되어 챔버의 제1공간 및 챔버의 외부에 걸쳐 배치되는 제4로드; 챔버의 제1공간에 중공 몰드를 둘러싸도록 설치되는 히터; 챔버의 외부에 설치되고, 제4로드를 가압하는 프레스를 구비하는 미니 핫 프레스 장치를 제공한다.

[0006] 본 발명에서 히터는 중공 원통 형상의 실린더 히터일 수 있다.

[0007] 본 발명에 따른 장치는 히터의 외부 둘레에 설치되는 열복사 차단재를 추가로 포함할 수 있다.

[0008] 본 발명에 따른 장치는 중공 몰드 및 히터 사이에 설치되는 열전대를 추가로 포함할 수 있다.

[0009] 본 발명에 따른 장치는 제2로드와 제4로드 사이 및 제3로드 하부에 각각 설치되는 저열전도판을 추가로 포함할 수 있다.

[0010] 본 발명에 따른 장치는 챔버의 제2공간과 연결되도록 설치되는 냉각매체 유입구 및 냉각매체 배출구를 추가로 포함할 수 있다.

[0011] 본 발명에 따른 장치는 챔버의 제1공간과 연결되도록 설치되는 가스 유입구 및 가스 배출구를 추가로 포함할 수 있다.

[0012] 본 발명에서 가스는 불활성가스, 고압가스, 냉각매체일 수 있다.

[0013] 본 발명에서 챔버에는 진공펌프가 연결되어 챔버 내부에 진공이 형성될 수 있다.

[0014] 본 발명에서 중공 몰드, 제3로드 및 제4로드는 알루미늄과 같은 절연체로 이루어져서 프레스 중 소재의 전기저항 측정이 가능하고, 제1로드 및 제2로드로 전류를 인가하면 자체 발열이 가능하다.

[0015] 본 발명에 따른 장치는 캡과 제4로드의 관통부위에 설치되는 급속-분리 커플링(quick-disconnect coupling), 내통과 외통 및 바닥판 사이, 내통과 외통 및 캡 사이, 캡 및 급속-분리 커플링 사이에 각각 설치되는 오링을 추가로 포함할 수 있다.

[0016] 본 발명에 따른 장치는 캡과 제4로드의 관통부위에 설치되는 초고진공 벨로우즈(UHV bellows), 내통과 외통 및 바닥판 사이, 내통과 외통 및 캡 사이에 각각 설치되는 구리 가스켓을 추가로 포함할 수 있다.

발명의 효과

[0017] 본 발명에 따른 장치는 크기가 작고 다양한 기능을 갖는다.

도면의 간단한 설명

[0018] 도 1은 본 발명의 일 실시형태에 따라 고진공 또는 고압가스용으로 사용될 수 있는 미니 핫 프레스 장치의 전체 구성을 나타내는 단면도이다.

도 2는 도 1의 평면도이다.

도 3은 본 발명의 다른 실시형태에 따라 초고진공용으로 사용될 수 있는 미니 핫 프레스 장치의 전체 구성을 나타내는 단면도이다.

도 4는 도 3의 평면도이다.

도 5는 본 발명에서 사용되는 몰드의 단면도이다.

발명을 실시하기 위한 구체적인 내용

- [0019] 이하, 첨부도면을 참조하여 본 발명을 상세하게 설명한다.
- [0020] 도 1은 본 발명의 일 실시형태에 따라 고진공 또는 고압가스용으로 사용될 수 있는 미니 핫 프레스 장치의 전체 구성을 나타내는 단면도이고, 도 2는 도 1의 평면도이며, 도 3은 본 발명의 다른 실시형태에 따라 초고진공용으로 사용될 수 있는 미니 핫 프레스 장치의 전체 구성을 나타내는 단면도이고, 도 4는 도 3의 평면도이며, 도 5는 본 발명에서 사용되는 몰드의 단면도이다.
- [0021] 본 발명에 따른 미니 핫 프레스 장치는 챔버(10), 제1공간(11), 내통(12), 제2공간(13), 외통(14), 캡(15), 바닥판(16), 결합부재(17a, 17b), 냉각매체 유입구(18a), 냉각매체 배출구(18b), 가스 유입구(19a), 가스 배출구(19b), 중공 몰드(20), 소재(21), 제1로드(30), 제2로드(31), 제3로드(32), 제4로드(33), 제1프레스(34), 제2프레스(35), 히터(40), 열복사 차단재(41), 열전대(42), 제1저열전도판(43), 제2저열전도판(44), 지지대(50), 멀티핀(51), 구리 가스켓(52, 56a, 56b, 56c), 오링(53a, 53b, 53c), 급속-분리 커플링(54), 진공펌프(55), 초고진공 벨로우즈(57) 등으로 구성될 수 있다.
- [0022] 본 발명에 따른 미니 핫 프레스 장치의 크기는 가로, 세로, 높이방향으로 각각 1 m 이하일 수 있다.
- [0023] 챔버(10)는 제1공간(11), 내통(12), 제2공간(13), 외통(14), 캡(15), 바닥판(16), 결합부재(17a, 17b), 냉각매체 유입구(18a), 냉각매체 배출구(18b), 가스 유입구(19a), 가스 배출구(19b) 등으로 구성될 수 있다.
- [0024] 제1공간(11)은 내통(12)의 안쪽에 형성되는 내통(12)의 내부공간으로서, 캡(15) 및 바닥판(16)에 의해 밀폐될 수 있다.
- [0025] 내통(12)은 예를 들어 원통형으로 구성될 수 있다. 내통(12)의 상부와 하부는 개방될 수 있고, 각각 캡(15) 및 바닥판(16)에 의해 밀폐될 수 있다.
- [0026] 제2공간(13)은 내통(12)과 외통(14) 사이에 형성되는 밀봉된 공간으로서 냉각매체를 수용할 수 있다.
- [0027] 외통(14)은 내통(12)보다 크기(직경)가 크고 내통(12)과 밀봉되도록 연결될 수 있다. 외통(14)은 예를 들어 원통형으로 구성될 수 있다.
- [0028] 캡(15)은 내통(12)과 외통(14)의 상단에 탈착 가능하게 설치될 수 있다.
- [0029] 바닥판(16)은 내통(12)과 외통(14)의 하단에 탈착 가능하게 설치될 수 있다.
- [0030] 결합부재(17a, 17b)는 내통(12)과 외통(14) 및 바닥판(16) 그리고 내통(12)과 외통(14) 및 캡(15)을 결합시키는 역할을 하며, 예를 들어 나사결합부재 등을 사용할 수 있다.
- [0031] 냉각매체 유입구(18a) 및 냉각매체 배출구(18b)는 챔버(10)의 제2공간(13)과 연결되도록 설치되고, 이를 통해 냉각매체가 챔버(10)에 유입되고 배출될 수 있다. 냉각매체를 통해 챔버(10)의 온도를 쉽게 제어하고 냉각할 수 있다. 냉각매체의 체류시간과 냉각효율 등을 고려하면, 냉각매체 유입구(18a)는 챔버(10)의 하부에 설치되고, 냉각매체 배출구(18b)는 챔버(10)의 상부에 설치되는 것이 바람직하다. 냉각매체로는 예를 들어 물, 액체질소 등을 사용할 수 있다.
- [0032] 가스 유입구(19a) 및 가스 배출구(19b)는 챔버(10)의 제1공간(11)과 연결되도록 설치되고, 이를 통해 가스가 챔버(10)에 유입되고 배출될 수 있다. 가스의 체류시간 등을 고려하면, 가스 유입구(19a)는 챔버(10)의 하부에 설치되고, 가스 배출구(19b)는 챔버(10)의 상부에 설치되는 것이 바람직하다. 가스 유입구(19a) 및 가스 배출구(19b)에는 가스의 흐름을 개폐하기 위한 밸브가 설치될 수 있다.
- [0033] 가스로는 예를 들어 불활성가스, 고압가스, 냉각매체 등을 사용할 수 있다. 불활성 가스는 산화되기 쉬운 소재(21)의 산화를 방지하기 위해 사용될 수 있다. 고압가스는 고온에서 증발되기 쉬운 소재(21)의 증발 온도를 중

가시킴을 위해 사용될 수 있다. 고압가스는 예를 들어 상온에서 2 내지 100 bar의 가스일 수 있다. 냉각매체는 소재(21)를 직접 냉각하기 위해 사용될 수 있다. 냉각매체는 고압의 가스 형태로 공급될 수 있다.

[0034] 한편, 챔버(10)에는 진공펌프(55)가 연결되어 챔버(10)의 제1공간(11)에 진공이 형성될 수 있다. 진공도는 저진공(1 내지 1000 mbar), 중진공(10^{-3} 내지 1 mbar), 고진공(10^{-7} 내지 10^{-3} mbar), 초고진공(10^{-10} 내지 10^{-7} mbar), 극고진공(10^{-10} mbar 미만) 중에서 적절하게 선택될 수 있다.

[0035] 이와 같이, 사용자의 필요에 따라, 챔버(10) 내부를 불활성가스 분위기, 고압가스 분위기, 냉각 분위기, 진공 분위기 등 다양한 분위기로 형성 가능하다.

[0036] 중공 몰드(20)는 챔버(10)의 제1공간(11)에 설치되고, 내부에 성형될 소재(21)를 수용할 수 있다. 몰드(20)는 압력에 강한 스테인리스 스틸, 세라믹, 금속, 그래파이트 등으로 제작될 수 있다. 몰드(20)는 바람직하게는 도 5에 예시된 바와 같이 원통형 중공체일 수 있다. 몰드(20)의 내벽은 그래파이트 박층으로 코팅될 수 있고, 이에 따라 몰드(20)와 소재(21) 사이의 화학반응이나 상호작용을 방지할 수 있고, 소재(21)를 몰드(20)로부터 쉽게 꺼낼 수 있다. 몰드(20)는 균일한 가열을 위해 실린더 히터(40) 내부에 히터(40)와 동축으로 배치될 수 있다.

[0037] 소재(21)는 다결정 소재로 성형할 경우에는 분말 소재를 사용할 수 있다. 분말 소재(21)는 몰드(20) 내에서 제1로드(30) 및 제2로드(31) 사이에 위치할 수 있다.

[0038] 제1로드(30)는 중공 몰드(20) 내부에 삽입되고, 소재(21)의 하부에 위치할 수 있다. 제1로드(30)의 상단은 그래파이트 박층으로 코팅될 수 있고, 이에 따라 제1로드(30)와 소재(21) 사이의 화학반응이나 상호작용을 방지할 수 있다.

[0039] 제2로드(31)는 중공 몰드(20) 내부에 삽입되고, 소재(21)의 상부에 위치할 수 있다. 제2로드(31)의 하단은 그래파이트 박층으로 코팅될 수 있고, 이에 따라 제2로드(31)와 소재(21) 사이의 화학반응이나 상호작용을 방지할 수 있다.

[0040] 제3로드(32)는 챔버(10)의 제1공간(11)에서 제1로드(30)의 하부에 위치할 수 있다. 제3로드(32)는 제1로드(30)와 일체로 형성될 수 있다.

[0041] 제4로드(33)는 제2로드(31)의 상부에 위치하고, 챔버(10)의 캡(15)을 관통하도록 설치되어 챔버(10)의 제1공간(11) 및 챔버(10)의 외부에 걸쳐 배치될 수 있다.

[0042] 제1프레스(34) 및 제2프레스(35)는 챔버(10)의 외부에 설치되고, 제4로드(33) 및/또는 챔버(10)의 바닥판(16)을 가압할 수 있다. 제1프레스(34) 및 제2프레스(35)는 유압 프레스일 수 있다.

[0043] 히터(40)는 챔버(10)의 제1공간(11)에 중공 몰드(20)를 둘러싸도록 설치될 수 있다. 히터(40)는 소재(21)를 가열하기 위해 사용될 수 있다. 히터(40)는 챔버(10)의 상부를 통해 쉽게 빼낼 수 있고, 소재(21)와 함께 가압되지 않는다. 히터(40)는 바람직하게는 중공 원통 형상의 실린더 히터일 수 있다. 히터(40)를 실린더 히터로 구성함에 따라, 중공 몰드(20) 및 소재(21) 등을 균일하고 신속하게 가열하여 가열효율을 개선할 수 있다. 히터(40)의 가열방식은 유도 기전력 가열방식(RF 방식 가열) 또는 직접 가열방식일 수 있다. 히터(40)는 PID(Proportional Integral Derivative) 온도 제어기와 연결될 수 있고, 온도는 PID 제어기를 이용하여 쉽고 정확하게 제어될 수 있다.

[0044] 중공 몰드(20), 제3로드(32) 및 제4로드(33)는 알루미늄과 같은 절연체로 이루어져서 프레스 중 소재의 전기저항을 실시간으로 측정할 수 있고, 또한 제1로드(30) 및 제2로드(31)로 전류를 인가하면 자체 발열이 가능하여 별도의 히터를 사용하지 않을 수 있다.

[0045] 열복사 차단재(41)는 히터(40)의 외부 둘레에 설치되어 외부로의 열복사를 차단하는 역할을 한다. 열복사 차단재(41)는 탄탈륨, 니크롬, 인코넬, 알루미늄, 탄화규소, 질화규소, 질화알루미늄, 질화붕소, 탄화텅스텐, 산화베릴륨, 바륨티타네이트, 지르코니아, 페라이트 등과 같은 금속 또는 세라믹 소재로 구성될 수 있다.

[0046] 열전대(42)는 중공 몰드(20) 및 히터(40) 사이에 설치되어 소재(21) 등의 온도를 실시간으로 측정할 수 있다.

[0047] 제1저열전도판(43) 및 제2저열전도판(44)는 제3로드(32) 하부, 제2로드(31)와 제4로드(33) 사이에 각각 설치되어 외부로의 열전달을 방지하는 역할을 한다. 제1저열전도판(43) 및 제2저열전도판(44)는 저열전도도를 갖는 소재로 구성될 수 있고, 예를 들어 상술한 세라믹 소재로 구성될 수 있다. 제1저열전도판(43) 및 제2저열전도판(44)의 열전도도는 예를 들어 0.1 내지 100 W/m·K일 수 있다.

- [0048] 지지대(50)는 챔버(10)의 제1공간(11)에 설치되어 히터(40) 등을 지지하는 역할을 한다.
- [0049] 멀티핀(51)은 챔버(10)의 외부에 설치되고, 히터(40) 및 열전대(42)와 전선을 통해 연결되어 이들을 외부와 연결하는 역할을 한다. 멀티핀(51)에는 밀봉을 위해 구리 가스켓(52)이 설치될 수 있다.
- [0050] 진공펌프(55)는 도 2 및 4에 예시된 별도의 통로를 통해 챔버(10)와 연결될 수 있다. 통로에는 고진공의 경우 고무 오링, 초고진공의 경우 구리 가스켓을 사용할 수 있다.
- [0051] 도 1 및 2의 실시형태는 고진공 또는 고압가스용으로 적합한 형태로서, 챔버(10) 내부의 고진공을 유지하기 위해 오링(53a, 53b, 53c) 및 급속-분리 커플링(54)이 설치될 수 있다.
- [0052] 오링(53a, 53b, 53c)은 내통(12)과 외통(14) 및 바닥판(16) 사이, 내통(12)과 외통(14) 및 캡(15) 사이, 캡(15) 및 급속-분리 커플링(54) 사이에 각각 설치되어 각 결합부위를 밀봉할 수 있다. 오링(53a, 53b, 53c)으로는 고무 오링을 사용할 수 있다.
- [0053] 급속-분리 커플링(54)는 캡(15)과 제4로드(33)의 관통부위에 설치되고, 신속한 분리 및 장착이 가능하다.
- [0054] 도 3 및 4의 실시형태는 초고진공용으로 적합한 형태로서, 챔버(10) 내부의 초고진공을 유지하기 위해, 도 1 및 2의 오링(53a, 53b, 53c) 및 급속-분리 커플링(54) 대신에, 구리 가스켓(56a, 56b, 56c) 및 초고진공 벨로우즈(57)가 설치될 수 있다.
- [0055] 구리 가스켓(56a, 56b, 56c)(Conflate flange)은 내통(12)과 외통(14) 및 바닥판(16) 사이, 내통(12)과 외통(14) 및 캡(15) 사이에 각각 설치되어 각 결합부위를 고도로 밀봉할 수 있다.
- [0056] 초고진공 벨로우즈(57)는 캡(15)과 제4로드(33)의 관통부위에 설치되어 결합부위를 고도로 밀봉할 수 있다.
- [0057] 본 발명의 장치는 다기능성 장치로서, 다양한 기능을 갖는다. 본 발명의 장치는 분말로부터 다결정 소재를 제조하는데 사용될 수 있고, 또한 어닐링 목적의 퍼니스로도 사용될 수 있다. 본 발명의 장치는 저진공, 고진공 또는 초고진공에서 작동하거나, 고압가스 또는 가스 흐름을 포함하거나, 심지어 공기 중에서도 작동할 수 있다. 본 발명에서는 실린더 히터 및 수냉이 작동 온도를 제어하기 위해 사용될 수 있고, 외부로의 열 흐름을 방지하기 위해 열복사 차단재 및 저열전도판이 특정 위치에 사용될 수 있다. 주변(ambient) 환경은 장치의 사용 목적에 따라 저진공, 고진공, 초고진공, 고압 가스, 가스 흐름, 공기 등일 수 있다.
- [0058] 핫 프레스 방법을 이용하여 다결정 소재를 만드는 경우에는, 분말을 실린더 몰드(20) 내부에 첨가한다. 몰드(20)는 실린더 히터(40) 내부에 히터(40)와 동축으로 배치한다. 히터(40)는 열복사 차단재(41)로 커버되어 외부로의 열복사를 방지할 수 있다. 또한, 저열전도 소재로 만들어진 2개의 판(43, 44)을 사용하여 몰드(20)로부터 외부로 열전도를 방지할 수 있다. 챔버(10) 내부에 진공(저진공, 고진공 또는 초고진공)을 만들거나, 소재 산화를 방지하기 위해 챔버(10)에 불활성 가스를 로딩하거나, 소재의 중발 온도를 증가시키기 위해 챔버(10)에 고압 가스를 첨가한 후, 몰드(20)와 소재(21)를 히터(40) 및 PID 제어기를 이용하여 적절한 온도로 가열한다. 열전대(42)를 사용하여 소재(21)의 온도를 측정할 수 있다. 이후, 소재(21)를 유압 프레스(34, 35)를 이용하여 적절한 압력으로 가압한다.
- [0059] 소재를 어닐링할 경우에는, 몰드(20), 제1로드(30), 제2로드(31) 및 제4로드(33)를 빼내고, 하부의 제3로드(32)만을 소재(21)의 지지대로서 사용한다. 소재(21)를 다양한 압력을 갖는 진공 또는 가스 분위기에서 어닐링할 수 있다.
- [0060] 가스 유입구(19a) 및 가스 배출구(19b)의 밸브를 닫고 챔버(10)와 진공펌프(55)를 연결하면 진공을 만들 수 있다. 진공펌프(55)를 차단하고 챔버(10)에 가스를 공급하면 가스 흐름 또는 고압 가스 분위기를 만들 수 있다. 고진공을 위해 고무 오링(53a, 53b, 53c)과 급속-분리 커플링(54)을 사용하고, 초고진공을 위해 구리 가스켓(Conflate flange)(56a, 56b, 56c)을 사용할 수 있다. 소재(21)의 냉각을 위해 가스 흐름 빔을 사용할 수 있다. 고무 오링과 구리 가스켓은 저진공, 고압가스 또는 가스흐름에서도 사용될 수 있으나, 이 경우에는 고무 오링의 사용을 권장하는데, 고무 오링은 챔버 개방 후 재사용할 수 있기 때문이다.

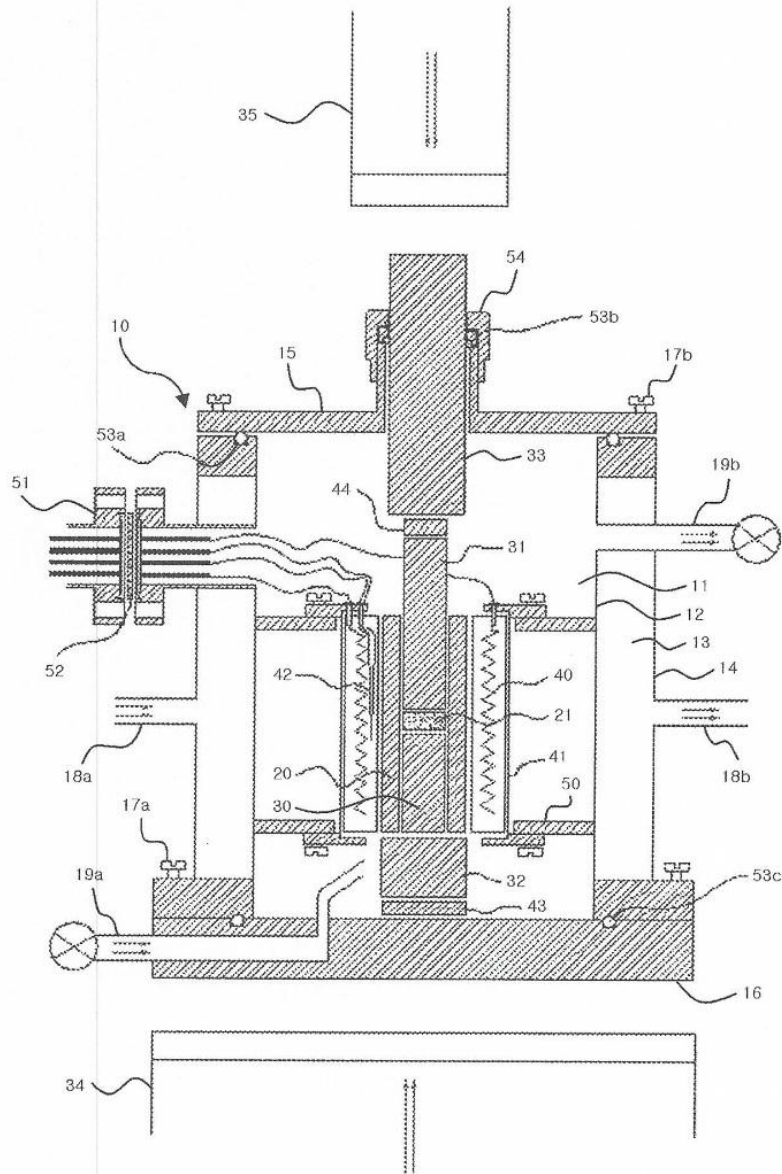
부호의 설명

- [0061] 10: 챔버, 11: 제1공간, 12: 내통, 13: 제2공간, 14: 외통, 15: 캡, 16: 바닥판, 17a, 17b: 결합부재, 18a: 냉각매체 유입구, 18b: 냉각매체 배출구, 19a: 가스 유입구, 19b: 가스 배출구, 20: 중공 몰드, 21: 소재, 30: 제1로드, 31: 제2로드, 32: 제3로드, 33: 제4로드, 34: 제1프레스, 35: 제2프레스, 40: 히터, 41: 열복사

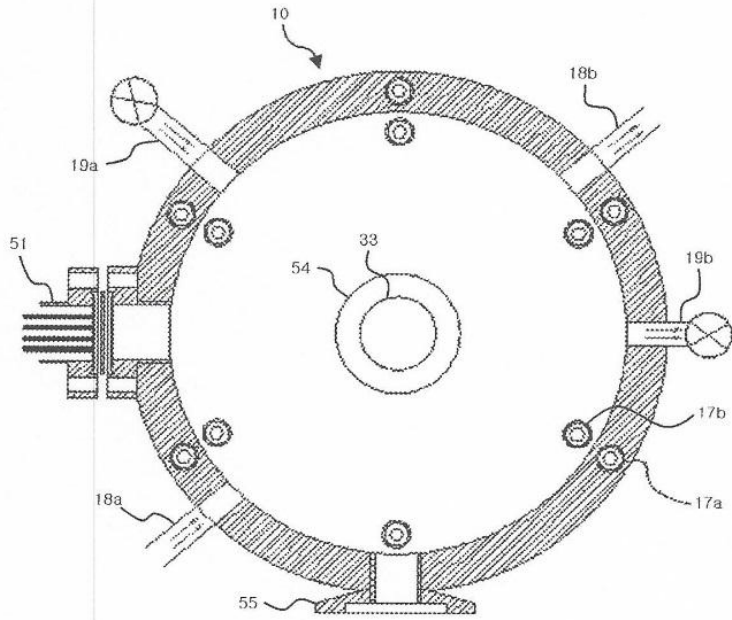
차단재, 42: 열전대, 43: 제1저열전도판, 44: 제2저열전도판, 50: 지지대, 51: 멀티핀, 52: 구리 가스켓, 53a, 53b, 53c: 오링, 54: 급속-분리 커플링, 55: 진공펌프, 56a, 56b, 56c: 구리 가스켓, 57: 초고진공 벨로우즈

도면

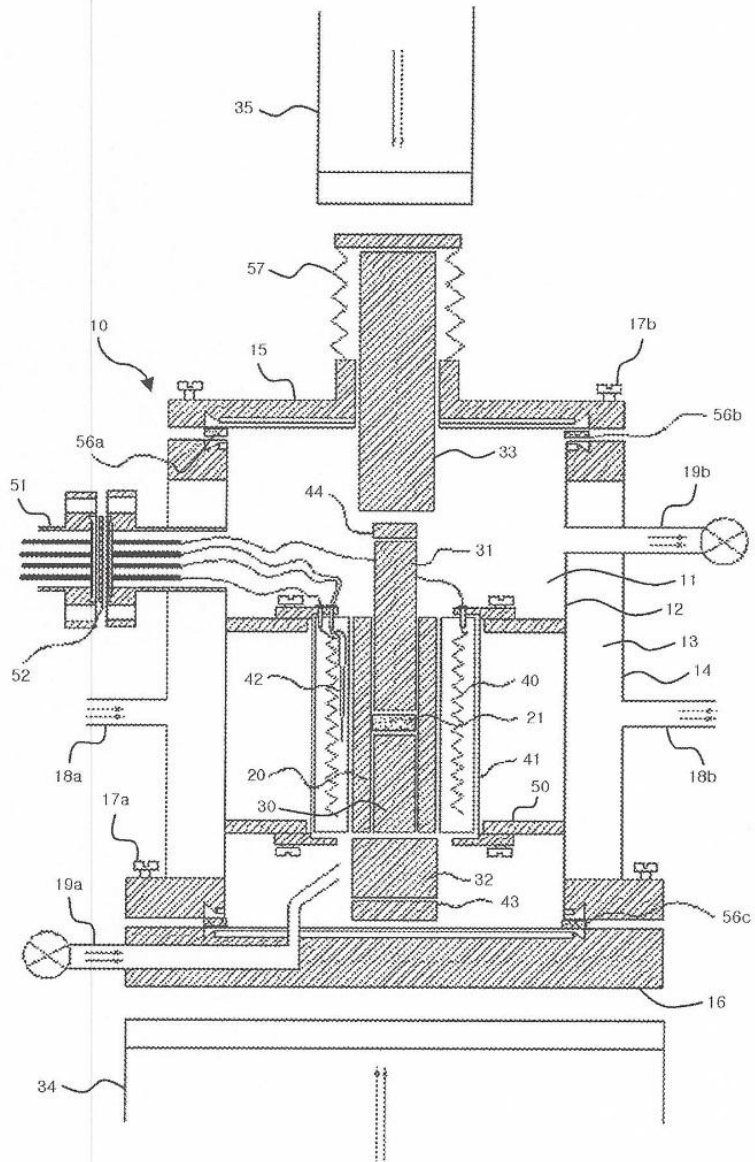
도면1



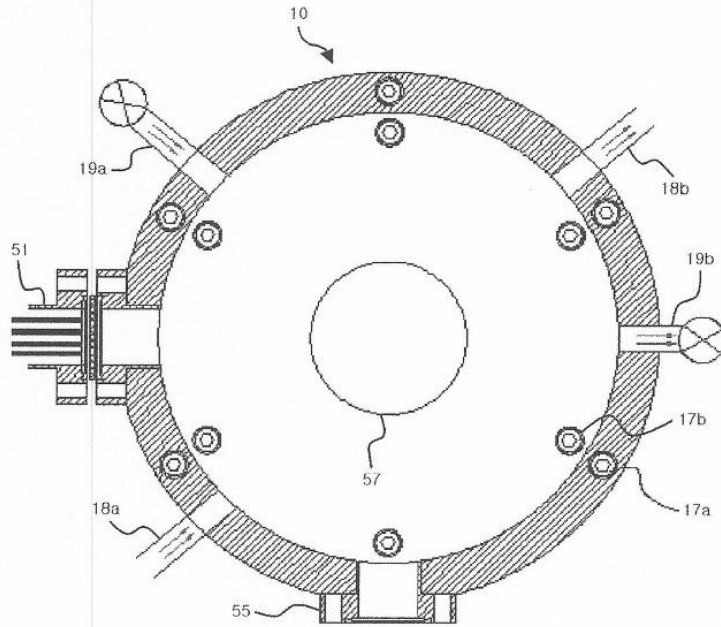
도면2



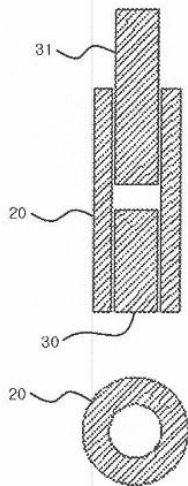
도면3



도면4



도면5



APPENDIX 5: PATENT CERTIFICATE

1. COMPACT HOT PRESS APPARATUS (미니 핫 프레스 장치)

특허증
CERTIFICATE OF PATENT

특허 제 10-1753980 호
Patent Number

출원번호 제 10-2015-0128968 호
Application Number

출원일 2015년 09월 11일
Filing Date

등록일 2017년 06월 28일
Registration Date

발명의 명칭 Title of the Invention
미니 핫 프레스 장치

특허권자 Patentee
울산대학교 산학협력단(230171-*****)
울산광역시 남구 대학로 93(무거동)

발명자 Inventor
등록사항란에 기재

위의 발명은 「특허법」에 따라 특허등록원부에 등록되었음을 증명합니다.
This is to certify that, in accordance with the Patent Act, a patent for the invention
has been registered at the Korean Intellectual Property Office.

2017년 06월 28일

특허청장
COMMISSIONER,
KOREAN INTELLECTUAL PROPERTY OFFICE



특허청
Korean Intellectual
Property Office

등 록 사 항

특 허

등록 제 10-1753980 호

Patent Number

발명자 Inventors

조성래(650408-*****)

부산광역시 해운대구 해운대해변로 349-25, 101동 1301호 (중동,
해운대중등두산위브아파트)

권해웅(541215-*****)

부산광역시 남구 분포로 111, 139동 504호(용호동,
엘지메트로시티아파트)

웬 반 광

울산 남구 대학로

박은지(661002-*****)

울산광역시 남구 옥현로2번길 11, 105호 (무거동)

박은정(680925-*****)

울산광역시 남구 옥현로2번길 11, 105호 (무거동)

김말식(630913-*****)

경상북도 포항시 북구 양학로34번길 14, 104동 1607호(학잠동,
대림힐타운)

2. SEMICONDUCTOR MATERIAL CONTAINING THE Fe₂SiO₄, AND PREPARATION METHOD (Fe₂SiO₄ 계 화합물을 포함하는 반도체 소재 및 이의 제조방법)

특허증
CERTIFICATE OF PATENT

특허 제 10-1676186 호
Patent Number

출원번호 제 10-2015-0123099 호
Application Number

출원일 2015년 08월 31일
Filing Date

등록일 2016년 11월 08일
Registration Date

발명의 명칭 Title of the Invention
Fe₂SiO₄계 화합물을 포함하는 반도체 소재 및 이의 제조방법

특허권자 Patentee
울산대학교 산학협력단(230171-*****)
울산광역시 남구 대학로 93(무거동)

발명자 Inventor
등록사항란에 기재

위의 발명은 「특허법」에 따라 특허등록원부에 등록되었음을 증명합니다.
This is to certify that, in accordance with the Patent Act, a patent for the invention has been registered at the Korean Intellectual Property Office.

2016년 11월 08일

특허청장
COMMISSIONER,
KOREAN INTELLECTUAL PROPERTY OFFICE



3. THERMOELECTRIC MATERIAL CONTAINING HIGHER MANGANESE SILICIDES,
AND PREPARATION METHOD (고망간실리사이드계 화합물을 포함하는 열전소재
및 이의 제조방법)

특허증
CERTIFICATE OF PATENT

특허 제 10-1726498 호
Patent Number

출원번호 제 10-2015-0074584 호
Application Number

출원일 2015년 05월 28일
Filing Date

등록일 2017년 04월 06일
Registration Date

발명의 명칭 Title of the Invention
고망간실리사이드계 화합물을 포함하는 열전소재 및 이의 제조방법

특허권자 Patentee
울산대학교 산학협력단(230171-*****)
울산광역시 남구 대학로 93(무거동)

발명자 Inventor
등록사항란에 기재

위의 발명은 「특허법」에 따라 특허등록원부에 등록되었음을 증명합니다.
This is to certify that, in accordance with the Patent Act, a patent for the invention
has been registered at the Korean Intellectual Property Office.

2017년 04월 06일

특허청장
COMMISSIONER,
KOREAN INTELLECTUAL PROPERTY OFFICE

최 동 규

특허청
Korean Intellectual
Property Office

